Polarization properties of GRMHD black hole accretion models

Alejandra Jiménez Rosales

München 2020

Polarization properties of GRMHD black hole accretion models

Alejandra Jiménez Rosales

Dissertation
an der Fakultät für Physik
der Ludwig–Maximilians–Universität
München

vorgelegt von
Alejandra Jiménez Rosales
aus Toluka, Mexiko

München, den 17.08.2020

Erstgutachter: Professor Dr. Reinhard Genzel
Zweitgutachter: Professor Dr. Andreas Burkert
Tag der mündlichen Prüfung: 01.10.2020

Contents

List of Figures

List of Tables

Zusammenfassung

Räumlich aufgelöste Polarisation ist eine nützliche beobachtbare Größe, die neue Möglichkeiten für die Untersuchung der Gravitation im Starkfeldlimit, der Magnetfeldkonfiguration und der Plasmaphysik in der Nähe von Schwarzen Löchern ermöglicht.

Das Ziel dieser Arbeit ist die Untersuchung der Eigenschaften der Polarisation von Synchotronstrahlung in Akkretionsmodellen von super-massereichen Schwarzen Löchern (SMBH). Des Weiteren werden Werkzeuge entwickelt, welche die Genauigkeit und Gültigkeit der Modelle überprüfen und mit den in der Natur vorkommenden Phänomenen vergleichbar machen. Die Studien werden mithilfe von modernsten Strahlungstransportberechnungen auf Basis von GRMHD (*general relativistic magnetohydrodynamic*) Simulationen durchgeführt. Diese Fragestellung ist besonders interessant aufgrund der neuen und bevorstehenden Polarisationsbeobachtungen auf Ereignishorizont-Skalen von den SMBH-Kandidaten, Sagittarius A* und M87*, welche mit dem interferometrischen Instrument GRAVITY und dem *Event Horizon Telescope* durchgeführt werden.

In Kapitel 2 wird eine Studie der räumlichen Eigenschaften der Polarisationsmuster von verschiedenen Akkretionsmodellen aus einer achsensymmetrischen Simulation von Sagittarius A* bei Millimeter-Wellenlängen vorgestellt. Es wird gezeigt, dass die Stärke der Faraday-Effekte, insbesondere die Faraday-Rotation im Inneren der Emissionsregion, zu substanziell unterschiedlichen Polarisationskonfigurationen im Sub-mm Bereich führt.

Jedes Muster kann mit einer „polarisierten Korrelationslänge“ charakterisiert werden. Dies ist eine räumliche Skala, die den Grad der Ordnung der Konfiguration in Abhängigkeit von der durchschnittlichen Faraday-Tiefe misst. Große Werte weisen auf geordnete Muster hin, bei denen die Faraday-Rotation schwach ist. Hier wird die räumliche Konfiguration durch die zugrunde liegende Magnetfeldgeometrie festgelegt.

Im Gegensatz dazu, charakterisieren kleine Werte ungeordnete Muster, bei denen Faraday-Effekte stark ausgeprägt sind. Diese Größe kann mit Beobachtungen assoziiert und zur Schätzung der magnetischen Feldstärke und Elektronentemperatur in der Emissionsregion genutzt werden.

Zeitvariable, dreidimensionale, Multi-Wellenlängen-Studien von GRMHD-Simulationen mit selbstkonsistenter Elektronenheizung und variabler magnetischer Feldstärke werden in Kapitel 3 vorgestellt. Insbesondere für die Polarisation zeigen diese Simulationen, dass niedrige Magnetfeldstärken zu weniger geordneten Polarisationsmustern führen und damit zu sehr niedrigen (bildintegrierten) linearen Polarisationseigenanteilen neigen. Dies ist unabhängig vom Elektronenheizmechanismus und der Neigung.

Stärker magnetisierte Akkretionsströme tendieren zu höheren Elektronentemperaturen. In diesem Fall sind die Polarisationsmuster sehr geordnet und zeigen signifikante poloidale Magnetfelder. Eigenschaften dieser Modelle, einschlielich Spektren, Variabilität der Lichtkurven und linearem Polarisationsanteil, werden ebenfalls mit Messungen von Sagittarius A* verglichen, und es wird festgestellt, dass stark magnetisierte Modelle durch die Beobachtungen begünstigt sind.

GRMHD-Simulationen zeigen, dass Gesamtintensität und polarisierte Flussbilder oft zu ähnlichen Morphologien führen, die durch einen markanten Photonenring, der im Akkretionsfluss eingebettet ist, gekennzeichnet sind. Aus diesem Grund stellt Kapitel 4 eine Technik vor, die die Eigenschaften des Photonenrings in einem Bild hervorhebt, wenn die Bedingungen im Plasma geeignet sind. Dies ist besonders wertvoll, da eine Extraktion der Photonenringeigenschaften nicht nur die Messung von Masse und Spin zulassen, sondern möglicherweise auch Tests der Allgemeinen Relativitätstheorie ermöglichen könnten. Der Photonenring scheint im Bezug auf den Rest des Bildes etwa um einen Faktor zwei weniger polarisiert zu sein. Dies ist weniger auf Absorption sowie Faraday-Effekte im Plasma zurückzuführen, als vielmehr vorwiegend auf eine Kombination aus magnetischer Turbulenz und Paralleltransport.

In Kapitel 5 wird eine detaillierte Studie der zeitvariablen linearen Polarisation von Sagittarius A* während eines hellen Infrarot-*Flares* vorgestellt, der mit GRAVITY beobachtet wurde. Die polarisierten Signaturen werden im Kontext einer kompakten Region („*Hotspot*“) untersucht, die ein Schwarzes Loch umkreist. Es wird gezeigt, dass ein laufender *Hotspot* die allgemein beobachtete Entwicklung der linearen Polarisation erklären kann. Darüber hinaus ist eine poloidale Komponente in der Magnetfeldstruktur erforderlich, um mit der astrometrischen Periode dieses *Flares* übereinzustimmen. Dies weist auf das Vorhandensein starker Magnetfelder auf Ereignishorizont-Skalen hin. Abschließend muss die *Flare*-Emissionsregion die Magnetfeldstruktur in der Nähe des Schwarzen Loches auflösen, um mit dem beobachteten linearen Polarisationsanteil übereinzustimmen.

Kapitel 6 fasst die Schlussfolgerungen zusammen und gibt einen kurzen Ausblick in die Zukunft.

Summary

Spatially resolved polarization is a powerful observable quantity that offers a new window to study strong gravity, magnetic field configurations and plasma physics around black holes.

The aim of this thesis is to study polarized properties of synchrotron radiation from accretion models of supermassive black holes (SMBH) and develop tools which test and unveil the conditions under which the models are not only valid, but accurate in their description of nature. The studies are carried out with state-of-the-art radiative transfer calculations of general relativistic magnetohydrodynamic (GRMHD) simulations. This problem is particularly interesting due to the new and upcoming polarization observations on event horizon scales of the SMBH candidates Sagittarius A* and M87*, taken with the interferometric instrument GRAVITY at the Very Large Telescope and the Event Horizon Telescope.

Chapter 2 presents a study of the spatial properties of polarization patterns of different accretion models from an axisymmetric simulation of Sagittarius A* at millimetre wavelengths. It is shown that the strength of Faraday effects, in particular Faraday rotation *internal* to the emission region, leads to substantially different predicted submm-wavelength polarization configurations. Each pattern can be characterised with the "polarized correlation length", a spatial scale that quantifies the degree of order of the configuration as a function of the average Faraday depth, the integrated rotation of the linear polarization angle. Large values indicate ordered maps where Faraday rotation is weak and the spatial configuration is set by the underlying magnetic field geometry. In contrast, small values characterise disordered maps where Faraday effects are strong. This quantity can be associated to Very Long Baseline Interferometry observables and be used to estimate the magnetic field strength and electron temperature in the emission region.

Time variable, three-dimensional, multi-wavelength studies of GRMHD simulations with self-consistent electron heating and variable magnetic field strength are presented in Chapter 3. Particularly for polarization, the simulations show that low magnetic field strengths tend to produce more disordered polarization maps and therefore very low net (image-integrated) linear polarization fractions, regardless of the electron heating mechanism and inclination. More strongly magnetised accretion flows tend to result in hotter electrons. In this case, the polarization maps are very ordered and show patterns of significant poloidal (vertical/radial) magnetic fields. Properties of these models, including spectra, variability in light curves and linear polarization fractions, are compared to mea-

surements of Sagittarius A*, and it is found that strongly magnetised models are favoured by the observations.

GRMHD simulations show that total intensity and polarized flux images often exhibit similar morphologies, with a prominent photon ring signature embedded within the accretion flow. Motivated by this, Chapter 4 presents a technique that enhances the photon ring features in an image when conditions in the plasma are suitable. This is particularly valuable since an extraction of the photon ring properties would allow not only for measurements of mass and spin, but potentially also tests of general relativity as well. The photon ring appears to be about a factor of two less polarized with respect to the rest of the image and this is neither due to absorption nor Faraday effects in the plasma, but rather a combination of magnetic turbulence and, mainly, parallel transport.

Chapter 5 presents a detailed study of the time-variable linear polarization of Sagittarius A* during a bright near-infrared flare observed with GRAVITY. The polarized signatures are studied within the context of a compact region orbiting a black hole, a "hotspot". It is found that an orbiting hotspot can explain the general observed evolution of the linear polarization and is in agreement with that inferred from astrometry for the night. Furthermore, a poloidal component is required in the magnetic field structure in order to match the astrometric period of this flare, indicating the presence of strong magnetic fields at horizon scales. Finally, the flaring emission region must resolve the magnetic field structure close to the black hole in order to be match the observed linear polarization fraction.

Chapter 6 summarises the conclusions and provides a brief forward look.

Chapter 1

Introduction

1.1 Black holes

Black holes (BH) are some of the most fascinating yet simplest objects in the universe. Their trademark feature is having a one-way membrane, the event-horizon, inside which the gravitational attraction is so strong that nothing, not even light, can escape.[1] First notions of the existence of similar systems were made at the end of the XVIII century by Michell (1784) and Laplace (1976), who independently proposed the existence of "dark stars", extremely compact objects for which the escape velocity at their surface could surpass the speed of light.

In 1915 Albert Einstein published the general theory of relativity (GR, Einstein, 1915), changing the paradigm of how nature had been perceived until then. Differently to the Newtonian gravitation theory, where space and time are considered to be independent and gravity is an attractive force between massive particles, GR interprets gravity as a geometric property of space and time, or "spacetime", and it is directly related to the distribution of energy and mass. These quantities are related though the Einstein field equations[2] (e.g., Misner, Thorne, & Wheeler, 1973)

$$G_{\mu\nu} = \frac{8\pi G}{c^4} T_{\mu\nu} \tag{1.1}$$

where G is the gravitational constant, c is the speed of light, $G_{\mu\nu}$ is the Einstein tensor which holds the information about the geometry of the spacetime and $T_{\mu\nu}$ is the stress-energy tensor which characterises the distribution of energy and mass. $G_{\mu\nu}$ is a function of the metric tensor, $g_{\mu\nu}$, used for measuring intervals (or "distances"). The subindices $\mu\nu$ denote the coordinates of spacetime (one temporal and three spatial).

Only a year after GR was published, Karl Schwarzschild found an exact solution of the Einstein field equations[3] (Schwarzschild, 1916). Now referred to as the *Schwarzschild*

[1] Black holes can "evaporate" via neutrinos and photons when quantum effects are included in GR (Hawking, 1974).

[2] Considering $\Lambda = 0$, with Λ the cosmological constant (Einstein, 1917).

[3] The general theory of relativity changed the paradigm of the interpretation of nature.

black hole, it describes the spacetime outside a spherically symmetric, static, uncharged mass in vacuum. In Schwarzschild black holes the characteristic spatial and time scales (r_g and τ) are a function of only the mass M of the black hole. The gravitational radius is $r_g = GM/c^2$ and $\tau = r_g/c$. For a mass $M \sim 10^6$, $r_s \sim 10^6$ km and $\tau \sim 5$ s. A mass of $M \sim 10^9$ will give $r_s \sim 10^9$ km and $\tau \sim 1$ hr, so that larger (more massive) black holes evolve more slowly (e.g., Bambi & Nampalliwar, 2018; Bambi, 2019).

The Schwarzschild spacetime has two interesting locations. The first is the event horizon at $r_s = 2\ r_g$. Any object with a physical radius smaller than its *Schwarzschild* radius (r_s) will be a black hole. The second at $r = 0$, where the radial coordinate is measured from the centre of the mass distribution, denotes the location of a *physical* singularity, where spacetime itself, is no longer well-defined.

In 1963, Roy Kerr found another exact solution of the field equations describing the spacetime around a spinning, uncharged, axisymmetric mass in vacuum (Kerr, 1963). This solution depends only on the mass and the angular momentum J of the mass. In Boyer-Lindquist coordinates (Boyer & Lindquist, 1967), the size of the horizon[4] of a *Kerr* black hole is given by

$$r_H = r_g\ (1 + \sqrt{1 - a^2}). \tag{1.2}$$

Here $a = Jc/(GM)$ is the dimensionless spin parameter. In the limit when $a \to 0$ the Schwarzschild solution is recovered. This equation shows that in order for a horizon to exist around the singularity, only values of $|a| \leq 1$ are permitted. Known as the cosmic censorship conjecture, the violation of this statement would result in a "naked" singularity.

Between the horizon and an outer boundary surface at $r = r_E = r_g\ (1 + \sqrt{1 - a^2 \cos^2\theta})$ lies the ergosphere. The factor $\cos^2\theta$ modifies the shape from being a perfect sphere to a shape resembling a flattened sphere that touches the event horizon at the poles. Inside this region, all inertial frames must co-rotate with the rotating spacetime. This is known an frame dragging.

The ergosphere is an interesting region. Roger Penrose (Penrose & Floyd, 1971) formulated a process whereby energy can be extracted from a rotating black hole. A particle with energy $E > 0$ inside the ergosphere could decay into two particles of energies $E_+ > 0$ and $E_- = -|E_-| < 0$. If the particle with positive energy would escape to infinity and the other fall into the black hole then, because $E_+ = E - E_- = E + |E_-| > E$, there would be a net gain of *positive* energy at expense of the rotational energy of the black hole.

In addition to the Schwarzschild and Kerr solutions, other types of black holes are possible. The *Reissner-Nordström* solution (Reissner, 1916; Nordström, 1918) describes the spacetime outside a spherically symmetric, static, *uncharged* black hole, and the *Kerr-Newman* that of an axisymmetric, *charged*, rotating black hole (Newman et al., 1965).

Altogether, the only free parameters in these solutions are the mass, angular momentum

[4] The Kerr solution has an outer and inner event horizon of the form $r_H\pm = (1 \pm \sqrt{1 - a^2})\ r_g$. In the context of this work only the outer horizon (+) given in Equation 1.2 will be considered. This is because it is physically identical to the event horizon in the Schwarzschild case, marking the limiting surface between the exterior and the interior of the black hole, inside of which everything is disconnected to an external observer.

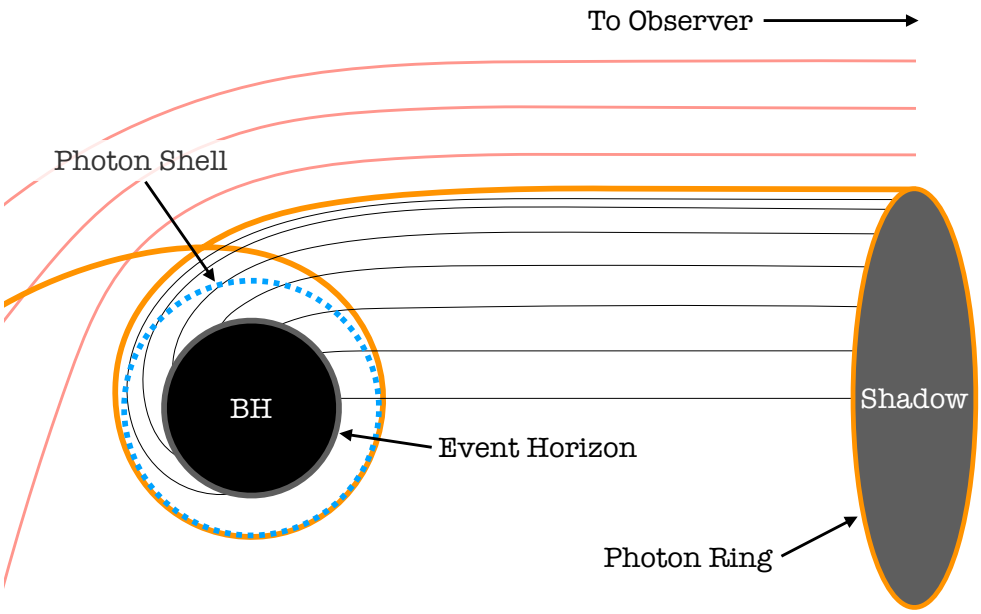

Figure 1.1: Schematic of light rays approaching a Schwarzschild black hole with different impact parameters. Due to strong lensing in the vicinity of the black hole, the trajectory of photons is curved. The photons need to have an impact parameter $b \geq \sqrt{27}\ r_g$ to not be captured by the black hole. The resulting shadow is larger than the photon sphere at $r = 3\ r_g$. At the outer edge of the shadow lies the photon ring.

and electrical charge of the system, making black holes the simplest macroscopic objects in nature. This is known as the "no hair" theorem. Violations to it would point out shortcomings in GR and lead modifications to the theory.

1.1.1 Black hole shadows

The first calculations of the apparent shapes of black holes as seen by an observer at "infinity"[5] were made in the 1970s (Cunningham & Bardeen, 1973; Bardeen, Carter, & Hawking, 1973; Luminet, 1979). The calculations of these images featured a Kerr black hole with a luminous source in its vicinity including, for example, an orbiting star or an extended stellar disk. The images showed the beamed image of the innermost edge of the luminous source rather than the actual event horizon of the black hole. This was achieved later with more complete numerical simulations and a fully backlit black hole (Sections 1.7 and 1.9).

The images typically show a bright extended source with a dark interior at the centre, where the black hole is. The shape of this black hole "shadow" relies on the closest distance photons can approach the object without falling into it. The limiting inner boundary is marked by the photon shell, the region where light can go around black holes on a closed

[5] In this context, infinity denotes the asymptotically flat spacetime region far away from the black hole.

loop or "bound orbits", neither disappearing across the event horizon nor escaping to infinity. In the case of a Schwarzschild spacetime, the photon shell is the two-dimensional sphere with radius $r = 3\ r_g$. For a Kerr black hole, this surface turns into a three-dimensional spherical shell that increases in thickness with increasing spin (e.g. Bardeen, Carter, & Hawking, 1973; Chandrasekhar, 1983; Vázquez & Esteban, 2004; Beckwith & Done, 2005; Johnson et al., 2020). In Boyer-Lindquist coordinates, all bound trajectories (geodesics) in the Kerr spacetime lie at some fixed value $r_- \leq r \leq r_+$, where

$$r_\pm = 2\ r_g\ (1 + \cos\left(\frac{2}{3}\cos^{-1}\left(\pm|a|\right)\right); \tag{1.3}$$

$r_g \leq r_- \leq 3\ r_g \leq r_+ \leq 4\ r_g$. Only two of the orbits are circular and reside entirely in the equatorial plane. These orbits correspond to $r = r_\pm$. The fact that $r_- \leq r_+$ results from frame dragging of inertial frames in the vicinity of a rotating black hole. An interesting feature of the Kerr spacetime is that the bound orbit at r_- is prograde whereas r_+ is retrograde.

Photons following bound orbits within the photon shell are "unstable" in the sense that, under any perturbation, they will either fall cross the event horizon or escape to infinity where they can reach the observer. In this context a photon could, in principle, orbit around the black hole many times before it becomes *marginally* bound and escapes to infinity (or crosses the horizon). The projected image that these *marginally* bound photons produce on the observer's "camera" is called the "photon ring" and it marks the outer edge of the black hole shadow. The photon ring can be decomposed into an infinite sequence of subrings indexed by the number of orbits around the black hole, each exponentially dimmer and narrower with increasing number of orbits (Johnson et al., 2020).

Because of the strong lensing, photons approaching the black hole from infinity must do so with a minimum impact parameter[6] b_{min} in order not to be captured. For a Schwarzschild spacetime $b \geq b_{min} = \sqrt{27}\ r_g \approx 5.2\ r_g$. As a consequence, the shadow of the black hole will be a circle (delineated by the photon ring) with radius $r = b_{min}$, larger than the photon sphere radius. In the case of Kerr, the shadow's outer contour is given by the curve

$$\rho = D^{-1}\sqrt{a^2(\cos^2\theta_{obs} - u_+u_-) + l^2}, \tag{1.4}$$

$$\varphi_\rho = \cos^{-1}\left(-\frac{l}{\rho D\sin\theta_{obs}}\right), \tag{1.5}$$

where (ρ, φ_ρ) are dimensionless polar coordinates on the observer's camera, situated at a distance D and inclined an angle θ_{obs} with respect to the black hole spin axis. $u_\pm$ are a function of (r, M, a) and l is energy-rescaled angular momentum (Johnson et al., 2020, Eqs. (4) and (6)).

Figure 1.1 shows a schematic of light rays approaching a Schwarzschild black hole with different impact parameters and the resulting shadow limited by the photon ring. Figure 1.2

[6] The impact parameter b is the perpendicular distance between the centre of the black hole and the trajectory of a photon approaching from infinity.

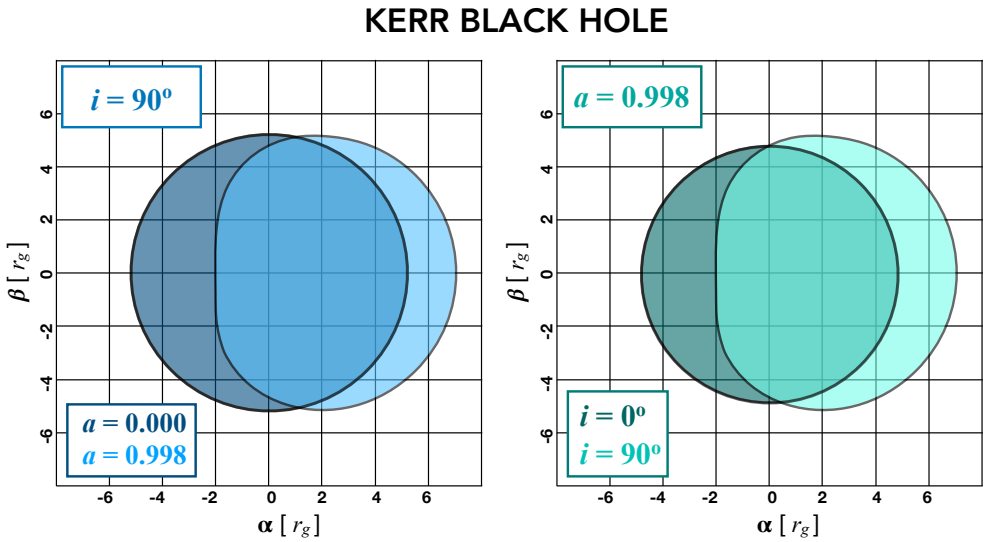

Figure 1.2: Apparent black hole shapes (shadows) of a Kerr black hole. **Left:** Non-rotating ($a = 0$) and highly fast rotating ($a = 0.998$) viewed edge-on (inclination $i = 90°$). At $a = 0$ the shadow is a perfect circle and corresponds to that of a Schwarzschild black hole. **Right:** Fixed spin $a = 0.998$ as a function of inclination ($i = 0, 90°$). The asymmetry in the shadows at $a = 0.998$ and $i = 90°$ is caused by the rotation of spacetime. The Schwarzschild spacetime is recovered when $a = 0$ (Bardeen, Carter, & Hawking, 1973).

shows a comparison of different shadow shapes as a function of inclination and spin in the case of a Kerr black hole.

1.2 Astrophysical black holes

After decades of being only theoretical curiosities, the existence of BH in nature was proposed with the discovery of active galactic nuclei (AGN), very distant and powerful galaxies with extremely high luminosities of the order of $\sim 10^{46} - 10^{47}$ erg s^{-1} (Lynden-Bell, 1969; Lynden-Bell & Pringle, 1974; Soltan, 1982). The observed fast variability in the flux of these sources implied that the enormous luminosity is produced in a relatively very compact region of ~ 1 AU (Astronomical Unit, 1.5×10^8 km). On the other hand, cosmologically redshifted emission lines showed that AGN are extragalactic. The combination of these constraints led to the consideration of very massive black holes at the centre of these sources powering them and producing the observed luminosities through a process called accretion (see section 1.6; e.g., Salpeter, 1964; Zel'dovich, 1964; Hoyle & Burbidge, 1966; Lynden-Bell, 1969). It is ironic that being objects from which no light can escape, black holes became the engine that powers some of the most luminous sources in the Universe.

Today, the presence of astrophysical black holes is considered almost inevitable in nature. Mass measurements of binary systems with strong X-ray emission (Webster & Murdin, 1972; Remillard & McClintock, 2006) and more recent gravitational-wave measure-

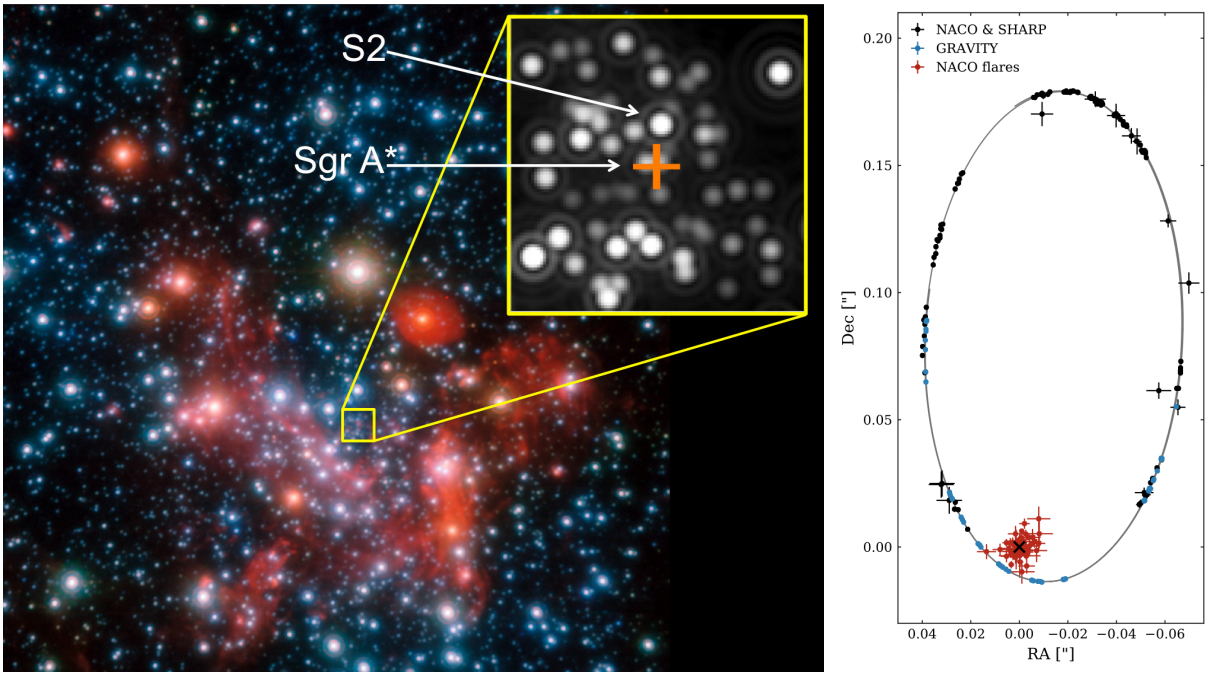

Figure 1.3: **Left:** the Galactic Centre and S-star cluster around Sgr A*. Credit: ESO/MPE/S. Gillessen et al. **Right:** the orbit of the star S2 with over more than twenty ears of observations. Credit: Gravity Collaboration et al. (2020a).

ments (Abbott et al., 2016) provide substantial proof of the existence of stellar mass black holes, thought to form via stellar collapse and with masses $M < 100 M_\odot$, where $M_\odot$ denotes the solar mass[7]. Supermassive black holes (SMBH), on the other hand, with masses larger than a million solar masses, are believed to lie at the centre of nearly every galaxy (e.g., Lynden-Bell, 1969; Kormendy & Richstone, 1995; Miyoshi et al., 1995) and to play a key part in their evolution (King, 2003; Kormendy & Ho, 2013).

Astrophysical black holes are expected to have completely negligible charge and should therefore be completely characterised only by their mass and angular momentum, or in other words, be fully described by the Kerr metric. The SMBH candidates the centre of our very own Galaxy and at the centre of the massive elliptical galaxy Messier 87 provide the best evidence for the existence of supermassive black holes in nature.

1.3 The Galactic Centre black hole

Closest to Earth, at a distance of 8.175 ± 0.013 kpc[8] and with a mass of $(4.148 \pm 0.014) \times 10^6$ $M_\odot$ (Gravity Collaboration et al., 2019), the SMBH candidate in the Galactic Centre is Sagittarius A* (Sgr A*, Genzel, Eisenhauer, & Gillessen, 2010).

[7] A solar mass is $M_\odot \sim 2 \times 10^{33}$ grams.
[8] A parsec is 1 pc $\sim 3 \times 10^{18}$ cm.

Originally discovered as a compact bright radio source (Balick & Brown, 1974), Sgr A* was first associated to a massive "dark" object of a few million solar masses from measurements of the high radial velocities of ionised gas in the inner parsec of the Galaxy (Wollman et al., 1977; Lacy et al., 1980; Lacy, Townes, & Hollenbach, 1982). Later, dynamical estimates based on the velocities of the inner early and late type stars (Haller, 1992; Genzel et al., 1996) confirmed this estimated mass and concluded that it was enclosed in a region of 0.1 pc.

With the advent of adaptive optics and speckle imaging on the Very Large Telescope (VLT) and the Keck telescope, accurate individual tracking of stars and gas clouds in the vicinity of the object became possible. Particularly for the latter, the compact gas cloud "G2" observed to be on a near-radial orbit about Sgr A* (Gillessen et al., 2012; Pfuhl et al., 2015; Plewa et al., 2017; Plewa, 2018), has been used to probe the ambient density and estimate gas temperatures at milliarcsecond scales in the Galactic Centre (Burkert et al., 2012; Ballone et al., 2013; De Colle et al., 2014; Guillochon et al., 2014; Gillessen et al., 2019).

Probably the most compelling evidence to date that Sgr A* is in fact a black hole comes from the continuous monitoring over the course of more than twenty years of the stellar motions in the central star cluster, the "S-stars", at scales of microarcseconds (μas, Figure 1.3, left; Schödel et al., 2002; Ghez et al., 2004; Gillessen et al., 2009; Meyer et al., 2012; Gravity Collaboration et al., 2017). To the present day, the orbits of forty stars located within the central parsec of the Galactic Centre have been determined (Gillessen et al., 2017) and appear to be orbiting a common dynamical centre. Of these, the orbit of the star "S2" yields the best constraints on the mass and distance to this central "dark" mass. It was with this star's orbit that the gravitational redshift and Schwarzschild precession effects, predicted by GR in the vicinity of black holes, were detected for the first time (Figure 1.12, right; Gravity Collaboration et al., 2018b, 2020a). Using the orbit of S2 alone, the inferred mass within ~ 1000 AU (its pericentre distance) is $\sim 4 \times 10^6\ M_\odot$, implying a high density that provides strong evidence for a SMBH. This dynamical mass can be associated to the radiative source Sgr A* given the lack of motion of the latter (Reid et al., 2008), indicating that the massive object lies at the centre of the Galaxy. In addition, the detection of the centroid emission of motion of gas in the immediate vicinity of Sgr A* (Gravity Collaboration et al., 2018a); the compact radio size constraints (Bower et al., 2004; Shen et al., 2005; Doeleman et al., 2008) and the spectral properties in the radio/submm bands, further argue for the case that this dark object is indeed a supermassive black hole.

Sgr A* has a low bolometric luminosity[9] of $\sim 10^{35}$ erg s^{-1}. As a result, it is classified as an (extremely) Low-Luminosity AGN (LLAGN). From radio to X-rays, Sgr A* shows emission in a broad range of energies over the electromagnetic spectrum (Figure 1.4; Zylka et al., 1995; Serabyn et al., 1997; Falcke et al., 1998; Cotera et al., 1999; Zhao, Bower, & Goss, 2001; Baganoff et al., 2003; Schoedel et al., 2007; Schödel et al., 2011; Dodds-Eden

[9] The bolometric luminosity is defined as the rate of emitted energy over all frequencies in the electromagnetic spectrum.

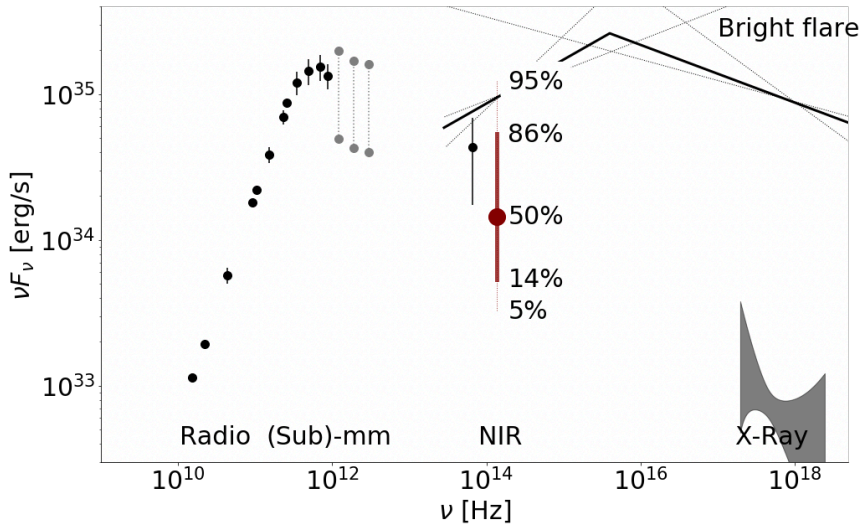

Figure 1.4: Observed spectral energy distribution of Sgr A*. Light is emitted over the entire electromagnetic spectrum. Credit: Gravity Collaboration et al. (2020d).

et al., 2009, 2011; Bower et al., 2015, 2019; Stone et al., 2016; von Fellenberg et al., 2018).

Most of the time Sgr A* is in a "quiescent" state, in which most of the energy is emitted at radio frequencies. Below ~ 50 GHz, the spectrum shows a power-law behaviour where the flux increases with frequency ($\nu L_\nu \sim \nu^{4/3}$, with L_ν the luminosity emitted at a frequency ν) , reaching a maximum of about $5{\times}10^{35}$ erg s^{-1} at millimetre (mm) wavelengths at ~ 230 GHz, above which the emission drops steeply towards the infrared to less than the detection limit of about 2×10^{34} erg s^{-1} at 2 μm. Optical and ultraviolet frequencies cannot be observed due to heavy extinction from intervening dust in the Galaxy. However, diffuse X-ray emission within 1-10" has been detected with the *Chandra* space telescope at energies from $2 - 10$ keV, showing a flux of about 2×10^{33} erg s^{-1} (Baganoff et al., 2003). This emission is likely produced by hot gas produced by stellar wind shocks from massive stars in the Galactic Centre. Unresolved polarization measurements show that Sgr A* is linearly polarized at a level of $\sim 2-9\%$ (e.g., Bower et al., 1999; Aitken et al., 2000; Bower et al., 2003; Macquart et al., 2006; Marrone et al., 2006, 2007; Macquart et al., 2006) and weakly circularly polarized $\sim 1-2\%$ at mm wavelengths (e.g., Bower, Falcke, & Backer, 1999; Sault & Macquart, 1999; Muñoz et al., 2012). This emission is associated to synchrotron emission from thermal electrons (Yuan, Quataert, & Narayan, 2003).

Aside from the quiescent state, a couple of times a day Sgr A* shows strong variations in the infrared and X-ray bands in which the flux increases up one to two orders of magnitude respectively (Baganoff et al., 2001; Genzel et al., 2003; Ghez et al., 2004; Gillessen et al., 2006). Multi-wavelength observations (e.g., Eckart et al., 2004, 2006; Yusef-Zadeh et al., 2006; Dodds-Eden et al., 2009; Trap et al., 2011) suggest that these "flaring" events at different energies are physically related and produced from synchrotron radiation of a

population of non-thermal electrons accelerated to ultrarelativistic speeds in magnetic reconnection events (Markoff et al., 2001; Ponti et al., 2017). NIR flares have been used as a probe of the magnetic field structure and spacetime near the event horizon of the object (Gravity Collaboration et al., 2018a, 2020c, Chapter 5).

1.4 The SMBH at the core of Messier 87

In the northern skies, the massive elliptical galaxy Messier 87 (M87) in the Virgo A galaxy cluster is thought to harbour another important SMBH candidate at its core: M87* (Gebhardt & Thomas, 2009). At a distance $D \sim 16$ Mpc (Mei et al., 2007) and with a mass $M \sim 6.2 \times 10^9$ $M_\odot$ estimated from stellar dynamics in the surrounding galaxy nucleus[10] (Gebhardt et al., 2011), M87* is the second largest SMBH as viewed from Earth, with an expected angular size on sky $\delta\theta \propto$ M/D of $\sim 37\mu$as, about 3/4 that of Sgr A* ($\sim 52\mu$as).

Unlike Sgr A*, optical images of M87 are characterised by a powerful, ultrarelativistic jet that shoots out of the plane of the galaxy, extends for a couple thousand parsecs and, with an inclination angle of $i \sim 17°$, is pointing almost directly at the Earth (Figure 1.5; Mertens et al., 2016). This jet was first observed by Curtis (1918) as a "bright stream of matter" in the image originating from a compact source and was later referred to as an astrophysical "jet" by Baade & Minkowski (1954).

The powerful jet in M87 has a measured kinetic power in the range of $10^{42} - 10^{45}$ erg s^{-1} (Reynolds et al., 1996; Owen, Eilek, & Kassim, 2000; Stawarz et al., 2006; de Gasperin et al., 2012; Broderick et al., 2015) and radiates over the entire electromagnetic spectrum (Figure 1.5; e.g., Baade & Minkowski, 1954; Turland, 1975; Junor, Biretta, & Livio, 1999; Nagar, Wilson, & Falcke, 2001; Wilson & Yang, 2001; Perlman et al., 2001, 2007, 2011; Krichbaum et al., 2006; Albert et al., 2008; Walker et al., 2018; Abdo et al., 2009; Harris et al., 2009; Hada et al., 2011, 2016; Abramowski et al., 2012; Doeleman et al., 2012; Prieto et al., 2016). Similarly to the Galactic Centre black hole, the radio spectrum of M87 shows a steady power-law energy increase with frequency that peaks in the submm and extends to optical bands. It is also linearly polarized at a level of $2 - 4\%$ (e.g., Hada et al., 2016). In the X-ray, M87 is a bright source suggesting the presence of very hot gas in the galaxy and shows variability on time scales of days (Harris et al., 2009).

Observations at radio and millimetre wavelengths have probed the jet structure on a scale of about a hundred Schwarzschild radii (Palmer et al., 1967; Reid et al., 1982; Junor, Biretta, & Livio, 1999; Kovalev et al., 2007; Ly, Walker, & Junor, 2007; Hada et al., 2011, 2016; Asada & Nakamura, 2012; Walker et al., 2018; Kim et al., 2018). As the base of the jet base becomes optically thin at higher frequencies, its size reduces with frequency, flattening at ~ 100 GHz in a bright compact radio "core". This allows for the determination of the upstream end of the jet. The data show that the putative SMBH is located within $14 - 23$ Schwarzschild radii of the unresolved radio core at 43GHz, implying that the jet remains collimated all the way into the central region (Hada et al., 2011).

[10] Mass measurements from gas dynamics (Walsh et al., 2013) estimate the value at 3.5×10^9 $M_\odot$, a factor of two smaller than that from stellar dynamics.

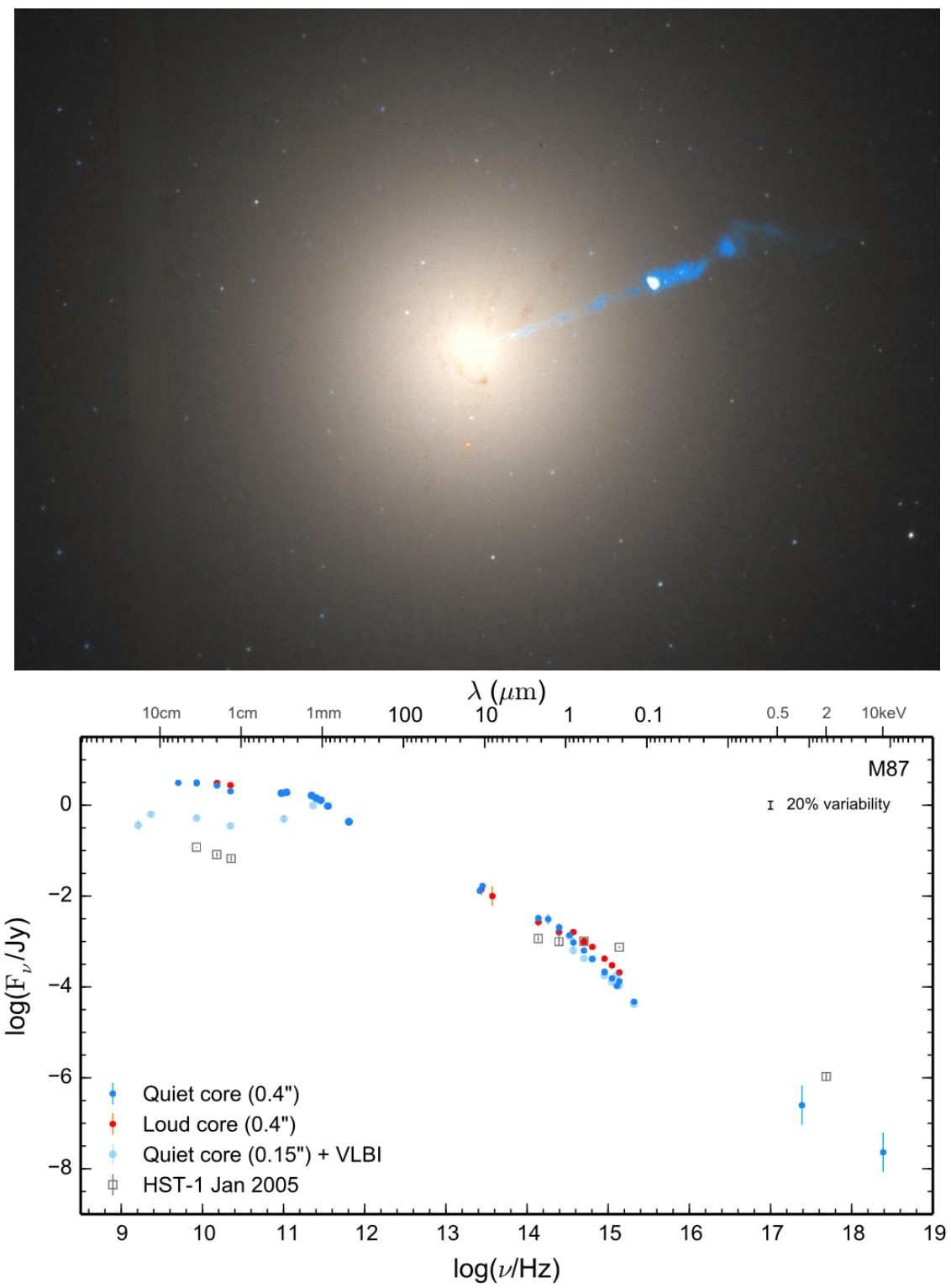

Figure 1.5: **Top:** the giant elliptical galaxy M87 showcasing its powerful jet. Credit: NASA/HST. **Bottom:** observed spectral energy distribution of M87. Emission from over the entire electromagnetic spectrum is radiated. Credit: Prieto et al. (2016).

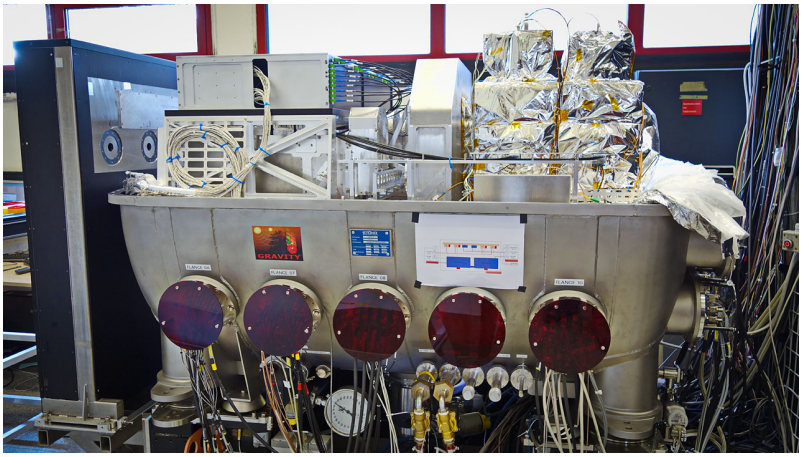

Figure 1.6: The GRAVITY instrument. Credit: ESO/Gravity Collaboration.

With M87* being about a thousand times more massive than Sgr A*, the dynamical timescale of the system is proportionally longer, with a light crossing timescale at the event horizon of about one day. This is advantageous when trying to image the source with Very Long Baseline Interferometry techniques (VLBI, Bouman et al., 2017; Chael, 2019).

1.5 GRAVITY and the Event Horizon Telescope

At the present time, the technological and scientific advancements made with GRAVITY, the second generation beam combiner at the Very Large Telescope Interferometer (VLTI); and the Event Horizon Telescope (EHT), a global array of radio antennas, have now made it possible to resolve for the first time emission at event horizon scales.

GRAVITY (Figure 1.6, Gravity Collaboration et al., 2017), operating in the near-infrared (NIR, $\sim 2\mu$m), combines the light of the four powerful "Unit Telescopes" at the VLT on Cerro Paranal in the chilean Atacama desert (Figure 1.7). With foundations in optical interferometry techniques, GRAVITY has not only pushed the limits of detection in Galactic Centre science with its improved angular resolution and sensitivity, but has also had remarkable results in other fields, including exoplanets (GRAVITY Collaboration et al., 2019) and AGN (Gravity Collaboration et al., 2018c, 2020e).

In 2018, the GRAVITY Collaboration discovered the motion of gas in the vicinity of Sgr A* during flaring events (Gravity Collaboration et al., 2018a). The scale of the apparent motion of $\sim 30-50$ μas in $40-70$ minutes, is consistent with clockwise compact orbiting emission regions (e.g., (Broderick & Loeb, 2005, 2006b; Hamaus et al., 2009) around a $\sim 4\times10^6 M_\odot$ black hole at $3-5r_s$, where $r_s \sim 10$ μas. Polarization measurements were also made and evidence for a continuous rotation of the linear polarization angle with periods comparable to the astrometric ones was found. By studying the observed polarization features, it was possible to make a first interpretation of the magnetic field geometry in

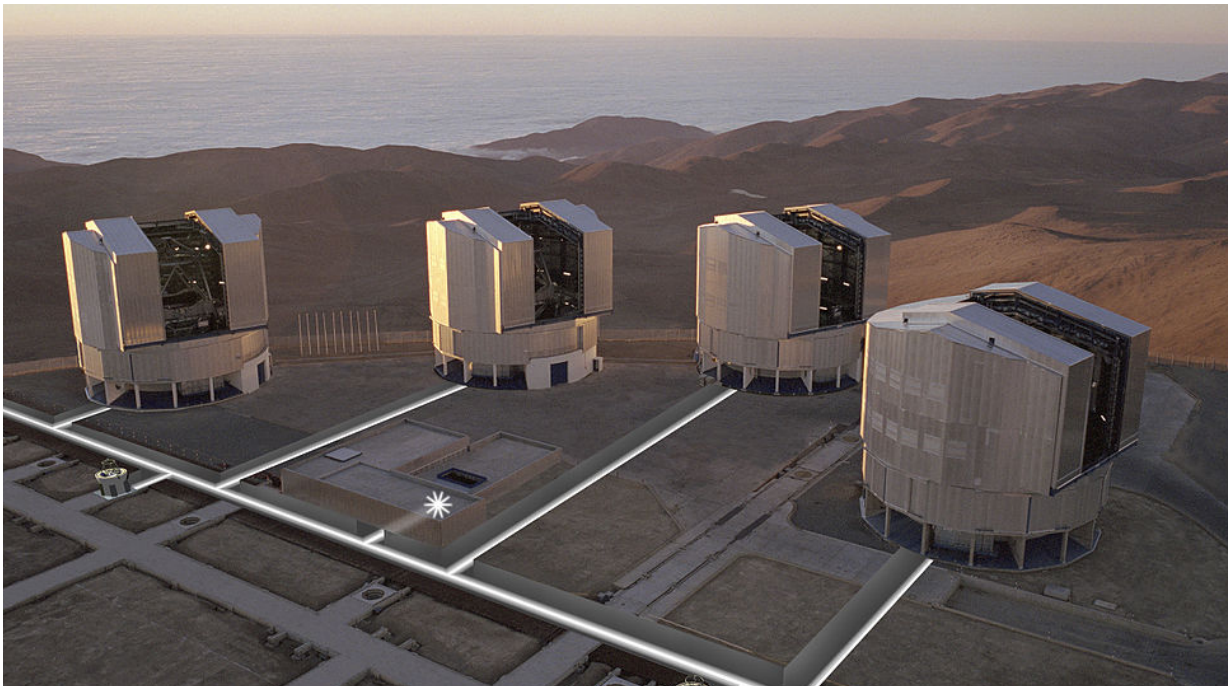

Figure 1.7: The Very Large Telescope featuring the four Unit Telescopes (UTs) at Cerro Paranal in the chilean Atacama desert. Credit: ESO.

the vicinity of the black hole and infer the presence of dynamically important fields.[11]

The EHT, operating at mm-wavelengths (1.3 mm), was able to observe the Galactic Centre and the core of M87 with a nominal resolution of 25 μas in 2017. This high angular resolution was achieved through VLBI techniques, where the data from different independent stations is correlated in order to achieve larger resolution. The maximum resolution attainable is proportional to the maximum separation between observing stations and the observed frequency of light. In the case of the EHT, different telescopes at various locations on the planet independently observed Sgr A* and M87*, rendering an effective *virtual* telescope with a size comparable to that of the Earth (Figure 1.8). The M87 data was later correlated, and by using cutting-edge image reconstruction methods (Bouman, 2017; Chael, 2019), the EHT Collaboration was able to publish the first ever images of the innermost area surrounding M87* (Figure 1.9; Event Horizon Telescope Collaboration et al., 2019a,b,c,d,e,f). In these images, a bright thick ring of hot material is seen surrounding a dark interior, a feature associated with being the shadow of the black hole (Bardeen, Carter, & Hawking, 1973; Falcke, Melia, & Agol, 2000). At the present time, data analysis and image reconstruction of Sgr A* is still being conducted.

Further observations and upgrades in instrumentation to come will provide more information for the further understanding of SMBH and the radiation physics around them. For example the combination of stellar orbit information in the Galactic Centre, astrometric

[11] A further, more detailed study of these data is presented in Chapter 5 of this Thesis.

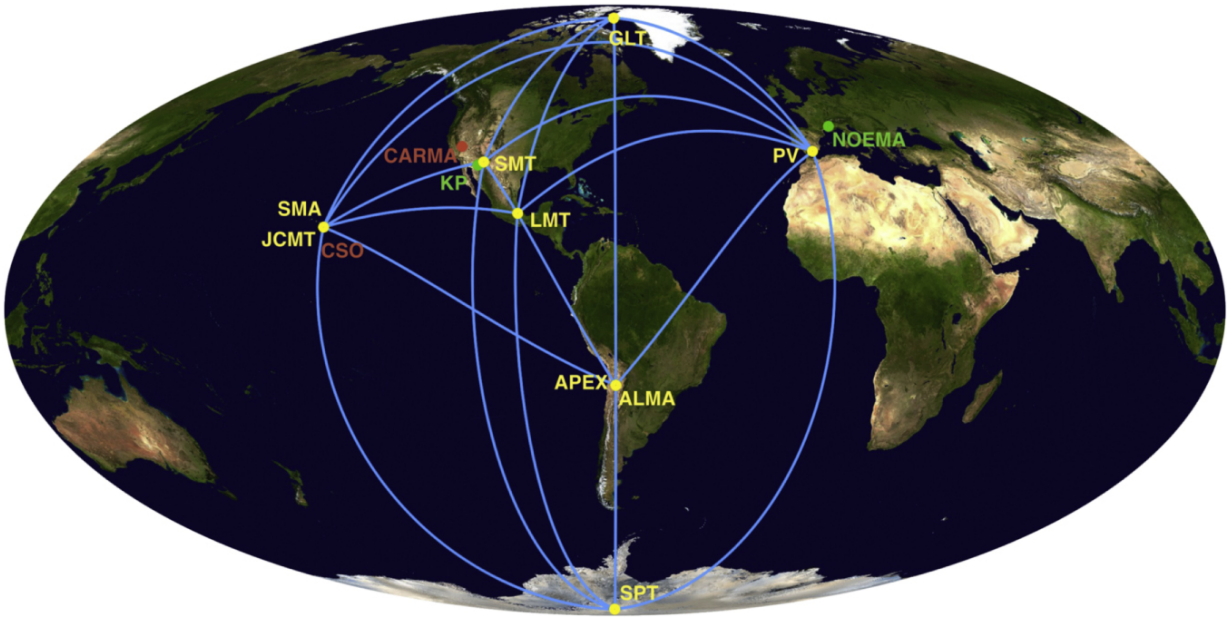

Figure 1.8: The EHT array in 2017. Credit: EHT Collaboration.

Figure 1.9: The M87* reconstructed image from EHT data taken in 2017. A bright ring is seen surrounding a dark interior associated to the black hole shadow. Credit: EHT Collaboration.

tracking of the centroid of emission during flaring events of Sgr A* and constraints from the (potential) black hole shadow from reconstructed images by the EHT Collaboration will also provide the possibility of measuring the spin of Sgr A* (Waisberg et al., 2018) and testing the "no hair" theorem predicted by GR (Psaltis, Wex, & Kramer, 2016; Waisberg, 2019). In addition, the upcoming planned upgrades of GRAVITY (GRAVITY+), the construction of the Extremely Large Telescope, the addition of new EHT stations to the current array and its possible expansion to space (Johnson et al., 2020) are very promising for the future.

It is then that an accurate interpretation of the wealth of these current and near future observations requires theoretical calculations of near horizon radiation from Sgr A* and M87*.

1.6 Black hole accretion theory

Black holes are considered to be the engines that power some of the most powerful astrophysical sources in the Universe, such as AGN (e.g., Koratkar & Blaes, 1999) and black hole X-ray binaries (BHBs, e.g., Remillard & McClintock, 2006; McClintock, 2013). The process behind it is called "accretion", where the gravitational energy of material falling onto the compact object is released in the form of radiation.

1.6.1 Bondi accretion

The simplest analytic model of accretion is that of spherical or "Bondi" accretion (Bondi, 1952), where the in-falling material has no angular momentum and falls radially (and adiabatically) towards the central object[12]. Using arguments of mass and energy conservation, it can be deduced that the accretion rate is $\dot{M}_{Bondi} \propto r_{Bondi}^2 \rho_\infty v_\infty \propto M^2 \rho_\infty / c_s^3$, where ρ_∞ is the ambient density far away from the accretor, M is the total mass of the gas reservoir, c_s is the ambient sound speed and $r_{Bondi} \approx GM/c_s^2$ is the "Bondi radius". It can be seen from this expression that if c_s exceeds v_∞, the thermal pressure of the system sets the main limitation on the accretion rate. On the other hand, if $v_\infty > c_s$, dynamical limitations are more important.

In spherical accretion the infall timescale time is short, the temperature of accreting material is nearly virial[13], reaching values of $\sim 10^{12}$K at the event horizon and the particle density increases towards the accreting object. The values, however, are low enough that

[12] The case where the accreting object is moving through an ambient medium at rest is referred to as "Bondi-Hoyle" accretion (Bondi & Hoyle, 1944).

[13] The virial theorem states that the total potential energy U of a gravitationally bound system is equal to twice its time averaged total kinetic energy E. The virial temperature T is then, that which the system would have in order to satisfy the virial theorem. For a system of mass M and radius r with constant density, the gravitational energy per unit mass is $U = GM/r$. The kinetic energy per unit mass is $E = 3k_BT/2\mu$, where k_B is Boltzmann's constant and μ the mean molecular weight. It follows that the virial temperature is $T = GM\mu/3k_Br$.

synchrotron radiation[14] dominates the emission, causing the bulk of the radiation to be emitted at millimetre and far infrared wavelengths.

The Bondi model allows for quick estimates of accretion rates from measurements of ambient densities and gas temperatures (Yuan & Narayan, 2014). To illustrate, in the case of Sgr A*, X-ray observations made with *Chandra* (Baganoff et al., 2003) give gas density and temperature estimates of 100 cm^{-3} and 2 keV on 1" scales. This would give a Bondi radius of $r_{Bondi} \sim 0.04 \sim 1''$ pc and an accretion rate $\dot{M}_{Bondi} \sim 10^{-5}\ M_{\odot}\ \mathrm{yr}^{-1}$. Close to the horizon, the particle density is $n \approx 10^{9} - 10^{10}\ \mathrm{cm}^{-3}$ and the magnetic field $B \approx 2 \times 10^{3}\ G$, assuming equipartition. In order to not overproduce the observed emission in the radio, electron temperatures of $T_e \sim 10^{9} - 10^{10}$ K are needed. If gas were accreted at this rate onto Sgr A* and all the gravitational energy were converted to radiation, the expected luminosity $L \approx \dot{M}_{Bondi}\ c^2 \sim 10^{42}\ \mathrm{erg\ s}^{-1}$, six orders of magnitude too large compared to the observed value. This would imply that despite the gas-rich environment in which it resides (Lo & Claussen, 1983; Cuadra et al., 2006), Sgr A* actually accretes very little mass.

Bondi accretion is simplistic and neglects the angular momentum of the accreting gas. This is likely a very poor assumption since the slightest non-zero angular momentum in the material will be amplified as it approaches the black hole, causing the formation of a rotating viscous flow referred to as an "accretion disk".

1.6.2 Thin disk accretion

In order to describe the broad band spectra of AGN and BHBs, the first analytic model featuring an accretion disk, the "thin disk model", was developed in the early 1970's (Shakura & Sunyaev, 1973; Novikov & Zel'dovich, 1973; Lynden-Bell & Pringle, 1974; Pringle, 1974, see reviews by Abramowicz & Fragile (2013); Blaes (2014); Yuan & Narayan (2014)).

In the thin disk model, starting from material arranged in a geometrically axisymmetric thin disk, accretion onto an object is caused by the outward transport of angular momentum of the orbiting material around the object. This is has been associated to a viscosity ν in the accretion flow, parametrised as $\nu = \alpha c_s H \simeq \alpha c_s^2/\Omega_k$, where H is the scale height of the disk[15], $\Omega_k = \sqrt{GM/r^3}$ is the Keplerian angular velocity and α is a dimensionless parameter generally assumed to be a constant ($0 \leq \alpha \leq 1$). Due to this prescription, the thin disk model is also known as the α-model.

From height-averaged mass, momentum and energy conservation laws, and assuming that all dissipated energy is radiated away locally, the equations of a thin disk and its radiated spectrum can be obtained. Though α is a free parameter, many of the observables depend only weakly on it, so that the thin disk model is predictive without relying on the detailed physical conditions and processes that cause the outward transport of angular

[14]The original version of Bondi accretion does not include magnetic fields. The inclusion of a magnetic field configuration in order to produce synchrotron radiation, was done by (Shapiro, 1974).

[15] The scale height represents the vertical distance at which the pressure decreases by a factor of $1/e$.

momentum and thus trigger the accretion process. Remarkably, this model successfully matches the luminosity and effective temperature of AGN and BHBs (Koratkar & Blaes, 1999; Remillard & McClintock, 2006; McClintock, 2013).

It is common to express accretion rates in units of the Eddington accretion rate, $\dot{M}_{Edd} = L_{Edd}/\eta c^2$, where η is the radiative efficiency of the accretor[16] and L_{Edd} is the Eddington luminosity, understood as the luminosity an object must have in order to counterbalance the gravitational force through radiation pressure. It can be written as

$$L_{Edd} = \frac{4\pi G M m_p c}{\sigma_T} \tag{1.6}$$

where G is the gravitational constant, M is the mass of the accreting object, m_p is the proton mass and σ_T is the Thompson cross-section.

In terms of these quantities, thin disk accretion applies whenever the mass accretion rate is somewhat below the Eddington rate ($0.1\dot{M}_{Edd} \lesssim \dot{M} \lesssim \dot{M}_{Edd}$). At these values, the infalling matter is thermalised and radiates efficiently due to Coulomb collisions between ions and electrons (producing a one-temperature plasma). The radiation is free to escape, producing a geometrically thin but optically thick disk, and the spectrum is the juxtaposition of blackbody spectra at each radius. Due to this model having an efficient cooling rate, it is characterised by having an accretion flow where the temperature of the gas ($\sim 10^4 - 10^7$ K) is much lower than the virial temperature ($\sim 10^{12}$ K).

A quick calculation using the thin disk model shows that if gas were accreted at the Bondi rate onto Sgr A* ($\dot{M}_{Bondi} \sim 10^{-5}\ M_\odot\ \mathrm{yr}^{-1}$), the expected luminosity $L \approx 0.1\dot{M}_{Bondi}\ c^2 \sim 10^{41}$ erg s^{-1} (where an accretion efficiency of 10% has been considered), still too large compared to the observations.

1.6.3 ADAF and RIAF solutions

Though the thin disk model is successful in matching the spectra of AGN and BHBs, this accomplishment does not extend to LLAGN like Sgr A* and M87, even at low accretion rates, indicating that the accretion process in this sources must be different.

At very low accretion rates ($\dot{M} \lesssim 10^{-4}\dot{M}_{Edd}$), the electromagnetic interactions between ions and electrons become inefficient. Below a critical mass accretion rate ($\dot{M}_{crit} \sim \alpha^2\dot{M}_{Edd}$), the inflow rate of material becomes faster than the cooling rate and the gravitational potential energy liberated in the accretion process is lost by advection across the black hole event horizon rather than being radiated away. The accretion flow then remains relatively dark and hot, and is described by a two-temperature plasma: being a thousand times more massive, ions remain hot and dictate the dynamics of the accretion flow while electrons have a much lower temperature from cooling via synchrotron radiation[17]. This

[16] Values for η vary in literature. Usually $\eta \sim 10\%$, but other values including 12 and 16%, or a dependency on black hole spin are also possible.

[17] Synchrotron radiation is intrinsically polarized, and therefore it is the natural choice for the main radiation mechanism in order to explain the non-zero linear polarization detected in Sgr A* and M87*.

gives origin to the "Advection Dominated Accretion Flow" (ADAF) models (e.g., Ichimaru, 1977; Rees et al., 1982; Narayan & Yi, 1994, 1995; Chen et al., 1995; Blandford & Begelman, 1999; Quataert, 2003; Abramowicz & Fragile, 2013; Yuan & Narayan, 2014). Because of the low radiative efficiency ($\eta \sim 10^{-6}$), unlike in thin disk accretion, the high temperatures in the accretion flow cause a large ram pressure that makes the gas in the disk "puff up", generating a geometrically thick (quasi-spherical) but diffuse disk. As a result of this low plasma density, the disk is optically thin and does not emit like a blackbody spectrum (as it would locally do in thin disks), but rather it is dominated by radiative processes like synchrotron, bremsstrahlung and inverse Compton scattering. The high thermal pressure also results in sub-Keplerian angular velocities ($\Omega \simeq 0.3 - 0.5\ \Omega_k$), as gravity is partially balanced by the radial pressure gradient (and therefore shorter infall timescales). The radial velocity follows $v_r \propto r^{-1/2}$ and the density profile $\rho \propto \dot{M} r^{-3/2}$, characteristic of spherical accretion, indicating that even in the presence of rotation, the accretion rate in ADAF models is comparable to the Bondi accretion rate ($\dot{M}_{ADAF} \lesssim \dot{M}_{Bondi}$).

Being much less luminous than the thin disk model, the ADAF models have been shown to reproduce the main features of the radio spectrum of low-luminosity sources including Sgr A* and M87 (e.g., Narayan, Yi, & Mahadevan, 1995a; Manmoto, Mineshige, & Kusunose, 1997; Narayan et al., 1998). However, ADAF are prone to strong outflows (winds) due to the significant internal energy stored in the accretion flow. In addition, their constant accretion rate (independent of radius), causes them to be too depolarized close to the black hole, not matching the observed linear polarization fractions.

For these reasons, various ADAF model extensions were developed to address both problems, generically resulting in smaller accretion rates with a radial dependence so as to match the density profile and linear polarization constraints, and higher electron temperatures to explain the observed spectral energy distribution. So it was that the "Radiatively Inefficient Accretion Flow" (RIAF; e.g., Yuan, Quataert, & Narayan, 2003, 2004) models were introduced. Both analytic and numerical calculations of RIAFs show that $\dot{M} \ll \dot{M}_{Bondi}$, so that very low radiative efficiencies ($\eta \sim 10^{-6}$, as in ADAF and Bondi models) are not necessary. These low accretion rates are also is in accordance with linear polarization constraints. With dynamics still dominated by the thermal gas pressure and having synchrotron emission as the dominant source of radiation, these models are appropriate for Sgr A* and M87.

Models with $\dot{M} \sim 10^{-8}\ M_\odot\ \mathrm{yr}^{-1} \ll \dot{\mathrm{M}}_{\mathrm{Bondi}}$ can explain the basic spectral properties of Sgr A*. The low-energy radio emission can be modelled with synchrotron radiation from a combination of non-thermal and thermal electrons within the accretion flow, and Bremsstrahlung for the high-energy X-ray band (Yuan, Quataert, & Narayan, 2003; Yuan & Narayan, 2014). This is motivated due to the fact that at lower accretion rates, electrons are not thermalised and their distribution function is expected to retain a stronger memory of the heating/acceleration processes (Yuan & Narayan, 2014). So a combination of thermal and non-thermal electron energy distributions is expected to be present in hot accretion flows.

Alternative models have been proposed. In the "jet model", the emission originates from a powerful outflowing jet emerging from the innermost accretion area, with synchrotron

radiation producing the radio spectrum and synchrotron self-Compton up-scattering the photons to higher energies (Falcke & Markoff, 2000a). To the present day, however, a jet emerging from Sgr A* is yet to be detected.

Similarly for M87*, theoretical models of the spectral energy distribution function include ADAF (Reynolds et al., 1996; Di Matteo et al., 2003) and jets (Prieto et al., 2016). The radio spectrum is associated to synchrotron emission either from the accretion flow or the powerful observed relativistic jet, which is then up-scattered by hot electrons to higher energies extending up to about 100 keV ($\sim k_B T_e$, k_B the Boltzmann constant and T_e the electron temperature) via the Compton process. In typical two-temperature plasmas, the importance of this Compton component is highly dependent on the accretion rate. At low values of $\dot{M}$, synchrotron radiation is bolometrically stronger and dominates the spectrum. This is reversed as $\dot{M}$ increases, with the synchrotron component becoming weaker. At very low $\dot{M}$, the Compton process is so weak that the X-ray luminosity is dominated by bremsstrahlung emission. Multi-wavelength observations of the jet in M87 measure its collimation profile and show that it originates near a bright radio core associated to the black hole (Hada et al., 2011). However, it is not clear if any of the observed emission comes from an accretion flow.

1.7 The MRI and GRMHD

In the α prescription the stresses in the plasma that set off the accretion process can be parametrised as an *effective* viscosity, without the need to specify the physical processes causing it. Ordinary molecular viscosity was showed to be orders of magnitude too weak to match the accretion rates required by AGN. Similarly, shear instabilities, sound waves and shocks were all insufficient mechanisms. Instead, the nature of the accretion process was suspected to be related to some sort of of magnetohydrodynamic instability.

Magnetic forces can act like a spring under tension connecting parts of the accretion flow, generating attractive forces on fluid elements that are displaced in the direction perpendicular to a magnetic field line. In a stationary medium this force is restorative and stabilises the system. However, if the fluid medium is rotating and the angular velocity of a fluid element increases with decreasing radius, the process is destabilising and the fluid quickly develops magnetohydrodynamic turbulence. First applied in the context of astrophysical disks by Balbus & Hawley (1991), this *magneto-rotational instability* (MRI, Velikhov, 1959; Chandrasekhar, 1960; Balbus & Hawley, 1991; Balbus, Hawley, & Stone, 1996; Balbus & Hawley, 1998) is now generally accepted as the mechanism responsible for the outward transport of angular momentum in an accreting magnetised flow.

Given their complexity, more detailed multidimensional, time-dependent calculations of magnetised accretion flows under the action of realistic MRI turbulence require numerical calculations[18]. With the increase of computer power and the development of better numerical algorithms, this is now possible[19].

[18] In order to sustain the turbulence, three-dimensional calculations are needed.

[19] It is important to adequately resolve the MRI in the simulations. One way to do this is is using the

"General Relativistic Magneto Hydrodynamic" (GRMHD) frameworks have been developed to simulate and evolve ionised, magnetised plasmas as ideal fluids in a fixed background spacetime[20] (e.g., Misner, Thorne, & Wheeler, 1973; Stone et al., 1992; Komissarov, 2001; Gammie, McKinney, & Tóth, 2003; De Villiers, Hawley, & Krolik, 2003; Tchekhovskoy, Narayan, & McKinney, 2011; Sadowski et al., 2013; Ryan, Dolence, & Gammie, 2015; White, Stone, & Gammie, 2016; Chandra, Foucart, & Gammie, 2017; Porth et al., 2017, see reviews by Martí & Müller (2003) and Font (2000)). Particularly, one can choose to solve and evolve the equations of magneto hydrodynamics (MHD) in what is referred to as the "conservative frame" (e.g., Koide, Shibata, & Kudoh, 1999; Komissarov, 2001; Gammie, McKinney, & Tóth, 2003; Tchekhovskoy, 2019; Porth et al., 2019), where the physical conditions in the fluid must satisfy conservation laws for mass, energy-momentum and the Maxwell equations:

$$\nabla_\mu(\rho u^\mu) = 0, \tag{1.7}$$
$$\nabla_\mu T^{\mu\nu} = 0, \tag{1.8}$$
$$\nabla_\mu F^{*\mu\nu} = 0, \tag{1.9}$$

∇_μ denotes the covariant derivative, ρ is the mass density, u is the four-velocity, $T^{\mu\nu}$ is the stress-energy tensor and $F^{*\mu\nu} = b^\mu u^\nu - b^\nu u^\mu$ is the dual of $F^{\mu\nu}$, the electromagnetic ("Faraday") tensor (with b^μ the magnetic four-vector, $b^2 = b_\mu b^\mu$). Note that the expression for $F^{*\mu\nu}$ has taken into account the approximation that in ideal MHD the electric field vanishes in the fluid rest frame due to high conductivity in the plasma ($u_\mu F^{\mu\nu} = 0$).

In GRMHD, the stress-energy tensor

$$T^{\mu\nu}_{MHD} = (\rho + \varepsilon + p + b^2)u^\mu u^\nu + (p + \frac{1}{2}b^2)g^{\mu\nu} - b^\mu b^\nu \ , \tag{1.10}$$

characterises a magnetised perfect fluid, and therefore contains contributions from the fluid variables $(\rho, \varepsilon, p, u)$ and the magnetic field four vector b^μ. Here $\varepsilon = \varepsilon_e + \varepsilon_i$ denotes the total internal energy density, $p = p_e + p_i = (\Gamma - 1)\varepsilon$ is the total pressure (related to ε through the ideal gas law) and Γ is the effective adiabatic index of the gas. The subindices e and i denote electron and ion quantities respectively.

In single-fluid GRMHD simulations, where the distinctions between ions and electrons are ignored and the species are treated together as a single fluid, the mass density is dominated by the ion mass so that $\rho = m_p n$ (n is the particle number density). Furthermore, the effective adiabatic index is typically fixed to the non-relativistic monoatomic value $\Gamma = 5/3$. It could, however, take on values in the range $4/3 \leq \Gamma \leq 5/3$ depending on the local energy densities and temperatures of the two species: $\Gamma = 5/3$ for non-relativistic (ions) and $\Gamma = 4/3$ for relativistic (electrons).

Q^x parameters, where x is a coordinate. Broadly speaking, this parameter measures how many cells in the simulation domain resolve the fastest growing mode of the MRI along x (Hawley, Guan, & Krolik, 2011).

[20] The self-gravity of the disk can often be ignored due to its mass being small compared to the mass of the central compact object.

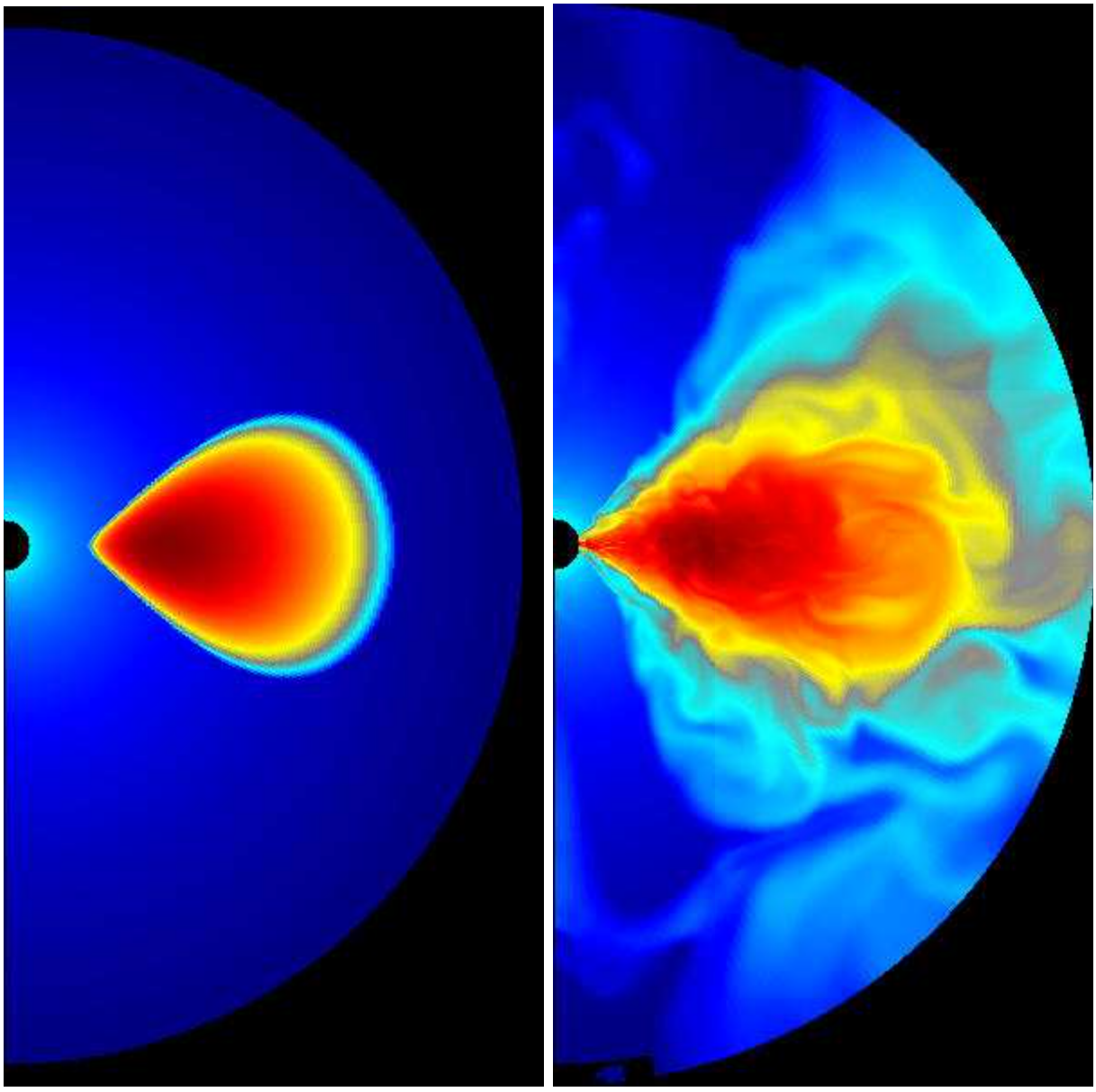

Figure 1.10: Instantaneous slice of a two dimensional GRMHD simulation of a magnetised torus around a rotating black hole with $a = 0.5$. Colour represents density in log scale. Black is low and red is high. **Left:** Initial condition ($t = 0$). The torus is in hydrostatic equilibrium and weakly magnetised with a single poloidal loop. **Right:** Later times ($t = 2000\ r_g/c$). Stresses in the accretion flow cause the outward transport of angular momentum in the plasma, setting off the accretion process onto the black hole. Credit: Gammie, McKinney, & Tóth (2003)

Standard global GRMHD simulations of accretion onto black holes are initialised with a single fluid rotating torus centred on the object in the Kerr spacetime, threaded with a weak poloidal magnetic field[21] (Figure 1.10, Fishbone & Moncrief, 1976). Starting from hydrostatic equilibrium, the fluid is evolved as the fluid moves around the compact object, differential rotation in the plasma will generate MRI that amplify the magnetic field and generate MHD turbulence in the gas. It is widely accepted that this acts as a viscosity parameter in the fluid and produces stresses in the plasma that transfer angular momentum outwards, setting off the accretion process onto the black hole.

In LLAGN the electrons are assumed to be responsible for the observed radiation. Even though they are not typically directly simulated in single-fluid GRMHD simulations, physical arguments such as charge neutrality in the plasma make it possible to obtain their particle density ($n_e = n_p = \rho/m_p$) and four-velocity u^μ from the simulation's output. The only unrestricted parameters are the electron internal energy density ε_e and their distribution function.

These can be obtained either by self-consistently evolving ε_e along with the MHD fluid (e.g., Ressler et al., 2015, 2017; Gold et al., 2017; Chael et al., 2018; Chael, Narayan, & Johnson, 2019; Dexter et al., 2020a, see Chael (2019); Ressler (2019) for more details) following some electron heating prescription (for example turbulent cascade scenarios or magnetic reconnection events; e.g., Howes, 2010; Rowan, Sironi, & Narayan, 2017; Werner et al., 2018; Kawazura, Barnes, & Schekochihin, 2019), or be assigned in post-process according to some parametrisation of electron-ion coupling. Choices of these include constant heating in the accretion flow (e.g., Dexter & Agol, 2009; Mościbrodzka et al., 2009, 2014; Dexter et al., 2010) and dependence on the magnetic energy densities in the plasma (e.g., Mościbrodzka, Falcke, & Shiokawa, 2016; Davelaar et al., 2019). An example of the latter is that introduced by Mościbrodzka, Falcke, & Shiokawa (2016), where

$$\frac{T_i}{T_e} = R_{High}\frac{\beta^2}{1+\beta^2} + R_{low}\frac{1}{1+\beta^2}. \tag{1.11}$$

Here the so called "plasma beta" parameter $\beta = p_{gas}/p_{mag} \propto n_i T_i/b^2$ is defined as the ratio of the local thermal ion pressure to the magnetic pressure. R_{High} and R_{Low} are temperature ratios that describe the electron-ion coupling in large β (weakly magnetised) and small β (strongly magnetised) regions. This prescription has been applied to M87* with $R_{High} = 100$, correctly matching the radio, mm and X-ray observations.

1.7.1 Outflows

An important result from GRMHD work has been the realisation that outflows are present in the form of winds or powerful jets in the system. GRMHD simulations show that as the accretion flow evolves, the system separates into three qualitatively different regions: main disk body, corona and funnel or jet (Figure 1.11, Yuan & Narayan, 2014).

[21] Recent studies have considered initial conditions where the accreting material comes from stellar wind material and falls onto the black hole from large scales (Ressler, 2019; Ressler, Quataert, & Stone, 2020)

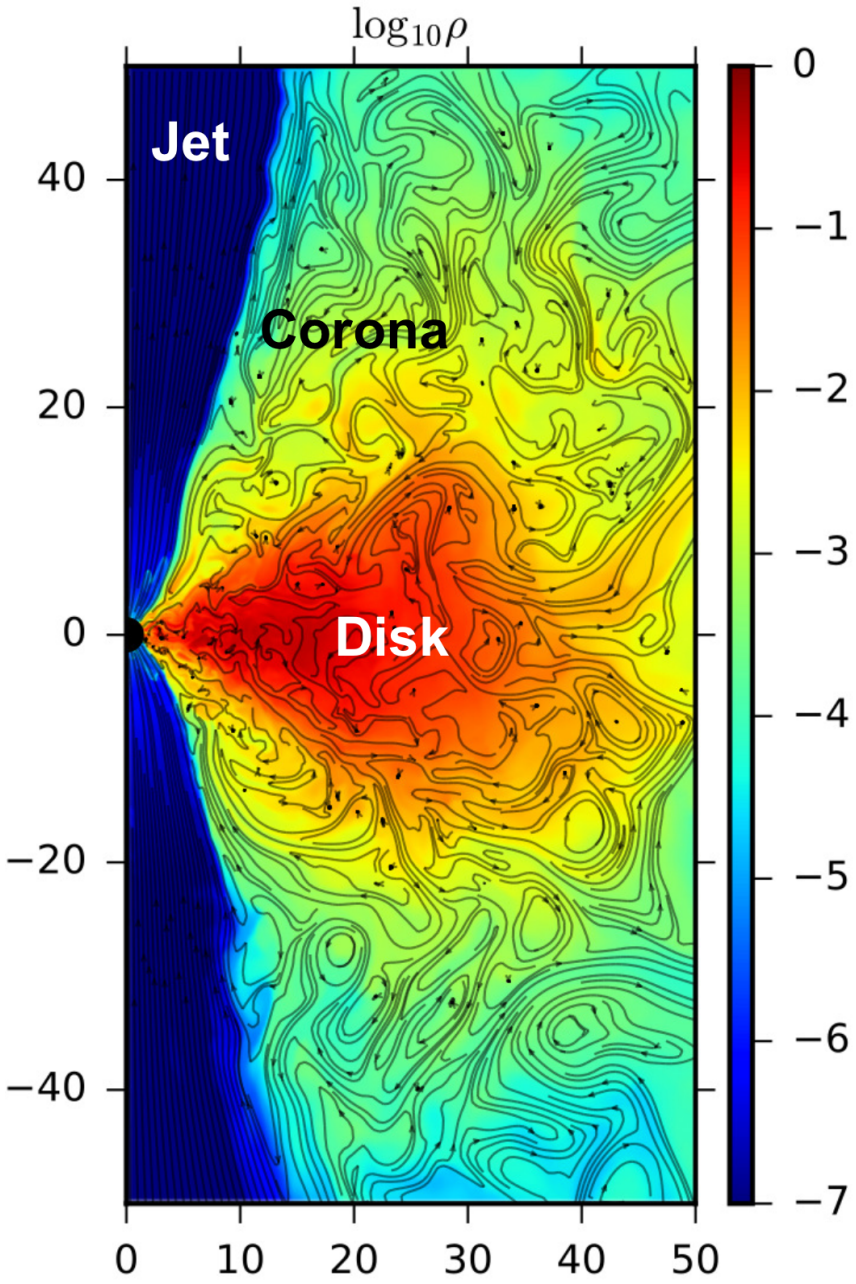

Figure 1.11: Instantaneous slice of a two dimensional GRMHD simulation of a magnetised rotating torus around an accreting black hole. Colour represents density in log scale and the lines trace the magnetic field. The arrows point the direction of the field. The spatial scale is in units of r_g. Three regions can be identified in the flow: disk, corona and jet. Credit: Porth et al. (2017)

The disk body is where most of the mass is located. It is dense with roughly constant scale height values ~ 0.4, full with MHD turbulence and is dominated by gas pressure, with typical values being $\sim 10 - 100$ times stronger than the magnetic pressure. In the disk the material can orbit steadily with increasing speed for decreasing radii, with velocities similar to Keplerian, up until it reaches the innermost stable circular orbit (ISCO), inside of which the flow is forced to spiral rapidly towards the black hole.

The corona is located above and below the disk and is the region from where powerful winds are ejected. Here, the gas density is much lower causing the magnetic field to be roughly in equipartition, with its strength augmenting with increasing separation from the midplane, and is able to reach values that are ten times stronger than the gas pressure above about two density scale heights (De Villiers, Hawley, & Krolik, 2003; De Villiers et al., 2005).

Transitioning from the corona to the polar regions of the black hole is the funnel. Magnetically dominated and with very low gas densities, this region generates powerful jets that arise from magnetic field lines threading the event horizon due to the rotation of the black hole.

The most famous mechanisms to power outflows in simulations are the Blandford-Payne model (BP, Blandford & Payne, 1982) and the Blandford-Znajek model (BZ, Blandford & Znajek, 1977). The main distinction between them is that while in the former the rotational energy of the accretion flow produces, at least partly, non-relativistic winds, in the latter, the rotational energy from the black hole spin is extracted, powering relativistic jets with high Poynting flux.

The extraction of the rotational energy from the black hole happens at a rate proportional to the square of both the magnetic flux on the event horizon $\Phi_{\rm BH}$ and the dimensionless black hole spin $a = Jc/GM^2$ (with J the angular momentum of the BH, Blandford & Znajek, 1977; Tchekhovskoy, Narayan, & McKinney, 2011). With mass and mass accretion rates similar to those in M87, and high (dimensionless) magnetic fluxes $\Phi_{\rm BH}/\sqrt{\dot{M}cr_g} \sim 50$ at the event horizon, the Blandford-Znajek mechanism is capable of producing jet powers of $10^{42} - 10^{45}$ erg s^{-1} (Tchekhovskoy, Narayan, & McKinney, 2010; McKinney, Tchekhovskoy, & Blandford, 2012; McKinney et al., 2014; Sadowski et al., 2013; Event Horizon Telescope Collaboration et al., 2019e), comparable to those observed in the M87 jet (Reynolds et al., 1996; Owen, Eilek, & Kassim, 2000; Stawarz et al., 2006).

These high (dimensionless) magnetic fluxes are characteristic of a particular set of GRMHD simulations. The "Magnetically Arrested Disks" (MADs; (Bisnovatyi-Kogan & Ruzmaikin, 1974; Narayan, Igumenshchev, & Abramowicz, 2003; Igumenshchev, Narayan, & Abramowicz, 2003; Igumenshchev, 2008) are highly magnetised systems in which a strong vertical bipolar magnetic field is advected into the central black hole by the accretion flow. Magnetic flux starts to build up coherently on the black hole, causing accretion to be limited due to the high magnetic pressure. This results in episodic powerful ejections of material from the inner zones of the accretion flow when the magnetic pressure saturates and exceeds the in-fall force of the accretion flow onto the black hole.

Systems with $0 \leq \Phi_{\rm BH} < \Phi_{\rm MAD}$, where $\Phi_{\rm MAD}$ denotes the MAD limit, are referred to as

Table 1.1: Comparison between SANE and MAD averaged hydrodynamic parameters from GRMHD calculations (Dexter et al., 2020a). The inflow equilibrium radius is set by r_{eq}, $\langle H \rangle / R$ is the density scale height of the system at the horizon and v^{ϕ}/v_K the ratio between the angular velocity v^{ϕ} and the Keplerian angular velocity at the horizon.

	$\phi_{\rm BH}$	β	r_{eq} (r_g)	$\langle H \rangle / R$	v^{ϕ}/v_K
SANE	~ 10	$10-30$	18	$0.2-0.3$	1.0
MAD	50-80	$5-10$	30	0.1	$0.4-0.6$

Table 1.2: Comparison between SANE and MAD average physical parameters of radiative models of Sgr A* at 230 GHz. The accretion rates $\dot{M}$ have been chosen so that the average luminosity at 230 GHz matches that of Sgr A* ($\sim$ 3 Jy, Dexter et al., 2020a). τ_I and τ_ρ denote the optical and Faraday depths respectively (Sections 1.9 and 3.5.8), n the particle density, B the magnetic field strength and $\theta_e = k_B T / m_e c^2$ is the dimensionless electron temperature (with k_B the Boltzmann constant and m_e the electron mass).

	$\dot{M}$ (10^{-8} $M_\odot$ yr^{-1})	τ_I	τ_{ρ_V}	n (10^6 cm^{-3})	B (G)	θ_e
SANE	$4-9.0$	$1.0-3.0$	$330-430$	$8.0-10.0$	$60-80$	$11-13$
MAD	$\sim$1.0	$0.6-0.9$	$10-20$	$2.0-4.0$	$70-80$	$11-14$

"Standard and Normal Evolution" models (SANE, Narayan et al., 2012). The differences between both systems are noticeable. Tables 1.1 and 1.2 show a few comparisons between them. While Table 1.1 shows typical hydrodynamic parameters between SANE and MAD models from GRMHD simulations, Table 1.2 focuses on the physical parameters of radiative models for Sgr A* (Dexter et al., 2020a).

Due to the high computational expense, GRMHD studies often do not include the individual tracking of photons and the radiative interactions these might have as they move within the accretion flow. In these cases, a separate calculation of images and spectra is made afterwards by post-processing the output of the simulation using Monte Carlo (Dolence et al., 2009) or ray-tracing radiative transfer methods[22].

1.8 Ray-tracing radiative transfer

Electromagnetic radiation that travels through a medium is subject to numerous radiative processes, including absorption, emission and scattering processes. The radiative transfer equation describes these numerous interactions mathematically. For non-relativistic, unpolarized transport without scattering, the frame dependent radiative transfer equation is (Rybicki & Lightman, 1979)

$$\frac{d}{ds} I_\nu = j_\nu - \alpha_\nu I_\nu \ , \tag{1.12}$$

[22]Neglecting radiative cooling of electrons seems to be a good approximation for Sgr A* (e.g., Dibi et al., 2012) but probably not for M87 (e.g., Mościbrodzka et al., 2011).

where ν is the observed frequency, I_ν denotes the specific intensity, j_ν and α_ν are, respectively, the coefficients that characterise emission and absorption in the medium through which the radiation propagates.

Images and spectra from GRMHD simulations can be calculated in post process employing ray-tracing methods. Given a radiative model of emission and absorption, the observed intensities are obtained by numerically solving the radiative transfer equation along a given path that extends from a pixel in an "observer's camera" and the place where the photon was emitted. In this framework, general relativistic effects can be naturally incorporated in the calculations by defining said path as the null geodesics that photons would follow in a given spacetime geometry. Ray tracing allows as well for the tracking of frequency shifts due to Doppler beaming and gravitational redshift.

Most of the radiation is emitted by a bulk of matter close to the black hole, where general relativistic effects are dominant (Figure 1.12). Given the high orbital velocities, total intensity images are subject to strong Doppler boosting, gravitational redshift and light bending, showing an apparent asymmetry in the disk where bright and faint emissions indicate, respectively, the approaching and receding sides of the accretion flow. Moreover, photons that reach observer which are emitted "behind" the black hole will follow "bent" trajectories around the object, which give the impression of a warped disk above and below the midplane. Properties of these images, such as variability and size, have been used to compare GRMHD simulations to observables of Sgr A* and M87* in order to restrict model parameters (Dexter et al., 2020a, Chapter 3).

1.9 Polarized radiative transfer

In addition to total intensity images, polarization information can be extracted from GRMHD simulations as well. This is an excellent improvement from analytic models since the magnetic field is evolved self-consistently from an initial condition. This, combined with turbulence driving time variability, offers a great opportunity to study flaring events (Dexter et al., 2020b).

Given the number of radiative effects in the accretion flow that can alter the polarized properties of the emitted light, particularly Faraday rotation (subsection 3.5.8), an accurate characterisation of these processes requires polarized radiative transfer (e.g., Dexter, 2016; Mościbrodzka & Gammie, 2018).

The non-relativistic polarized radiative transfer equation, including emission and absorption but not scattering is given by (Gammie & Leung, 2012)

$$\frac{d}{ds}\begin{pmatrix} I \\ Q \\ U \\ V \end{pmatrix} = \begin{pmatrix} j_I \\ j_Q \\ j_U \\ j_V \end{pmatrix} - \begin{pmatrix} \alpha_I & \alpha_Q & \alpha_U & \alpha_V \\ \alpha_Q & \alpha_I & \rho_V & -\rho_U \\ \alpha_U & -\rho_V & \alpha_I & \rho_Q \\ \alpha_V & \rho_U & -\rho_Q & \alpha_I \end{pmatrix} \begin{pmatrix} I \\ Q \\ U \\ V \end{pmatrix} \tag{1.13}$$

where (I, Q, U, V) are specific intensities associated with the Stokes parameters, $j_{I,Q,U,V}$ are the polarized emissivities, $\alpha_{I,Q,U,V}$ the absorption coefficients and $\rho_{Q,U,V}$ are the Faraday

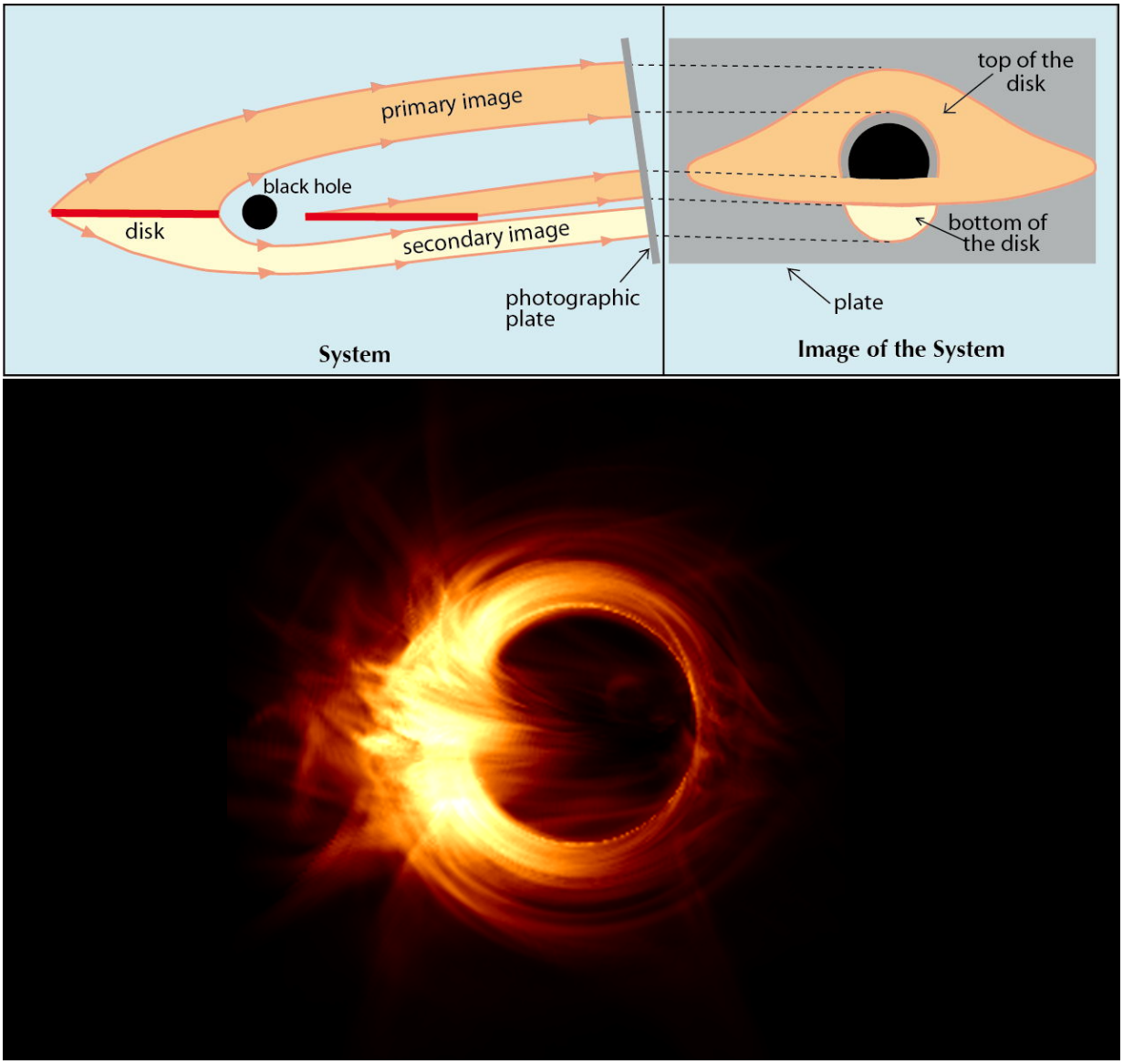

Figure 1.12: **Top:** schematic of the optical distortions near a black hole due to the cured spacetime around it. The object is surrounded by a thin static disk. Light on top of the image comes from regions behind the black hole, similarly to the bright bottom region. Credit: Luminet (1992). **Bottom:** simulated 230 GHz non-rotating black hole surrounded by a thick rotating disk viewed at 50°. Intensity is shown as false colour with more emission coming from brighter areas. The bent image of the disk can be appreciated. The asymmetry in the emission is produced by strong Doppler boosting. The inner dark region at the centre of the image is the shadow of the black hole.

rotation and conversion coefficients. The total intensity I is positive definite while Q, U and V are signed quantities. This is similar for the emissivities as well. While $Q < 0$ indicates linear polarization along one axis in the plane perpendicular to the wave vector, $Q > 0$ characterises linear polarization along the second axis. Similarly, U describes polarization at $\pm 45°$ from the first axis. V corresponds to circular polarization, with positive values meaning right-hand circular polarization. By definition, $I^2 \geq Q^2 + U^2 + V^2$, which implies that $j_I^2 > j_Q^2 + j_U^2 + j_V^2$.

Equation 1.13 is reference-frame dependent due to the fact that the definition of Q and U depend on the orientation of the axes of the observer. However, it can be re-written in invariant form using $\mathcal{I} = g^3\mathbf{I}$, $\mathcal{J} = g^2\mathbf{J}$ and $\mathcal{K} = g^{-1}\mathbf{K}$, where $\mathbf{I}$ and $\mathbf{J}$ are the intensity and emissivity vectors, $\mathbf{K}$ is the transfer matrix from Equation 1.13 and $g = \nu_{obs}/\nu_{em}$ is the combined redshift and Doppler factor that relates the emitted frequency, ν_{em}, to the observed, ν_{obs}.

In terms of these quantities, Equation 1.13 is re-written as

$$\frac{d}{d\lambda}\mathcal{I} = \hat{\mathcal{J}} - \hat{\mathcal{K}}\mathcal{I} \tag{1.14}$$

where λ is and affine parameter, $\hat{\mathcal{J}} = g^2 R(\chi_0)\mathbf{J}$, $\hat{\mathcal{K}} = g^{-1}R(\chi_0)\mathbf{K}R(-\chi_0)$, and

$$R(\chi) = \begin{pmatrix} 1 & 0 & 0 & 0 \\ 0 & \cos 2\chi_0 & -\sin 2\chi_0 & 0 \\ 0 & \sin 2\chi_0 & \cos 2\chi_0 & 0 \\ 0 & 0 & 0 & 1 \end{pmatrix} \tag{1.15}$$

where χ_0 is the angle between the projected magnetic field and the polarization basis.

1.10 Polarization maps and time-dependent polarization

Polarized radiative transfer allows for the calculation images of the different Stokes parameters. The images often resemble the morphology of the total intensity, however, unlike I which is positive definite, they can show regions with negative values. From the polarized quantities per pixel it is possible to generate "polarization maps", where the polarization vectors are calculated and plotted. Their magnitude is usually chosen to be proportional to the linear polarization $LP = \sqrt{Q^2 + U^2}$ in the pixel. The direction is set by the *electric vector polarization angle* (EVPA) χ defined as:

$$\chi = \frac{1}{2}\tan^{-1}\left(\frac{U}{Q}\right) \tag{1.16}$$

Polarization maps can be useful in visualising the underlying magnetic field $\mathbf{B}$ in a system. In an electromagnetic wave, the electric field ($\mathbf{E}$), magnetic field ($\mathbf{B}$) and wave ($\mathbf{k}$)

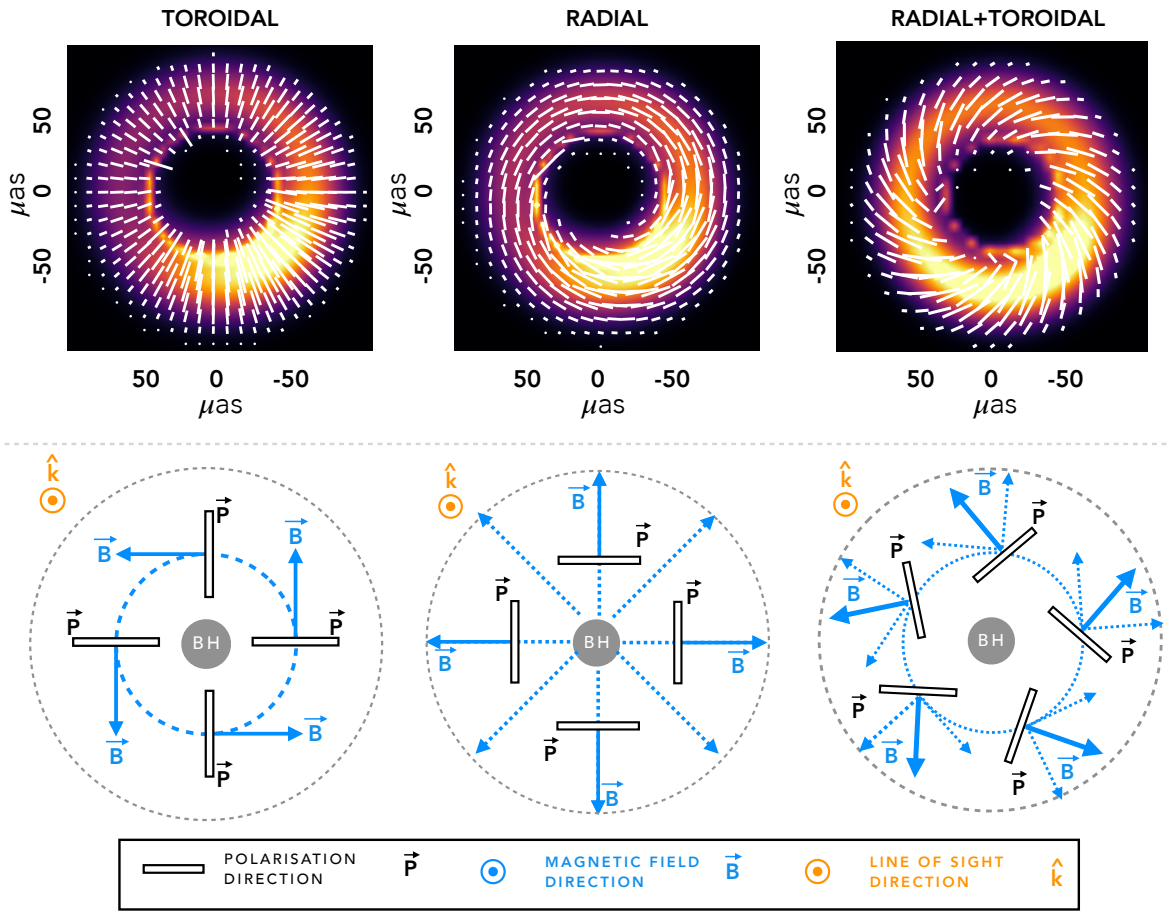

Figure 1.13: **Top:** example polarization maps of numerical calculations at low inclinations. The simulations feature an optically thin rotating disk around a black hole. Different underlying magnetic field geometries have been considered in the calculations and are labeled on top of each panel. The order, starting from the left, is: toroidal, radial and radial plus toroidal. Total intensity is shown in false colour with more emission coming from from brighter regions. In the foreground, the spatial configuration of the polarization is shown as white ticks with length proportional to the linear polarization in the pixel. It can be seen that in the absence of radiative transport effects, the polarization vectors trace the magnetic field geometry. **Bottom:** corresponding schematics to the numerical calculations in the top panels.

vectors are perpendicular to each other, so that $\mathbf{k} \cdot \mathbf{p} = \mathbf{p} \cdot \mathbf{B} = \mathbf{k} \cdot \mathbf{B} = 0$. By convention, the polarization vector $\mathbf{p}$ is aligned with the electric vector $\mathbf{E}$, resulting in $\mathbf{p} = \mathbf{k} \times \mathbf{B}$. From this last expression, it can be seen that in the absence of radiative effects that may affect the direction of the emitted polarization state, for example internal Faraday rotation (subsection 3.5.8), the direction of the polarization vectors is a clear tracer of magnetic field structure. Figure 1.13 shows examples of GRMHD calculations of an optically thin rotating torus with different static magnetic field configurations in optically thin medium and their corresponding schematics. Since this direction is sensitive to the local conditions in the plasma, the spatial configuration of the polarization can be used to study accretion models and parameter regimes (e.g. Jiménez-Rosales & Dexter, 2018; Dexter et al., 2020a, Chapters 2 and 3).

Time-dependent polarization can also be used to study the properties of a system (Chapter 5). The top panel of Figure 5.5 shows an example of this. Here, an optically thin compact emission region is orbiting a black hole in a medium with a static magnetic field configuration. As it moves, the observed linear polarization pattern characterised by Q and U changes in time. Since the emission region is optically thin, it effectively samples the magnetic field configuration in time. This generates time-dependent behaviour of the net linear Stokes parameters Q and U in the image, as shown in the bottom panel of Figure 5.5, which depends on the particulars of the model, like the orbital radius r and the viewer inclination i, but specially on the underlying magnetic field structure. With this idea in mind, by studying the time-dependent polarization behaviour of the Stokes parameters it is possible to infer information on the underlying magnetic field structure of the system.

1.11 Faraday rotation

As the synchrotron radiation produced by the hot, magnetised plasma (Faraday screen) travels through the accretion flow, birefringence in the emitting region will alter the properties of the polarized light.

Faraday rotation is the phenomenon in which the plane of polarization of an electromagnetic wave is rotated as it passes through a magnetised medium (Rybicki & Lightman, 1979; Longair, 2011). This is based on the fact that a linearly polarized wave can be decomposed into two opposite-handed circularly polarized components that propagate with different phase velocities within the plasma.

Being substantially sensitive to the physical conditions in the accretion flow, Faraday rotation is characterised by the Faraday rotation coefficient, $\rho_V \propto f n_e B \nu^{-2}$, where the n_e is the electron density, B the magnetic field strength in the medium, ν the frequency of light and the factor $f = 1$ in the case of a non-relativistic plasma. As the electron population becomes relativistically hot, $f = \log T_e / 2T_e^2$ where the T_e is the electron temperature (Jones & Hardee, 1979).

The Faraday rotation depth, $\tau_{\rho_V} = \int \rho_V dl$ along the light ray trajectory reflects the difference in radians between the intrinsic polarization angle of the emitted light and the one observed at a certain point in the accretion flow.

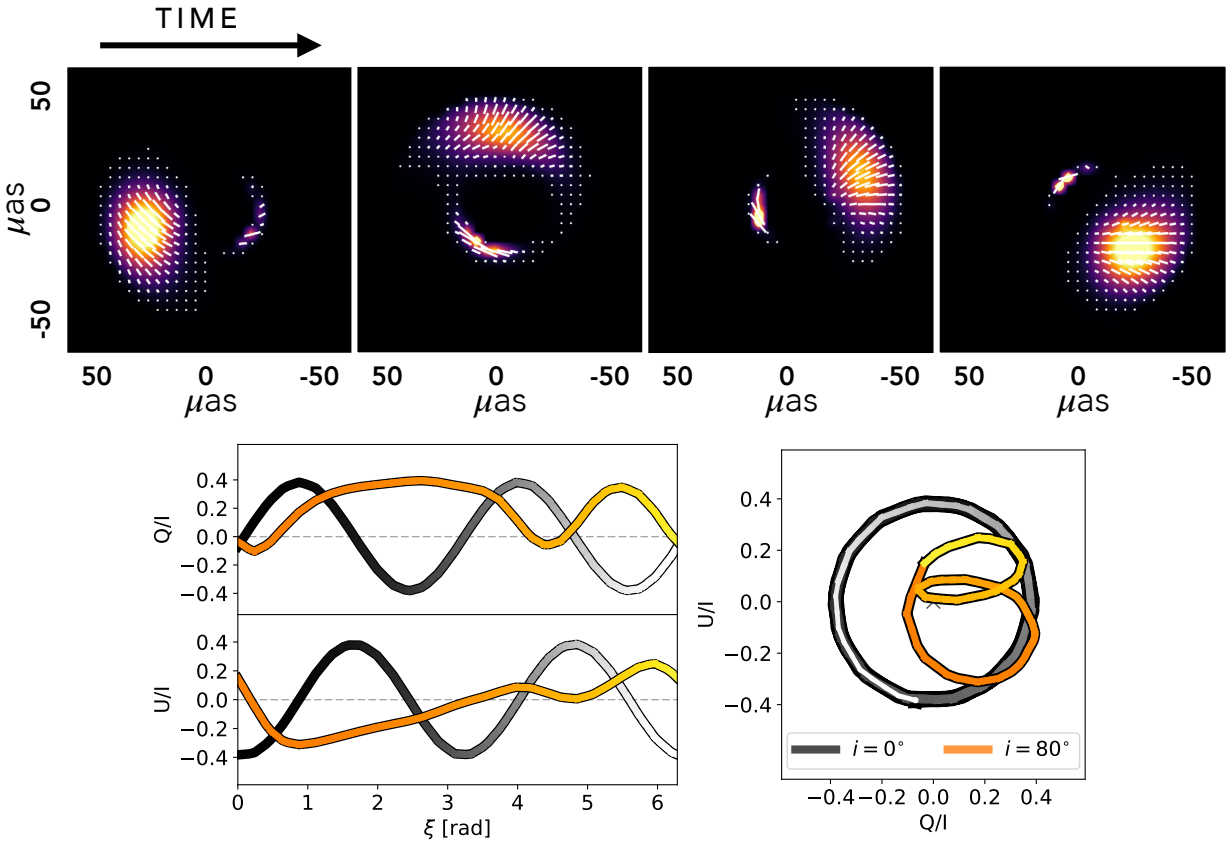

Figure 1.14: **Top:** snapshots of numerical calculations of an optically thin, compact emission region ("hotspot") orbiting a black hole. Total intensity is shown in false colour. The silhouette of the black hole shadow is traced by direct emission from the hotspot and the secondary images resulting from strong lensing. Polarization is shown in the foreground as white ticks with length proportional to the linear polarization in the pixel. As the hotspot moves around the black hole, it generates a time dependent linear polarization pattern characterised by the net Stokes parameters in the image Q and U and effectively sampling the underlying magnetic field structure in time. **Bottom:** evolution of net linear Stokes parameters in the image as the hotspot orbits the black hole (colour coded). Two viewer inclinations are shown here: $i = 0°, 80°$.

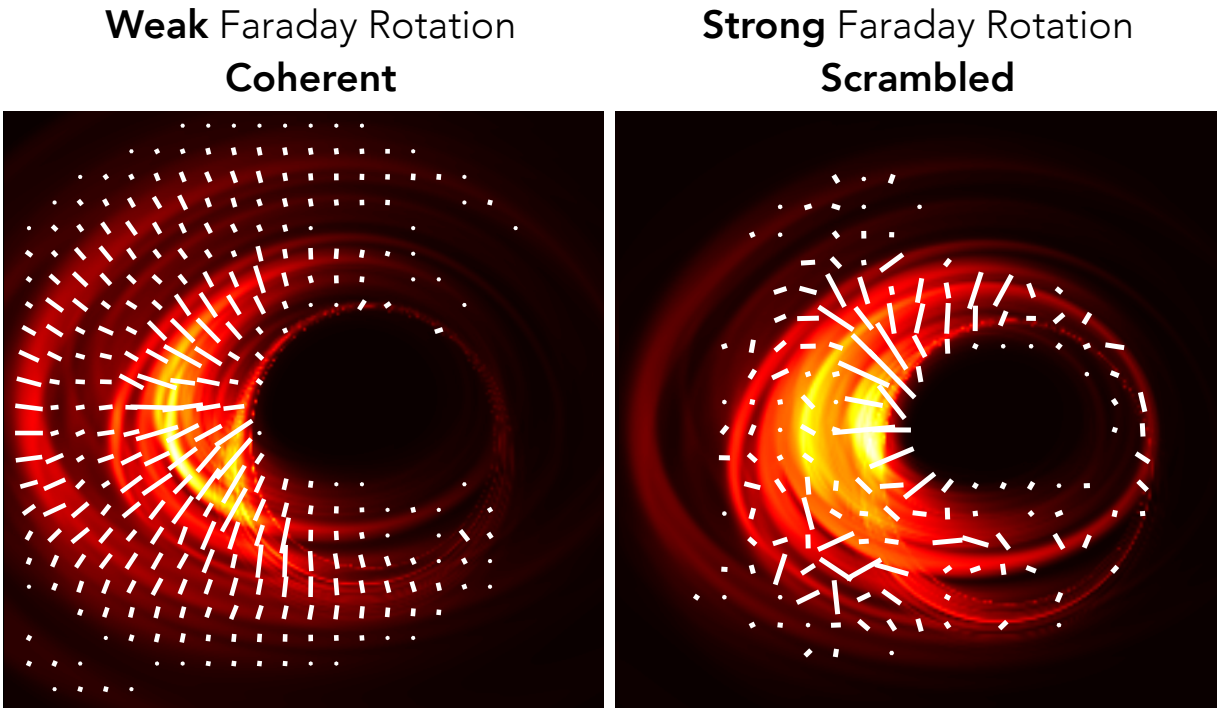

Figure 1.15: Polarization maps showing the effects of Faraday rotation. **Left:** weak faraday effects. The initial emitted polarization state is mostly unaltered as light travels through the accretion flow and shows an ordered configuration that traces the magnetic field. **Right:** strong Faraday effects. The initial polarization direction is highly affected by the local conditions in the plasma and shows disordered patterns that reduce the observed linear polarization in the image. It is noticeable that while the total intensity images shown in the background are similar, the spatial polarization patterns are completely different. This is useful in restricting plasma parameters in models (Chapter 2).

In the cases where $\tau_{\rho_V} \ll 1$, the degree of rotation of the polarization plane follows a single wavelength dependence, with an observable rotation measure (RM) given by

$$RM = \frac{\chi(\lambda_2) - \chi(\lambda_1)}{\lambda_2^2 - \lambda_1^2} = 10^4 \frac{e^3}{2\pi m_e^2 c^4} \int f n_e B_{||} dl \ [\text{rad m}^{-2}] \tag{1.17}$$

where $\chi = 1/2 \arctan(U/Q)$ is the position angle of the polarization plane, Q and U are Stokes parameters that characterise linear polarization and λ_1, λ_2 are two closely spaced observing wavelengths. The relation $\rho_v \propto f n_e B \nu^{-2}$ has been used for the right most side and $B_{||}$ is the magnetic field strength integrated along the line of sight. In these cases ($\tau_{\rho_V} \ll 1$), the plasma screen effectively acts as a homogeneous screen that rotates the plane of polarization evenly, causing no depolarization. This is known as external Faraday rotation.

Depolarization of a source, however, can occur as a result of *internal* Faraday rotation. As the electromagnetic wave travels within the plasma, small scale structure in the accretion flow with variable ρ_V will contribute differently to the rotation of the polarization angle. Large values of τ_{ρ_V} are associated to this scenario. The higher the value, the more "random" the overall observed electric vector position will appear to be with respect to the initial emitted state (module 2π) and the level of observed polarization will be reduced (Figure 3.10).

The key difference between internal and external depolatization is that the former is correlated to the RM such that regions with small values of RM should be more or even almost completely polarized. External beam depolarization, on the other hand, should exhibit a dependence on the gradient of the RM. Very high resolution data at multiple frequencies is needed in order to differentiate between these types of Faraday rotation.

1.12 Polarization observations

Polarization information has been a key element in setting limits on accretion model quantities. Unresolved observables including linear polarization fractions and rotation measures have been used to limit accretion rates and electron temperatures (e.g., Agol, 2000; Quataert & Gruzinov, 2000). Particularly for the rotation measures, it is notable that submm wavelengths are more advantageous than other radio bands since the opacities of the accretion flow are smaller, implying that regions closer to the black hole can be probed.

In the case of Sgr A*, linear polarization fractions of $2-9\%$ are reported (Aitken et al., 2000; Bower et al., 2003, 2017; Marrone et al., 2006) and a mean rotation measure between 227 and 343 GHz of about -6×10^5 rad m^{-2} (Marrone et al., 2006, 2007). Using semi-major axis size constraints of Sgr A* from mm-VLBI at 230 GHz of $a_{230} = 51 - 63$ μas (Johnson et al., 2018), it is possible to estimate the brightness temperature T_b of Sgr A* if it were radiating as a black body. At 230 GHz, black body radiation $B_\nu(T)$ can be approximated with the Rayleigh-Jeans law, where $B_\nu(T) \propto \nu^2 T_b$. Assuming an emitting area of $\pi(a_{230}/2)^2$, this gives $T_b \sim 10^{10}$ K. Since black body radiation is the most efficient way of emitting radiation, T_b sets a lower limit on the actual temperature of a system

of size a_{230}. The detection of a non-zero linear polarization fraction indicates that the Faraday rotation depth must be $\tau_{\rho_V} \sim 1$ (Agol, 2000; Quataert & Gruzinov, 2000). In this regime, $\tau_{\rho_V} \propto nB/T^2$, so that $nB \propto T^2$. Numerical simulations show that plasma beta $\beta = p_{gas}/p_{mag} \approx 10$, from which it is possible to obtain order of magnitude estimates close to the horizon of $B \sim 0.1$ G, $n \sim 10^5$ cm^{-3} and $10^{-8} M_\odot$ yr^{-1}.

In a similar manner, this can be done for M87. Radio observations at centimetre wavelengths estimate RM values of around -10^3 rad m^{-2} in the radio lobes and -10^2 rad m^{-2} in the jet (Owen, Eilek, & Keel, 1990; Algaba, Asada, & Nakamura, 2013). On upstream parsec scales, RM values of -10^3 rad m^{-2} have been found (Junor & Biretta, 2001; Zavala & Taylor, 2002). By fitting the wavelength dependence of the polarization angles, $\chi(\lambda)$, at four independent frequencies around 230 GHz, (Kuo et al., 2014) determined a rotation measure value at the core of 10^5 rad m^{-2}. Assuming a power-law density profile and an ordered, radial magnetic field in equipartition, gives an upper limit on the accretion rate of $\sim 10^{-3} M_\odot$ yr^{-1}.

More recently, spatially resolved polarization has been useful in estimating the strength of Faraday effects within the emission region (which allows for setting limits on the accretion flow properties) and in studying magnetic field structure and strength at event horizon scales (Johnson et al., 2015; Mościbrodzka et al., 2017; Jiménez-Rosales & Dexter, 2018; Dexter et al., 2020a, Chapter 5).

Whereas in the past polarization data have been interpreted with semi-analytic models and imposed magnetic field geometries, GRMHD simulations provide the opportunity to study these in the context of more complex, dynamic systems. This, together with the new spatially resolved polarization observations from the EHT (Johnson et al., 2015) and GRAVITY (Gravity Collaboration et al., 2018a), make it now possible to study the role of magnetic fields and Faraday rotation effects in shaping the polarization properties of black hole accretion models.

1.13 This Thesis

This Thesis focuses on the theoretical study of the polarized properties of GRMHD models of Sgr A* and M87* and their relation to observables in nature.

Chapter 2 presents a study of the spatial correlation in polarization configurations from different models of accretion in the submm wavelength regime and its dependence on the plasma parameters. This is particularly useful for Sgr A* and M87* since now it is possible to reconstruct the real patterns of the sources from the new, horizon scale, spatially resolved, polarization measurements of the EHT, with which the magnetic field strength and electron temperature in the emission region can be potentially estimated.

Chapter 3 investigates the general and polarized properties of a variety of models from time variable, three-dimensional, GRMHD, multi-wavelength simulations. The state-of-the-art calculations include a variety of self-consistent electron heating prescriptions, magnetic field strengths and inclinations as well. Observables of these models are calculated and compared to measurements of Sgr A* in an effort to uniformly test the viability of the

models for this source.

In Chapter 4 a study of the polarized properties of the photon ring in GRMHD calculations is presented. Motivated by the similarity in total intensity and polarized flux images, a technique is developed to enhance the photon ring properties in an image when conditions in the plasma are suitable. Given that in GR black holes are are fully described by their mass, angular momentum and charge, this powerful technique can allow for measurements of the mass and the spin of a black hole in an image and for potential tests of general gravity in regimes where the gravitational potential is large.

Chapter 5 presents a study of time-variable linear polarization signatures of a compact emission region orbiting a black hole with a given underlying magnetic field. This model is applied to measurements of Sgr A* during a bright NIR flare observed with the GRAVITY instrument during 2018, taking into account a new improved calibration that includes the instrument's response as a function of time. A variety of magnetic field geometries are explored in an effort to model the data and their physical implications in the surroundings of the black hole.

Finally, Chapter 6 presents the overall conclusions of this work and an outlook within the context of expected technological and scientific advancements in the upcoming years.

Chapter 2

Faraday effects on polarized black hole images of Sagittarius A*

Original publication: A. Jiménez-Rosales & J. Dexter, 2018, MNRAS, 478, 1875, *The impact of Faraday effects on polarized black hole images of Sagittarius A**, DOI:10.1093/mnras/sty1210

Abstract: We study model images and polarization maps of Sagittarius A* at 230 GHz. We post-process GRMHD simulations and perform a fully relativistic radiative transfer calculation of the emitted synchrotron radiation to obtain polarized images for a range of mass accretion rates and electron temperatures. At low accretion rates, the polarization map traces the underlying toroidal magnetic field geometry. At high accretion rates, we find that Faraday rotation internal to the emission region can depolarize and scramble the map. We measure the net linear polarization fraction and find that high accretion rate "jet-disc" models are heavily depolarized and are therefore disfavoured. We show how Event Horizon Telescope measurements of the polarized "correlation length" over the image provide a model-independent upper limit on the strength of these Faraday effects, and constrain plasma properties like the electron temperature and magnetic field strength.

2.1 Introduction

The compact radio source Sagittarius A* (Sgr A*) is the closest supermassive black hole candidate to Earth (e.g. Genzel, Eisenhauer, & Gillessen, 2010; Falcke & Markoff, 2013). With a mass $M \sim 4.3\times10^6$ solar masses and at a distance $D \sim 8.3$ kpc (Boehle et al., 2016; Gillessen et al., 2017), Sgr A* is the black hole with the largest apparent angular size on

the sky (with a shadow of $\sim 50\mu$as[1]), which makes it an excellent laboratory for studying accretion physics around black holes and for probing general relativistic effects. Sgr A* emits most of its luminosity from synchrotron radiation in what is called the "submillimetre bump." At these wavelengths (~ 1 mm), the radiation is expected to be optically thin and originate from close to the black hole (Falcke & Markoff, 2000b; Bower et al., 2015).

Models of radiatively inefficient accretion flows (RIAFs, Narayan & Yi (1995); Quataert & Narayan (1999); Yuan, Quataert, & Narayan (2003)) and magnetised jets (Falcke & Markoff, 2000b; Yuan, Markoff, & Falcke, 2002) have been developed to explain the radio spectrum of Sgr A*. Such models can now be realised using general relativistic magnetohydrodynamic (GRMHD) simulations, which capture the time-dependent accretion process as a result of the magnetorotational instability (MRI, Balbus & Hawley, 1991) including all relativistic effects. This is particularly important for interpreting mm-VLBI data from the Event Horizon Telescope (EHT), which now resolves the emission at 230 GHz on event horizon scales. The compact size found for Sgr A* is $\simeq 4$ Schwarzschild radii (Doeleman et al., 2008; Fish et al., 2011).

Total intensity images of submm synchrotron emission from such models predict somewhat different morphologies (size, degree of asymmetry) due to differences in the initial conditions, such as magnetic field configuration, electron-proton coupling, electron temperature distribution function and evolution, to name a few. Although any particular model is well constrained (e.g., Dexter et al., 2010; Broderick et al., 2011), the images are often dominated by the relativistic effects of light bending and Doppler beaming due to an emission radius close to the event horizon, resulting in a characteristic crescent shape (e.g., Bromley, Melia, & Liu, 2001; Broderick & Loeb, 2006b; Mościbrodzka et al., 2009; Dexter et al., 2010; Kamruddin & Dexter, 2013; Mościbrodzka et al., 2014; Chan et al., 2015b; Ressler et al., 2017). As a result, model-dependence in parameter estimation from total intensity images is a major current issue.

The discovery of $5-10\%$ linear polarization from Sgr A* at 230 GHz (Aitken et al., 2000) showed that the accretion rate is much less than that inferred from X-ray observations (Baganoff et al., 2001) of hot gas at the Bondi radius (Agol, 2000; Quataert & Gruzinov, 2000). At the Bondi accretion rate, the *internal* Faraday rotation within the emitting plasma should depolarize the synchrotron radiation at 230 GHz. Later detections of *external* Faraday rotation allow an estimate of the accretion rate $\sim 10^{-9}-10^{-7}M_\odot$ yr^{-1} (Bower et al., 2003; Marrone et al., 2006), a factor $\simeq 100$ smaller than the Bondi value.

EHT observations provide the opportunity to measure the *spatially resolved polarization*, and show that this fraction can rise to up to $20-40\%$ on event horizon scales (Johnson et al., 2015). They interpret this as evidence for a balance of order and disorder in the underlying polarization map, which can be well matched by maps from GRMHD simulations (Gold et al., 2017).

Here we use polarized radiative transfer calculations of a single snapshot from an axisymmetric GRMHD simulation (§3.3) to understand how the resulting polarization prop-

[1]The angular size of Sgr A* is given by $R_{\rm s}/D \sim 10$ μas, where $R_{\rm s} \sim 1.36\times10^{12}$ cm is the Schwarzschild radius.

erties depend on the physical parameters of the emitting plasma. We show that internal Faraday effects become strong in a significant range of model parameter space, scrambling and depolarizing the resulting polarization maps (§3.5). Measuring the correlation length of the polarization direction from spatially resolved data provides the cleanest way to set limits on the underlying properties of the plasma. We show how this can be measured from future EHT data as a novel constraint on the mass accretion rate and electron temperature of the Sgr A* accretion flow.

2.2 Accretion Flow and Emission models

We consider a snapshot of a 2D axisymmetric numerical solution (Dexter et al., 2010) from the public version of the GRMHD code HARM (Gammie, McKinney, & Tóth, 2003; Noble et al., 2006), where the initial conditions consist of a rotating black hole with dimensionless spin $a = 0.9375$ surrounded by a torus in hydrostatic equilibrium (Fishbone & Moncrief, 1976) threaded with a weak poloidal magnetic field. The system evolves according to the ideal MHD equations in the Kerr spacetime.[2] Turbulence due to the MRI produces stresses within the torus and leads to an outward transport of angular momentum, causing accretion of material onto the black hole.

Synchrotron radiation is produced by the hot, magnetised plasma and travels through the emitting medium. In the absence of any other effects, the resulting polarization configuration seen by a distant observer traces the magnetic field structure of the gas.[3] However, as light travels the polarization angle is rotated both by parallel transport in the curved spacetime near the black hole and by Faraday rotation in the magnetised accretion flow, the latter being characterised by the Faraday rotation depth, $\tau_{\rho_V} = \int \rho_V dl$, where

$$\rho_V = (e^3/\pi m_{\rm e}^2 c^2) \cos\theta_B n_{\rm e} B f(T_{\rm e}\ , \vec{B})/\nu^2; \tag{2.1}$$

ρ_V is the Faraday rotation coefficient, $e, m_{\rm e}, n_{\rm e}$ are the electron charge, mass and number density respectively, θ_B is the angle between the line of sight and the magnetic field $\vec{B}$ with $|\vec{B}| = B$, c and ν are the light speed and frequency, and $f(T_{\rm e}\ , \vec{B})$ is a function of $\vec{B}$ and the electron temperature $T_{\rm e}$, but approximately $f \approx T_{\rm e}^{-2}$ (Jones & Hardee, 1979; Quataert & Gruzinov, 2000). All quantities are measured in the comoving orthonormal fluid frame (Shcherbakov & Huang, 2011; Dexter, 2016).

MHD simulations without radiation self-consistently evolve $P_{\rm gas}/n \sim T_{\rm p}$ and B^2/n, where $P_{\rm gas}$ is the gas pressure, n and $T_{\rm p}$ are the proton density and temperature respectively. Choosing the black hole mass sets the length and timescales, while the mass accretion rate $\dot{M}$ is a free parameter which sets the density scale. The electron temperature

[2] Our snapshot is taken at time $t = 2000\ GM/c^3$, where G is the gravitational constant, M is the mass of the black hole and c is the light speed.

[3] So that the emitted polarization vector is perpendicular to the local magnetic field direction, we use EVPA $= 1/2 \tan^{-1}(\mathrm{U/Q})$, where EVPA is the electric vector position angle and Q and U are Stokes parameters.

$T_{\rm e}$ is not self-consistently computed, and one must make a choice for it. Different approaches have been taken to parametrise $T_{\rm e}$, from a constant $T_{\rm p}/T_{\rm e}$ within the accretion flow (Mościbrodzka et al., 2009) to directly evolving it with the fluid (Ressler et al., 2015, 2017; Chael et al., 2018) assuming some electron heating prescription (Howes, 2010; Rowan, Sironi, & Narayan, 2017; Werner et al., 2018). We assume that $T_{\rm e}(\eta\ ,\alpha) = \eta\ T_{\rm p}/\alpha$, with $\eta \in (0\ ,1]$ a constant ratio between the electron and proton temperatures and $\alpha = \alpha(\mu\ ,\beta)$ a function that depends on the magnetisation of the plasma similar to the one used in Mościbrodzka, Falcke, & Shiokawa (2016): [4]

$$\alpha = \mu\frac{\beta^2}{1+\beta^2} + \frac{1}{1+\beta^2}, \tag{2.2}$$

where the plasma parameter $\beta = P_{\rm gas}/P_{\rm mag}$ states the ratio between the gas and magnetic pressures and μ is a free parameter that describes the electron to proton coupling in the weakly magnetised zones (disc body) of the simulation.

The numerical solution we use has a Blandford-Znajek jet (McKinney, 2006). Different choices of μ, the electron-proton coupling factor in Eq. 2.2, can cause the wall between the accretion flow and the jet to shine. When μ in equation 2.2 is small, the disc has a very high temperature and lights up at 230 GHz due to the fact that, compared to the jet, it has both the highest density and magnetic field strength. However, the larger the μ the colder the disc is and the fainter it gets. If one wishes to maintain a fixed flux, the accretion rate onto the black hole $\dot{M}$ must increase. As a consequence, the jet wall can light up first even given its lower density and field strength.

For a given choice of η and $\mu = (1\ ,2\ ,5\ ,10\ ,40\ ,100)$, $\dot{M}$ is then chosen in such a way that the total flux F_ν at 230 GHz is either 3 Jy or 0.3 Jy. We chose the first value to model Sgr A* and the second, 0.3 Jy, arbitrarily to decrease α_I/ρ_V, where α_I is the total absorption coefficient. This second option for F_ν gives us the opportunity to study models in the optically thin regime to separate the effects of absorption and Faraday rotation.

Given that $n_{\rm e} \propto \dot{M}$, $B \propto \dot{M}^{1/2}$, $F_\nu \propto n_{\rm e}^{\xi} B^{\kappa} {T_{\rm e}}^{\sigma}$ (where typically $\xi \in [0,1]$, $\kappa \in [0,2]$, $\sigma \in [1,4]$), and assuming a constant F_ν, we can express the Faraday rotation depth, τ_{ρ_V}, as a function of $\dot{M}$:

$$\tau_{\rho_V} \sim n_{\rm e} B {T_{\rm e}}^{-2} \propto \dot{M}^{\delta}; \tag{2.3}$$

where $\delta \equiv 3/2 + (2\xi+\kappa)/\sigma \simeq 3/2 - 7/2$. It can be seen from eq. 2.3 that τ_{ρ_V} has a strong dependence on $\dot{M}$ and small changes of this quantity reflect as big differences in τ_{ρ_V}. Due to this, models with similar physical parameters can vary widely in the strength of the internal Faraday effects and, for $\tau_{\rho_V} \gtrsim 1$, in the resulting polarization structure.

To account for emission, absorption, parallel transport and Faraday effects locally within the accretion flow, we employ the publicly available numerical code GRTRANS (Dexter & Agol, 2009; Dexter, 2016)[5] to do a self-consistent fully relativistic ray tracing radiative transfer calculation at 230 GHz. The output of the calculation is a polarized image of our

[4] We have taken $\mu = R_{\rm high}$ and $R_{\rm low} = 1$ in the Mościbrodzka, Falcke, & Shiokawa (2016) expression.
[5] http://www.github.com/jadexter/grtrans

GRMHD snapshot as seen by a distant observer at a 50 degree inclination from the black hole (and accretion flow) rotation axis.

2.3 Results

Fig. 2.1 shows the resulting intensity-weighted, image-averaged electron temperature $\langle T_{\rm e} \rangle$, polar angle $\langle \cos\theta \rangle$, and Faraday rotation depth $\langle \tau_{\rho_V} \rangle$ for each input model with varying $(\dot{M}, T_{\rm e})$. The steady decrease of $\langle T_{\rm e} \rangle$ with $\dot{M}$ in the upper left panel of Fig 2.1 points to "disc-like" systems. The transition to "jet-like" systems happens when the circles show a constant behaviour with $\dot{M}$ and is highly dependent on μ. As discussed before, at large μ the jet has a high enough temperature that it can outshine the cold disc.

This is shown as well in the right panel of Fig. 2.1, where the cosine of the inclination angle where most of the emission comes from, $\langle \cos\theta \rangle$, as a function of $\dot{M}$ is plotted. It can be seen that at high $\dot{M}$, models that have the same accretion rate but different μ values have different emission regions. As the electron-proton coupling μ increases, the emission region moves towards the poles indicating a transition to a more "jet-like" system.

In the bottom panel of Fig. 2.1 we plot the intensity-weighted image-averaged Faraday rotation depth $\langle \tau_{\rho_V} \rangle$ *vs* $\dot{M}$ and the scaling relation in eq. 2.3, with $\delta = 2$.[6] This panel shows very nicely the wide spread in $\langle \tau_{\rho_V} \rangle$ values as a function of $\dot{M}$, supporting the idea that systems with similar physical parameters can have widely varying strengths of Faraday rotation. This makes $\langle \tau_{\rho_V} \rangle$ a sensitive tracer of the physical conditions of the plasma.

Fig. 2.2 shows four sample polarized images. Plotted in the background is the total intensity image centred on the black hole (colour shows total flux on a linear scale where the lighter the shade the greater the emission).

These images show the accreting material in characteristic asymmetric crescent shapes: due to Doppler beaming in the rotation torus, the left side where the gas approaches the observer is much brighter than the right side. Furthermore, strong relativistic light bending lets us see behind the black hole, whose emission appears to be coming from above and below it in the images. In the foreground, white ticks show linear polarization fraction (LP) direction with their length proportional to the LP magnitude (given by $\sqrt{Q^2 + U^2}$). This is what we refer to as a polarization map (PM).

The images shown in Fig. 2.2 have a variety of model parameters. In the upper left panel an optically thick image is shown. In this case, the system resembles a black body, dominated by optical absorption and is completely depolarized from self-absorption. We can see a case of the Blandford-Znajek jet wall lighting up in the upper right panel of Fig. 2.2 for a case where $\mu = 100$.

The bottom panels of Fig 2.2 are optically thin. In the case of weak Faraday effects (hot, tenuous emitting medium - high $T_{\rm e}$ and low $\dot{M}$, $\langle \tau_{\rho_V} \rangle < 1$; bottom left panel), the polarization traces the toroidal magnetic field (horizontal where the light comes from the approaching gas and vertical where it comes from gas behind the black hole) and displays

[6] We included the effects of Faraday conversion in the radiative transfer calculation as well, but it is significantly weaker than Faraday rotation, and so we focus our study to the latter.

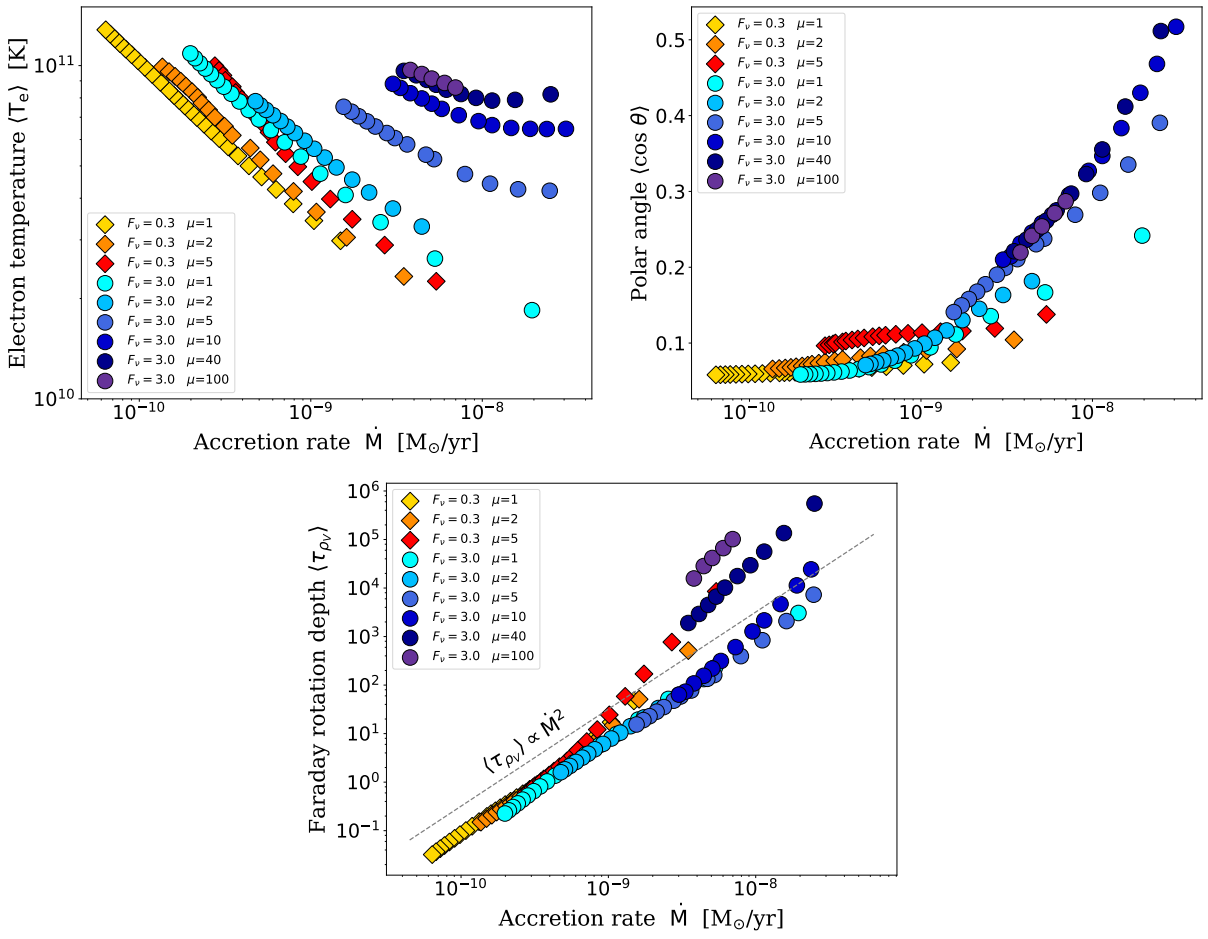

Figure 2.1: Intensity-weighted, image-integrated model quantities. Each dot is a chosen $(\dot{M}, T_e)$ pair with F_ν indicated by a colour scale: diamonds for $F_\nu = 0.3$ Jy and circles for $F_\nu = 3$ Jy. The colour gradient shows the choice for μ, where the lighter (darker) the shade, the lower (higher) the μ value is. **Upper left**: Intensity-weighted, image-averaged electron temperature $\langle T_e \rangle$ *vs* $\dot{M}$. The models that show a steady decrease of $\langle T_e \rangle$ with $\dot{M}$ are more "disc-like" systems. The transition to "jet-like" systems happens where the decrement stops and becomes constant with $\dot{M}$. **Upper right**: Intensity-weighted image-averaged emission angle $\langle \cos\theta \rangle$ as a function of $\dot{M}$. At high $\dot{M}$, as μ increases the emission region moves towards the poles, indicating the transition to a more "jet-like" system. **Bottom**: Intensity-weighted image-averaged Faraday rotation depth $\langle \tau_{\rho_V} \rangle$ *vs* $\dot{M}$. It can be seen how $\langle \tau_{\rho_V} \rangle$ extends over a wide range of values with $\dot{M}$. A scaling relation between both quantities is shown with a dotted line where $\delta = 2$.

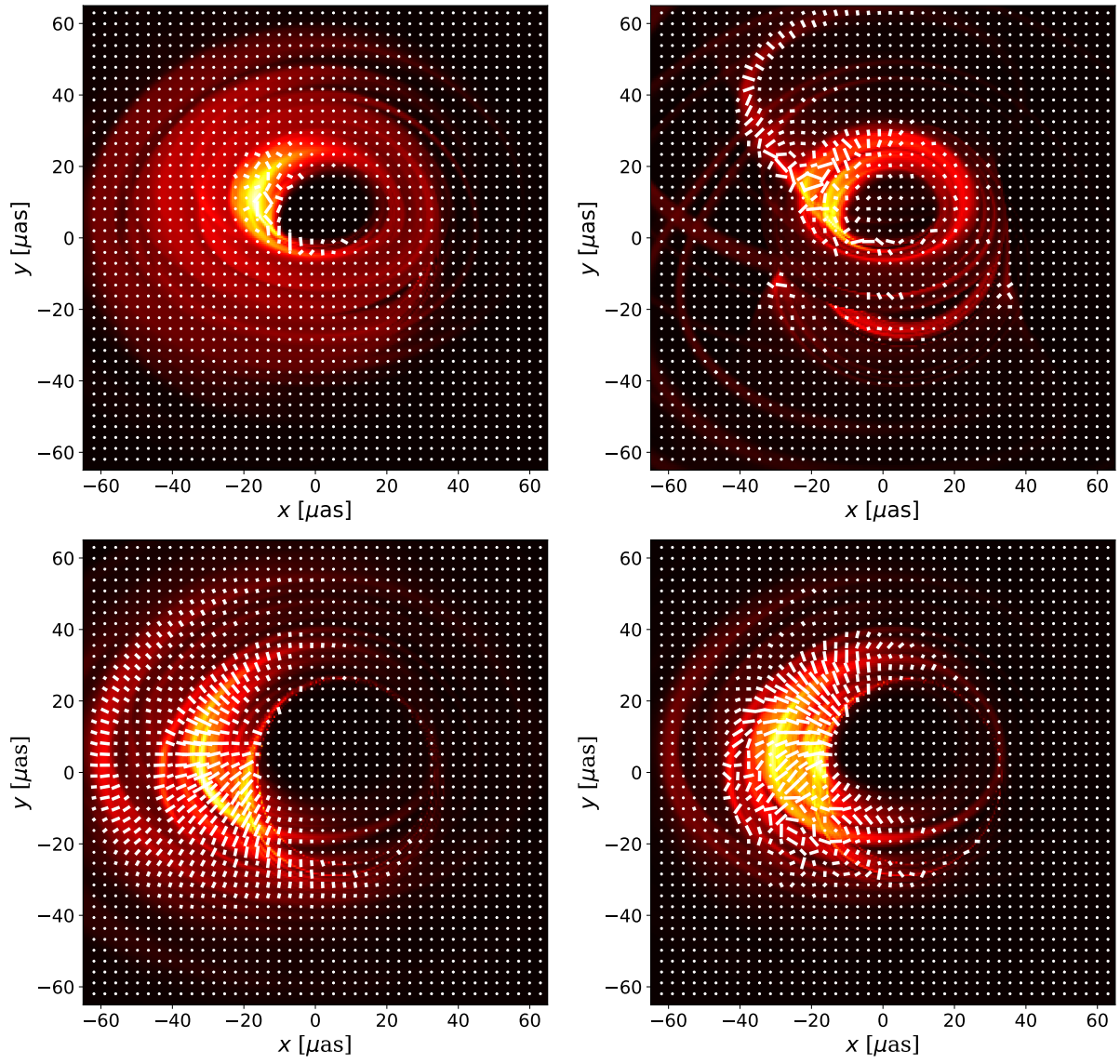

Figure 2.2: Polarization maps obtained from different μ and $(\dot{M}, T_{\mathrm{e}})$ pairs. It can be seen how the Faraday effects affect the polarization. **Upper left panel**: optically thick image. The accretion flow emits like a blackbody and is depolarized. **Upper right panel**: depending on the choice for the electron to proton coupling, the wall between the Blandford-Znajek jet and the accretion flow may become apparent. **Bottom left panel**: weak Faraday effects. The ticks trace the smooth magnetic field configuration. **Bottom right panel**: strong Faraday effects. The ticks are disordered and the underlying magnetic field structure is less evident.

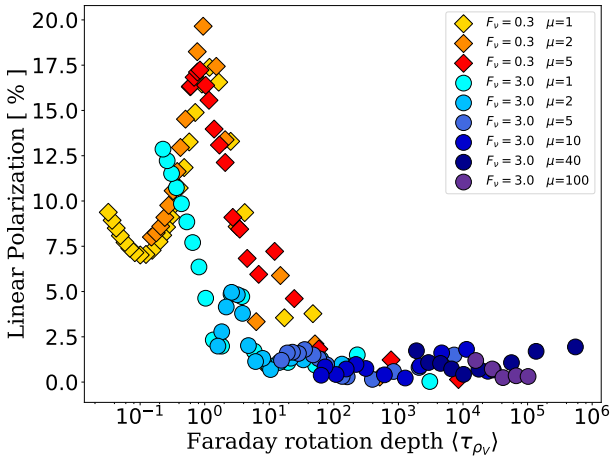

Figure 2.3: Net linear polarization fraction plotted against the intensity-weighted image-averaged Faraday rotation depth $\langle \tau_{\rho V} \rangle$. The same colour and marker criteria has been used as that in figure Fig. 2.1. As the Faraday effects become stronger, the LP decreases, as expected. However the behaviour is neither smooth nor universal ($\langle \tau_{\rho V} \rangle \lesssim 10^2$). "Jet-like" models have high Faraday optical depths ($\langle \tau_{\rho V} \rangle \gtrsim 10^2$) from the cold, dense disc and are heavily depolarized, failing to reproduce the Sgr A* LP of $\simeq 5 - 10\%$.

an ordered behaviour (due to the axisymmetry of the system). The combination of this with the crescent shape background image leads to such a characteristic polarization map (Bromley, Melia, & Liu, 2001). When considering the polarization over the whole image, the contributions from each of the vector components may cancel, resulting in a lower LP over the image (*beam depolarization*). Strong Faraday effects (colder, denser medium - low T_e, high $\dot{M}$; bottom right panel of Fig. 2.2) can scramble and depolarize the image on small scales.

2.3.1 Linear Polarization Fraction and Rotation Measure in the models.

Fig. 2.3 shows the net intensity-weighted LP integrated over the image versus the intensity-weighted image-averaged Faraday rotation depth, $\langle \tau_{\rho V} \rangle$. The images generally depolarize with increasing $\langle \tau_{\rho V} \rangle$, as expected. However, the individual behaviour between both sets of models (diamonds and circles) is different, and no smooth or uniform LP trend as a function of $\langle \tau_{\rho V} \rangle$ can be extracted.

Given a measurement of LP, one could use Fig. 2.3 to set an upper limit on $\langle \tau_{\rho V} \rangle$ and obtain the models that satisfy the restriction set by the LP. As an example, a variety of our "disc-like" models where $\langle \tau_{\rho V} \rangle$ varies over many orders of magnitude ($\sim 5 \times 10^{-2} - 1 \times 10^2$) satisfy the measured $5 - 10\%$ LP for Sgr A* at 230 GHz (Aitken et al., 2000). The emission is locally strongly polarized ($\gtrsim 40\%$) but is naturally beam depolarized due to

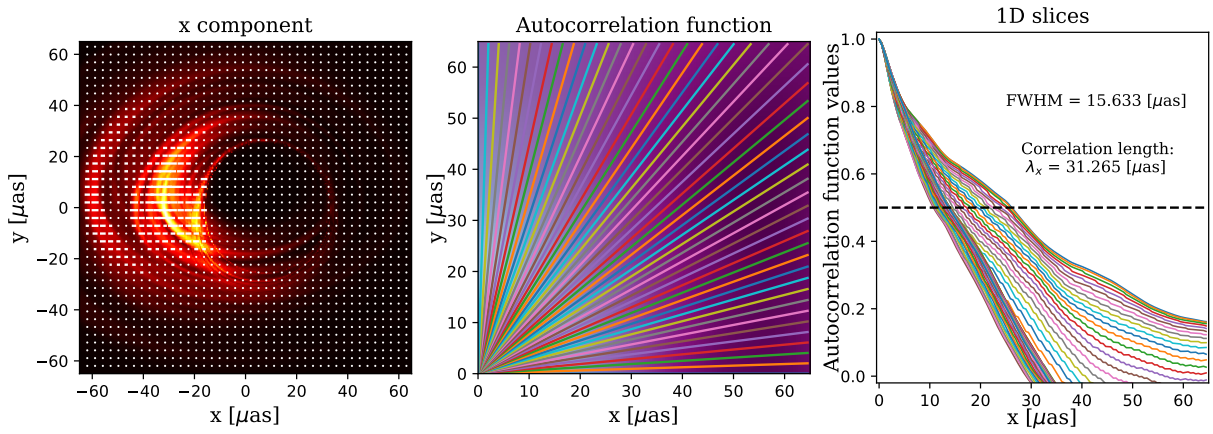

Figure 2.4: Illustration of the calculation of the polarized correlation length. **Left:** take one of the vector components of the polarization (x component shown here) and autocorrelate the map. **Middle:** Plotted in the background in shades of purple is the 2D autocorrelation function. We take 1D slices of this function in different angular directions (coloured solid lines in the foreground) to account for the 2D behaviour. **Right:** 1D slices from the autocorrelation function. Twice the average of their values at 0.5 (FWHM) is how we define as the polarized correlation length, λ_x, in μas.

the combination of the crescent image and toroidal magnetic field configuration. The "jet-like" models ($\langle\tau_{\rho_V}\rangle \gtrsim 10^2$) on the other hand are heavily depolarized, and cannot match the observed LP of Sgr A*.

We looked at the dependence of the rotation measure (RM) of the images with $\langle\tau_{\rho_V}\rangle$ as well and found, as expected, that the RM increases with $\langle\tau_{\rho_V}\rangle$. However, we could not get a clean measurement like in Bower et al. (2003) and Marrone et al. (2006) because our simulation domain is not as large as that in their work. We can look at this in the future, but it would require very long duration simulations (e.g., Narayan et al., 2012) to reach inflow equilibrium at the large radii of the external Faraday screen.

2.3.2 The Correlation Length.

The upper panels of Fig 2.2 can be easily distinguished from their total intensity images alone and might be disfavoured already from the measured size of the source and spectral observations. In the optically thin regimes however (bottom panels), the total intensity images are hard to tell apart and are generally consistent with the observational constraints (Mościbrodzka et al., 2009; Dexter et al., 2010). The polarization maps however, vary substantially. This spatial configuration of the polarization offers an alternative to learning about the physical parameters of the models.

To characterise the degree of order of each map produced by a particular ($\dot{M}$, T_e) pair, we use a quantity which we call the "correlation length", λ. Large values of λ point to an ordered configuration, limited by the coherence of the magnetic field structure, whereas

small values indicate a more disordered configuration.

To calculate this quantity we autocorrelate each map. Because the PM is a vector field, we look at each component separately and weight their value at each pixel by Stokes I at the same pixel[7] (left panel of Fig. 2.4). The result is a 2D function that gives information on how the polarization component varies spatially. We then take 50 "1D slices" of this function in different angular directions to account for the spatial changes in 2D and take the average of their widths at 0.5 (FWHM, middle and right panels of Fig. 2.4). Twice this value is the polarized correlation length in μas.

Figure 2.5 shows the correlation length (λ_x and λ_y, x and y subindices for each vector component) of each simulation's PM as a function of the intensity-weighted image-averaged Faraday rotation depth $\langle\tau_{\rho V}\rangle$.

The overall behaviour of the correlation length for both components is as expected. At small $\langle\tau_{\rho V}\rangle$ (small $\dot{M}$, large $T_{\rm e}$), the Faraday effects are weak implying coherent PMs in which the changes are given by the geometry of the magnetic field in the gas, resulting in a maximum of the correlation length. As $\langle\tau_{\rho V}\rangle$ increases, the Faraday effects become stronger, the scrambling becomes more apparent and the correlation length decreases, showing a sharp drop at around $\langle\tau_{\rho V}\rangle \approx 1$. In the case of the correlation length for the x component, there is a small increase after the minimum that remains until high values for $\langle\tau_{\rho V}\rangle$ which we associate with the internal structure of the polarization. This does not appear in the λ_y plot.

Unlike the LP (Fig. 2.3), the 0.3 Jy and 3 Jy correlation length curves have the same shape and eventually overlap, which points towards a universal behaviour for this quantity (in the limited range of models studied so far). This has powerful implications, since measuring λ sets a model-independent upper limit on $\langle\tau_{\rho V}\rangle(\dot{M}, T_{\rm e}, \beta, {\rm H/R})$, where H/R is the scale height of the disc.

One can relate the correlation length directly to observable quantities in VLBI (Johnson et al., 2015). In their paper, Johnson et al. (2015) show examples with Gaussian intensity distributions and constant net LP ($\sim 6-7\%$), and a varying polarization structure with a prescribed coherence length. They find a correlation length of 0.29 times the Gaussian FWHM of the model. Measuring an approximate Gaussian FWHM for our images and multiplying it by 0.29 gives us an estimated correlation length of $\sim 11.6\mu$as. We then use Fig. 2.5 to set an upper limit on the $\langle\tau_{\rho V}\rangle \lesssim 1$, in agreement with the qualitative argument of Agol (2000) and Quataert & Gruzinov (2000). However, our models are not Gaussians and it is not clear that the λ value inferred by Johnson et al. (2015) applies here.

We can extend the analysis further into visibility space. Fig. 2.6 shows the Stokes parameters I, Q and U (top) and their respective visibilities $\widetilde{I}$, $\widetilde{Q}$ and $\widetilde{U}$ (bottom) of one of our simulations. On large scales, it can be seen that Q and U resemble I, showing the same crescent structure. However, on smaller scales some deviation becomes evident because the polarization, $\vec{p}$, is changing. Therefore, on the largest scales one gets information on I and on the smallest scales one sees the polarization properties.

[7]The reference system is orthonormal with one of the axes aligned with the spin axis of the black hole and the other in a direction perpendicular to the observer (Bardeen, Press, & Teukolsky, 1972).

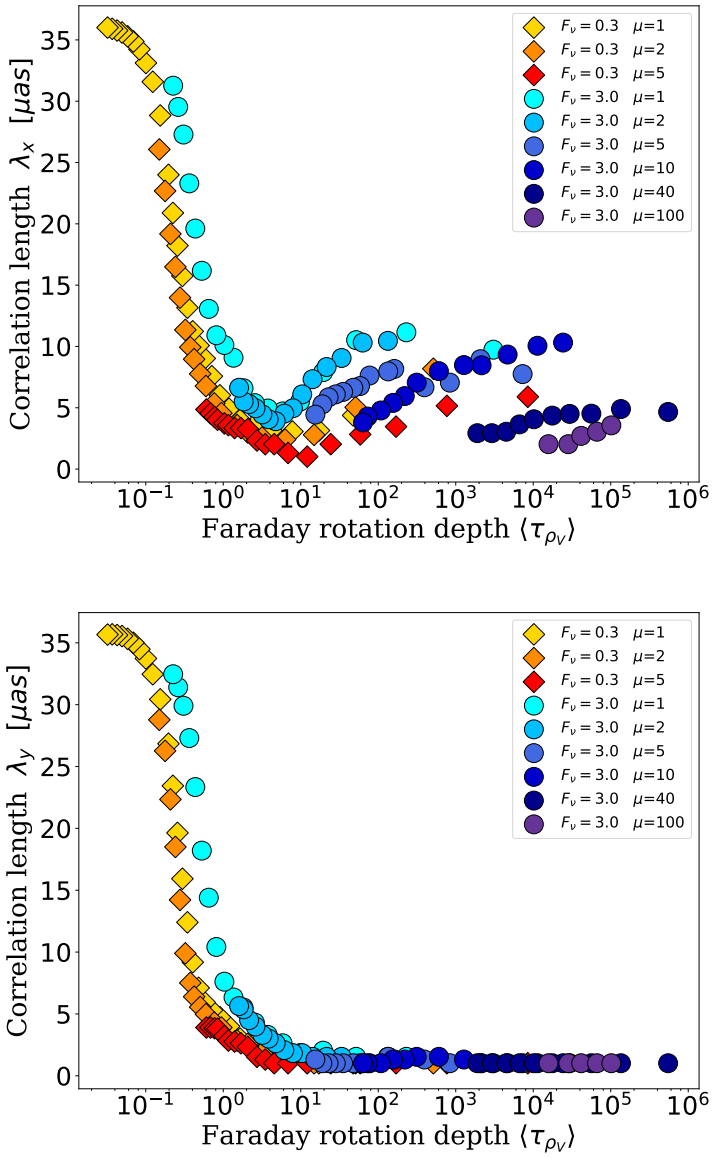

Figure 2.5: Correlation length measured for x and y vector components (left and right panels respectively) of PMs with different μ and ($\dot{M}$,$T_{\rm e}$) values plotted against the intensity-weighted image-averaged Faraday rotation depth $\langle\tau_{\rho_V}\rangle$. The same colour and marker criteria is used as that in Fig. 2.1 and Fig. 2.3. Coherent maps are obtained when $\langle\tau_{\rho_V}\rangle \lesssim 1$ and scrambling appears as the Faraday effects become stronger. A measurement of the correlation length places a model-independent upper limit on $\langle\tau_{\rho_V}\rangle$, and in turn the lower limits on the plasma electron temperature and relative magnetic field strength.

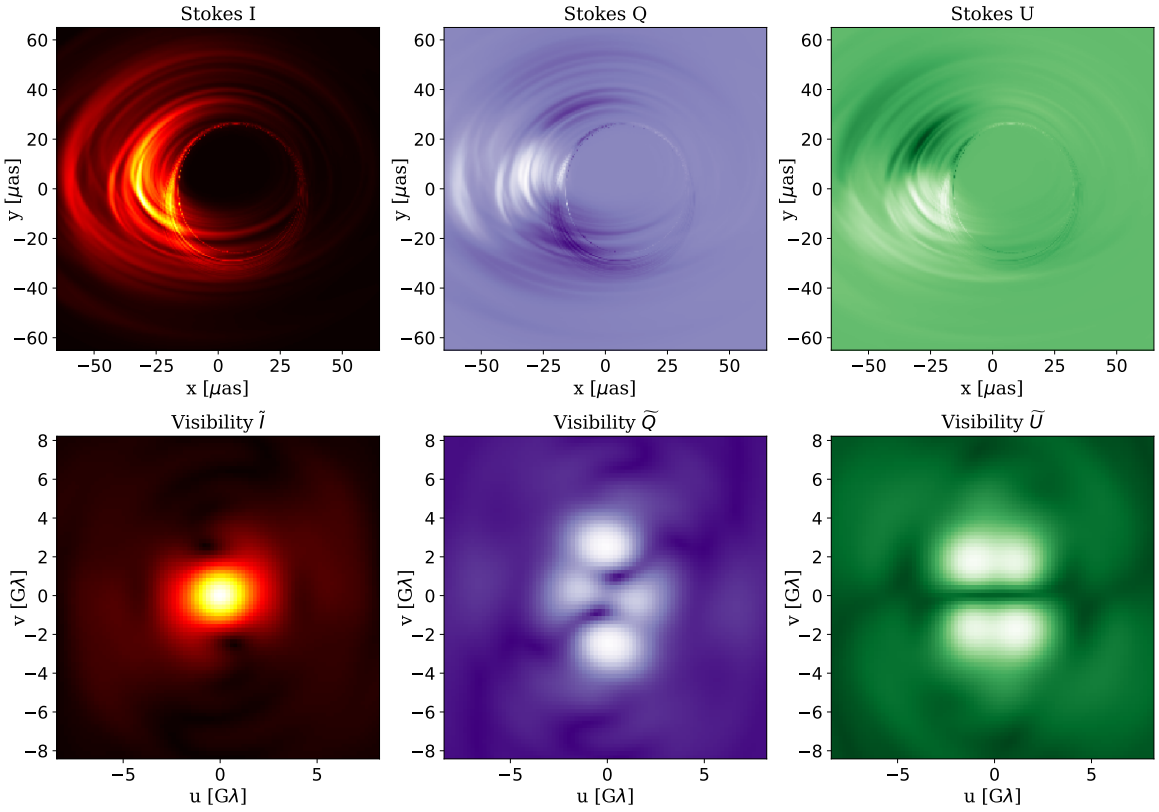

Figure 2.6: I, Q and U Stokes parameters for one of our simulations in image (top panels) and visibility space (bottom panels). On the top images, it can be seen that Q and U resemble I on large scales, with different substructure due to the changing polarization. On the visibility space however (bottom panels), small scale features in $\widetilde{Q}$ and $\widetilde{U}$ give information on I whereas the large scale structure corresponds to the polarization.

If we study this in the visibility space uv and take the Fourier Transform (FT) of the Stokes parameters (bottom images of Fig. 2.6), the roles are inverted. Large scale features become small and vice versa. In this respect, the shape of the total intensity image becomes a small "beam" in uv, whereas the large scale structure observed in the $\widetilde{Q}$ and $\widetilde{U}$ images corresponds to the smallest angular scales in Q and U and reflects the properties of the polarization map.

One can think of the images as the convolution of I with $\vec{p}$, with the result interpreted as I being smeared out by $\vec{p}$ with some characteristic scale that reflects the inner structure of the latter. In the case of a completely disordered polarization map, taking the FT of the image would give what would basically be a noise map in the visibility space, with no characteristic scale at which the polarization's behaviour stands out. On the other hand, the FT of the convolution between I and a completely ordered $\vec{p}$ would give an image with a nice beam centred at $uv = 0$ and no noise whatsoever.

We are interested in finding the characteristic scale at which the random fluctuations or noise in the polarization is suppressed. We call this the polarized correlation length of the visibility, $\lambda_{\widetilde{x}}$, where x is one of the Stokes parameters.

We measure this as the uv distance at which the visibility's amplitude drops permanently below a certain value. As an example, we have chosen this quantity to be 10% of $\widetilde{Q}_{\max}$ and $\widetilde{U}_{\max}$, where $\widetilde{Q}_{\max}$ and $\widetilde{U}_{\max}$ are the maximum visibility amplitudes. We define the visibility correlation length as the inverse of the averaged distances which satisfy this criteria. The calculated $\lambda_{\widetilde{Q}}$ and $\lambda_{\widetilde{U}}$ for our models are shown in Fig. 2.7.

As shown in Fig. 2.7, the correlation length measured in the visibility space can also constrain $\langle \tau_{\rho_V} \rangle$ and is measured directly from VLBI observables. With upcoming data from the EHT, this quantity may be promising for inferring the characteristics of the plasma in the system.

2.4 Discussion

Sgr A* is a great laboratory for testing accretion physics and general relativity. Polarization is a powerful tool for determining the plasma properties and the magnetic field structure.

From a GRMHD simulation of a torus of magnetised plasma in initial hydrostatic equilibrium with a poloidal magnetic field, we have done self-consistent fully relativistic ray tracing radiative transfer calculations of the radiation at 230 GHz. We have analysed the different polarized images and characterised the degree of coherence in the polarization map as a function of the Faraday rotation depth. This coherence scale we call the correlation length. Large values of this quantity are expected when the Faraday effects are weak and the maps are ordered. Small values of the correlation length in our models point to large Faraday rotation depth values and disordered maps.

We have proposed a method to relate the polarized correlation length calculated from the images to direct observables of VLBI by taking the Fourier Transform of the images and analysing the large scale structure of the visibilities in the Fourier domain. This shows a similar behaviour to that showed in the image space, with the advantage that it uses

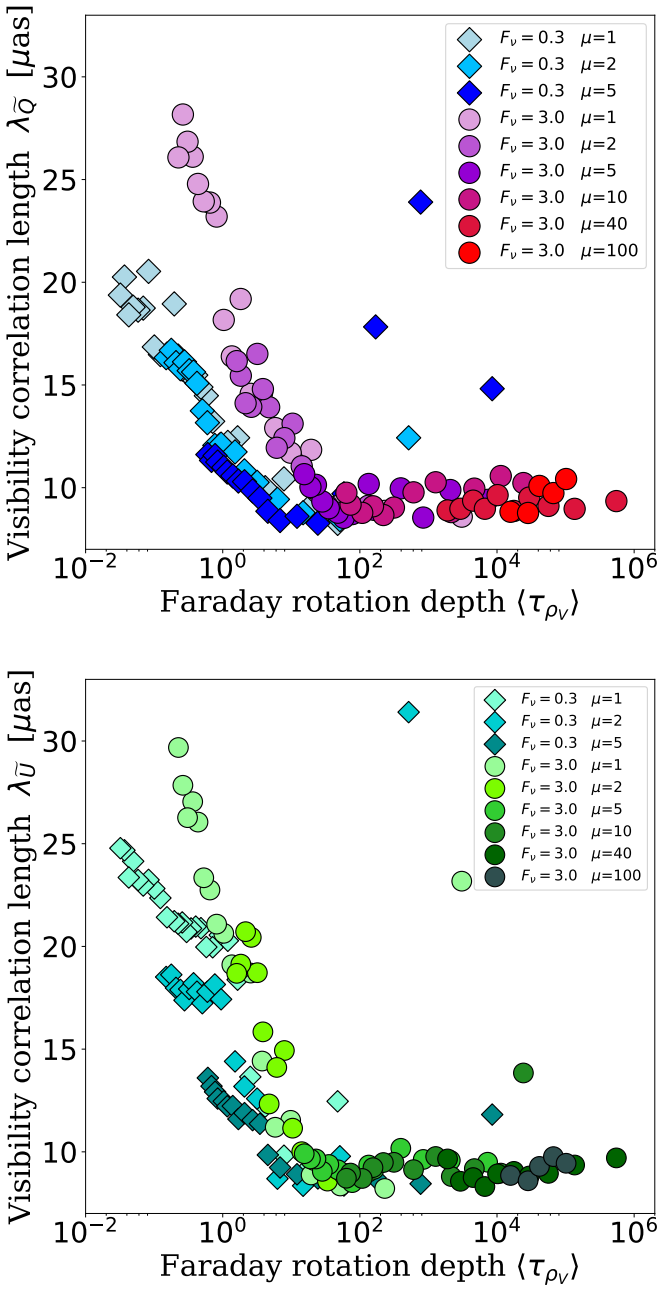

Figure 2.7: Polarized correlation length in the Fourier domain using $\widetilde{Q}$ (left panel) and $\widetilde{U}$ (right panel) for our models. The criteria used was to take the inverse of the averaged uv distances at which the amplitude of the visibility drops below 10% of each respective visibility maximum, $\widetilde{Q}_{\rm max}$ and $\widetilde{U}_{\rm max}$ for each model. As in the image domain, the correlation length drops sharply for $\langle\tau_{\rho_V}\rangle \gtrsim 1$.

VLBI observables.

In the past, unresolved polarization of Sgr A* has been very helpful in constraining models. With the new EHT measurements this can be done with the polarization map itself for the first time through the correlation length. So far, the behaviour of this new quantity appears to be model independent, which makes it a promising approach that can be used to set restrictions on the plasma parameters around the black hole and distinguish models robustly in a way that is often difficult with total intensity images alone.

Constraining $\langle \tau_{\rho_V} \rangle \sim n_\mathrm{e} B T_\mathrm{e}^{-2}$ places limits on the physical properties of the accreting gas, most directly T_e. In addition, $B^2 \sim \beta^{-1} n T_\mathrm{p}$. From hydrostatic equilibrium, $T_\mathrm{p} \sim T_\mathrm{vir}(H/R)^2$, where $T_\mathrm{vir} \sim m_\mathrm{p} c^2/r$ is the virial temperature at dimensionless radius $r = R/R_\mathrm{s}$ and H/R is the scale height of the accretion flow. The relative field strength then scales as $B^2/n \sim \beta^{-1}(H/R)^2$. At fixed flux density, a limit on $\langle \tau_{\rho_V} \rangle$ constrains a combination of the magnetic field strength and disc scale height as well as the electron temperature.

We have only considered one inclination. We expect that the trend of decreasing LP and correlation length with increasing Faraday rotation optical depth holds at all viewing geometries, but their maximum values at low Faraday rotation depth will be model-dependent.

We have also neglected the effects of interstellar scattering. The diffusive part of the scattering should not affect the correlation length results, since we use ratios of the Stokes parameters which are all modified in the same way. The refractive part of the scattering (e.g., Gwinn et al., 2014) could in particular complicate our proposed method for measuring the correlation length in the Fourier domain, since it will introduce signal beyond that corresponding to small scale structure in the polarization map.

We have demonstrated the technique with a single snapshot from an axisymmetric GRMHD simulation. This is has some limitations given that the MRI is unsustainable in 2D and the simulation can only be studied for short times. Therefore, the degree of order seen for $\langle \tau_{\rho_V} \rangle < 1$ (bottom left panel of Fig. 2.2) is somewhat overestimated compared to 3D simulations. Extensions to 3D and studying time variability are goals for future work. The time variable polarized correlation length could for example be used to measure the properties of MRI turbulence in EHT data.

We have focused here on the case of mm-VLBI of Sgr A*, but the same technique should apply to M87 (Mościbrodzka et al., 2017) or any other synchrotron source with a resolved polarization map. In particular, in polarized VLBI images of radio jets past work has focused on measuring the Faraday rotation across the image (e.g., Zavala & Taylor, 2003; O'Sullivan et al., 2018). Here we have shown that the correlation length may be a more robust indicator of the Faraday optical depth, if there is a significant contribution from within the emission region.

Acknowledgements

The authors thank M. Johnson, M. Mościbrodzka, C. Gammie, A. Broderick, R. Gold, J. Kim, and D. P. Marrone for useful discussions related to Sgr A* polarization and radiative transfer. This work was supported by a CONACyT/DAAD grant (57265507) and by a Sofja Kovalevskaja award from the Alexander von Humboldt foundation.

Chapter 3

A parameter survey of Sgr A* radiative models from GRMHD simulations with self-consistent electron heating

Original publication: J. Dexter, A. Jiménez-Rosales, S. M. Ressler, A. Tchekhovskoy, M. Bauböck, P. T. de Zeeuw, F. Eisenhauer, S. von Fellenberg, F. Gao, R. Genzel, S. Gillessen, M. Habibi, T. Ott, J. Stadler, O. Straub & F. Widmann, 2020, MNRAS, 494, 4168, *A parameter survey of Sgr A* radiative models from GRMHD simulations with self-consistent electron heating*, DOI:10.1093/mnras/staa922

Abstract: We study model images and polarization maps of Sagittarius A* at 230 GHz. The Galactic center black hole candidate Sgr A* is the best target for studies of low-luminosity accretion physics, including with near-infrared and submillimeter wavelength long baseline interferometry experiments. Here we compare images and spectra generated from a parameter survey of general relativistic MHD simulations to a set of radio to near-infrared observations of Sgr A*. Our models span the limits of weak and strong magnetization and use a range of sub-grid prescriptions for electron heating. We find two classes of scenarios can explain the broad shape of the submillimeter spectral peak and the highly variable near-infrared flaring emission. Weakly magnetized "disk-jet" models where most of the emission is produced near the jet wall, consistent with past work, as well as strongly magnetized (magnetically arrested disk) models where hot electrons are present everywhere. Disk-jet models are strongly depolarized at submillimeter wavelengths as a result of strong Faraday rotation, inconsistent with observations of Sgr A*. We instead favor the strongly magnetized models, which provide a good description of the median and highly variable linear polarization signal. The same models can also explain the observed mean Faraday rotation measure and potentially the polarization signals seen recently in

Sgr A* near-infrared flares.

3.1 Introduction

The most extensively studied low-luminosity accretion flow is that onto the Galactic centre massive black hole candidate Sagittarius A* (Sgr A*). Detected in the radio (Balick & Brown, 1974), Sgr A* shows an inverted spectrum up to a peak at submillimeter (submm) wavelengths (Serabyn et al., 1997; Falcke et al., 1998; Stone et al., 2016; von Fellenberg et al., 2018; Bower et al., 2019). The bolometric luminosity is $\simeq 5 \times 10^{35}\,\mathrm{erg\,s^{-1}}$ (Bower et al., 2019), roughly 9 orders of magnitude sub-Eddington for the mass of $4 \times 10^6 M_\odot$ measured from the orbit of the star S2 (Ghez et al., 2008; Gillessen et al., 2009, 2017; Gravity Collaboration et al., 2018b, 2019; Do et al., 2019a). Due to its proximity, Sgr A* is the largest black hole in angular size on the sky. It has long been a target of radio very long baseline interferometry (VLBI, (Lo et al., 1975; Backer, 1978; Krichbaum et al., 1998; Bower et al., 2006). With 1.3mm VLBI, the source size is as compact as $\simeq 8 - 10\ r_g$ (Doeleman et al., 2008; Fish et al., 2011; Lu et al., 2018; Johnson et al., 2018), where $r_g = GM/c^2 \simeq 6 \times 10^{11}$ cm is the gravitational radius.

Sgr A* shows large-amplitude "flares" simultaneously at near-infrared (NIR, Genzel et al., 2003; Ghez et al., 2004) and X-ray (Baganoff et al., 2001) wavelengths. They originate from transiently heated electrons, likely as a result of magnetic reconnection or shocks (Markoff et al., 2001) close to the black hole (Barrière et al., 2014; Haggard et al., 2019). The observed emission is due to synchrotron radiation at radio to NIR (and likely also X-ray, Dodds-Eden et al. (2009)) wavelengths and is strongly polarized from the submm to NIR (Aitken et al., 2000; Bower et al., 2003; Marrone et al., 2006; Eckart et al., 2006; Trippe et al., 2007).

The flares can now be spatially resolved with the second generation VLT Interferometer beam combiner instrument GRAVITY. In 2018, three flares were shown to continuously rotate clockwise at relativistic speeds (Gravity Collaboration et al., 2018a). The astrometric data are consistent with orbital motion around Sgr A* at a radius of $6 - 10 r_g$ (Gravity Collaboration et al., 2020c). A matching polarization angle evolution suggests the presence of dynamically important magnetic fields in the emission region on event horizon scales. There is also evidence for ordered magnetic fields from 1.3mm VLBI (Johnson et al., 2015).

Theoretical models of the near horizon regions of low-luminosity accretion flows (Rees et al., 1982; Narayan, Yi, & Mahadevan, 1995b; Yuan, Quataert, & Narayan, 2003) are now commonly realized using general relativistic MHD (GRMHD) simulations (Gammie, McKinney, & Tóth, 2003; De Villiers, Hawley, & Krolik, 2003). These calculations capture the self-consistent evolution of the magnetic field, which drives accretion via the magnetorotational instability (Balbus & Hawley, 1991) and extracts black hole spin energy to power relativistic jets (BZ, Blandford & Znajek, 1977). Past models of Sgr A* based on such calculations have found submm spectra (e.g., Noble et al., 2007; Mościbrodzka et al., 2009; Shcherbakov, Penna, & McKinney, 2012; Mościbrodzka et al., 2014) variability (Dexter, Agol, & Fragile, 2009; Dexter et al., 2010; Chan et al., 2015a), source sizes (Mościbrodzka

et al., 2009; Dexter et al., 2010; Shcherbakov, Penna, & McKinney, 2012), and polarization (Shcherbakov, Penna, & McKinney, 2012; Gold et al., 2017) consistent with observations. Similar to analytic models (Falcke, Melia, & Agol, 2000; Bromley, Melia, & Liu, 2001; Broderick & Loeb, 2006a), they generically find that the submm and shorter wavelength emission originates near the event horizon, resulting in "crescent" shaped images.

Many of those calculations made two important, simplifying assumptions regarding the radiating electrons: i) that they are thermally distributed in energy, despite low densities implying a collisionless plasma (e.g., Mahadevan & Quataert, 1997); and ii) that the electron to proton temperature ratio is a constant value (Goldston, Quataert, & Igumenshchev, 2005). Alternative, physically motivated prescriptions have instead put more of the available internal energy in electrons where the magnetic fields are stronger (Mościbrodzka & Falcke, 2013; Chan et al., 2015b) or according to kinetic prescriptions taking into account anisotropic viscosity (Sharma et al., 2007; Shcherbakov, Penna, & McKinney, 2012). Anantua, Ressler, & Quataert (2020) recently studied a wide range of electron temperature prescriptions.

Those prescriptions were applied in post-processing to calculate the electron energy density (temperature) from single fluid MHD simulations. GRMHD algorithms can now evolve a separate electron fluid, which receive a fraction of the local dissipated energy according to a chosen sub-grid prescription (Ressler et al., 2015). Such models self-consistently heat electrons, and can incorporate more directly results from kinetic calculations (e.g., Howes, 2010; Rowan, Sironi, & Narayan, 2017; Werner et al., 2018; Kawazura, Barnes, & Schekochihin, 2019; Zhdankin et al., 2019, H10, R17, W18, K19). Ressler et al. (2017) showed that "disk-jet" models are a natural outcome of turbulent heating prescriptions based on gyrokinetic theory, where the electrons are heated preferentially in strongly magnetized regions (H10). Chael et al. (2018) showed that electron heating is more uniform in alternative scenarios based on heating mediated by magnetic reconnection (R17).

Here we carry out a parameter survey, expanding the range of electron heating models and magnetic field strength compared to previous work (section 3.2). We constrain radiative models (section 3.3) using the updated submm to NIR polarized spectrum, total intensity rms variability, and 86/230 GHz image size (section 3.4). We show (section 3.5) that two combinations of heating prescriptions and magnetic field strengths can explain the broad submm peak and large amplitude NIR variability of Sgr A*. Those correspond to disk-jet models considered in previous work (Mościbrodzka et al., 2014; Ressler et al., 2017), as well as magnetically arrested accretion flow scenarios (MADs, Shcherbakov & McKinney, 2013; Gold et al., 2017). Our disk-jet models underproduce the observed submm linear polarization, and so are disfavored. We show that very long duration GRMHD simulations can produce the observed Faraday rotation measure of Sgr A*. Finally, we discuss the prospects of future observations and improvements to the theoretical models (section 5.5).

Table 3.1: Parameters and convergence criteria of GRMHD simulations averaged over $8 - 10 \times 10^3\, r_g/c$.

magnetic field	spin parameter	$\phi_{\rm BH}$	$\langle b_r b^r \rangle / \langle b_\phi b^\phi \rangle$	$\langle Q^{(\theta)} \rangle$	$\langle Q^{(\phi)} \rangle$	$\langle \beta \rangle$	$r_{\rm eq}$ (r_g)
SANE	0	7.3	0.14	16.3	23.7	19.9	19.4
SANE	0.5	7.9	0.16	16.3	21.4	26.7	17.8
SANE	0.9375	8.6	0.19	19.6	24.4	27.1	19.8
MAD	0	49.7	0.21	55.6	56.4	7.9	31.1
MAD	0.5	72.4	0.34	87.9	67.0	8.0	25.6
MAD	0.9375	56.5	0.41	138.1	95.7	5.8	34.6

Table 3.2: Time evolution of convergence criteria, magnetic field strength, and inflow equilibrium radius for our long duration SANE $a = 0$ simulation.

time $(10^3\, r_g/c)$	$\phi_{\rm BH}$	$\langle b_r b^r \rangle / \langle b_\phi b^\phi \rangle$	$\langle Q^{(\theta)} \rangle$	$\langle Q^{(\phi)} \rangle$	$\langle \beta \rangle$	$r_{\rm eq}$ (r_g)
$5 - 10$	7.9	0.13	15.2	21.5	23.0	17.8
$10 - 25$	6.0	0.16	18.7	24.8	21.1	28.8
$25 - 50$	6.7	0.17	22.6	29.8	17.8	41.0
$50 - 100$	8.0	0.18	26.8	35.3	14.5	61.3
$100 - 200$	12.8	0.19	30.1	38.8	13.3	89.0

Table 3.3: Time evolution of convergence criteria, magnetic field strength, and inflow equilibrium radius for our long duration MAD $a = 0.9375$ simulation.

time $(10^3\, r_g/c)$	$\phi_{\rm BH}$	$\langle b_r b^r \rangle / \langle b_\phi b^\phi \rangle$	$\langle Q^{(\theta)} \rangle$	$\langle Q^{(\phi)} \rangle$	$\langle \beta \rangle$	$r_{\rm eq}$ (r_g)
$5 - 10$	61.4	0.37	112.5	91.3	6.4	13.4
$10 - 20$	59.2	0.37	111.4	92.6	6.5	30.0
$20 - 30$	62.7	0.38	125.9	100.2	7.8	52.5
$30 - 40$	62.7	0.34	112.7	96.1	8.2	66.7
$40 - 60$	62.6	0.40	141.8	103.9	7.5	65.9

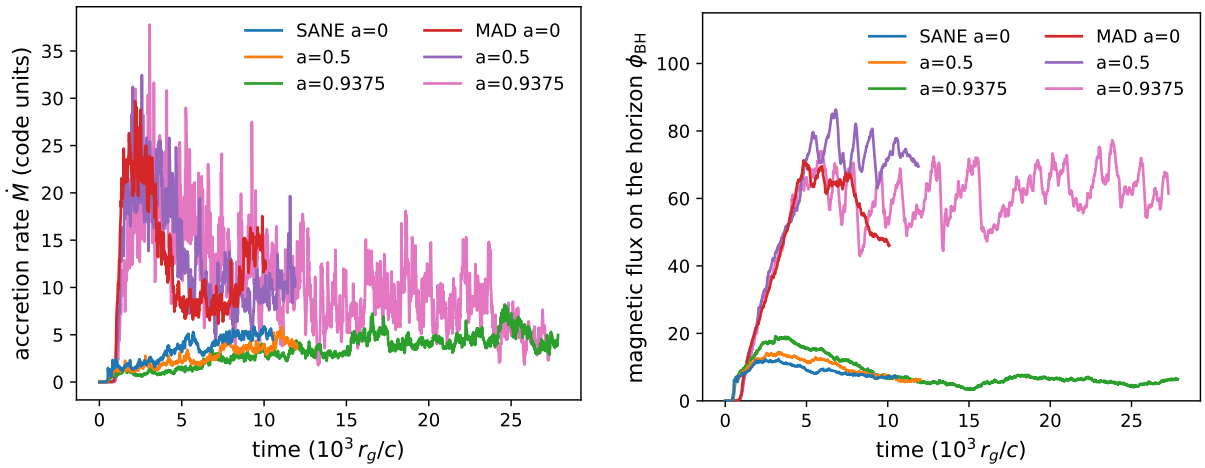

Figure 3.1: Accretion rate and dimensionless magnetic flux on the black hole event horizon $\phi_{\rm BH}$ as a function of time for the simulations used here. The SANE and MAD limits are reached as intended, with low and saturated dimensionless magnetic flux accumulated on the black hole. In the SANE case, the accretion rate remains steady or rises as the large initial torus drains. In the MAD case, strong magnetic fields lead to rapid accretion of the torus.

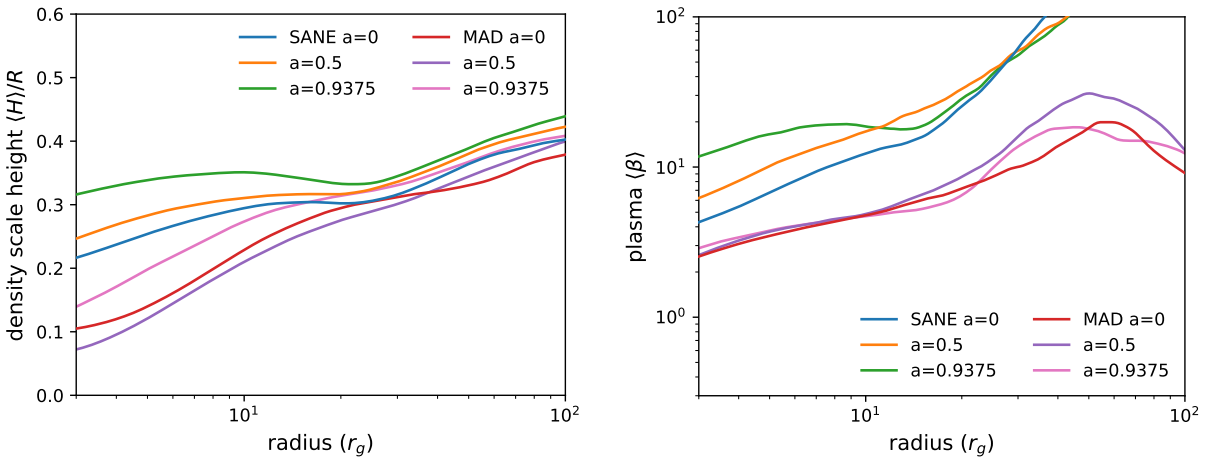

Figure 3.2: Radial profiles of density scale height and plasma β for the simulations used here. SANE simulations show roughly constant scale height in the region of inflow equilibrium ($r \lesssim 20 r_g$) with plasma $\beta \simeq 10 - 30$. MADs are geometrically compressed at small radii by the wide jet base (McKinney, Tchekhovskoy, & Blandford, 2012) and are more strongly magnetized with lower values of $\beta < 10$.

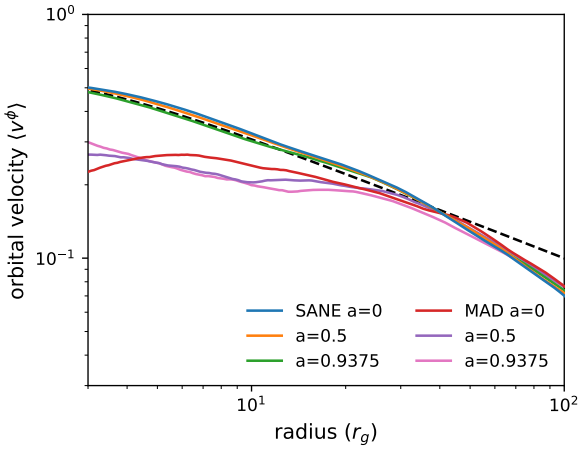

Figure 3.3: Radial profile of azimuthal velocity for our simulations. The black line shows the Keplerian coordinate velocity for a spin of $a = 0.9375$. SANE simulations show Keplerian rotation, while MADs are significantly sub-Keplerian in the inner regions as a result of magnetic pressure support.

3.2 GRMHD simulations with multiple electron heating prescriptions

We have carried out a set of 3D GRMHD black hole accretion simulations using the `harmpi`[1] code (Tchekhovskoy, 2019). `harmpi` is a 3D implementation of the `HARM` algorithm (Gammie, McKinney, & Tóth, 2003; Noble et al., 2006) for conservative MHD in a fixed spacetime. Simulations were initialized from a Fishbone-Moncrief steady state hydrodynamic equilibrium torus in a Kerr spacetime with inner radius $r_{\rm in} = 12r_g$ and pressure maximum at $r_{\rm max} = 25r_g$. The torus was seeded with a single loop of poloidal magnetic field, whose radial profile is designed to supply either relatively modest (SANE) or maximal (MAD) magnetic flux. For each case, black hole spin values of $a = 0$, 0.5, 0.9375 were used. The simulations were carried out in modified spherical polar Kerr-Schild coordinates, with resolution concentrated towards the equatorial plane to resolve the accretion flow at small radius and towards the pole to resolve the jet at larger radius. The outer radial boundary was extended to $10^5 r_g$ using a super-exponential radial coordinate. The grid was chosen to provide a cylindrical innermost cell in polar angle (Tchekhovskoy, Narayan, & McKinney, 2011; Ressler et al., 2017). This significantly increases the time step allowed by the Courant condition. The resolution used was $320 \times 256 \times 160$ cells, including the full 2π azimuthal domain. All simulations are evolved for at least $10^4\, r_g/c$, and we analyze the period from $5 \times 10^3 - 10^4\, r_g/c$, once the emission region has established inflow equilibrium. We also evolve one SANE $a = 0$ and one MAD $a = 0.9375$ simulation for a much longer time ($2 \times 10^5\, r_g/c$ and $6 \times 10^4\, r_g/c$, respectively), in order to allow larger radii $\simeq 100\, r_g$ to reach inflow equilibrium. That location is thought to produce the bulk of the observed

[1] `https://github.com/atchekho/harmpi`

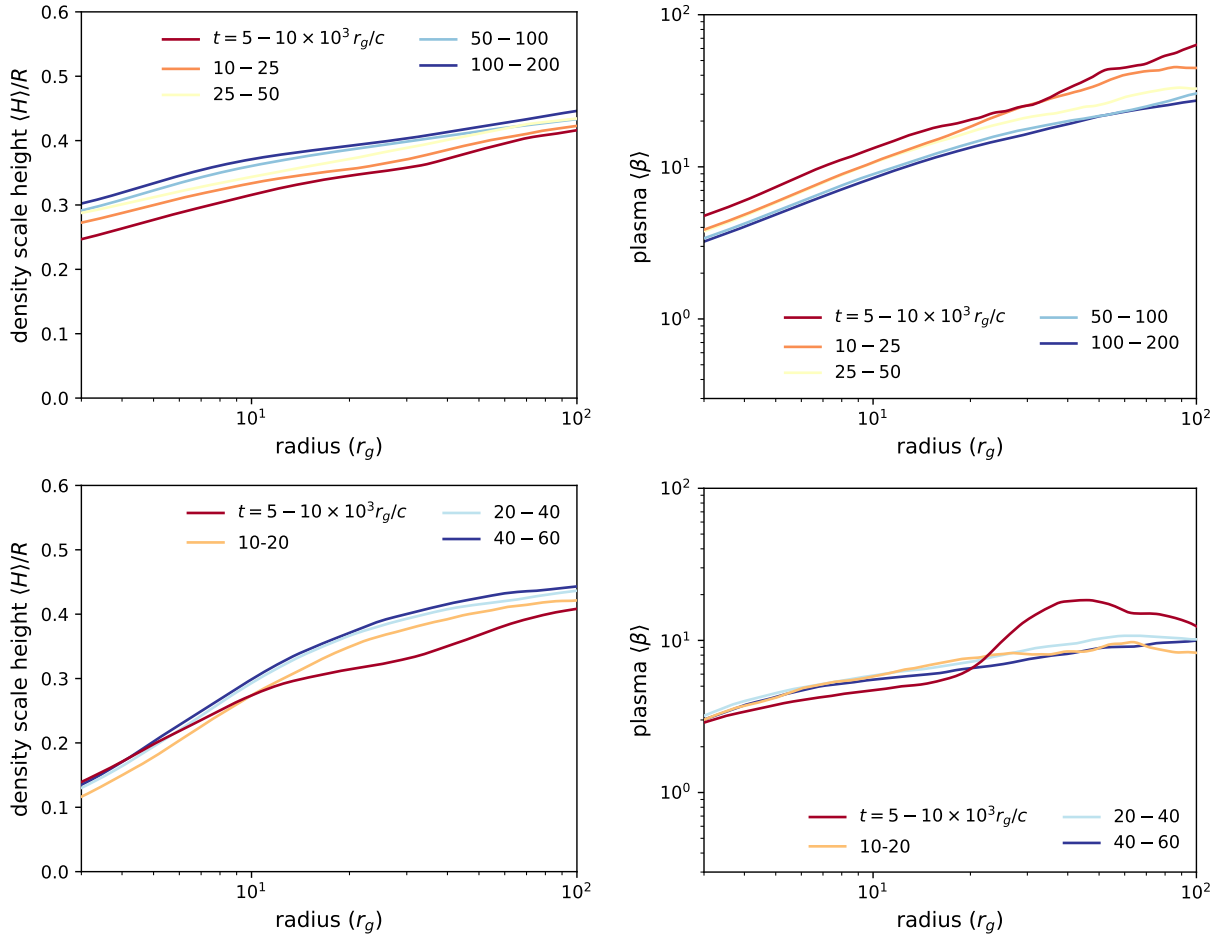

Figure 3.4: Radial profiles of density scale height and plasma β averaged over early (red) to late (blue) time intervals for the long duration SANE (top) and MAD (bottom) simulations used here. Over time the average scale height and magnetization increase, at all radii for SANE simulations and at larger radii for MAD simulations.

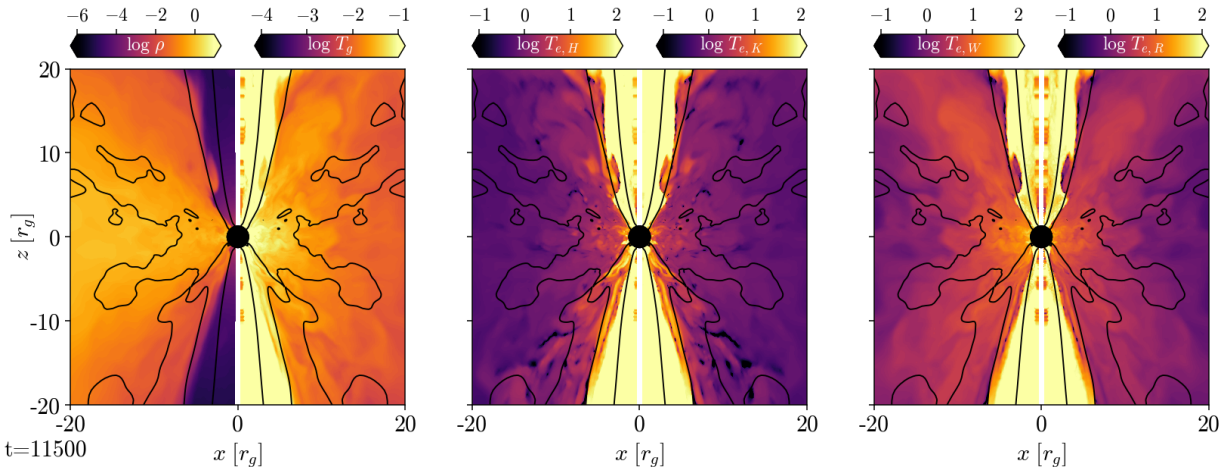

Figure 3.5: Snapshot azimuthal averages from the SANE a=0.9375 simulation of ρ, $T_{\rm gas}$ (left, in units of $m_p c^2/k$), and T_e for the four electron heating schemes (middle and right panels, H10, K19, W18, R17, in units of $m_e c^2/k$). The H10/K19 ("turbulence") and W18/R17 ("reconnection") pairs show similar behavior. The turbulence models heat electrons significantly only in polar jet regions where the magnetization is high, while the reconnection models also substantially heat the dense accretion flow near the midplane.

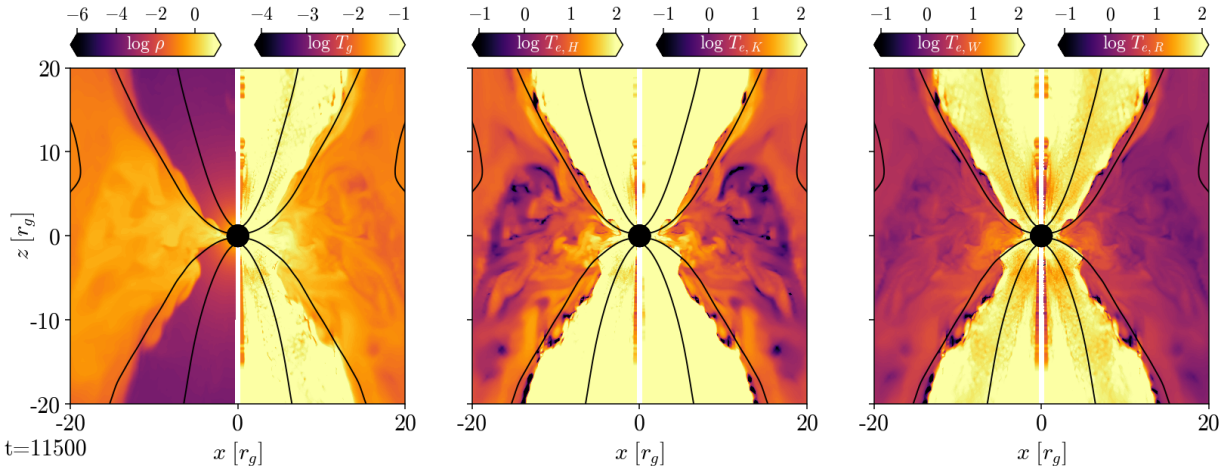

Figure 3.6: Snapshot azimuthal averages from the MAD a=0.9375 simulation of ρ, $T_{\rm gas}$, and T_e for the 4 electron heating schemes (H10, K19, W18, R17). Again the turbulence and reconnection pairs show very similar behavior. Here, there is strong electron heating near the midplane in both scenarios due to regions of high magnetization in the MAD accretion flow.

submm Faraday rotation from Sgr A* (Marrone et al., 2007; Ressler, Quataert, & Stone, 2018).

We use the version of `harmpi` with a separate electron fluid as implemented by Ressler et al. (2015). Magnetic and kinetic energy dissipated at the grid scale is recaptured as internal energy. A fraction is also assigned to a separate electron internal energy. This electron internal energy is evolved independently of the fluid dynamics, which allows us to incorporate multiple electron heating prescriptions within a single simulation. Some error is introduced in this approximation, since it effectively assumes that the electron and proton adiabatic indices are the same (e.g., see Sadowski et al., 2017; Ressler et al., 2017).

The electron heating mechanism is uncertain, as is its sub-grid implementation. We explore a total of 4 prescriptions based on 2 physical scenarios. We use fitting formulae derived from gyrokinetic linear theory (H10) and numerical simulations (K19) of heating in a turbulent cascade, as well as fitting formulae derived from particle-in-cell simulations of electron heating in magnetic reconnection (R17, W18).

We assess the convergence of our simulations using criteria from the literature (Hawley, Guan, & Krolik, 2011; Shiokawa et al., 2012; Hawley et al., 2013). We define the 1D radial, density-weighted profile of a quantity X as:

$$\langle X \rangle = \frac{\int d\theta d\phi \sqrt{-g} \rho X}{\int d\theta d\phi \sqrt{-g} \rho}, \tag{3.1}$$

where ρ is the fluid mass density and $\sqrt{-g}$ is the Jacobian. We define the shell-averaged plasma $\beta = p_{\rm gas}/p_B$ as,

$$\langle \beta \rangle = 8\pi \frac{\langle p_{\rm gas} \rangle}{\langle b^2 \rangle}. \tag{3.2}$$

We evaluate simulation resolution quality using Q values (Hawley, Guan, & Krolik, 2011) calculated in the locally non-rotating frame (LNRF), $Q^{(i)} = \lambda^{(i)}_{\rm MRI}/\Delta x^{(i)}$ (Porth et al., 2019), where $\lambda_{\rm MRI}$ is the fastest growing MRI wavelength,

$$\lambda^{(i)}_{\rm MRI} = \frac{2\pi\, b^\mu e^{(i)}_\mu}{\sqrt{\rho + \gamma u + b^2}}, \tag{3.3}$$

u is the fluid internal energy and γ is the adiabatic index. The tetrad vectors $e^{(i)}_\mu$ describe the transformation to the LNRF (e.g., Takahashi, 2008), and $\Delta x^{(i)} = \Delta x^\mu e^{(i)}_\mu$ is the LNRF grid cell spacing. Finally we report on the relative strength of the radial and azimuthal field, here taken to be Kerr-Schild coordinate values of $b_r b^r / b_\phi b^\phi$.

3.3 Radiative models of Sgr A*

From each simulation and electron heating prescription, we compute radiative models of Sgr A*. The electron temperature is taken directly from the GRMHD electron internal energy density. We then scale the mass density until the median observed flux density at

230 GHz is $\simeq 3$ Jy (e.g., Dexter et al., 2014; Bower et al., 2015). We exclude emission from regions where $\sigma = b^2/\rho > 1$.

Observables are calculated using a ray tracing method with the public code `grtrans` (Dexter & Agol, 2009; Dexter, 2016). We follow Kerr photon geodesics corresponding to uniformly sampled camera pixels of a distant observer at a viewing orientation of $i = 25$, 45, and 60 degrees. The image resolution is 192 pixels over a $42\,r_g$ ($210\,\mu$as) field of view. Rays are sampled evenly in $1/r$ from an outer boundary $r_{\rm out}$ until they either reach the black hole event horizon or return to $r_{\rm out}$. Near radial turning points, we switch to sampling evenly in $\cos\theta$ to avoid taking large steps. Along each ray, we solve the full polarized radiative transfer equations for synchrotron emission and absorption and Faraday rotation and conversion, assuming a purely thermal electron distribution function. Coefficients are taken from (Dexter, 2016), with the Faraday rotation coefficient ρ_V modified to correctly reproduce the non-relativistic limit (see appendix 3.7). This is important for calculations of the Faraday rotation measure through the extended torus where the dimensionless electron temperature $\theta_e = kT_e/mc^2 \lesssim 1$. We do not include inverse Compton scattering, which allows comparisons to the observed X-ray luminosity (e.g., Dolence et al., 2009; Mościbrodzka et al., 2009). We calculate images at radio to NIR frequencies for all snapshots from $(5-10)\times10^3\,r_g/c$ spaced by $10\,r_g/c$. Here we focus on results for time-averaged observables and their rms variability.

3.4 Observational constraints

We compare our models to observational constraints derived from millimeter to NIR observations of Sgr A*.

3.4.1 Spectrum and variability

First, we consider the shape of the submm to NIR total intensity spectrum (e.g., Falcke et al., 1998; Bower et al., 2015; Stone et al., 2016; von Fellenberg et al., 2018; Bower et al., 2019; Schödel et al., 2011; Dodds-Eden et al., 2011; Witzel et al., 2018) and the rms variability fraction as a function of wavelength (Dodds-Eden et al., 2011; Witzel et al., 2018; Dexter et al., 2014; Bower et al., 2015).

Quantitatively, we require a submm spectral index between 230 and 690 GHz of $-0.35-0.25$ (Marrone, 2006; Bower et al., 2019) and an upper limit to the median NIR flux density of < 1.4 mJy (Dodds-Eden et al., 2011; Witzel et al., 2018; Gravity Collaboration et al., 2020d), and a 230 GHz total flux density rms of $20-40\%$ for a model to be considered viable.

3.4.2 86 and 230 GHz source sizes and NIR centroid motion

We also consider constraints on the image size at 86 and 230 GHz (Krichbaum et al., 1998; Doeleman et al., 2008; Fish et al., 2011; Johnson et al., 2018; Issaoun et al., 2019).

We adopt semi-major axis size constraints of $a_{86} = 86 - 154\,\mu$as (Issaoun et al., 2019) and $a_{230} = 51 - 63\,\mu$as (Johnson et al., 2018). In the latter case, we have for simplicity assumed that the intrinsic source semi-major axis aligns with that of the interstellar scattering kernel.

We further compare our results with the evolution seen in the NIR centroid (Gravity Collaboration et al., 2018a).

3.4.3 Polarization

We also compare to median submm observed linear and circular polarization fractions (Aitken et al., 2000; Eckart et al., 2006; Trippe et al., 2007; Muñoz et al., 2012; Liu et al., 2016; Bower et al., 2018; Gravity Collaboration et al., 2018a). Specifically, we enforce constraints on the median polarization fractions of $LP = 2 - 8\%$ (Bower et al., 2018) and $|CP| = 0.5 - 2\%$ (Muñoz et al., 2012).

Sgr A* also shows a dependence of electric vector position angle EVPA $\propto \lambda^2$ as expected for Faraday rotation "external" to the emission region (so that the polarized source has its EVPA coherently rotated, e.g. appears point-like on the Faraday screen). The rotation measure is RM $\simeq -6 \times 10^5\,\mathrm{rad/m^{-2}}$ (Marrone et al., 2007), with a consistent sign in measurements over many years (e.g., Bower et al., 2003; Marrone et al., 2006, 2007; Bower et al., 2018). The RM is thought to result from the extended accretion flow, and has been used to constrain the accretion rate onto the black hole (Marrone et al., 2006). We do not use the RM to select models, since it originates outside of the region of inflow equilibrium in standard GRMHD models. We show that that an RM signature can be generated with approximately the right magnitude in radiative models from our long duration simulations.

3.5 Results

We discuss accretion flow and convergence properties for our GRMHD simulations, compare their properties in radiative models of Sgr A* to the above observational constraints, and then study the properties of their multi-wavelength images and polarization maps.

3.5.1 Convergence and accretion flow properties

Our GRMHD simulations reach the MAD and SANE limits as expected. Figure 3.1 show the accretion rate histories and accumulated dimensionless magnetic flux on the horizon. SANE simulations have a relatively low net magnetic flux, $\phi_{\rm BH} \simeq 5 - 10$, while the flux saturates in the MAD case at a maximum value of roughly $\phi_{\rm BH} \simeq 50 - 70$ (Tchekhovskoy, Narayan, & McKinney, 2011).

Table 3.1 lists average values of those quantities for all of our simulations. The magnetic flux $\phi_{\rm BH}$ is measured on the horizon, while the Q values and magnetic field tilt angle are averaged over the region $r = 6 - 15 r_g$. MAD models are well resolved according to these criteria, while SANE models are more difficult to resolve due to their lower net vertical

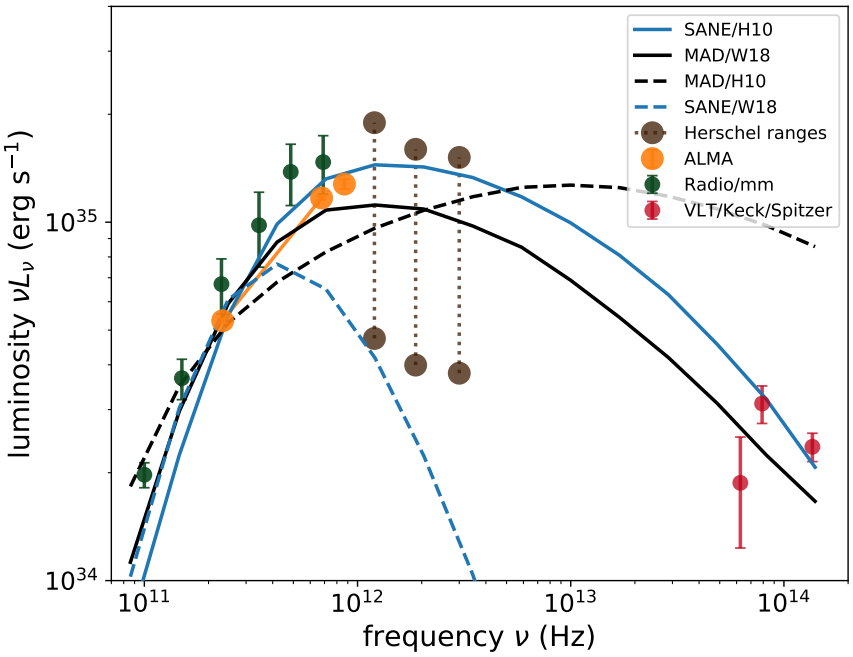

Figure 3.7: Median spectra from sample SANE (blue) and MAD (black) models with $a = 0.5$ and $i = 45°$ and the H10 and W18 electron heating models compared to Sgr A* mm to NIR data. The SANE/H10 and MAD/W18 models are consistent with the observed spectral shape. The SANE/W18 model does not produce sufficiently hot electrons and can't explain the broad submm peak in Sgr A*. The MAD/H10 model produces too many hot electrons. It fails to match the submm peak and overproduces the observed NIR emission.

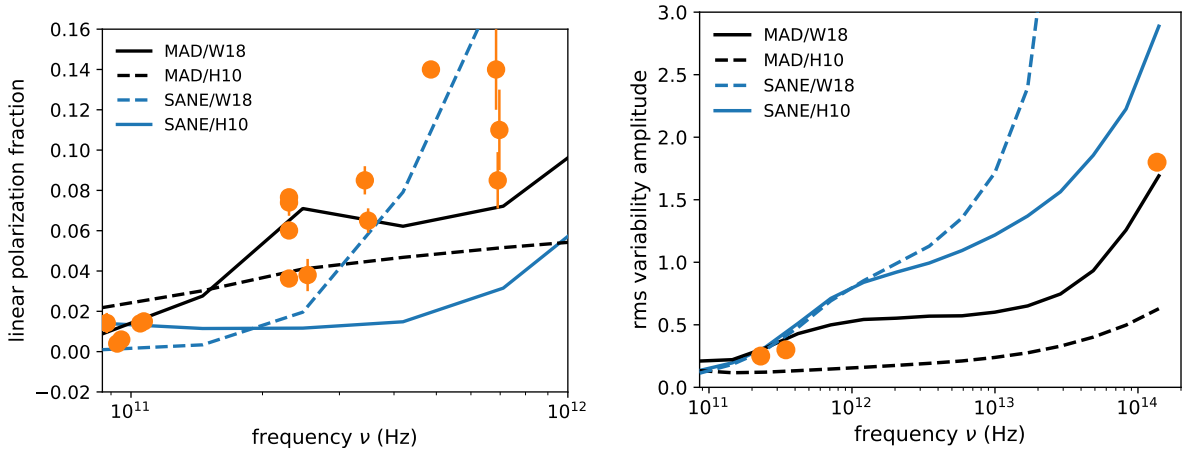

Figure 3.8: Linear polarization fraction (left) and rms variability amplitude (right) for sample SANE (blue) and MAD (black) simulations with $a = 0.5$ and $i = 45°$ for the H10 and W18 electron heating models compared to Sgr A* mm to NIR data. The SANE/H10 (disk-jet) model is heavily depolarized as a result of Faraday rotation in the emission region. The MAD/W18 model is consistent with both constraints.

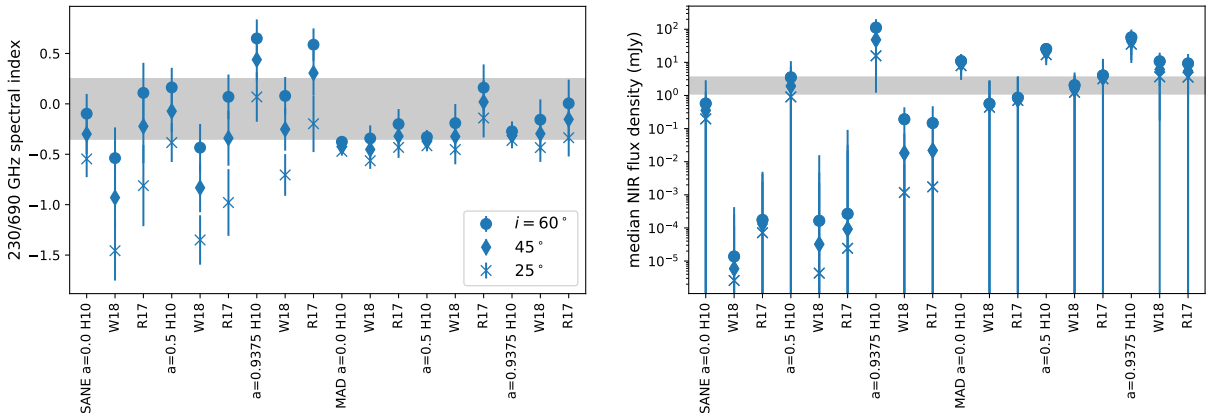

Figure 3.9: Model median (points) and rms (error bars) submm spectral indices (left) and NIR flux densities (right). The different symbols for each model are 3 values of the observer inclination angle. The shaded regions correspond to the observed ranges, although we use the NIR flux density as an upper limit when constraining models. Higher inclinations correspond to larger submm spectral indices and NIR flux densities as a result of increased Doppler beaming. The SANE/reconnection models produce negligible NIR emission for the thermal distribution function assumed here.

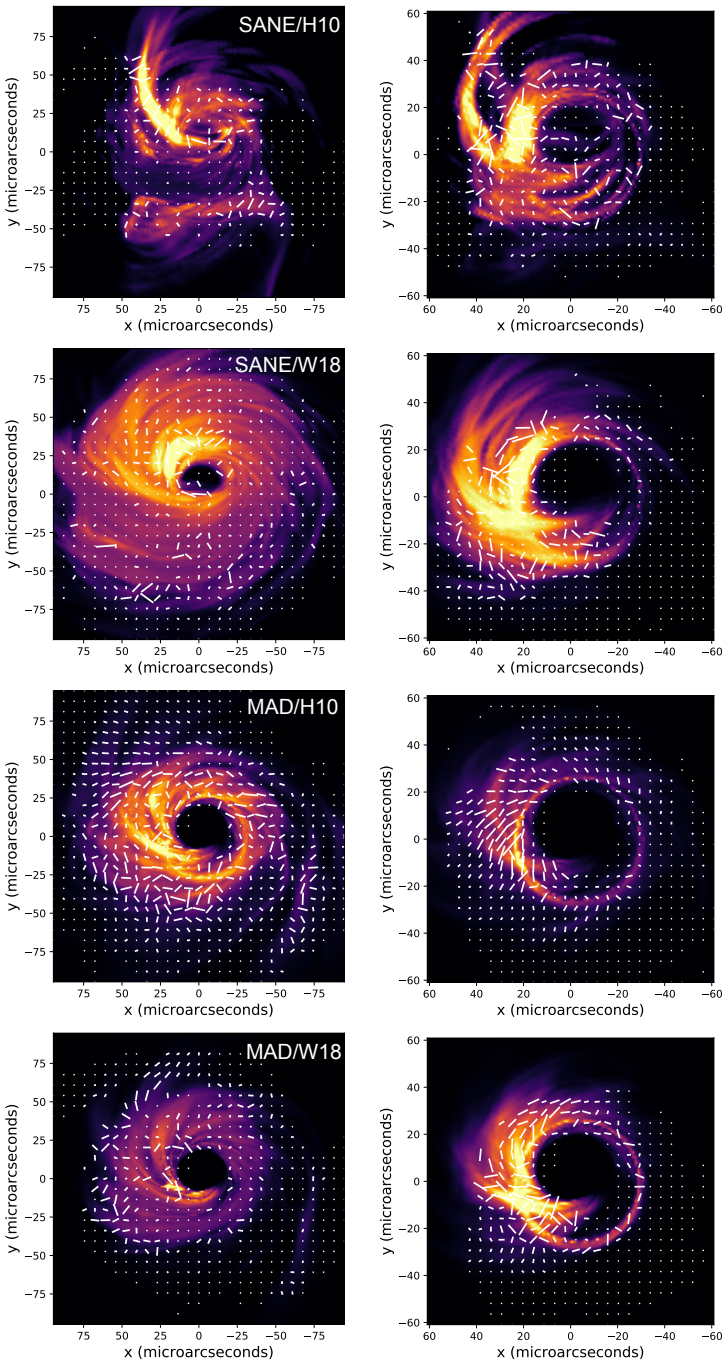

Figure 3.10: Sample snapshot 86 (left) and 230 (right) GHz linearly scaled false color images and polarization maps for $a = 0.5$ and $i = 45°$. Polarization tick length is proportional to polarized flux. The models are ordered from top to bottom as SANE/H10, SANE/W18, MAD/H10, MAD/W18. All models at 230 GHz show a characteristic crescent morphology from the combination of Doppler beaming and light bending. The SANE/H10 model shows a "disk-jet" structure with prominent polar emission from the jet wall at 86 GHz. In the other cases, the emission is predominantly from close to the midplane. All models are substantially depolarized from Faraday rotation at 86 GHz, and the SANE models are also depolarized at 230 GHz. Images of the K19 and R17 models are similar to those of the H10 and W18 models, respectively.

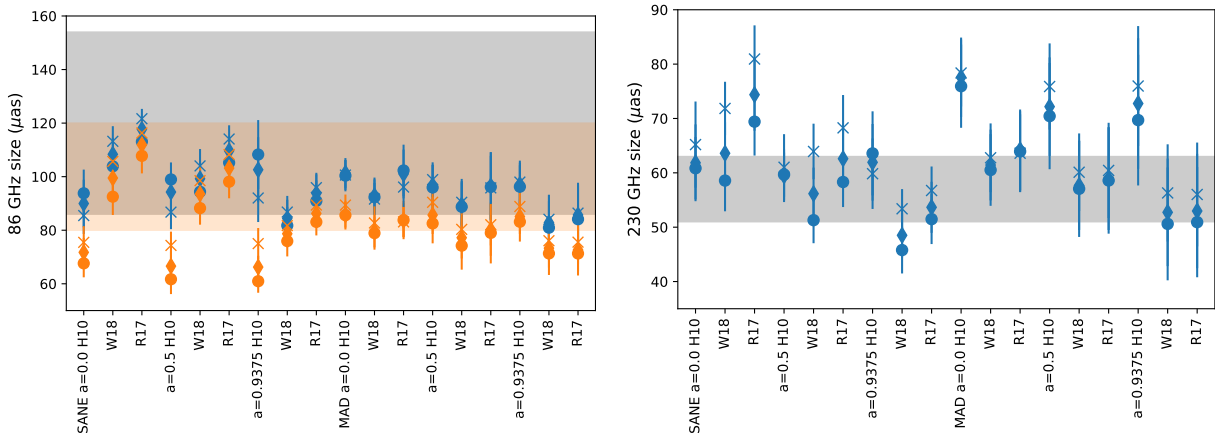

Figure 3.11: Model image sizes at 86 (left) and 230 (right) GHz. The image second moments are shown along semi-major (blue) and semi-minor (orange, 86 GHz only) axes, multiplied by a factor of 2.35 for comparison with the Gaussian FWHM sizes reported in the literature (gray bands). In each model column, the three points correspond to three viewing inclinations and the error bars correspond to the rms scatter over time. Many models can satisfy both constraints, although they are generally small compared with the 86 GHz size. SANE/H10 models are too elliptical at 86 GHz for high viewing inclinations, and MAD/H10 models are too large at 230 GHz.

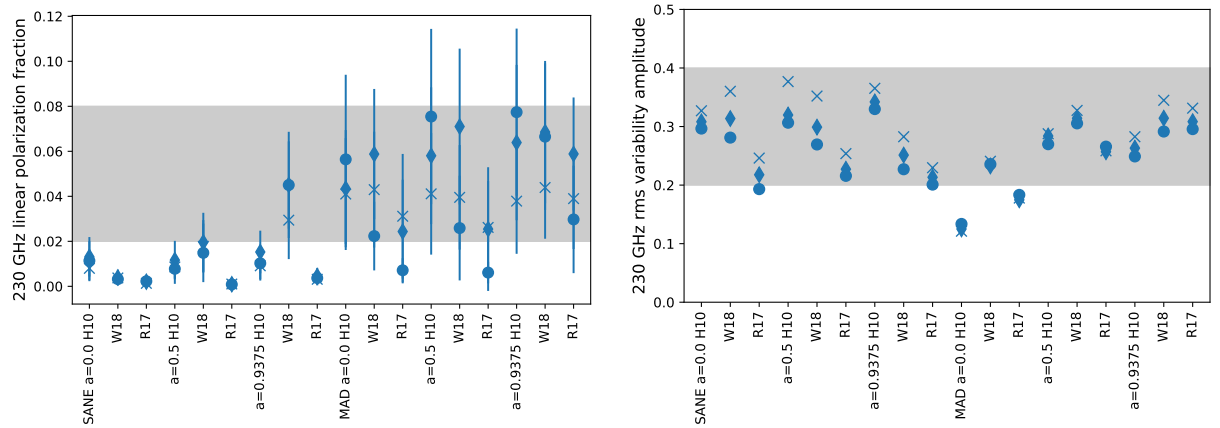

Figure 3.12: Model 230 GHz linear polarization fractions (left) and rms variability amplitudes (right). All SANE models except $a = 0.9375$ W18 show low linear polarization fractions as a result of Faraday rotation internal to the emission region. MAD models by contrast are frequently consistent with the range of median 230 GHz linear polarization seen from Sgr A*. All scenarios considered here can show 230 GHz variability with an rms amplitude $\simeq 20 - 40\%$, consistent with that observed. The variability is the result of turbulence driven by the MRI.

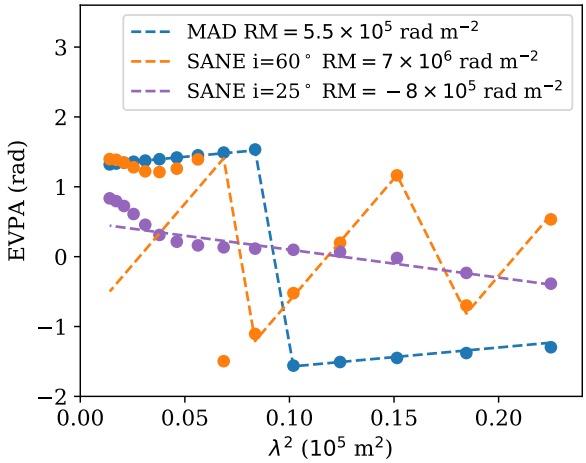

Figure 3.13: Image-integrated EVPA as a function of squared wavelength for late time snapshots at $i = 60°$ of sample MAD and SANE models, as well as the same SANE model at $i = 25°$. The EVPA behavior is consistent with external Faraday rotation. The inferred RM values for the MAD and low inclination SANE cases are consistent with that found in submm observations of Sgr A*. Many models (e.g. the SANE models shown here) show significant departures from a λ^2 dependence at short wavelengths $\lesssim$ 1mm.

magnetic flux. Still, we find satisfactory convergence in all cases, generally defined as $\langle Q^{(\phi)} \rangle \langle Q^{(\theta)} \rangle \gtrsim 200$, tilt $\simeq 0.15 - 0.20$, and $\langle \beta \rangle \simeq 10 - 20$ (radial profiles of β are shown in Figure 3.2). We define inflow equilibrium following Narayan et al. (2012) as the outermost radius where the elapsed time exceeds a viscous time, $t \langle v^r \rangle (r_{\rm eq}/r_{\rm eq} \gtrsim 1$. Inflow equilibrium at these early times only reaches out to $r_{\rm eq} \simeq 20 r_g$. This is sufficient to capture the submm to NIR emission (e.g., Mościbrodzka et al., 2009), but complicates our studies of linear polarization and Faraday rotation. All convergence criteria are readily satisfied for MAD simulations. The MAD models show lower equilibrium values of plasma $\beta \simeq 5 - 10$ and inflow equilibrium reaches larger radius $r_{\rm eq} \simeq 25 - 30 r_g$.

In SANE models the scale height is roughly constant in the region of inflow equilibrium ($H/R \simeq 0.3 - 0.4$), similar to past GRMHD (Shiokawa et al., 2012; Narayan et al., 2012) and recent pseudo-Newtonian (Dhang & Sharma, 2019) results. In the MAD case, we find a strong decrease in the inner radii. This is due to magnetic pressure from the strong surrounding magnetosphere (McKinney, Tchekhovskoy, & Blandford, 2012). The azimuthal velocity profile is nearly Keplerian for SANE models, while MADs are sub-Keplerian in the region of inflow equilibrium due to magnetic pressure support (e.g., McKinney, Tchekhovskoy, & Blandford, 2012).

3.5.2 Long duration runs and inflow equilibrium

We have also run sample MAD and SANE simulations to long durations, similar to what was done by Narayan et al. (2012) and White, Quataert, & Gammie (2020). Averaged

properties of those simulations over various time intervals are listed in Table 3.2 and Table 3.3. Our SANE model evolves to a slightly larger scale height, lower median β, higher magnetic tilt angle, and larger $Q^{(\phi)}$ and $Q^{(\theta)}$ convergence values. Radial profiles averaged over different time intervals are shown in Figure 3.4. The inflow equilibrium radius $r_{\rm eq} \simeq 90 r_g$ reached is similar to that from (Narayan et al., 2012) in the same elapsed coordinate time of $2 \times 10^5 r_g/c$. Our MAD model is run for much shorter ($\simeq 6 \times 10^4 r_g/c$) but nonetheless reaches inflow equilibrium out to $r_{\rm eq} \simeq 70 r_g$.

3.5.3 Electron heating

Azimuthally averaged snapshots of electron temperature T_e are shown in Figure 3.5 and Figure 3.6. We find similar behavior for the various electron heating models as in previous work for SANE (Ressler et al., 2015, 2017; Chael et al., 2018; Ryan et al., 2018) and MAD (Chael, Narayan, & Johnson, 2019) simulations. In the SANE case, the dense accretion flow near the midplane has relatively large plasma $\beta \simeq 10-20$. The electrons there are only significantly heated for the reconnection models. In the turbulent case, electrons in the disk body remains cold. For MAD solutions, the average plasma β is lower and electrons are heated efficiently everywhere in both scenarios. We find mild spin dependence, in the sense that for higher black hole spin the fluid and in turn the electrons have higher energies. More details on the time evolution and convergence of the electron heating solutions are provided in appendix 3.7.

3.5.4 Spectrum and variability

Sample spectra are shown in Figure 3.7 for the four general classes of model considered. The spectra show median values over time at each frequency. The black hole spin is fixed at $a = 0.5$ and the inclination at $i = 45°$. We compare SANE (blue) with MAD (black), and turbulence (H10) and reconnection (W18) cases. Data are taken from the references listed in subsection 3.4.1. The combinations of SANE/reconnection (blue dashed) generically underproduce the observed THz emission from Sgr A*. They do not produce sufficiently hot electrons, and therefore show steep spectral breaks which are ruled out by recent Herschel and ALMA data. The combinations of MAD/turbulence by contrast strongly heat electrons to the degree that the spectral energy distribution (SED) peaks in the infrared. These models strongly overproduce the median NIR while underproducing the submm emission. The other two combinations, SANE/turbulence and MAD/reconnection, can match the Sgr A* SED shape at least for some combinations of inclination angle and black hole spin. The same general results hold for our full parameter survey. In particular, we have not found combinations of parameters for SANE/reconnection or MAD/turbulence models which reproduce the submm spectral index and NIR flux density upper limit.

Most models we consider produce submm variability consistent with that observed from Sgr A*. The SANE/turbulence and MAD/reconnection models show highly variable NIR emission, which can in principle account for the flaring emission seen from Sgr A*. In those cases, the frequency-dependent rms (Figure 3.8) is often in fairly good agreement

with that observed, rising from the radio through the submm and NIR. A more detailed comparison to the NIR flux distribution is forthcoming (GRAVITY collaboration 2020, in prep).

The detailed results for submm spectral index and median NIR flux density are further separated into our 6 simulations (MAD/SANE at 3 values of black hole spin) and 3 electron heating models (H10/W18/R17) in Figure 3.9. The 3 points at each x-axis location correspond to 3 values of observer inclination ($i = 25°$, $45°$, $60°$). The gray bands show our allowed ranges for Sgr A*. The general trends from our chosen $a = 0.5$ models can be found there, but also with systematic trends of higher submm spectral index and median NIR flux density with increasing black hole spin and observer inclination angle. Both effects result in part from increased Doppler beaming at higher inclination.

The SANE/turbulence and MAD/reconnection models studied produce interesting NIR flaring events (large rms variability in Figure 3.9). MAD models show associated time-variable polarization and image photocenter (centroid) motion. Typical linear polarization fractions are $\simeq 10 - 30\%$, consistent with observations of NIR flares from Sgr A* (Eckart et al., 2006; Trippe et al., 2007; Gravity Collaboration et al., 2018a). The rms centroid motion during flares is only $\simeq 10\mu$as, a factor of $2-3$ smaller than seen from Sgr A*. Given the uncertainty in electron heating and distribution function, we nonetheless consider MAD accretion flows as promising for explaining the NIR (and X-ray) flares from Sgr A*.

3.5.5 86 and 230 GHz image sizes

Sample snapshot images and polarization maps corresponding to those same 4 model combinations are shown in Figure 3.10. The SANE/turbulence model shows a jet-like, elongated 86 GHz image, while the others are dominated by emission from the dense inflow in the midplane. The SANE/reconnection images have much higher optical depth and a larger source size, particularly at 86 GHz.

Figure 3.11 shows semi-major (blue) and semi-minor (orange, 86 GHz only) axis sizes for each model considered. Except when viewed at low inclination, SANE/turbulence models are disfavored due to their small semi-minor axis size (large axis ratio). Most other model combinations can satisfy both the 86 and 230 GHz semi-major axis size constraints.

We generally find increasing 86 GHz size with decreasing emission region electron temperature in the order H10, W18, R17. The trend is stronger in SANE than in MAD models. At 230 GHz, the emission region size systematically decreases with black hole spin for the reconnection heating models (W18, R17) although all spins considered can produce median values falling within the allowed range.

We also note that all models produce 86 GHz sizes on the smaller end of the allowed range. In particular, all sizes found are too small when compared to the model-fitting results of Johnson et al. (2018) at 86 GHz. To be viable, many or all models may require an additional non-thermal component to the electron distribution function which can produce mm-wavelength emission further from the black hole.

3.5.6 Polarization

The snapshot polarization maps show that all SANE models explored are highly depolarized as a result of strong Faraday rotation internal to the emission region. We also find that the outer torus ($r \gtrsim 20r_g$) can significantly alter the linear polarization degree and polarization map structure for SANE models. That region is not in inflow equilibrium, and we omit it from the radiative transfer calculations presented here. Even excluding that material altogether, few SANE models can match the median observed linear polarization fraction of Sgr A*. Our MAD polarization maps frequently show signatures of strong poloidal field, leading to azimuthal EVPA structure (e.g., Gravity Collaboration et al., 2018a).

Figure 3.8 shows the median image-integrated linear polarization fraction for our 4 sample models. The SANE models, and particularly SANE/turbulence, are too depolarized compared to observations of Sgr A*. MAD/reconnection models capture the frequency-dependent polarization fraction fairly well. In detail (Figure 3.12), MAD models show highly variable LP within the observed range of Sgr A*. The polarization fraction is lowest for the R17 model, and slightly higher at higher black hole spin values. Our SANE models are too depolarized to explain the relatively large 230 GHz LP from Sgr A*, except the W18 model at high spin. The depolarization is the result of Faraday rotation near the dense accretion flow midplane.

In all cases, the polarized emission is more time variable than the total intensity. This is due to a variable EVPA pattern over the images resulting from turbulence and/or Faraday rotation. Time-variable beam depolarization then drives large variability of the integrated Stokes parameters. One way to see this is to note that the integrated polarized flux $\sqrt{Q^2 + U^2}$ from each image pixel shows similar variability as in Stokes I, while both are much less variable than the net polarization integrated over images. This finding agrees with Sgr A* submm polarization observations (e.g., Marrone et al., 2006; Bower et al., 2018). By contrast, the NIR polarization degree seems much less variable (Eckart et al., 2008a; Shahzamanian et al., 2015), likely as a result of a more compact emission region and negligible Faraday rotation at high frequency ($\nu/\nu_c \gtrsim 10^3$ with $\nu_c \sim T_e^2 B$ the critical synchrotron frequency).

3.5.7 Summary of comparison with observational constraints

Table 3.4 provides median observed and model values of the quantitative constraints used here: the submm spectral index, NIR flux density, 230 GHz LP and CP, image semi-major axis size at 230 and 86 GHz, the 230 GHz rms variability fraction. Comparing to the set of observed ranges, we produce a final pass/fail score for each model. Italicized entries indicate where models fail to match Sgr A* data.

Several MAD models can match all constraints considered, and several others fail in only one category. They also produce highly variable NIR emission, similar to that observed. While we have not exhaustively explored the parameter space of either the simulations or the radiative transfer models, we expect the results to hold for other viewing angles and black hole spin values. All SANE models are ruled out by multiple constraints. Match-

ing the spectral shape with only thermal electrons requires disk-jet models where the jet wall electrons are heated and the accretion flow is cold. Those models are too strongly depolarized to explain the measured submm linear and circular polarization of Sgr A*.

3.5.8 Faraday rotation in long duration runs

Using our long duration SANE $a = 0$ model, we have also explored Faraday rotation and depolarization once inflow equilibrium has reached large radius $r \simeq 100r_g$. For the turbulent electron heating, there is little difference. The accretion flow remains cold, and the emission from close to the black hole is depolarized to a maximum of $1 - 2\%$. For the reconnection heating models, at late times the large-scale accretion flow can substantially heat. This increases the observed polarization fraction to values consistent with Sgr A* data.

For both long duration SANE and MAD models, we also find behavior consistent with external Faraday rotation, where the EVPA $\propto \lambda^2$ over a range of frequencies $\simeq 200 - 300$ GHz. Figure 3.13 shows example fits to a MAD $a = 0.9375$ model with an inflow equilibrium radius of $r_{\rm eq} \simeq 50r_g$ ($t \simeq 2.7 \times 10^4 r_g/c$) and a SANE $a = 0$ model with $r_{\rm eq} \simeq 100r_g$ ($t \simeq 2 \times 10^5 r_g/c$). Both models are viewed at an inclination $i = 60°$. The EVPA shows a clear linear trend with λ^2, particularly at longer wavelength. We infer Faraday rotation measures of $\simeq 6 \times 10^5$ rad m^{-2} (MAD) and 7×10^6 rad m^{-2} (SANE). The typical MAD values are in good agreement with the observed Faraday rotation measure of Sgr A* (e.g., Bower et al., 2003; Marrone et al., 2006, 2007; Bower et al., 2018). The external RM decreases to $\lesssim \times 10^6$ rad m^{-2} for $i = 25°$. We also find rapid changes in the sign of the RM at high inclination, while low inclinations can show a persistent sign (although our longest simulation only spans a few weeks for Sgr A*). Studies of the RM time variability, departures from λ^2, and spatially resolved maps are left to future work. Small RM values for the SANE long duration models are possible even when there is strong depolarization due to Faraday rotation internal to the emission region. For more details see appendix 3.7.

3.6 Discussion

We have carried out a parameter space survey of Sgr A* models using ray tracing radiative transfer calculations based on GRMHD simulation data output. We consider both low (SANE) and saturated (MAD) magnetic flux limits, and sub-grid prescriptions for dividing dissipated energy at the grid scale between electrons and protons.

Both prescriptions assign more dissipated heat to electrons in strongly magnetized regions, resulting in higher jet wall (outflow) than accretion flow (inflow) electron temperatures. The electron temperature contrast between jet wall and disk body is larger in the SANE case and for the turbulent heating prescription. This results in a relatively cold accretion flow ($\theta_e \lesssim 1$ for $r \gtrsim 30r_g$). For strongly magnetized MAD models, there are hot electrons everywhere. Our results for electron heating are consistent with those from

Table 3.4: Comparison of the allowed ranges of various observational constraints considered with median values calculated for each model and a final pass/fail score.

model	i (°)	$\alpha_{\rm submm}$	$\log F_{\rm NIR}$ (mJy)	LP	—CP—	a_{230} (μas)	a_{86} (μas)	rms	summary
		$-0.35-0.25$	<0.3	$0.02-0.08$	$0.005-0.02$	$51-63$	$86-154$	$0.2-0.4$	
SANE a=0.0 H10	25	*-0.55*	-0.7	*0.008*	*0.002*	*65.2*	*85.5*	0.33	*fail*
	45	-0.30	-0.5	*0.004*	*0.003*	61.8	90.0	0.31	*fail*
	60	-0.10	-0.2	*0.004*	*0.003*	60.8	93.8	0.30	*fail*
SANE a=0.0 W18	25	*-1.46*	-5.6	*0.003*	*-0.004*	*71.8*	113.2	0.36	*fail*
	45	*-0.93*	-5.2	*0.002*	*-0.002*	*63.6*	108.3	0.31	*fail*
	60	*-0.54*	-4.9	*0.002*	*-0.001*	58.6	103.9	0.28	*fail*
SANE a=0.0 R17	25	*-0.81*	-4.1	*0.001*	*-0.001*	*80.9*	121.6	0.25	*fail*
	45	-0.22	-3.9	*0.001*	*0.001*	*74.4*	117.7	0.22	*fail*
	60	0.11	-3.8	*0.001*	*0.001*	*69.4*	113.1	*0.19*	*fail*
SANE a=0.5 H10	25	*-0.38*	-0.0	*0.008*	*0.002*	61.0	86.8	0.38	*fail*
	45	-0.07	0.3	*0.004*	*0.001*	59.5	94.3	0.32	*fail*
	60	0.16	0.5	*0.004*	*0.001*	59.7	99.0	0.31	*fail*
SANE a=0.5 W18	25	*-1.35*	-5.4	*0.017*	-0.010	*63.9*	104.0	0.35	*fail*
	45	*-0.83*	-4.5	*0.004*	-0.007	56.2	99.2	0.30	*fail*
	60	*-0.43*	-3.8	*0.003*	*-0.005*	51.3	94.4	0.27	*fail*
SANE a=0.5 R17	25	*-0.98*	-4.6	*0.001*	*-0.002*	*68.3*	114.1	0.25	*fail*
	45	-0.34	-4.0	*0.001*	*0.001*	62.6	109.6	0.23	*fail*
	60	0.07	-3.6	*0.001*	*0.001*	58.3	105.2	0.22	*fail*
SANE a=0.9375 H10	25	0.07	*1.2*	*0.011*	*0.000*	59.8	92.0	0.37	*fail*
	45	*0.44*	*1.7*	*0.003*	*-0.000*	61.9	102.6	0.34	*fail*
	60	*0.65*	*2.0*	*0.003*	*-0.001*	*63.6*	108.3	0.33	*fail*
SANE a=0.9375 W18	25	*-0.71*	-2.9	0.038	*-0.029*	53.4	86.8	0.28	*fail*
	45	-0.25	-1.7	*0.015*	*-0.028*	*48.5*	*84.4*	0.25	*fail*
	60	0.08	-0.7	*0.005*	-0.019	*45.8*	*81.8*	0.23	*fail*
SANE a=0.9375 R17	25	-0.20	-2.8	*0.003*	*-0.003*	56.7	95.9	0.23	*fail*
	45	*0.31*	-1.7	*0.002*	*-0.002*	53.7	93.8	0.21	*fail*
	60	*0.59*	-0.8	*0.001*	*-0.001*	51.5	90.9	0.20	*fail*
MAD a=0.0 H10	25	*-0.47*	*0.9*	0.041	0.007	*78.4*	100.6	*0.12*	*fail*
	45	*-0.43*	*1.0*	0.043	0.006	*77.6*	101.4	*0.13*	*fail*
	60	*-0.38*	*1.0*	0.056	*0.005*	*75.9*	100.4	*0.13*	*fail*
MAD a=0.0 W18	25	*-0.56*	-0.4	0.043	0.011	62.8	91.6	0.24	*fail*
	45	*-0.45*	-0.3	0.059	0.010	61.4	92.9	0.23	*fail*
	60	-0.34	-0.2	0.022	0.008	60.5	92.3	0.24	**pass**
MAD a=0.0 R17	25	*-0.43*	-0.1	0.031	0.018	*63.6*	96.1	*0.18*	*fail*
	45	-0.32	-0.1	0.024	0.013	*64.2*	101.0	*0.17*	*fail*
	60	-0.20	-0.1	*0.007*	0.009	*63.9*	102.3	*0.18*	*fail*
MAD a=0.5 H10	25	*-0.42*	*1.2*	0.041	*0.003*	*75.9*	98.9	0.29	*fail*
	45	*-0.37*	*1.3*	0.058	*0.003*	*72.2*	96.8	0.28	*fail*
	60	-0.33	*1.4*	0.075	*0.002*	*70.4*	96.0	0.27	*fail*
MAD a=0.5 W18	25	*-0.45*	0.1	0.040	0.008	60.1	90.4	0.33	*fail*
	45	-0.32	0.2	0.071	0.008	57.7	89.4	0.31	**pass**
	60	-0.19	0.3	0.026	*0.003*	57.1	88.7	0.31	*fail*
MAD a=0.5 R17	25	-0.14	0.5	0.026	0.013	60.4	95.8	0.26	**pass**
	45	0.02	0.5	0.025	0.007	58.9	96.5	0.26	**pass**
	60	0.16	*0.6*	*0.006*	*0.001*	58.6	96.2	0.27	*fail*
MAD a=0.9375 H10	25	*-0.36*	*1.5*	0.038	*0.004*	*76.0*	98.0	0.28	*fail*
	45	-0.32	*1.6*	0.064	*0.002*	*72.8*	97.1	0.26	*fail*
	60	-0.27	*1.8*	0.077	*0.000*	*69.7*	96.2	0.25	*fail*
MAD a=0.9375 W18	25	*-0.43*	*0.6*	0.044	0.008	56.3	*84.1*	0.34	*fail*
	45	-0.30	*0.8*	0.069	*0.002*	52.7	*82.8*	0.31	*fail*
	60	-0.16	*1.0*	0.067	*-0.002*	*50.6*	*80.9*	0.29	*fail*
MAD a=0.9375 R17	25	-0.34	0.6	0.039	0.012	56.0	86.4	0.33	**pass**
	45	-0.15	*0.7*	0.059	*0.004*	53.0	*85.7*	0.31	*fail*
	60	0.00	*1.0*	0.030	*-0.002*	*50.9*	*84.1*	0.30	*fail*

Table 3.5: Average physical parameters of our radiative models at 230 GHz.

model	$\dot{M}$ ($10^{-8}\,M_\odot\,\mathrm{yr}^{-1}$)	τ_I	$\tau_{\rho V}$	r (r_g)	θ	n ($10^6\,\mathrm{cm}^{-3}$)	B (G)	θ_e
SANE a=0.0 H10	9.0	1.3	394.7	6.7	1.7	7.7	63.3	10.9
SANE a=0.0 W18	8.1	2.1	124.0	7.8	1.6	15.4	59.4	4.0
SANE a=0.0 R17	30.5	7.9	1586.0	8.8	1.5	53.0	100.4	2.4
SANE a=0.5 H10	6.0	1.7	431.8	6.2	1.7	7.9	66.4	12.2
SANE a=0.5 W18	3.3	1.7	52.4	7.1	1.5	9.6	48.3	5.1
SANE a=0.5 R17	10.5	5.4	544.1	7.6	1.5	29.8	81.5	3.0
SANE a=0.9375 H10	3.4	3.2	332.8	6.1	1.6	10.0	77.8	13.4
SANE a=0.9375 W18	1.0	1.5	13.6	5.6	1.6	5.1	43.4	8.9
SANE a=0.9375 R17	3.1	5.3	129.5	6.1	1.5	14.1	68.7	4.9
MAD a=0.0 H10	3.4	0.2	6.6	8.1	1.6	1.1	40.2	24.3
MAD a=0.0 W18	1.0	0.6	18.5	6.3	1.6	3.2	71.9	11.9
MAD a=0.0 R17	3.1	1.1	50.9	6.4	1.6	4.8	100.5	10.0
MAD a=0.5 H10	0.6	0.2	4.4	7.9	1.6	1.3	40.3	24.1
MAD a=0.5 W18	1.2	0.9	16.2	6.2	1.6	4.2	78.0	10.6
MAD a=0.5 R17	2.1	2.2	60.8	6.2	1.5	7.6	115.5	8.2
MAD a=0.9375 H10	0.4	0.2	3.1	7.8	1.5	0.9	38.8	30.7
MAD a=0.9375 W18	1.0	0.7	8.0	5.7	1.6	2.3	72.7	13.6
MAD a=0.9375 R17	2.0	1.1	18.4	5.8	1.6	3.2	91.9	11.0

recent work (Ressler et al., 2015, 2017; Chael et al., 2018; Chael, Narayan, & Johnson, 2019).

We find two general paradigms for successfully reproducing the observed Sgr A* submm to NIR time-variable spectrum (including NIR flares), as well as 86 and 230 GHz resolved image sizes. Those combinations are SANE simulations with turbulent electron heating, and MAD simulations with reconnection electron heating. Other combinations underproduce or overproduce hot electrons for the black hole spin and inclination angles tried. The SANE/turbulence models have been proposed previously and result in a "disk-jet" morphology where jet emission becomes prominent at longer 3mm and 7mm wavelengths (Mościbrodzka et al., 2014; Ressler et al., 2017; Chael et al., 2018).

We have also calculated submm to NIR polarized images and spectra from our models. We find that all SANE/turbulence models are strongly depolarized due to Faraday rotation in the cold disk body, and cannot explain the net linear polarization observed from Sgr A* at 1.3mm. The SANE/turbulence models also show elongated morphologies at 86 GHz due to extended jet structure, inconsistent with recent measurements except at low inclination (as previously by Issaoun et al. (2019)).

MAD/reconnection models can explain the highly time-variable net linear polarization of Sgr A* in the submm, and are only mildly depolarized. As a result, we favor MAD/reconnection models of Sgr A*. Within those models, the moderate black hole spin of $a = 0.5$ is more successful at matching the observed properties than the high spin of $a = 0.9375$. At high black hole spin, the models tend to overproduce hot electrons, resulting in too much NIR emission relative to that in the submm. They are also too compact at 86 GHz.

3.6.1 Comparison to past work

Many groups have done similar studies in the last several years. Ressler et al. (2015) introduced the method used here for evolving multiple electron temperatures with subgrid heating prescriptions. This method has been used in recent work on Sgr A* (Ressler et al., 2017; Chael et al., 2018) and radiation GRMHD models of M87 (Ryan et al., 2018; Chael, Narayan, & Johnson, 2019). Compared to those studies, we have considered a larger parameter space with multiple electron heating models, varying black hole spin, and considering both MAD and SANE solutions.

Our SANE/reconnection models are similar to early GRMHD models (Noble et al., 2007; Mościbrodzka et al., 2009; Dexter, Agol, & Fragile, 2009; Dexter et al., 2010; Drappeau et al., 2013) based on the assumption of constant proton-electron temperature ratio T_p/T_e everywhere. This behavior is also seen in R17 models at low and high spin from Chael et al. (2018). Our SANE/turbulence models are similar to "disk-jet" models realized by assuming highly magnetized regions receive more heat in post-processing (Mościbrodzka & Falcke, 2013; Mościbrodzka et al., 2014; Chan et al., 2015b) or using self-consistent electron heating with the H10 model (Ressler et al., 2017). We have shown that such models, while otherwise promising, are highly depolarized as the result of Faraday rotation internal to the emission region (all inclination angles). Additionally they show very high Faraday rotation measure unless viewed at low inclination (here $i = 25°$).

Previous MAD models of Sgr A* (Shcherbakov & McKinney, 2013; Gold et al., 2017) have used different post-processing electron heating prescriptions. Some of those models are at least broadly consistent with the spatially resolved submm polarization of Sgr A* (Johnson et al., 2015). We seem to find more coherent submm polarization maps than in those studies.

Average properties of our radiative models are given in Table 3.5. The accretion rate $\dot{M}$ is measured at the event horizon, while the others are intensity-weighted averages taken along each ray and over each pixel of the 230 GHz images. Viable models we identify have $\dot{M} = (1.0 - 2.1) \times 10^{-8}\, M_\odot\, \mathrm{yr}^{-1}$, resulting in low radiative efficiencies $\lesssim 0.1\%$. The plasma parameters generally agree with one zone estimates (e.g., von Fellenberg et al., 2018; Bower et al., 2019) and physical conditions in previous analytic (e.g., Falcke & Markoff, 2000a; Özel, Psaltis, & Narayan, 2000; Yuan, Quataert, & Narayan, 2003) and GRMHD (e.g., Mościbrodzka et al., 2009; Dexter et al., 2010) models.

3.6.2 Future measurements

The 230 GHz image morphology is primarily the result of relativistic effects of Doppler beaming and light bending, and does not depend strongly on the details of the magnetic field, black hole spin, or electron model (e.g., Kamruddin & Dexter, 2013) when the emission region is optically thin.

Polarization encodes plasma and magnetic field properties (e.g., Shcherbakov, Penna, & McKinney, 2012; Dexter, 2016; Mościbrodzka et al., 2017; Jiménez-Rosales & Dexter, 2018). For the viable MAD models studied here, we find fairly coherent, azimuthal ("twisty")

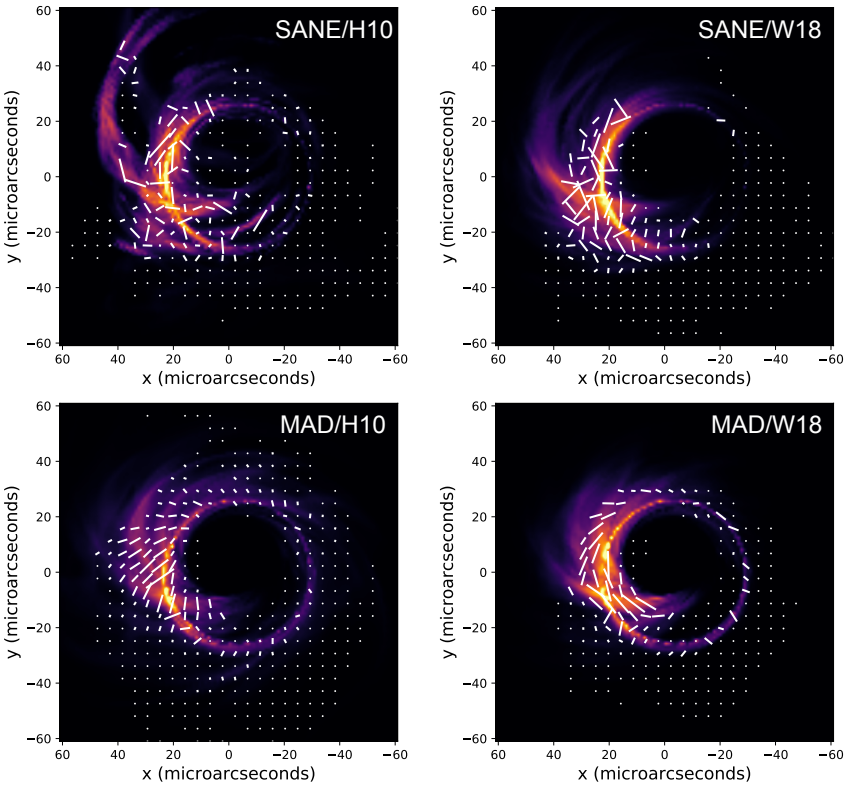

Figure 3.14: Sample snapshot 345 GHz linearly scaled false color images and linear polarization maps for $a = 0.5$ and $i = 45°$. Polarization tick length is proportional to polarized flux. At 345 GHz, the MAD polarization maps show negligible scrambling from Faraday rotation. Instead, the polarization maps trace the underlying magnetic field configuration.

EVPA maps (Figure 3.10). The structure is due to significant poloidal magnetic field near the event horizon. Radial magnetic field and light bending both produce azimuthal EVPA structure, which is balanced by vertical magnetic field which results in a preferred horizontal EVPA direction (e.g., Gravity Collaboration et al., 2018a). The azimuthal EVPA maps are far more evident at 345 GHz (or potentially in NIR flares) than at 230 GHz where external Faraday rotation can coherently rotate the EVPA by $\simeq 20-40$ degrees. Faraday rotation internal to the emission region produces additional disorder, but does not strongly depolarize the source or scramble the EVPA map.

We have also studied the image-integrated polarization angle as a function of wavelength for the models run to late times. The EVPA is defined as EVPA $= 1/2 \tan^{-1} U/Q$, where U and Q are image-integrated Stokes parameters. The EVPA $\sim \lambda^2$ behavior matches the expectation of Faraday rotation produced in the extended accretion flow (Figure 3.13, Marrone et al., 2006). The favored MAD models show rotation measure values consistent with those observed from Sgr A* (Marrone et al., 2007; Bower et al., 2018) for all inclination angles considered. The SANE models show Faraday rotation measures a factor $\simeq 10$ too large when viewed at high inclination. At low inclination ($i = 25°$), the rotation measure is much lower and can be consistent with Sgr A* data.

Figure 3.14 shows 345 GHz images and polarization maps for our four sample models. At 345 GHz, the emission region is more compact than at 230 GHz. The morphology is similar in all cases. Faraday effects are weaker, resulting in higher net linear polarization and a more coherent polarization map. The emission is concentrated to still smaller radius, producing a bright photon ring feature. At moderate to high inclination, however, the strong Doppler beaming makes this feature highly asymmetric.

3.6.3 Limitations

The parameter survey presented here is both sparsely sampled and incomplete. We have used simplistic analytic models for sub-grid electron heating, based on a small number of recent kinetics calculations. As those calculations improve, so will the predictive power of our radiative models. In general, we expect that successful models of Sgr A* will need relatively high electron temperatures in the disk body, to avoid significant depolarization of the submm radiation. Within the prescriptions tried, that disfavors SANE/turbulence models. Successful models of the submm spectrum also require a range of electron temperatures, which disfavors the SANE/reconnection scenario. This qualitative understanding can be applied to future heating prescriptions as well.

MAD accretion flows produce regions of high magnetization throughout the simulation domain, where truncation errors can lead to negative internal energy which are corrected by imposing numerical floors. The convergence properties of MADs have been explored (White, Stone, & Quataert, 2019), but remain less well understood than for the SANE case. For calculating radiative models of MADs, the treatment of high magnetization regions plays an important role (Chael, Narayan, & Johnson, 2019). Here we follow Event Horizon Telescope Collaboration et al. (2019a) and exclude emission from regions where $\sigma > 1$. That choice is arbitrary and for MAD models effects the NIR flux density (see

appendix 3.7).

We have also assumed a thermal electron distribution function, while non-thermal emission can broaden the submm spectrum (Özel, Psaltis, & Narayan, 2000; Yuan, Quataert, & Narayan, 2003; Broderick & Loeb, 2009) and increase the image size (Özel, Psaltis, & Narayan, 2000; Mao, Dexter, & Quataert, 2017; Chael, Narayan, & Sadowski, 2017; Davelaar et al., 2018). In particular, it may be possible to find viable SANE/reconnection models when non-thermal electrons are included. Their inclusion is also promising for comparing theoretical models with X-ray flare data (e.g., Ball et al., 2016). We have also assumed an accretion flow angular momentum axis aligned with that of the black hole spin. This may be a poor assumption in the Galactic center. The orientation of the stellar winds providing the extremely low accretion rate (Quataert, 2004; Cuadra et al., 2006; Ressler, Quataert, & Stone, 2018) is unlikely to align with those of earlier accretion episodes. Disk tilt can change both the image morphology and spectrum (Dexter & Fragile, 2013; White et al., 2020; Chatterjee et al., 2020) as a result of shock heating (Fragile & Blaes, 2008; White, Quataert, & Blaes, 2019). We also neglect radiative cooling, which has found to be unimportant for the low accretion rate of Sgr A* (Dibi et al., 2012; Ryan et al., 2018).

With the above caveats, our results favor a strongly magnetized MAD accretion flow in Sgr A*. The resulting magnetic field structure is consistent with that inferred from the combined time-variable polarization and astrometric motions seen in NIR flares (Gravity Collaboration et al., 2018a). The MAD limit is associated with the strongest Poynting flux driven jets from black holes (Tchekhovskoy, Narayan, & McKinney, 2011), but no powerful jet has conclusively been found from Sgr A*. The kinetic luminosity of our models remains modest compared to the energy associated with $\gtrsim 1$ pc scales in the Galactic center. Our models are also restricted to a limited computational domain. They do not make predictions for non-thermal radio emission on larger scales, as seen in jetted systems. For a MAD to operate in Sgr A*, either the acceleration mechanism is inefficient in the Galactic center, it only accelerates particles relatively close to the black hole where the extended radio emission can be hidden by interstellar scattering along the line of sight (e.g., Markoff, Bower, & Falcke, 2007), and/or the black hole spin is small in magnitude resulting in a low BZ jet power.

3.7 Conclusions

We have carried out a large parameter survey of GRMHD models of Sgr A* with self-consistent electron heating. We have considered a range of (prograde) black hole spin, vertical magnetic field strength (weak/SANE or strong/MAD), and sub-grid electron heating models (relatively uniform heating, "reconnection" or strongly β-dependent, "turbulent" heating). We have studied radiative models of the radio to NIR emission from Sgr A* based on our model survey. The main findings are as follows:

- Parameter combinations of magnetic fields and electron heating of SANE/turbulence and MAD/reconnection can explain the mm to NIR SED shape, variability including large-amplitude NIR flares, and mm/submm source sizes;

- SANE/turbulence models are heavily depolarized due to Faraday rotation effects, while some of our MAD/reconnection models remain viable for explaining a wide range of Sgr A* observations;
- MAD models show azimuthal ("twisty") EVPA maps due to significant near horizon poloidal fields and this pattern should be apparent especially at 345 GHz or higher frequency where Faraday rotation becomes negligible;
- limitations include uncertainty in the sub-grid electron heating schemes, the use of thermal electron distribution functions, the treatment of highly magnetized regions, particularly for NIR emission, and an accretion flow aligned with the spin axis of the central black hole.

Acknowledgements

We thank the anonymous referee for constructive suggestions, which led to an improved paper. J.D. and A.J.-R. were supported in part by a Sofja Kovalevskaja award from the Alexander von Humboldt foundation, by a CONACyT/DAAD grant (57265507), and by NASA Astrophysics Theory Program Grant 80NSSC20K0527. S.M.R. was supported by the Gordon and Betty Moore Foundation through Grant GBMF7392. The calculations presented here were carried out on the MPG supercomputers Hydra and Cobra hosted at MPCDF.

Appendix A: Updated Faraday rotation coefficient for a thermal plasma

Dexter (2016) presented approximate, analytic forms for synchrotron and Faraday coefficients appropriate for relativistic electrons ($\theta_e \gtrsim 1$), including for the case of purely thermal electrons. Their expression for the Faraday rotation coefficient (ρ_V, their equation B14) fails at low ν/ν_c and $\theta_e \ll 1$. This can be seen from:

$$\rho_V = \rho_{V,\mathrm{NR}}\, f(\theta_e, \nu/\nu_c), \tag{3.4}$$

where $\nu_c = (3eB/4\pi mc)\,\theta_e^2\,\cos\theta_B$ is the critical synchrotron frequency and θ_B is the angle between the emission and magnetic field directions in the fluid frame. The coefficient $\rho_{V,\mathrm{NR}}$ is the correct non-relativistic limit,

$$\rho_{V,\mathrm{NR}} = \frac{2ne^3 B\cos\theta_B}{m^2c^2\nu^2}, \tag{3.5}$$

related for example to the usual Faraday rotation measure. For $\nu/\nu_c \gg 1$, the function $f(\theta_e, \nu/\nu_c) = K_0(\theta_e^{-1}/K_2(\theta_e^{-1}$ (Shcherbakov, 2008), while for general ν/ν_c and $\theta_e \gg 1$, there is an additive correction term (Jones & Hardee, 1979) which (Dexter, 2016) included approximately with a fitting function $\Delta J_5(\nu/\nu_c)$:

$$\rho_V = \rho_{V,NR} \left(\frac{K_0(\theta_e^{-1} - \Delta J_5(\nu/\nu_c)}{K_2(\theta_e^{-1}} \right). \tag{3.6}$$

For cold electrons $\theta_e \ll 1$, the modified Bessel function $K_n(x)$ reaches an asymptotic limit independent of n. Then the ratio $K_0/K_2 \to 1$, correctly reproducing the non-relativistic limit. Adding the ΔJ_5 term violates this limit. As a simple fix, in GRTRANS we now multiply the ΔJ_5 term by a narrow step function at $\theta_e = 1$, so that it is suppressed in the non-relativistic limit. We additionally set $f(\theta_e, \nu/\nu_c) = 1$ whenever $\theta_e < 10^{-2}$ to avoid numerical errors in the ratio of modified Bessel functions of large argument. These changes are necessary for accurate calculations of Faraday rotation at larger radii where the electrons can be non-relativistic.

Appendix B: Electron temperature evolution and convergence

Our simulations evolve multiple electron energies starting from an initial condition with $T_p/T_e = 10$. The long duration simulations achieve equilibrium electron temperature profiles for roughly the last half of their duration ($1-2\times10^5 r_g/c$ for SANE and $4-6\times10^4 r_g/c$ for MAD). Figure 3.15 shows shell-averaged radial profiles of the equilibrium electron temperature for the H10 and W18 models (solid lines) for the SANE simulation, compared to the same profiles for the time interval used for calculating the models in our parameter survey (dashed) and the initial condition (dotted). The electrons heat gradually and are too cold by a factor $\simeq 1.5$ everywhere at early times. For the SANE case at early times, the electron temperature has apparently not relaxed from its initial condition for $r \gtrsim 20r_g$.

We mitigate this effect in our analysis by excluding material outside of $20r_g$ in calculating the SANE models, since otherwise the cold electrons Faraday depolarize the emission region. We have also checked that polarization properties excluding $r \gtrsim 20r_g$ are similar to the full radiative transfer results from the long duration SANE model at late times, once the electron temperature distribution has converged. The effect of excluding emission (or running to very long durations) is large for the W18 model, where the electrons heat efficiently. It is modest for the H10 model, where the equilibrium temperature profile at those radii turns out to be similar to our assumed initial condition. In particular, Faraday rotation through an accretion flow is generally thought to be dominated by the location where $\theta_e = 1$ (e.g., Marrone et al., 2006). That location is at $r \simeq 30r_g$ and $300r_g$ for the H10 and W18 models. We also measure this directly in the simulation data (Figure 3.15), where we find contributions to the RM peaking at $\simeq 30r_g$ and $\simeq 80r_g$. As a result of cold electrons near the midplane, our H10 models show large Faraday rotation measures and

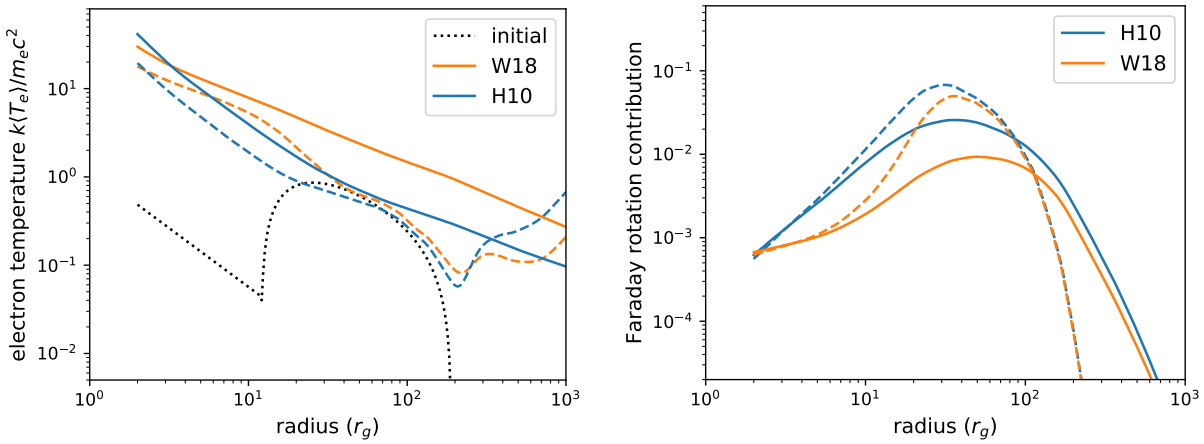

Figure 3.15: Shell-averaged electron temperature (left) and relative contribution to the Faraday rotation measure (right) for our long duration SANE $a = 0$ simulation. We compare the assumed initial conditions in our simulations (black dotted line) with the converged final state (solid) and time interval used for calculating radiative models (dashed) for the H10 and W18 electron heating models. The electron temperature profile used at early times is systematically colder the converged profile by a factor $\simeq 1.5$ at all radii. For $r \gtrsim 20r_g$ at early times the solution does not seem to have heated much beyond its initial state. As a result, the W18 model electrons (orange dashed curve) are far too cold at large radius. The effect is much weaker in the H10 case, where the equilibrium electron temperature at large radius happens to be close to that assumed in the initial condition. For both electron models, at earlier times the low temperatures causes a stronger Faraday rotation peak at smaller radii. As described in the main text, we exclude material with $r > 20r_g$ in calculating radiative models.

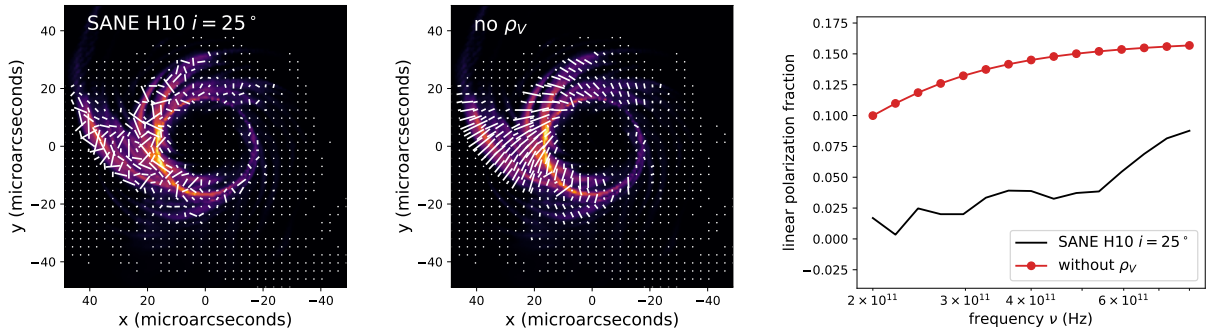

Figure 3.16: Total intensity images (false color) and polarization maps (white ticks, length proportional to polarized flux) for a snapshot from our long duration SANE $a = 0$ simulation using the H10 electron heating model and viewed at an inclination of $i = 25°$. The full calculation (left) shows substantial disorder in the polarization pattern due to internal Faraday rotation. Setting $\rho_V = 0$ (middle) leads to an ordered polarization pattern. The right panel shows polarization fraction as a function of frequency for the same models. The net linear polarization is much higher when $\rho_V = 0$.

significant depolarization from cold electrons at relatively small radii.

Appendix C: Internal and external Faraday rotation

The Faraday rotation measure (RM) is related to the Faraday optical depth $\tau_{\rho_V} = \int dl \rho_V$ by $\tau_{\rho_V} = 2RM\lambda^2$. For Sgr A*, the observed RM magnitude of $6x10^5$ rad m^{-2} at 230 GHz corresponds to $\tau_{\rho_V} \lesssim 1$, depending on the frequency bands used. The total EVPA rotation is still $< \pi$, insufficient to produce strong Faraday depolarization. We report much larger values of τ_{ρ_V} in Table 3.5, despite the fact that the models can show EVPA $\propto \lambda^2$ with realistic values of the RM magnitude (Figure 3.13).

The RM is measured from the change in EVPA, which comes from the observed polarized flux. Strongly depolarized regions contribute little polarized flux. As a result, Faraday thick regions internal to the source do not necessarily lead to large RMs. Mościbrodzka et al. (2017) found that in submm models of M87 from SANE GRMHD simulations, the RM measured from the change in EVPA could be roughly constant, even as τ_{ρ_V} varied by several orders of magnitude.

Figure 3.16 shows sample polarization maps for a snapshot of our long duration SANE $a = 0$ simulation at late times using the H10 electron model and viewed at $i = 25°$. The full calculation shows a scrambled polarization map due to Faraday rotation internal to the emission region. The RM inferred for this snapshot is only $\simeq -3 \times 10^5$ rad m^{-2}. When we neglect Faraday rotation by setting $\rho_V = 0$, the polarization map appears ordered and the inferred RM drops to $\simeq 0$. The net linear polarization is also much higher when $\rho_V = 0$, $\simeq 12\%$ at 230 GHz compared to $\simeq 2\%$ in the full calculation. Evidently the depolarization in SANE H10 models is due to Faraday rotation, even when viewed at low inclination.

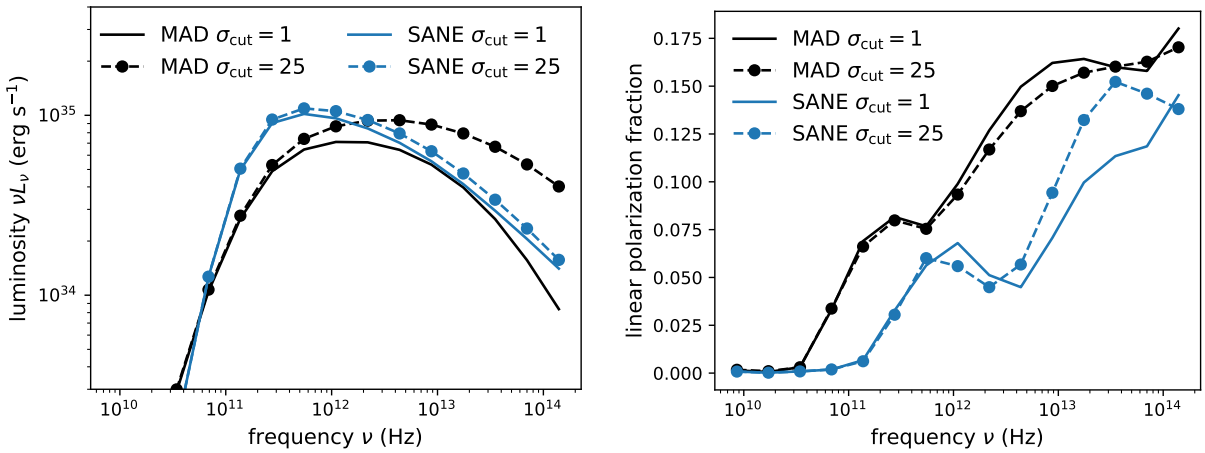

Figure 3.17: Sample spectra (left) and linear polarization fractions (right) for snapshots from near the end of our long duration SANE $a = 0$ and MAD $a = 0.9375$ simulations, using the H10 and W18 electron heating models respectively. Each model is calculated with magnetization cutoffs of $\sigma_{\rm cut} = 1$ and 25. High $\sigma > 1$ plasma contributes little of the total emission at any frequency in the SANE case. In the MAD case, we see little difference in the polarization fraction but the submm spectral slope and particularly the NIR flux density can change by factors of several depending on the choice of $\sigma_{\rm cut}$.

Internal Faraday rotation can also be strong enough to substantially depolarize the image without showing up as a large RM as inferred by the change of EVPA with frequency.

Appendix D: Effect of emission from highly magnetized regions

In this work we follow Event Horizon Telescope Collaboration et al. (2019e) and neglect emission from all regions where the magnetization $\sigma > 1$. Highly magnetized regions are difficult to evolve accurately in ideal MHD and may have mixed with artificially injected mass and energy (due to "floors"). Ressler et al. (2017) show that this choice makes little difference for SANE models, where most of the fluid is weakly magnetized. Highly magnetized regions are more prevalent in MAD models, and Chael, Narayan, & Johnson (2019) explored the effects of various cuts on σ in their images and spectra of M87.

Figure 3.17 shows Sgr A* spectra and linear polarization fractions for two sample snapshots, one each from late times in our long duration SANE $a = 0$ and MAD $a = 0.9375$ simulations. We adopt the H10 (SANE) and W18 (MAD) electron heating models since those best describe the Sgr A* spectrum. In the SANE case, we confirm that high σ material does not contribute significantly to the radio to NIR emission.

In the MAD case, $\sigma > 1$ plasma produces an increasing fraction of the emission at higher frequencies beyond the THz spectral peak and dominates the radiation in the NIR.

Adopting a higher σ cutoff value would therefore lead to higher NIR flux densities and slight changes to the submm spectral index. The choice of σ cutoff value remains interesting to explore further in future work, but seems unlikely to be a major source of uncertainty in the analysis presented here.

Chapter 4

Relative depolarization of the black hole photon ring in GRMHD models of Sgr A* and M87*

Original publication: A. Jiménez-Rosales, J. Dexter, S. M. Ressler, A. Tchekhovskoy, M. Bauböck, Y. Dallilar, P. T. de Zeeuw, F. Eisenhauer, S. von Fellenberg, F. Gao, R. Genzel, S. Gillessen, M. Habibi, T. Ott, J. Stadler, O. Straub & F. Widmann, 2020, *Relative depolarization of the black hole photon ring in GRMHD models of Sgr A* and M87**. MNRAS, *submitted*.

Abstract: Using general relativistic magnetohydrodynamic simulations of accreting black holes, we show that a suitable subtraction of the linear polarization per pixel from total intensity images can enhance the photon ring feature. We find that the photon ring is typically a factor of $\simeq 2$ less polarized than the rest of the image due to primarily a combination of magnetic turbulence and parallel transport. When there are no other persistently depolarized image features, summing the subtracted residuals over time results in a sharp image of the photon ring. We show that the method works well for sample, viable GRMHD models of Sgr A* and M87*, where measurements of the photon ring properties would provide new measurements of black hole mass and spin, and potentially allow for tests of the "no-hair" theorem of general relativity.

4.1 Introduction

Long baseline interferometry techniques have the power to resolve and explore the innermost regions of accretion flows around supermassive black holes. Interferometric measurements made with GRAVITY at the Very Large Telescope (Eisenhauer et al., 2008; Paumard et al., 2008; Gravity Collaboration et al., 2017) and the Event Horizon Tele-

scope (EHT; Doeleman et al., 2008, 2012; Fish et al., 2011), have offered unprecedented capability to study these systems at angular scales of tens of microarcseconds (μas). That resolution is comparable to the size of the event horizon on the sky for the Galactic Centre black hole, Sagittarius A* (Sgr A*), and the supermassive black hole in M87 (M87*). The observations probe not only the geometrical and physical properties of matter around the compact object, but also allow for tests in the strong-field regime of general relativity (Gravity Collaboration et al., 2018b,a, 2020c,b; Event Horizon Telescope Collaboration et al., 2019a,b,c,d,e,f).

Theoretical studies of low-luminosity accretion onto black holes encompass analytic models (e.g., Ichimaru, 1977; Rees et al., 1982; Narayan & Yi, 1994; Yuan, Quataert, & Narayan, 2003), semi analytic calculations (e.g., Falcke & Markoff, 2000a; Bromley, Melia, & Liu, 2001; Broderick & Loeb, 2005, 2006b) and numerical simulations. The latter include general relativistic magnetohydrodynamic (GRMHD) calculations, where the equations of ideal magnetohydrodynamics are written, solved and self-consistently evolved taking into account general relativistic effects (e.g., Gammie, McKinney, & Tóth, 2003; De Villiers, Hawley, & Krolik, 2003; Noble et al., 2006; Tchekhovskoy, Narayan, & McKinney, 2011; Narayan et al., 2012; Shiokawa, 2013).

While predicted total intensity images of emission arising at event horizon scales are useful in studying the properties of the accretion flow (e.g. size, shape, variability; Dexter, Agol, & Fragile, 2009; Mościbrodzka et al., 2009; Chan et al., 2015b; Anantua, Ressler, & Quataert, 2020; Dexter et al., 2020a), they are often dominated by light bending and Doppler boosting. Polarization information has proven to be a key element in complementing these studies, setting limits on model quantities such as accretion rate and electron temperature from observables like linear polarization fraction (e.g., Aitken et al., 2000; Agol, 2000; Quataert & Gruzinov, 2000; Bower et al., 2017), rotation measure (Bower et al., 2003; Marrone et al., 2006, 2007; Kuo et al., 2014; Bower et al., 2018) and spatially resolved magnetic field structure (e.g., Johnson et al., 2015; Mościbrodzka et al., 2017; Jiménez-Rosales & Dexter, 2018, Gravity Collaboration: Jiménez-Rosales et al., submitted).

The emission around a black hole is gravitationally lensed. At event horizon scales, the strength of this effect is such that it produces a sequence of strongly lensed images of the surrounding emission (e.g., Cunningham & Bardeen, 1973; Luminet, 1979; Viergutz, 1993) that result in an annulus of enhanced brightness (we henceforth refer to all indirect images as the "photon ring"). Analytic studies show that if the emission around the black hole is optically thin, the photon ring may show universal features both in total intensity and polarization that are completely governed by general relativity (Johnson et al., 2020; Himwich et al., 2020).

The EHT Collaboration's published images of M87* show a bright ring of emission surrounding a dark interior (Event Horizon Telescope Collaboration et al., 2019d). The presence of a photon ring is expected within this emission, surrounding the black hole shadow (Falcke & Markoff, 2000a). Measuring its properties, including the size and shape, provide new measurements of the mass and spin of the black hole and could even test the "no-hair" theorem of general relativity (e.g., Johannsen & Psaltis, 2010). Typically, the photon ring contributes $\simeq 5-10\%$ of the total flux in GRMHD models (e.g., Ricarte &

Dexter, 2015). The challenge is to separate this feature from surrounding direct emission. Psaltis et al. (2015) showed that the edge of the photon ring feature is generally sharp, which may help with its extraction. This may also be possible using extremely long baselines (e.g., with one telescope in space), if stochastic source features can be smoothed by coherently averaging (Johnson et al., 2020).

Here, we use GRMHD calculations to show that the polarized radiation may provide another method. In many current GRMHD models, the photon ring is enhanced when suitably subtracting the linear polarized flux per pixel from the total intensity (Section 4.2). We find that the photon ring is persistently depolarized compared to rest of the image by a factor of $\simeq 2$ (Section 4.3). The relative depolarization is due to a combination of magnetic field disorder and gravitational effects. We discuss our results and conclude in Section 4.4.

4.2 Photon ring extraction

In this work we use two long duration, 3D GRMHD simulations of black hole accretion flows described in Dexter et al. (2020a): one in a strongly magnetised (magnetically arrested disc, MAD) regime and the other in a weakly magnetised (standard and normal evolution, SANE) one. The simulation's framework allows for the independent, self-consistent evolution of four electron internal energy densities in pair with that of the single MHD fluid (Ressler et al., 2015). Here, we use a turbulent heating prescription based on gyrokinetic theory (Howes, 2010) for the MAD model and electron heating in magnetic reconnection events from particle-in-cell simulations (Werner et al., 2018) for the SANE model.

Both simulations are run with the HARMPI[1] code (Tchekhovskoy, 2019). The initial condition is that of a Fishbone-Moncrief torus (Fishbone & Moncrief, 1976) with inner radius at $r_{\rm in} = 12\ r_g$ ($r_g = GM/c^2$), pressure maximum radius $r_{\rm max} = 25\ r_g$, threaded with a single poloidal loop of magnetic field and black hole spin parameter of $a = 0$ and $a = 0.9375$ for the SANE and MAD cases respectively.

In the MAD case, the simulation was run for a time of $6 \times 10^4\ r_g/c$, each snapshot spaced by $10\,r_g/c$, establishing inflow equilibrium out to $r \simeq 90\ r_g$. In the SANE case, the simulation is studied at late times ($17 \times 10^4\,r_g/c$, each snapshot spaced by $10\,r_g/c$ as well), once radii $r \gtrsim 100\ r_g$ have reached inflow equilibrium. By doing this, we avoid "artificial" depolarization in the images from external Faraday rotation from zones far out in the accretion flow that are not yet in equilibrium. See Dexter et al. (2020a) for more details.

We calculate post-processed images using the general relativistic ray-tracing public code GRTRANS[2] (Dexter & Agol, 2009; Dexter, 2016). The electron temperature is taken directly from the GRMHD electron internal energy density, $kT_e = (\gamma_e - 1)m_p u_e/\rho$, where we use $\gamma_e = 4/3$ and have assumed a composition of pure ionised hydrogen. The mass of the black hole is set to $4 \times 10^6\ {\rm M}_\odot$ and the mass accretion rate is scaled until the observed flux

[1] https://github.com/atchekho/harmpi
[2] https://github.com/jadexter/grtrans

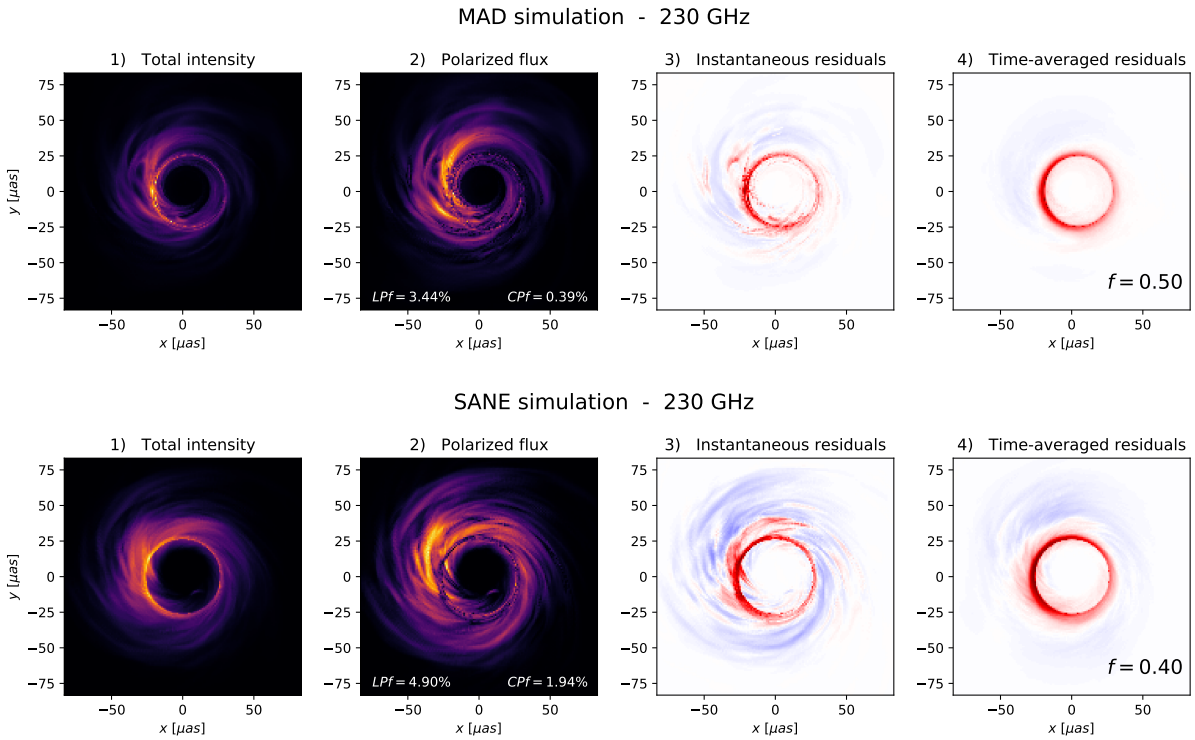

Figure 4.1: Top row: MAD simulation. Bottom row: SANE simulation. Panels 1 and 2 show respectively the total intensity and the polarized flux at 230 GHz for a snapshot of the simulations. Emission is shown in false colour. Higher emission zones are denoted by lighter colours. Both images exhibit similar morphologies, with the difference that the polarized flux image has many more dark areas in the accretion flow due to depolarization. The photon ring is a prominent feature in both and appears depolarized compared to the rest of the image. The net LPf and CPf in the image are indicated in Panel 2. 3) Instantaneous residuals for this snapshot, $I - 1/f\ LP$, with $f = 0.5$ and $f = 0.4$ for the MAD and SANE cases respectively. 4) Time-averaged residuals over thirty frames. The snapshots are separated by 10 GM/c^3. If the depolarized image features change over time except at the photon ring, the residuals average out everywhere else, enhancing the ring in the residual image.

density at 230 GHz matches that of Sgr A* at this frequency ($\simeq 3$ Jy; e.g., Dexter et al., 2014; Bower et al., 2015). In our calculations, we exclude emission from regions where $\sigma = u_B/\rho c^2 > 1$, with $u_B = b^2/4\pi$ the magnetic energy density. We calculate observables at 230 GHz and a viewing orientation of $i = 50$ degrees. The image resolution is 192 pixels over a 42 r_g ($\sim 210\,\mu$as) field of view (a discussion of resolution effects can be found in Appendix 4.4).

Panels 1 and 2 in the top and bottom rows of Fig. 4.1 show total intensity (Stokes I) and linear polarized flux, $LP = \sqrt{Q^2 + U^2}$, of snapshot images of the MAD and SANE simulations respectively, where the Stokes parameters Q and U denote the linear polarization states at 0/90 and $\pm$45 degrees. In both cases, the total intensity and linear polarized flux images exhibit similar morphologies. We note as well that the images present a sharp, bright photon ring with many depolarized areas on it. The net linear and net circular polarization fractions (LPf[3] and CPf[4] respectively) in the image are indicated in Panel 2.

Suitably subtracting the polarized flux from the total intensity per pixel results in a residual image with a clearer photon ring. We introduce a scaling factor f that accounts for the difference between the image's polarized flux $\langle$LP$\rangle$ and total intensity $\langle I\rangle$ [5]. The residual image is then $I - 1/f\ LP$. An example of the "instantaneous" (one snapshot) residuals for the values shown in Panels 1 and 2 is shown in Panel 3 in the top and bottom rows of Fig. 4.1. Here we have run through a set of values of f ($0.3 - 1.0$ spaced every 0.05 and $f = \langle$LP$\rangle/\langle$I$\rangle$) and chosen the value which minimises the sum of the residuals outside of a thin ring on the sky with a width from $4.8 - 5.5\,r_g$. This is close to expected position of the photon ring ($\sqrt{27}\,r_g$ for a Schwarzschild black hole and $\simeq 5\,r_g \pm 4\%$ and nearly circular across all spins; Johannsen & Psaltis (2010)) and where most of the emission is contained. In our calculations we consider as "photon ring pixels" those that lie within this ring. Note that our definition of photon ring pixels includes foreground "contamination" from the direct image. This is generally a minor contribution.

The total intensity and LP images vary in time due to turbulent fluctuations in the accretion flow. These variations are strongly correlated, except that the LP image varies somewhat more. This is because the direction of the polarization vector depends strongly on the underlying magnetic turbulence and/or Faraday effects, resulting in transient depolarization of some image pixels. The photon ring, however, remains visible and depolarized over time. The stability of the photon ring properties implies that the extraction technique benefits from source variability. Adding residual images tends to average out the residuals everywhere but the photon ring, increasing its contrast. Panel 4 in the top and bottom rows of Fig. 4.1 shows the cumulative residual images over thirty frames of our simulations for each case, starting from $5.1 \times 10^3\,r_g/c$ for the MAD simulation and $17 \times 10^4\,r_g/c$ for the SANE simulation. This corresponds to a time span of ~ 1.7 hr for Sgr A* and ~ 100 days for M87*. In each individual frame, the best f value that minimises the residuals in the image is applied. It can be seen that an optimal choice of f leads to the residuals

[3] LPf=$\sqrt{\sum(Q_i)^2 + \sum(U_i)^2}/\sum(I_i)$, where the sum is over all the pixels.

[4] CPf=$\sum(V_i)/\sum(I_i)$, with V the circular polarization Stokes parameter.

[5] Since light might not be completely linearly polarized, $I \geq$ LP, so that $\langle I\rangle = \sum I \geq \langle$LP$\rangle = \sum$LP. To account for this difference, the factor f should then be similar to $\langle$LP$\rangle/\langle$I$\rangle$.

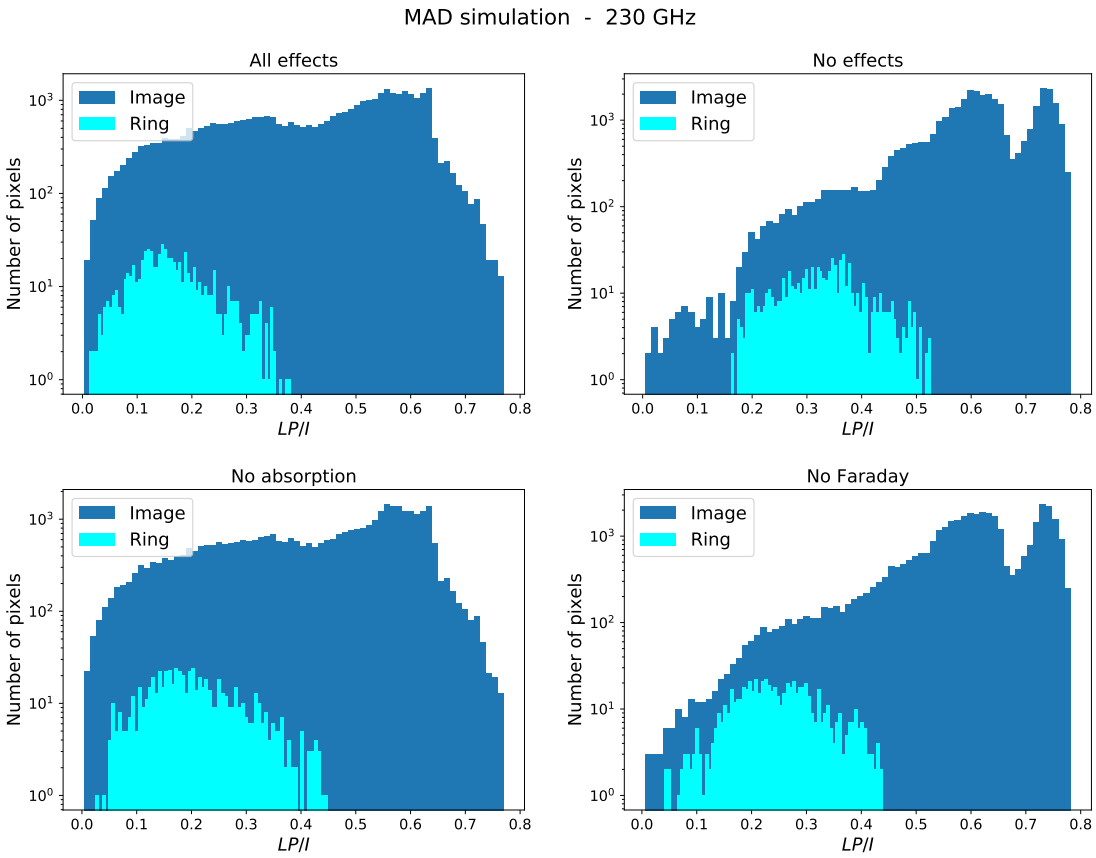

Figure 4.2: Distribution of image and ring fractional polarized flux (LP/I) per pixel for the MAD simulation. Image pixels are in dark blue, ring pixels are in cyan. LP/I is calculated from thirty-frame averaged images where different effects are considered. Top left: all effects. Top right: no effects. Bottom left: no absorption. Bottom right: no Faraday effects. In all cases the photon ring pixels are preferentially depolarized.

successfully averaging out over time, sharpening the photon ring.

4.3 Numerical properties of the photon ring

We investigate the reasons for which the photon ring has different properties from the rest of the image. To do this, we study how the polarization properties of the photon ring are affected in the presence/absence of effects that can depolarize an image. We consider four effects: absorption, Faraday rotation and conversion, magnetic turbulence and parallel transport.

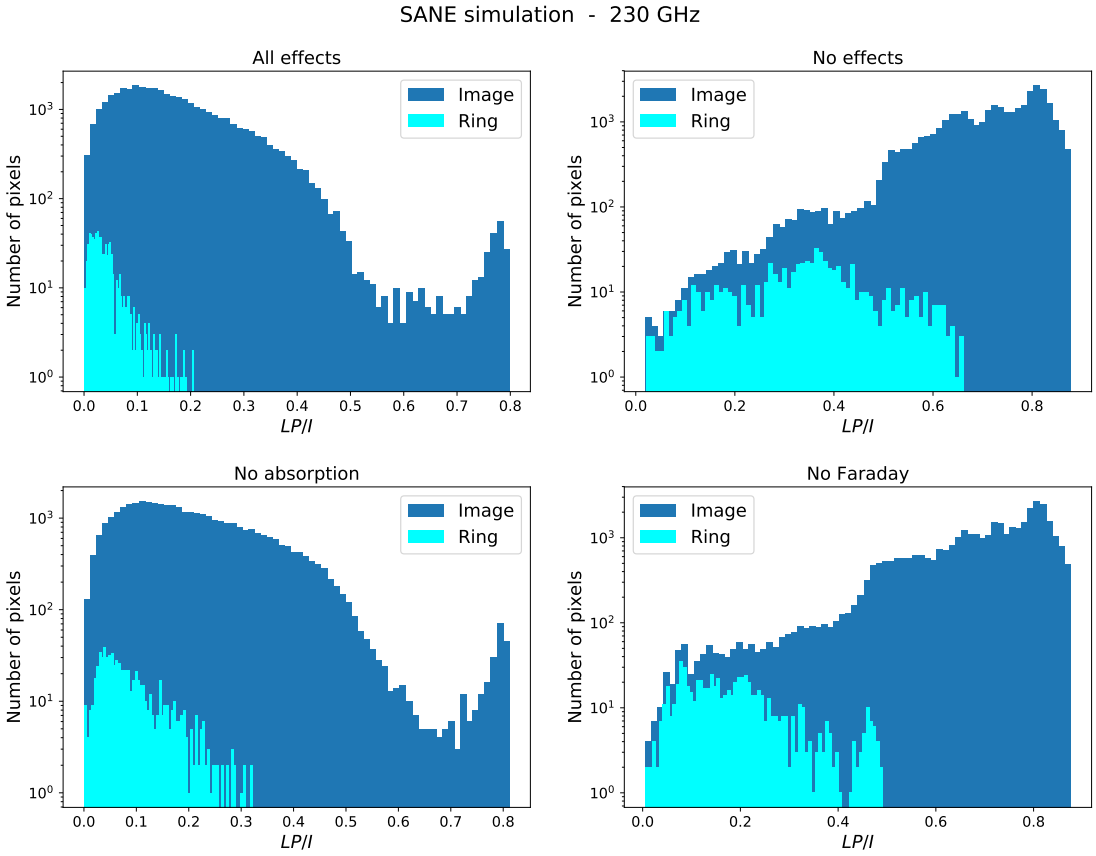

Figure 4.3: Distribution of LP/I per pixel for the SANE simulation. The values are calculated from thirty-frame averaged images where different effects are considered. Image pixels are in dark blue, ring pixels are in cyan. Top left: all effects. Top right: no effects. Bottom left: no absorption. Bottom right: no Faraday effects. In all cases the photon ring pixels are clear outliers in the distribution.

Table 4.1: Image and ring image-integrated fractional LP (m, Eq. (4.1)) of the MAD simulation. The values are calculated from a thirty-frame averaged image including effects of absorption and/or Faraday rotation and conversion at a time.

		All effects	No effects	No absorption	No Faraday
MAD	$m_{\rm Image}$ [%]	44.87	52.12	48.13	48.40
	$m_{\rm Ring}$ [%]	22.97	35.25	30.59	26.05
	$m_{\rm Ring}$ / $m_{\rm Image}$	0.51	0.68	0.64	0.54

4.3.1 Effects of absorption, Faraday rotation and Faraday conversion

GRTRANS calculates images by solving the polarized radiative transfer equation along geodesics traced between where a photon was emitted and the observer's camera. By setting the absorption, Faraday rotation or conversion coefficients in the radiative transfer equation to zero, we can study the influence of these effects straightforwardly.

We first look at the distribution of fractional linear polarization (LP/I) in the image and photon ring pixels from a set of images where either all (or none) of the effects have been taken into account. Figures 4.2 and 4.3 show that the photon ring is a clear outlier in the distribution of polarized flux in all cases. When absorption and/or Faraday rotation are neglected, the polarization fraction increases everywhere. Still the photon ring remains depolarized compared to the rest of the image.

The image-integrated fractional LP in the ring and image is given by

$$m_x = \sum_i^n \mathrm{LP_i}/\ \mathrm{I_i} = \sum_{\mathrm{i}}^{\mathrm{n}} (\sqrt{\mathrm{Q_i^2 + U_i^2}}\ /\ \mathrm{I_i}) \tag{4.1}$$

where x denotes whether the calculation uses image or photon ring pixels and n is the number of pixels. The values of m for the MAD and SANE cases are shown in Tables 4.1 and 4.2. In all cases the photon ring is about a factor of $\simeq 2$ less polarized than the rest of the image, with maximum depolarization obtained when all effects are included in the calculations. As expected, the highest degree of polarization in the ring ($\sim 60\%$ of that of the image) is achieved when neither effect is included in the calculation. A comparison of the cases shows that even though the effects of absorption have larger impact on the depolarization degree of the ring ($\sim 20\%$ more than Faraday effects), neither effect alone (or combined) amounts to the total observed level of depolarization in the photon ring.

4.3.2 Effects of magnetic turbulence and parallel transport

We next look into the effects of magnetic field turbulence and gravitational effects. We expect magnetic field turbulence and parallel transport to depolarize emission in the ring due to multiple contributions to the polarized intensities $j_{Q,U}$ along the light rays (which wrap around the black hole), which will tend to average down. However, while parallel

Table 4.2: Image and ring image-integrated fractional LP (m, Eq. (4.1)) of a thirty-frame averaged SANE image with different effects included in the calculations.

		All effects	No effects	No absorption	No Faraday
SANE	m_{Image} [%]	36.84	55.38	45.71	47.27
	m_{Ring} [%]	15.76	37.92	30.96	19.63
	m_{Ring} / m_{Image}	0.43	0.68	0.68	0.42

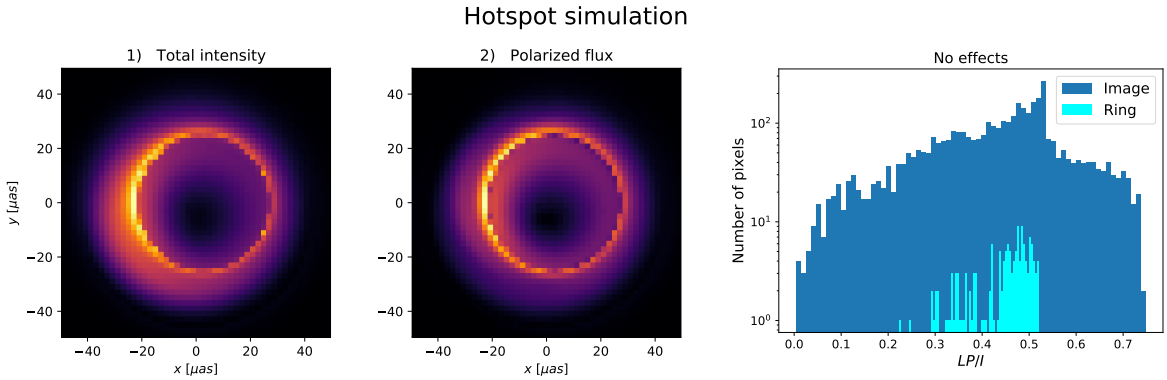

Figure 4.4: Stacked frames of hotspot orbiting a black hole at 4 r_g in a completely vertical field. The hotspot does one revolution around the black hole tracing clockwise motion. In this simplified model the magnetic field is fully ordered and both self-absorption and Faraday rotation are negligible. Left: total intensity. Middle: linear polarization. Right: Distribution of fractional polarized flux LP/I of the image and photon ring pixels. Image pixels are in dark blue, ring pixels are in cyan. Unlike the MAD and SANE cases, the photon ring pixels have a similar distribution compared to the rest of the image.

Table 4.3: Image-integrated fractional LP (m, Eq. (4.1)) of stacked images over one revolution of the hotspot model.

		No effects
Hotspot	$m_{\rm Image}$ [%]	40.59
	$m_{\rm Ring}$ [%]	43.29
	$m_{\rm Ring}$ / $m_{\rm Image}$	1.07

transport is constant in time and model independent, magnetic field structure can be vastly different in models and exhibit time dependent behaviour.

In order to study turbulent magnetic field structure effects more, we compare our MAD and SANE GRMHD results to an idealized semi-analytical model with an ordered magnetic configuration and no radiative transfer effects. We consider an optically-thin compact emission region ("hotspot"; Broderick & Loeb, 2006b) orbiting a black hole in a vertical magnetic field with strength ~ 100 G. The hotspot is moving with constant speed (matching that of a test particle at its center) in the equatorial plane at radius R_0. The maximum particle density $n_{\rm spot} \sim 2\times10^7\,{\rm cm}^{-3}$ falls off as a 3D Gaussian with characteristic size $R_{\rm spot}$. We fix the viewer's inclination at $i \sim 160$ degrees, consistent with GRAVITY flare observations (Gravity Collaboration et al., 2018a, 2020c). We assume a black hole spin of zero and calculate synchrotron radiation from a power law distribution of electrons with a minimum Lorentz factor of 1.5×10^3.

Total intensity and linear polarization images stacked over one revolution of a hotspot orbiting at $R_0 = 4\ r_g$ are shown in Fig. 4.4 (left and middle panels respectively). Since the emission is subject to no effects other than magnetic field structure and gravitational effects, there is a lack of dark depolarized zones in the LP image. We can see gravitational lensing and beaming in the form of secondary images, asymmetry in the emission (top brighter than bottom due to Doppler beaming from the hotspot approaching the observer), and a very bright photon ring.

The distribution of fractional LP per pixel in this idealized model (right Panel of Fig. 4.4) shows that the photon ring pixels have a similar distribution to that of the rest of the image. This is supported by the m values (Table 4.3). We find similar results in the case of a hotspot moving in a completely toroidal field. In contrast to the MAD and SANE cases, in the hotspot model the photon ring is more polarized than the rest of the image, which suggests that complex magnetic field structure is an important factor for depolarizing the photon ring.

Tables 4.1 and 4.2 show that generally speaking, the SANE simulation is more depolarized than the MAD (up to $\sim 60\%$ depolarization with respect to the rest of the image when all effects are considered). Comparing both "no effects" cases for the MAD and SANE simulation, where no radiative transfer effects are included in the calculations, we see that their image-integrated polarized fluxes have very similar values. In the SANE case the weak fields are sheared into a predominantly toroidal configuration in the accretion flow, while in the MAD case significant poloidal components remain. While complex

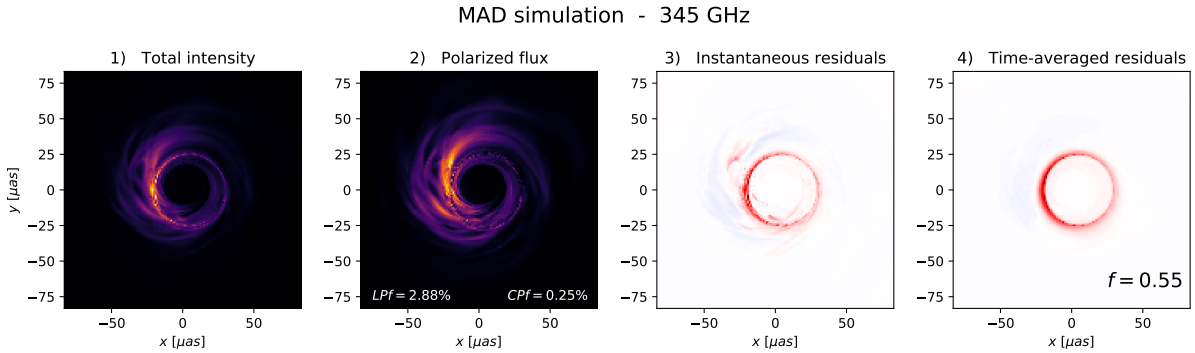

Figure 4.5: Total intensity (1), polarized flux (2), instantaneous residuals $I - 1/f\ LP$ with $f = 0.55$ (3) and time-averaged residuals over thirty frames (4) of images at 345 GHz of the long duration, MAD 3D GRMHD simulation. The net LPf and CPf in the image are indicated in Panel 2. The extraction of the photon ring works better at higher frequency, where other depolarizing effects of self-absorption and Faraday rotation are weaker.

or turbulent magnetic field structure appears to be an important contributor to depolarization of the photon ring, the effect is not strongly model-dependent, e.g., the details appear to be less important.

4.4 Summary and discussion

We have shown that an optimal subtraction of linear polarized flux images from total intensity images calculated from GRMHD simulations can enhance the photon ring feature when the conditions in the plasma are suitable. The method relies on the fact that both kinds of images are highly correlated, except at the photon ring. The photon ring is preferentially and persistently depolarized with respect to the rest of the image.

The latter implies that time variability in the source favours a better extraction of the ring. If the photon ring is the only persistently depolarized image feature, residuals from depolarized pixels in the rest of the image will be suppressed when time-averaging, sharpening the photon ring feature. Given that the black hole mass sets the length and timescales of the system, compared to Sgr A*, M87* is about a thousand times more massive and a thousand times slower. Time-averaging for Sgr A* could be done within a single day or epoch of observing, while for M87* it would require many observational campaigns spanning months to years.

Extracting the photon ring by subtracting polarized flux requires a prominent photon ring feature in the total intensity image, and fails when regions other than the photon ring are persistently depolarized, e.g., due to self-absorption or Faraday rotation. As a result, the method works best at low to moderate observer inclinations. M87* is known to be viewed at low inclination and viable theoretical models of the EHT image show prominent photon ring features (Event Horizon Telescope Collaboration et al., 2019e). A

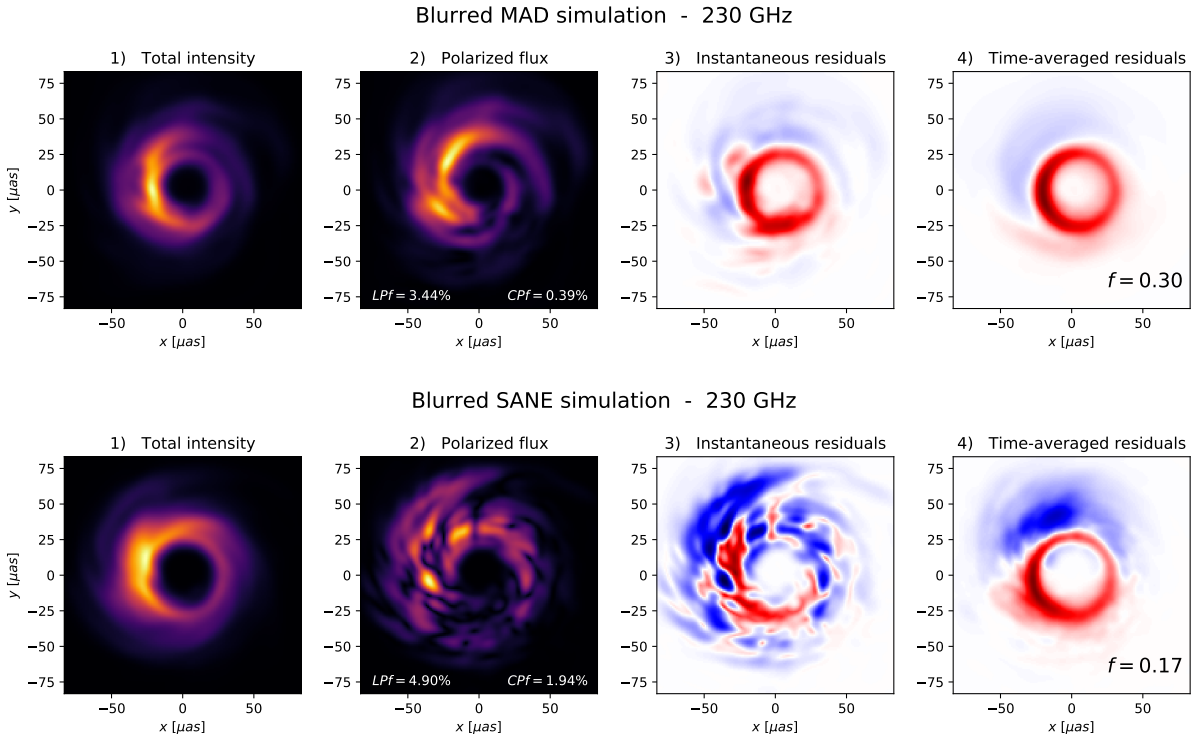

Figure 4.6: Photon ring extraction technique applied to GRMHD images blurred with a 20μas Gaussian. Top row: MAD simulation. Bottom row: SANE simulation. (1) Total intensity. (2) Polarized flux. (3) Instantaneous residuals. (4) Time-averaged residuals over thirty frames. The technique is still effective for the MAD case. In the SANE case however, the polarized flux image does not show a prominent ring and it is not clear if the ring features in time-averaged residuals are better than the total intensity image.

low to moderate inclination angle is consistent with recent observations of Sgr A* flares (Gravity Collaboration et al., 2018a, 2020c).

Frequency is an important factor as well. At low frequencies where the emission is self-absorbed, and in local thermodynamic equilibrium, the intensity is that of a blackbody. The radiation will tend to be unpolarized not only at the photon ring, but anywhere in the accretion flow where the optical depth is large. In this case, the photon ring will no longer be an outlier and time variability will not improve the residuals image over time since the location of zones with high optical depth will not vary much. Faraday effects will affect the image in a similar manner, becoming stronger with decreasing frequency and introducing depolarization all over the image. Frequencies $\nu \gtrsim 230$ GHz produce even more favourable results. In particular, Fig. 4.5 shows a sharp ring residual image at 345 GHz for our MAD model.

We have looked into the numerical properties of the photon ring in our GRMHD images. The lower degree of linear polarization with respect to the rest of the image (~ 2 less polarized) is not caused mainly by either absorption or Faraday effects, but rather by a combination of gravitational effects that are constant in time (parallel transport) and magnetic field turbulence in the plasma. The method appears to work as well for sample snapshot polarized images (C. J. White, private communication) from Ressler et al. (2020), where the simulations are initialised from larger scale MHD simulations of accretion onto Sgr A* via magnetised stellar winds. Those simulations show a complex magnetic field structure, where the magneto rotational instabilities are not important at any time (Ressler, Quataert, & Stone, 2020). We have also compared our GRMHD results to those of a semi-analytical hotspot model in an idealized vertical magnetic field configuration. In this case, the results seem consistent with analytic predictions for optically thin emission around black holes (Himwich et al., 2020), where parallel transport is not expected to depolarize emission in the photon ring. Evidently, both parallel transport and some degree of disorder in the magnetic field configuration are required to cause the depolarization of the photon ring that we find. The results appear insensitive to the model chosen, among the few we have explored.

So far the technique has been presented for the image domain only, using an angular resolution of $\simeq 1\mu$as, far superior to that available with the EHT ($\simeq 10 - 20\mu$as). Given the non-linearity of the polarized flux in terms of the observable Stokes parameters Q and U, an extension to the Fourier domain, where the observables are measured, is non-trivial and is left for future work.

We tried blurring images by convolving the map of each Stokes parameter with a 20μas FWHM Gaussian kernel and then applying the technique. The results are shown in Figure 4.6. Whereas for the MAD scenario the method still appears to be promising, resulting in a prominent blurred ring, in the SANE case the ring features in the time-averaged residual map do not appear much clearer than in the original total intensity image.

For conditions similar to those found in many viable GRMHD models of Sgr A* and M87*, the relative depolarization of emission from the black hole photon ring may provide a powerful method for extracting it from horizon scale images and movies. The method naturally benefits from the turbulent variability expected from accreting black holes.

Acknowledgements

We thank Chris J. White for providing sample images. A.J.-R. thanks Daniel Palumbo for his constructive comments. J.D. and A.J.-R. were supported in part by a Sofja Kovalevskaja award from the Alexander von Humboldt foundation, by a CONACyT/DAAD grant (57265507), and by NASA Astrophysics Theory Program Grant 80NSSC20K0527. S.M.R. is supported by the Gordon and Betty Moore Foundation through Grant GBMF7392. AT was supported by the National Science Foundation AAG grants 1815304 and 1911080. The calculations presented here were carried out on the MPG supercomputers Hydra and Cobra hosted at MPCDF.

Appendix A: Dependence of results on ray tracing image resolution

We have checked how image resolution affects the results presented in this work. Figure 4.7 shows histograms of pixel fractional polarization from the MAD simulations at 230 GHz with different resolutions. In all cases the photon ring pixels show different properties to those of the image pixels, with the photon ring being a factor of $\sim 2 - 2.5$ less polarized.

It can be seen as well that while the image-integrated LP of the image stays relatively constant with resolution, the image-integrated LP of the photon decreases with increasing resolution, though not by large amounts. We have also included a case where an image is binned to lower resolution by averaging the original over 2×2 pixel sub-grids. The binned image (bottom right) shows a somewhat lower value of $m_{\rm Ring}$, but not $m_{\rm Image}$, than the original at the same resolution.

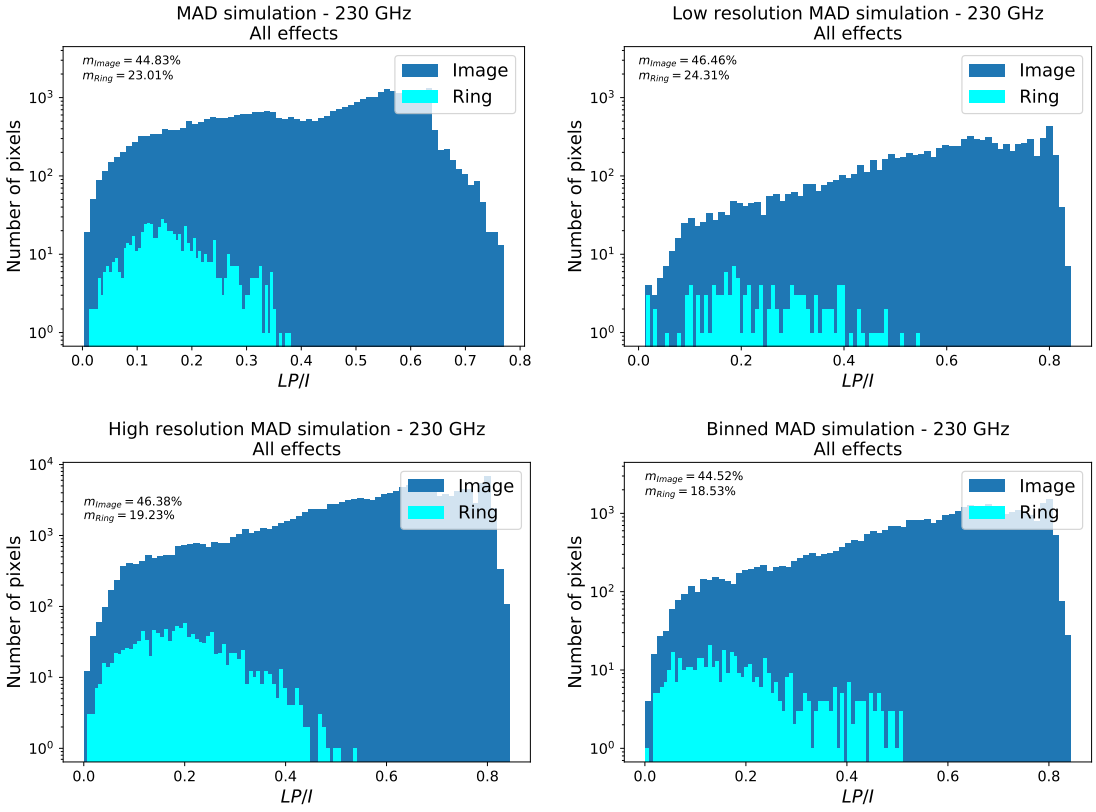

Figure 4.7: Distribution of LP/I per pixel for the MAD simulation with different resolutions. Top left: fiducial MAD simulation used in the calculations ($192 \times 192 \times 1600$ pixels). Top right: a lower resolution of ($96 \times 96 \times 800$). Bottom left: higher resolution ($384 \times 384 \times 1600$). Bottom right: higher resolution image binned to lower resolution by averaging 2×2 pixel squares. The final resolution is $192 \times 192 \times 1600$. The image-integrated LP of the image and the ring are indicated on each panel. It can be seen that as the resolution increases, $m_{\rm Ring}$ decreases, though not by large factors, and $m_{\rm Image}$ stays relatively constant. In all cases the photon ring pixels show different properties to the image pixels and are a factor $\sim 2 - 2.5$ less polarized.

Chapter 5

Dynamically important magnetic fields near the event horizon of Sgr A*

Original publication: GRAVITY Collaboration: A. Jiménez-Rosales, J. Dexter, F. Widmann, M. Bauböck, R. Abuter, A. Amorim, J. P. Berger, H. Bonnet, W. Brandner, Y. Clénet, P.T. de Zeeuw, A. Eckart, F. Eisenhauer, N.M. Föster Schreiber, P. Garcia, F. Gao, E. Gendron, R. Genzel, S. Gillessen, M. Habibi, X. Haubois, G. Heissel, T. Henning, S. Hippler, M. Horrobin, L. Jochum, L. Jocou, A. Kaufer, P. Kervella, S. Lacour, V. Lapeyrère, J.-B. Le Bouquin, P. Léna, M. Nowak, T. Ott, T. Paumard, K. Perraut, G. Perrin, O. Pfuhl, G. Rodríguez-Coira, J. Shaanhuan, S. Scheithauer, J. Stadler, O. Straub, C. Straubmeier, E. Sturm, L.J. Tacconi, F. Vincent, S. von Fellenberg, I. Waisberg, E. Wieprecht, E. Wiezorrek, J. Woillez, S. Yazici and G. Zins, 2020, *Strong magnetic fields near the event horizon of Sgr A**. ApJ. DOI:10.1051/0004-6361/202038283

Abstract: We study the time-variable linear polarization of Sgr A* during a bright NIR flare observed with the GRAVITY instrument on July 28$^{\text{th}}$ 2018. Motivated by the time evolution of both the observed astrometric and polarimetric signatures, we interpret the data in terms of the polarized emission of a compact region ("hotspot") orbiting a black hole in a fixed, background magnetic field geometry. We calculate a grid of general relativistic ray-tracing models, create mock observations by simulating the instrumental response, and compare predicted polarimetric quantities directly to the measurements. We take into account an improved instrument calibration that now includes the instrument's response as a function of time, and explore a variety of idealized magnetic field configurations. We find that the linear polarization angle rotates during the flare, consistent with previous results. The hotspot model can explain the observed evolution of the linear polarization. In order to match the astrometric period of this flare, the near horizon magnetic field is required to have a significant poloidal component, associated with strong/dynamically important

fields. The observed linear polarization fraction of $\simeq 30\%$ is smaller than that predicted by our model ($\simeq 50\%$). The emission is likely beam depolarized, indicating that the flaring emission region resolves the magnetic field structure close to the black hole.

5.1 Introduction

There is overwhelming evidence that the Galactic center harbours a massive black hole, Sagittarius A* (Sgr A*, Ghez et al., 2008; Genzel, Eisenhauer, & Gillessen, 2010) with a mass $M \sim 4 \times 10^6$ $M_\odot$ as inferred from the orbit of the star S2 (Schödel et al., 2002; Ghez et al., 2008; Genzel, Eisenhauer, & Gillessen, 2010; Gillessen et al., 2017; Gravity Collaboration et al., 2017, 2018b, 2019, 2020b; Do et al., 2019a). Due to its close proximity, Sgr A* has the largest angular size of any existing black hole observable from Earth, and provides a unique laboratory for investigating the physical conditions of the matter and the spacetime around the object.

The observed emission from Sgr A* is variable at all wavelengths from the radio to X-rays (e.g., Baganoff et al., 2001; Zhao, Bower, & Goss, 2001; Genzel et al., 2003; Ghez et al., 2004; Eisenhauer et al., 2005; Macquart et al., 2006; Marrone et al., 2008; Eckart et al., 2008b; Do et al., 2009; Witzel et al., 2018; Do et al., 2019b). The simultaneous, large amplitude variations ("flares") seen in the near-infrared (NIR) and X-ray (Yusef-Zadeh et al., 2006; Eckart et al., 2008c) are the result of transiently heated relativistic electrons near the black hole, likely heated in shocks or by magnetic reconnection (Markoff et al., 2001; Yuan, Quataert, & Narayan, 2003; Barrière et al., 2014; Haggard et al., 2019).

The linear polarization fraction of $\simeq 10 - 40\%$ (Eckart et al., 2006; Trippe et al., 2007; Eckart et al., 2008b; Zamaninasab et al., 2010; Shahzamanian et al., 2015) implies that the NIR emission is the result of synchrotron emission from relativistic electrons. The NIR to X-ray spectral shape favours direct synchrotron radiation from electrons up to high energies ($\gamma \sim 10^5$, Dodds-Eden et al., 2009; Li et al., 2015; Ponti et al., 2017), although inverse Compton scenarios may remain viable (Porquet et al., 2003; Eckart et al., 2010; Yusef-Zadeh et al., 2012).

Using precision astrometry with the second generation beam combiner instrument GRAVITY at the Very Large Telescope Interferometer (VLTI) operating in the NIR (Gravity Collaboration et al., 2017), we recently discovered continuous clockwise motion associated with three bright flares from Sgr A* (Gravity Collaboration et al., 2018a, 2020c). The scale of the apparent motion $\simeq 30 - 50$ μas is consistent with compact orbiting emission regions ("hotspots", e.g., Broderick & Loeb, 2005, 2006b; Hamaus et al., 2009) at $\simeq 3 - 5R_S$, where $R_S = 2GM/c^2 \simeq 10$ μas, is the Schwarzschild radius. In each flare, we also find evidence for a continuous rotation of the linear polarization angle. The period of the polarization angle rotation matches that inferred from astrometry. An orbiting hotspot sampling a background magnetic field can explain the polarization angle rotation, as long as the magnetic field configuration contains a significant poloidal component. For a rotating, magnetized fluid, remaining poloidal in the presence of orbital shear implies a dynamically important magnetic field in the flare emission region.

Here we analyze the GRAVITY flare polarization data in more detail, accounting for an improved instrument calibration that now includes the VLTI's response as a function of time (Section 5.2). We find general agreement with our previous results of an intrinsic rotation of the polarization angle during the flare Using numerical ray tracing simulations (Section 5.3), we create mock observations by folding hotspot models forward through the observing process. We compare directly to the data to show that the hotspot model can explain the observed polarization evolution, and to constrain the underlying magnetic field geometry and viewer's inclination (Section 5.4). Matching the observed astrometric period and linear polarization fraction requires a significant poloidal component of the magnetic field structure on horizon scales around the black hole, and an emission size big enough to resolve it. We discuss the implications of our results and limitations of the simple model in Section 5.5.

5.2 GRAVITY Sgr A* flare polarimetry

GRAVITY observations of Sgr A* have been carried out in split-polarization mode, where interferometric visibilities are simultaneously measured in two separate orthogonal linear polarizations. A rotating half-wave plate can be used to alternate between the linear polarization directions P_{00} — P_{90} and P_{-45} — P_{45}. As a function of these polarized feeds, the Stokes parameters as measured by GRAVITY are $I' = (P_{00}+P_{90})/2$, $Q' = (P_{00}-P_{90})/2$ and $U' = (P_{45} - P_{-45})/2$. The circularly polarized component V' cannot be recorded with GRAVITY.

We relate on-sky (unprimed) polarized quantities with their GRAVITY measured (primed) counterparts by

$$\bar{S} = M\ \bar{S}' \tag{5.1}$$

where $\bar{S}$ and $\bar{S}'$ are the on-sky and GRAVITY Stokes vectors respectively, and M is a matrix that characterizes the VLTI's optical beam train response as a function of time, taking into account the rotation of the field of view during the course of the observations and birefringence. The former is calculated from the varying position of the telescopes during the observations and calibrated on sky by observing stars in the Galactic center (Gravity Collaboration et al., 2018a). The latter are newly introduced in the analysis here and are obtained from modelling the effects of reflections on a long optical path through the individual UT telescopes and the VLTI.

During 2018, GRAVITY observed several NIR flares from Sgr A* (Gravity Collaboration et al., 2018a). Figure 5.1 shows the linear polarization Stokes parameters for four of them as measured by the instrument. On the top left, top right and bottom left, the flares on May 27$^{\text{th}}$, June 27$^{\text{th}}$ and July 22$^{\text{nd}}$ are shown respectively. Only Stokes Q' was measured on these nights. For the July 28$^{\text{th}}$ flare (bottom right), both Q' and U' were measured. All of the flares observed during 2018 exhibit a change in the sign of the Stokes parameters during the flare, consistent with a rotation of the polarization angle with time. The linear polarization fractions are $\gtrsim 10 - 40\%$, in agreement with past measurements

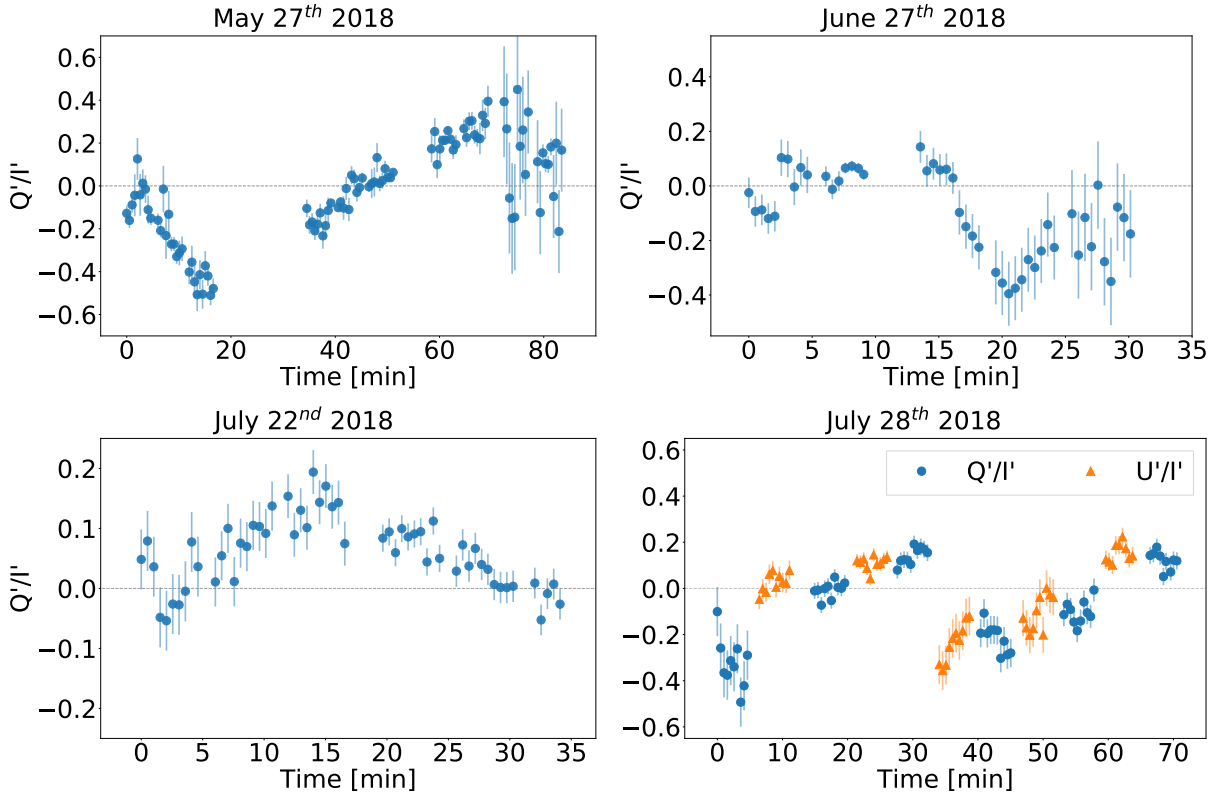

Figure 5.1: Linear polarization Stokes parameters of four Sgr A* NIR flares observed by GRAVITY during 2018. The prime notation denotes the quantities as recorded by the instrument (including effects of field rotation and systematics). Top left: Stokes Q' on May 27$^{\text{th}}$. Top right: Stokes Q' on June 27$^{\text{th}}$. Bottom left: Stokes Q' on July 22$^{\text{nd}}$. Bottom right: Stokes Q' and U' on July 28$^{\text{th}}$. All flares show $\gtrsim 10-40\%$ linear polarization. A common, continuous evolution is seen on all nights. In three cases, Q' shows a change in sign, consistent with rotation of the polarization angle. The implied period of the polarization evolution matches that seen in astrometry.

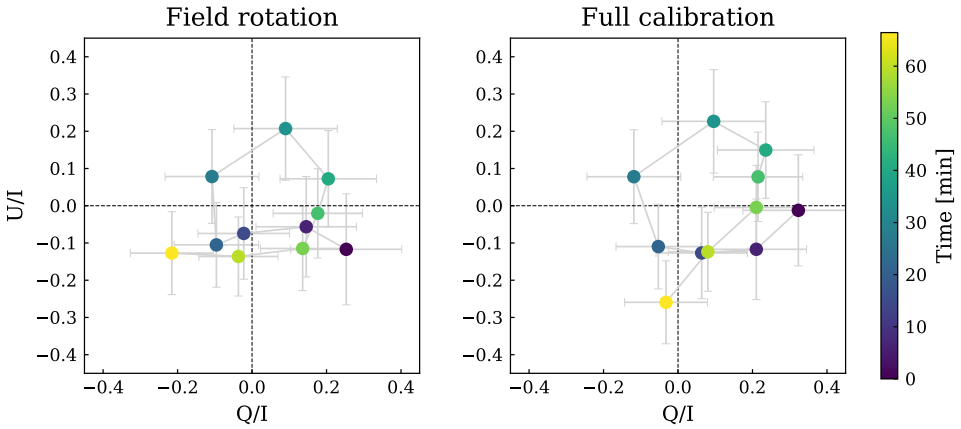

Figure 5.2: Reconstructed evolution of the on-sky linear Stokes parameters in QU space for the July 28$^{\text{th}}$ flare, linearly interpolating to fill in U' and Q' where the other is measured. Color indicates time in minutes. Left: previous calibration where the quantities have been subjected only to a field rotation correction (Gravity Collaboration et al., 2018a). Right: full new calibration including VLTI systematics and Stokes V' reconstruction. In both cases, the flare traces 1.5 loops during its $60 - 70$ minute evolution.

(Eckart et al., 2006; Trippe et al., 2007; Eckart et al., 2008b). Polarization angle swings have also been previously seen in NIR flares with NACO (e.g., Zamaninasab et al., 2010).

The smooth polarization swings in both flares and the July 28$^{\text{th}}$ single loop in U vs. Q ("QU loop", Figure 5.2) support the astrometric result of orbital motion of a hotspot close to event horizon scales of Sgr A*.

Two assumptions have been made in the calculation of this loop. Since GRAVITY cannot register both linear Stokes parameters simultaneously, one has to interpolate the value of one quantity while the other is measured. In the case of Figure 5.2, this has been done by linearly interpolating between the median values over each exposure of $\simeq 5$ min. Second, no circular polarization data are recorded (Stokes V'). This implies that transforming the GRAVITY measured Stokes parameters (primed) to on-sky values (unprimed) requires not only a careful calibration of the instrument systematics (contained in the matrix M, Eq. 5.1), but an assumption on Stokes V'. In Figure 5.2, the assumption is that $V' = 0$. While in theoretical models Stokes $V = 0$ is well justified for synchrotron radiation from highly relativistic electrons, birefrigence in the VLTI will introduce a non-zero V'. It is therefore important to characterize it properly.

In this work, we adopt a forward modelling approach. We take intrinsic Stokes parameters Q and U from numerical calculations of a hotspot orbiting a black hole in a given magnetic field geometry, transform them to the GRAVITY observables Q' and U' following Eq. (5.1), and compare them to the data. This not only allows us to fit the July 28$^{\text{th}}$ polarization data directly without having to make assumptions on Stokes V' or interpolate between gaps of data due to the lack of simultaneous measurements of the Stokes parameters, but to make predictions for Q' when it is the only quantity measured, as is the case

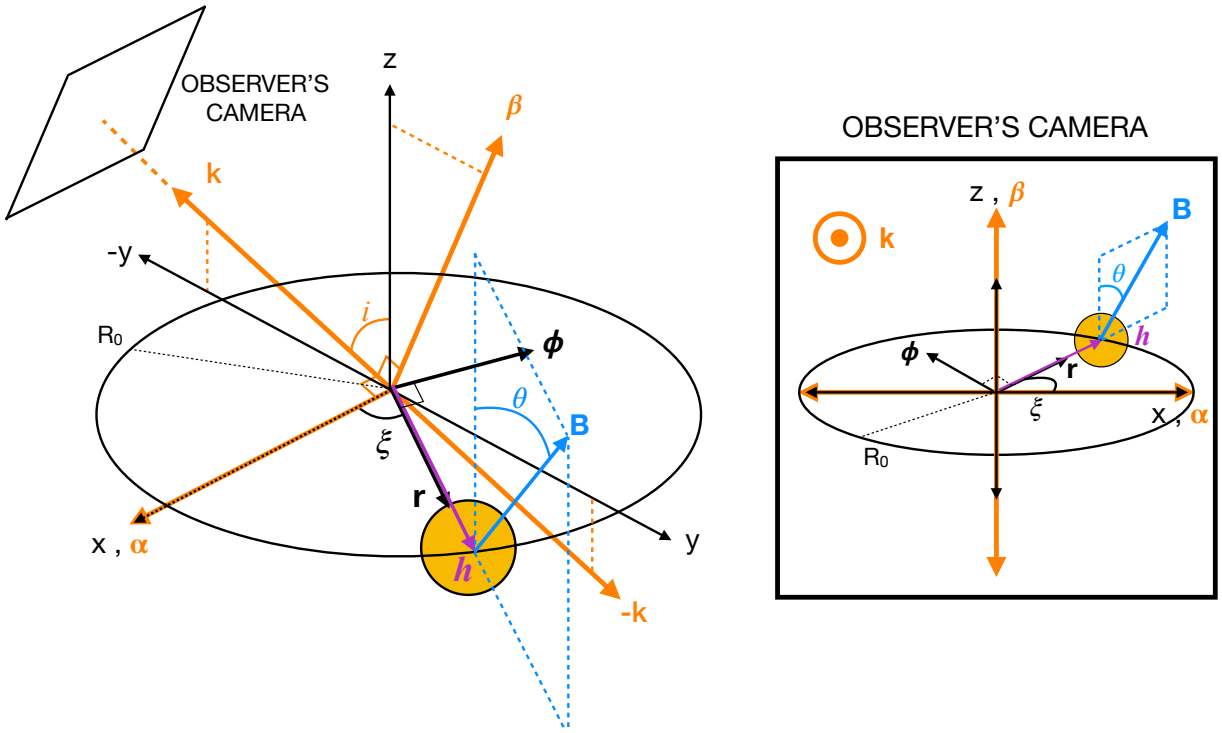

Figure 5.3: Lab frame diagram of a hotspot orbiting in the $\hat{x}\hat{y}$ plane with position vector $\bar{h} = R_0\,\hat{r}$, where $\hat{r}$ is the unit vector in the radial direction. $\bar{h}$ makes an angle $\xi(t)$ with $\hat{x}$. The magnetic field $\bar{B}$ is a function of ξ and consists of a vertical plus radial component. The strength of the latter is given by $\tan\theta$, θ the angle between the vertical and $\bar{B}$. The observer's camera is defined by impact parameters $\hat{\alpha}$, $\hat{\beta}$ and a flat space line of sight $\hat{k}$. The line of sight makes an angle i with the spin axis of the black hole. The observer's view is shown on the right. $\hat{\phi}$ is the unit vector in the azimuthal direction.

for the other 2018 flares.

5.3 Polarized synchrotron radiation in orbiting hotspot models

An optically thin hotspot orbiting a black hole produces time-variable polarized emission depending on the spatial structure of the polarization map (Connors & Stark, 1977). For the case of synchrotron radiation, the polarization traces the underlying magnetic field geometry (Broderick & Loeb, 2005). We first discuss an analytic approximation to demonstrate the polarization signatures generated by a hotspot in simplified magnetic field configurations, before describing the full numerical calculation of polarization maps used for comparison to the data.

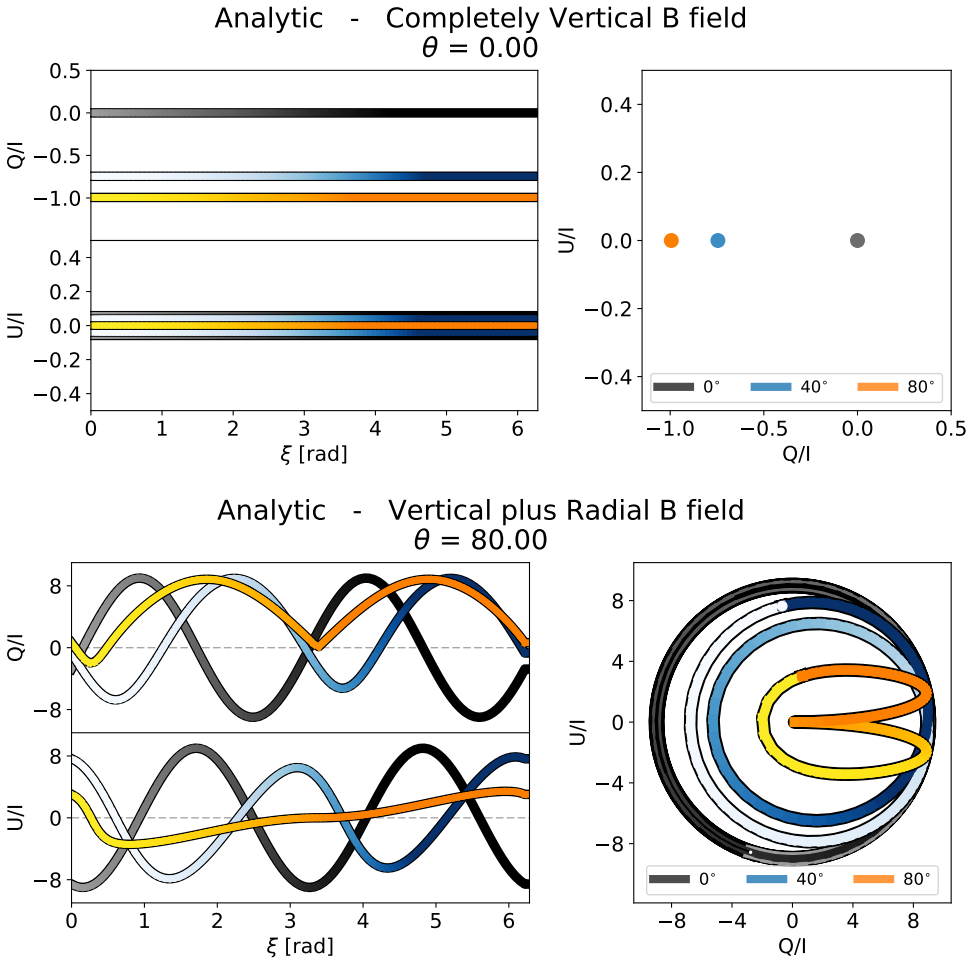

Figure 5.4: Analytic non-relativistic calculations of the linear Stokes parameters Q and U in a vertical plus radial magnetic field at three different viewer inclinations: $i = 0°, 40°, 80°$. The colour gradient denotes the periodic evolution of the hotspot along its orbit, moving from light to dark as the hotpot completes one revolution. The changes in the width of the curves are only to facilitate visualization. Top: completely vertical magnetic field ($\theta = 0$). Q and U are constants in time and have static values in QU space. Bottom: significantly radial magnetic field with $\theta = 80$. Q and U oscillate and trace two QU loops in time that change in amplitude with inclination. High inclination counteracts the presence of QU loops.

5.3.1 Analytic approximation

We define the observer's camera centered on the black hole with impact parameters $\hat{\alpha}$ and $\hat{\beta}$ perpendicular and parallel to the spin axis, with a line of sight direction $\hat{k}$ (Bardeen, Carter, & Hawking, 1973). In terms of these directions and assuming flat space, the Cartesian coordinates are expressed by

$$\hat{x} = \hat{\alpha}, \hat{y} = \cos i\ \hat{\beta} - \sin i\ \hat{k}, \hat{z} = \sin i\ \hat{\beta} + \cos i\ \hat{k}. \tag{5.2}$$

where i is the inclination of the spin axis to the line of sight. Equivalently,

$$\hat{\alpha} = \hat{x}, \hat{\beta} = \cos i\ \hat{y} + \sin i\ \hat{z}, \hat{k} = -\sin i\ \hat{y} + \cos i\ \hat{z}. \tag{5.3}$$

When face-on, $\hat{k}$ points along $\hat{z}$ and $\hat{\beta}$ points along $\hat{y}$. When edge-on, $\hat{k}$ points along $-\hat{y}$ and $\hat{\beta}$ points along $\hat{z}$.

Let a hotspot be orbiting in the $\hat{x}\hat{y}$ plane (Figure 5.3). In terms of $\hat{\alpha}$, $\hat{\beta}$ and $\hat{k}$, the hotspot's position vector $\bar{h}$ is given by

$$\begin{aligned} \bar{h} &= R_0\ \hat{r} \\ &= R_0\ (\cos\xi\ \hat{\alpha} + \cos i \sin\xi\ \hat{\beta} - \sin i \sin\xi\ \hat{k}) \end{aligned} \tag{5.4}$$

where $\hat{r}$ is the canonical radial vector, R_0 is the orbital radius and ξ is the angle between $\hat{\alpha}$ and $\hat{r}$.

Let us consider magnetic field with vertical and radial components given by

$$\bar{B}\ = \frac{B_0}{\sqrt{1+\delta^2}}\ (\hat{z} + \delta\ \hat{r})\ ;\ \delta \equiv \tan\theta \tag{5.5}$$

where B_0 is the magnitude of $\bar{B}$ and θ is the angle between $\hat{z}$ and $\bar{B}$. The polarization is given as $\bar{P} = \hat{k} \times \bar{B}$. In flat space and in the absence of motion (no light bending or aberration),

$$\begin{aligned} \bar{P} &\propto \hat{k} \times (\hat{z} + \delta\ \hat{r}) \\ &\propto\ -(\sin i + \tan\theta \cos i \sin\xi)\ \hat{\alpha} + \tan\theta \cos\xi\ \hat{\beta}\ . \end{aligned} \tag{5.6}$$

The polarization angle on the observer's camera is $\tan\psi = \bar{P}\cdot\hat{\beta}/\bar{P}\cdot\hat{\alpha}$, so that

$$\psi = \tan^{-1}\left(-\frac{\tan\theta\cos\xi}{\sin i + \tan\theta\cos i\sin\xi}\right). \tag{5.7}$$

Given that $U/Q = 1/2\tan\psi$, the Stokes parameters as a function of the polarization angle are

$$Q = |\bar{P}|\cos 2\psi, U = |\bar{P}|\sin 2\psi. \tag{5.8}$$

With equations (5.6), (5.7) and (5.8), Stokes Q and U are obtained.

It is important to note that a single choice of i and θ will return $Q{=}Q(\xi)$ and $U{=}U(\xi)$. Assuming constant velocity along the orbit, the angle ξ can be mapped linearly to a time value by setting the duration of the orbital period and an initial position where the $\xi = 0$.

Additionally, an inclination of $i = i_0 < 90°$ and $i = 180° - i_0$ will produce the same polarized curves but reversed in ξ with respect to each other. This is expected since, for an observer at $i = i_0$ and one at $i = 180° - i_0$, the hotspot will sample the same magnetic field geometry but will appear to be moving in opposite directions with respect to each other. This means that the relative order in which the peaks in Q and U appear will be reversed between observers at $i = i_0$ and at $i = 180° - i_0$.

Given that light bending has not been considered in this approximation, in a significantly vertical field ($\theta \simeq 0$, top of Fig. 5.4) the polarization remains constant in ξ (and time) proportional to $-\sin i$. In QU space, this means a static value as the hotspot goes around the black hole. A particular case of this is $\bar{P} \simeq 0$ at $i \simeq 0$, since $\hat{k}$ and $\bar{B}$ are parallel. As $\theta \to \pi/2$, $\tan\theta \to \infty$ (bottom of Fig. 5.4) and the magnetic field becomes radial. In this case and at low inclinations, the polarization configuration is toroidal ($\bar{P} \propto \hat{\phi}$, the azimuthal canonical vector, Eq. 5.14). As the hotspot orbits the black hole, Q and U will show oscillations of the same amplitude. In one revolution, two superimposed QU loops will be traced. If the viewer's inclination increases, one of the loops decreases more in size than the other and eventually disappears at very high inclinations, leaving only one behind. Increasing inclination, therefore, counteracts the presence of QU loops in an analytical model with a vertical plus radial magnetic field.

It is noted that the normalized polarization configurations of a completely radial magnetic field and a toroidal one are equivalent with just a phase offset of 90° in ξ (Eq. 5.15 in Appendix 5.5).

5.3.2 Ray tracing calculations

Next, we use numerical calculations to include general relativistic effects. We use the general relativistic ray tracing code `grtrans` (Dexter & Agol, 2009; Dexter, 2016) to calculate synchrotron radiation from orbiting hotspots in the Kerr metric.

The hotspot model is taken from Broderick & Loeb (2006b), and consists of a finite emission region orbiting in the equatorial plane at radius R_0. The orbital speed is constant for the entire emission region, and matches that of a test particle motion at its center. The maximum particle density $n_{\rm spot} \sim 2 \times 10^7\,{\rm cm}^{-3}$ falls off as a three-dimensional Gaussian with characteristic size $R_{\rm spot}$. The magnetic field has a vertical plus radial component[1]. Its strength is taken from an equipartition assumption, where we further assume a virial ion temperature of $kT_i = (n_{\rm spot}/n_{\rm tot})\ (m_p c^2/R)$, $(n_{\rm spot}/n_{\rm tot}) = 5$, where $n_{\rm tot}$ is the total particle density in the hotspot. For the models considered here, a typical magnetic field strength in the emission region is $B \simeq 100$ G. We calculate synchrotron radiation from a power law distribution of electrons with a minimum Lorentz factor of 1.5×10^3 and

[1] See Appendix 5.5 for details.

consider a black hole with spin zero[2]. The model parameters for field strength, density, and minimum Lorentz factor are chosen as typical values for models of Sgr A* which can match the observed NIR flux. Other combinations are possible.

Example snapshots of a hotspot model in a vertical field ($\theta = 0$) and the resulting polarization configuration are shown in Figure 5.5. The effects of lensing can be appreciated in the form of secondary images. It can be seen as well that as the hotspot moves along its orbit around the black hole, it samples the magnetic field geometry in time, so that the time-resolved polarization encodes information about the spatial structure of the magnetic field.

Figure 5.6 shows the numeric calculations of hotspot models with the same magnetic field angles as those in the analytic approximation. Inclination and θ are key parameters in the observed number and shape of QU loops. In contrast to the analytic case, in a significantly vertical field ($\theta \simeq 0$, top of Fig. 5.6) the polarization is not zero. This is due mainly to light bending, which introduces an effective radial component to the wave-vector in the plane of the observer's camera. This radial component of $\hat{k}$ leads to an additional azimuthal contribution to $\bar{P}$. The $\theta = 0$ cases show that this effect alone is able to generate QU loops. We see again that increasing inclination leads to a change from two QU loops per hotspot revolution at low inclinations to a single QU loop at high inclinations.

The cases where $\theta \to 90°$ (bottom of Fig. 5.6), show that increasing this parameter also leads to scenarios with two QU loops per hotspot orbit. The shape of the numerical Q and U curves is similar to the analytic versions. The differences are due to the inclusion of relativistic effects in the ray tracing calculations.

We note that numerical models with a vertical plus toroidal magnetic field show similar features and behaviour to those in the vertical plus radial case (see Appendix 5.5).

5.4 Model fitting

We calculate normalized Stokes parameters Q/I and U/I from ray tracing simulations of a grid of hotspot models, fold them through the instrumental response (Eq. 5.1), and compare them to GRAVITY's measured Q'/I' and U'/I'. The parameters of the numerical model are the orbital radius R_0, the size of the hotspot $R_{\rm spot}$, the viewing angle i and the tilt angle of the magnetic field direction θ.

We understand qualitatively how the hotspot size and the orbital radius affect the Q and U curves. "Smoother" curves, where the amplitude of the oscillations is reduced, are produced either with increasing hotspot sizes at fixed orbital radius or with decreasing R_0 at fixed hotspot size, due to beam depolarization (see Appendix 5.5). Since performing full ray tracing simulations is computationally very expensive, and due to the fact that the curves change smoothly and gradually with R_0 and $R_{\rm spot}$, we choose to fix their values to $R_0 = 8R_g$ and $R_{\rm spot} = 3R_g$, R_g the gravitational radius. We then scale them in both period and amplitude to match the data better in the following manner.

[2]Given the scales at which the hotspot is orbiting, a change in the spin of the black hole does not alter the results significantly. See Appendix 5.5 for more details.

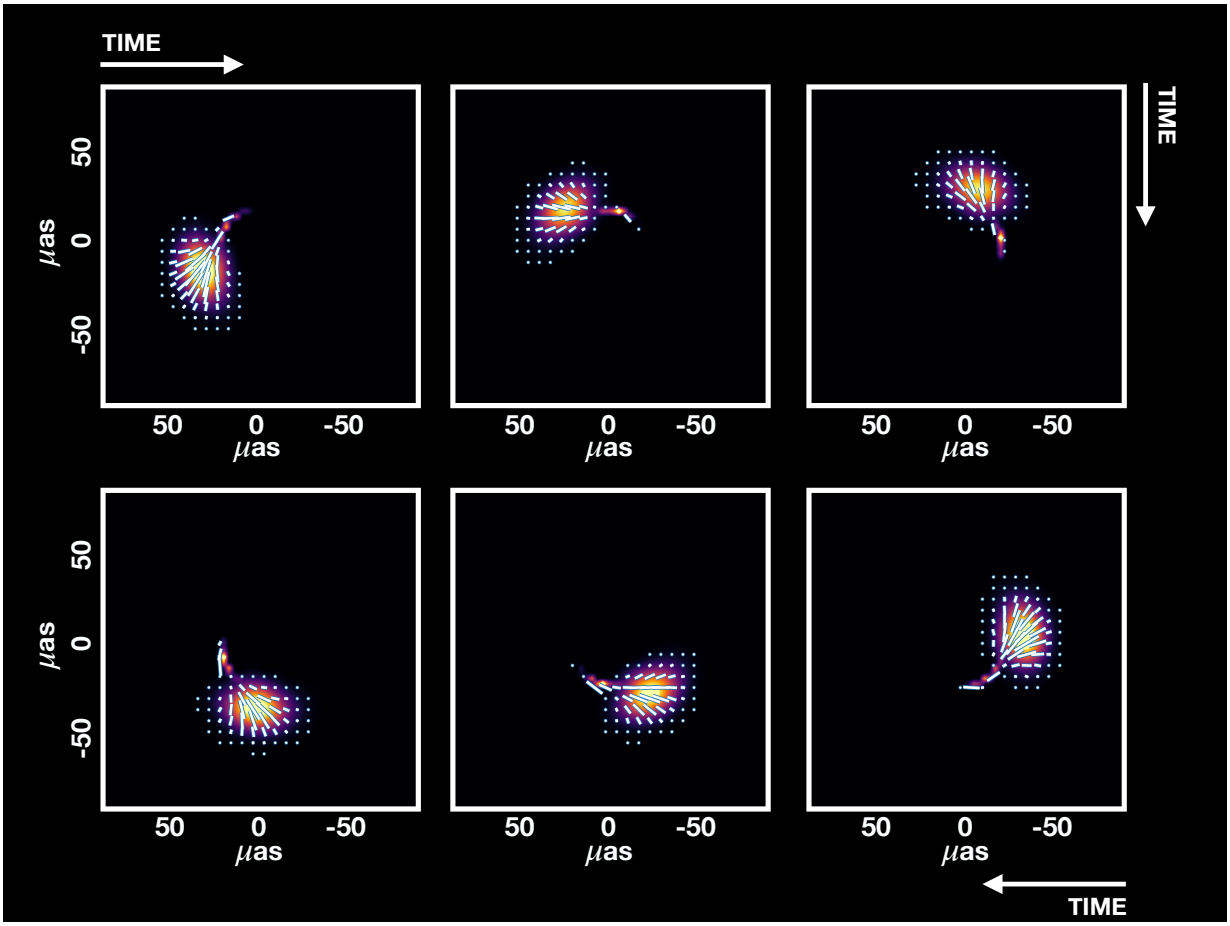

Figure 5.5: Snapshots of the hotspot as it orbits the black hole clockwise on sky in a vertical magnetic field. The orbital radius is eight gravitational radii. Total intensity is shown as false color in the background. Polarization direction is shown as white ticks in the foreground. Their length is proportional to the linear polarization fraction in that pixel. The hotspot samples the magnetic field geometry in time as it moves along the orbit, so that the time-resolved polarization encodes information about the spatial structure of the magnetic field.

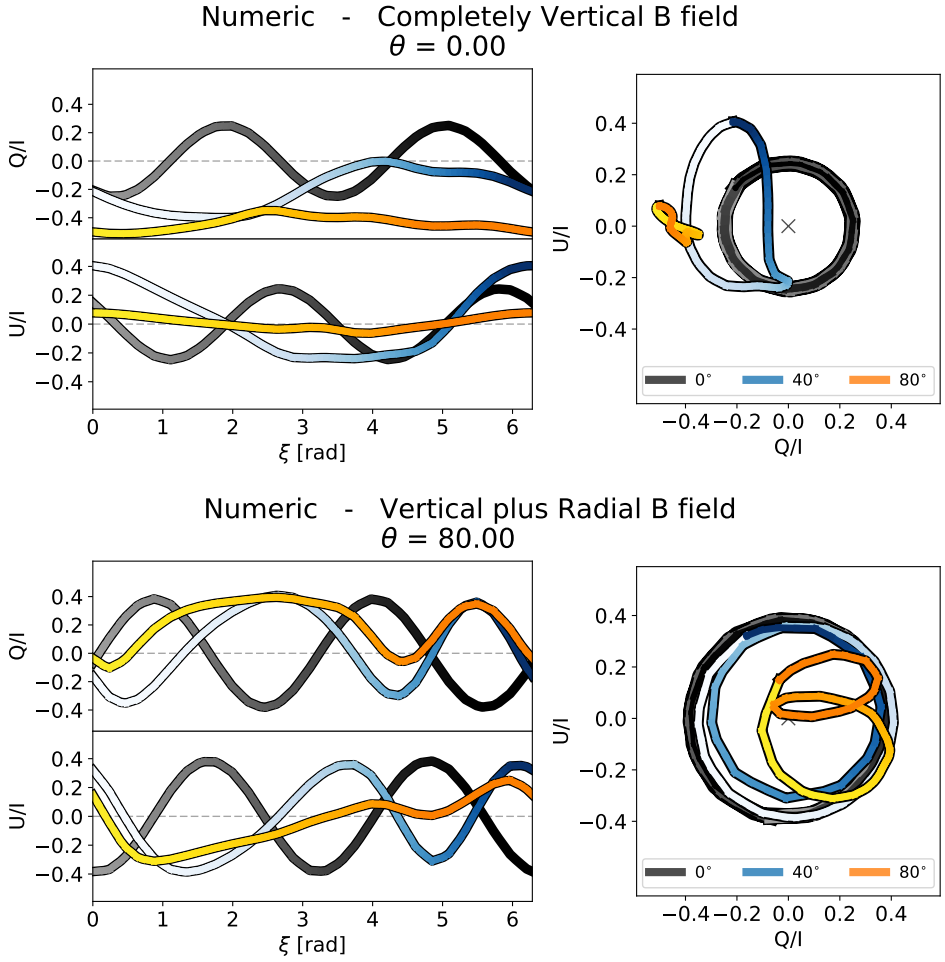

Figure 5.6: Ray tracing calculations of the linear Stokes parameters Q and U in a vertical plus radial magnetic field with the same θ as those in the analytic model. The coarse QU loops are due to the time sampling in our simulations. Top: magnetic field inclination of $\theta = 0$ (completely vertical). Bottom: significantly radial magnetic field ($\theta = 80$). In contrast to the analytic case, numerical calculations in a completely vertical magnetic field at low inclinations show that Q and U oscillate in time and trace loops in QU space due to light bending.

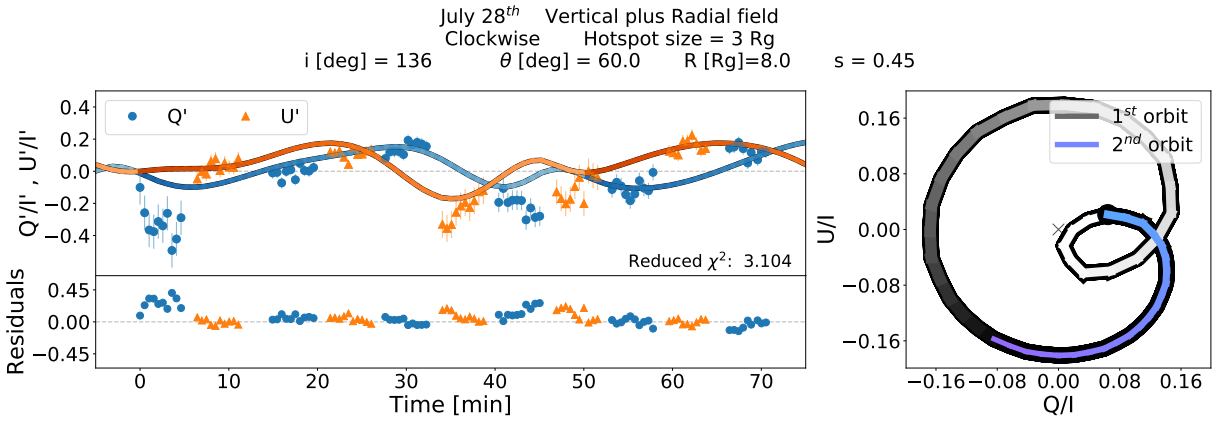

Figure 5.7: Best fit to the July 28th NIR flare. The color gradient denotes the periodic evolution of the hotspot along its orbit, moving from darker shades to lighter as the hotpot completes one revolution. The curves qualitatively reproduce the data. The preferred parameter combination favours a radius of 8 R_g, both moderate i and θ values.

Given the duration of a flare Δt, we can scale a hotspot's period by a factor nT to set the fraction of orbital periods that fit into this time window. The new radius of the orbit is then $R \propto (\Delta t/nT)^{2/3}$. This rescaling introduces small changes in fit quality compared to re-calculating new models, within our parameter range of interest (see Appendix 5.5). We absorb the effect of beam depolarization into a factor s that scales the overall amplitude of both Q and U and therefore, the linear polarization fraction as well.

Given a hotspot's period, the relative phase reflects the hotspot position relative to an initial position measured at some initial time, where the phase is defined to be zero. We choose the initial position of the hotspot based on the astrometric measurement of the orbital motion of the flare in Gravity Collaboration et al. (2020c). Specifically, we choose the initial phase ξ to match the initial position of the best-fit orbital model to the astrometry.

5.4.1 Application to the July 28th flare

The observed Q'/I' and U'/I' are measured from fitting interferometric binary models to GRAVITY data. The binary model measures the separation of Sgr A* and the star S2, which were both in the GRAVITY interferometric field of view ($\simeq$ 50 mas) during 2018. For more details see Gravity Collaboration et al. (2020d). We measure polarization fractions assuming that S2's NIR emission is unpolarized. The 70 minute time period analyzed is limited by signal-to-noise: binary signatures were largest when Sgr A* is brightest. As a result, we focus on data taken during the flare. We fit to data binned by 30 seconds, since the flux ratio can be rapidly variable. We further adopt error bars on polarization fractions using the rms of measurements within 300s time intervals, since direct binary model fits generally have $\chi^2 > 1$ and as a result underestimate the fit uncertainties.

We compute a grid of models with i, θ, s and nT as parameters: $i \in [0 - 180]$ in increments of $\Delta i = 4°$; $\theta \in [0 - 90)$, $\Delta\theta = 4°$; $s \in [0.4 - 0.8]$, $\Delta s = 0.05$ and nT such that the allowed range of radii for the fit is $R = 8 - 11\ R_g$ with $\Delta R = 0.2$. We have included this prior in radii to match the constraint from the combined astrometry of the three bright GRAVITY 2018 flares (Gravity Collaboration et al., 2020c). The best fit parameters and corresponding polarized curves are shown in Figure 5.7. We find that the curves qualitatively reproduce the data and that the statistically preferred parameter combination for July 28$^{\rm th}$, with a reduced $\chi^2 \sim 3.1$, favours a radius of 8 R_g and moderate i and θ values (left panel of Figure 5.7). In QU space, these parameters produce two intertwined/embedded QU loops of very different amplitudes in time (right panel of Figure 5.7). The outer one is fairly circular, centred approximately around zero and with an average radius of 0.18. The inner one has a horizontal oblate shape with a QU axis ratio of approximately 2:1, does not go around zero and represents a much smaller fraction of the orbit than the larger loop. These moderate values of θ imply that a magnetic field with significant components in both the radial and vertical directions is favored.

The hotspot is free to trace a clockwise ($i > 90°$) or counter clockwise ($i < 90°$) motion on-sky. At fixed θ, this change in apparent motion results in an inversion of the order in which the maxima of the Q and U curves appear[3]. This effect is due to relativistic motion (Blandford & Königl, 1979; Bjornsson, 1982). When the magnetic field is purely toroidal (velocity parallel to $\bar{B}$), the polarization angle is independent of velocity. When there is a field component perpendicular to the velocity (poloidal field), relativistic motion induces an additional swing of the polarization angle in the direction of movement whose magnitude depends on the velocity. We ignore this effect in the analytic approximation above, but it is included in our numerical calculations.

The data favour models where the maxima in U'/I' precede those of Q'/I'. This behaviour is observed in the case of clockwise motion ($i > 90°$) with $\theta \in [0° - 90°]$ and in counter clockwise motion ($i < 90°$) with $\theta \in [90° - 180°]$. In fact, model curves at a given $i > 90°$ and $\theta \in [0° - 90°]$ are identical to those with their "mirrored" values $i' = 180° - i$ and $\theta' = 180° - \theta$. In our analysis we consider $\theta \in [0° - 90°]$, which favours clockwise motion. However, we cannot uniquely determine the apparent direction of motion of the hotspot due to this degeneracy.

Our models overproduce the observed linear polarization fraction by a factor of ~ 1.7 (scaling factor $s \simeq 0.4 < 1$). The maximum observed polarization fraction is $\simeq 30\%$, while in our models it is $\simeq 50\%$. The degree of depolarization introduced by the VLTI is not enough to reduce the model linear polarization fraction to the observed one. Moreover, in the NIR there are no significant depolarization contributions from absorption or Faraday effects. As a result, we conclude that the low observed polarization fraction is likely the result of beam depolarization. The observed low polarization fraction implies that the flare emission region is big enough to resolve the underlying magnetic field structure. In the context of our model, this could imply a larger spot size. It could also indicate a degree of

[3] This is also equivalent to an inversion of the curve in time and does not modify the features of the curve.

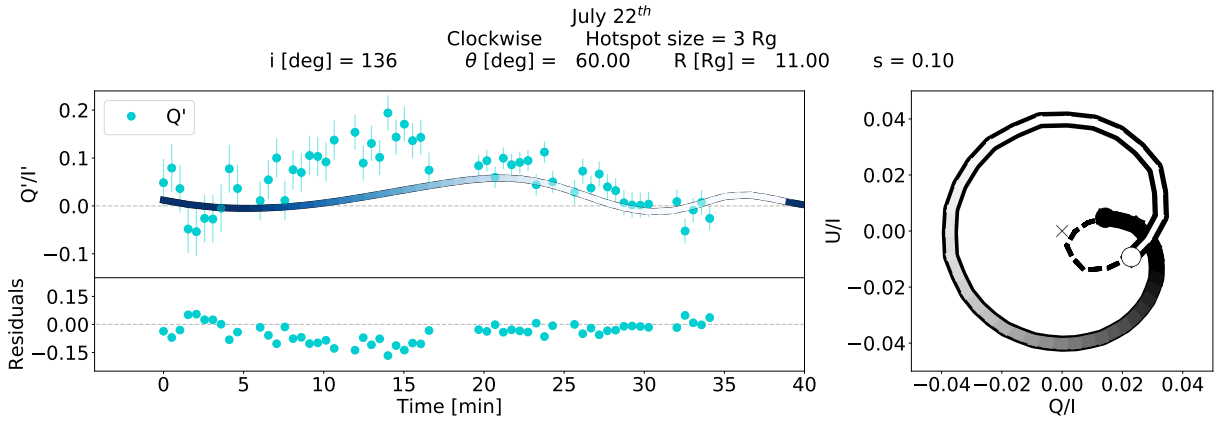

Figure 5.8: Fit to the July 22nd NIR flare without restricting the phase difference between this night and July 28th. The color gradient denotes the evolution of the hotspot as it completes one revolution. The viewer's inclination, magnetic field geometry and orbital direction have been fixed to the values found from the for to the July 28th flare. The fit favours values of $R_0 \sim 11\ R_g$ and no initial phase difference between the nights (no difference in starting position on-sky), which is out of the allowed uncertainty range for the astrometry.

disorder in the background magnetic field structure, for example as a result of turbulence.

5.4.2 Application to the July 22nd flare

July 28th is the only night with an observed infrared flare in which GRAVITY recorded both Stokes Q' and U'. Since a single polarization channel is insufficient to constrain the full parameter space used in our numerical models, we restrict ourselves to the night of July 22nd, as this observation has the highest precision astrometry[4], and fix the viewer inclination and magnetic field geometry to be the same as the best fit model to the July 28th data. We scale the curves in amplitude with $s \in [0.05 - 0.35]$, $\Delta s = 0.05$.

The initial position on sky for both flares is constrained by astrometric data, and therefore, so is the phase offset between both curves. With a fixed phase difference between the curves and free range of radii, we find that the July 22nd data favours extremely large values of $R_0 > 20\ R_g$, outside of the allowed range obtained from astrometric measurements. Allowing the phase difference to be free and constraining the radii to $8 - 11\ R_g$, with $\Delta R = 0.2$, we find that the data tends to values of $R_0 \sim 11\ R_g$ and a phase difference between curves of 0° (Figure 5.8). This phase difference value (and position difference associated with it) is outside of the allowed uncertainties in the initial position indicated by the astrometric data.

[4]The astrometry of the May 27th and June 27th flares is not good enough pin point their starting location on sky, so it is not possible to restrict at all the phase difference between them and the July 28th flare.

The fact that the magnetic field parameters that describe the July 28$^{\text{th}}$ flare fail to adequately fit the data from July 22$^{\text{nd}}$ may indicate that the background magnetic field geometry changes on a several-day timescale.

5.5 Summary and discussion

In this work we present an extension of the initial analysis of polarization data performed in Gravity Collaboration et al. (2018a).

We forward model Q and U Stokes parameters obtained from ray tracing calculations of a variety of hotspot models in different magnetic field geometries, transform them into quantities as seen by the instrument and fit directly to the polarized data taken with GRAVITY.

This allows us to not only fit data directly without assumptions on Stokes V or the interpolation of data in non-simultaneous Q and U measurements, but also predict the behaviour in time of the polarized curves and loops for the cases where only one of the parameters is measured.

We have shown that the hotspot model serves to qualitatively reproduce the features seen in the polarization data measured with GRAVITY. Moderate inclination and moderate mix of both vertical and radial fields provide the best statistical fit to the data. Consistent results are found by fitting the data with a vertical plus toroidal field component (Appendix 5.5). We note that this result does not rely on the assigned strength of the magnetic field, since the model curves are scaled in amplitude, but rather it is only from the geometry of the field. Magnetic fields with a non-zero vertical component fit the data statistically better. This supports the idea that there is some amount of ordered magnetic field in the region near the event horizon with a significant poloidal field component. The presence of this component is associated with magnetic fields which are dynamically important and confirms the previous finding of strong fields in Gravity Collaboration et al. (2018a). Matching the clockwise direction of motion inferred by the astrometric data would require that $\theta \in [0° - 90°]$. Under this assumption, the results are also in accordance with the angular momentum direction and orientation of the clockwise stellar disk and the gas cloud G2 (Bartko et al., 2009; Gillessen et al., 2019; Pfuhl et al., 2015; Plewa et al., 2017).

We have chosen the bright NIR flare on July 28$^{\text{th}}$ 2018 since it is the only one for which both linear Stokes parameters have been measured. Naturally, increasing the number of full data sets in future flares will be useful in constraining the parameter range more.

Our models overproduce the observed NIR linear polarization fraction of $\sim 30\%$ by a factor of ~ 1.7, and must be scaled down to fit the data. In the compact hotspot model context, this implies that an emission region size larger than 3 R_g is needed to depolarize the NIR emission through beam depolarization. Including shear in the models would naturally introduce depolarization since a larger spread of polarization vector directions (or equivalently magnetic field structure) would be sampled at any moment (e.g., Gravity Collaboration et al., 2020c; Tiede et al., 2020). However, this might smooth out the fitted curves and would probably change the fits. In any case, the observed low NIR polarization

fraction means that the observed emission region resolves the magnetic field structure around the black hole.

Though simplistic, the hotspot model appears to be viable for explaining the general behaviour of the data. It would be interesting to study the polarization features of more complex total emission scenarios explored in other work. Ball et al. (2020) study orbiting plasmoids that result of magnetic reconnection events close to the black hole, where some variability in the polarization should be caused by the reconnecting field itself. Dexter et al. (2020b) found that material ejected due to the build up of strong magnetic fields close to the event horizon can produce flaring events where the emission region follows a spiral trajectory around the black hole. In their calculations, ordered magnetic fields result in a similar polarization angle evolution as we have studied here. Disorder caused by turbulence reduces the linear polarization fraction to be consistent with that observed.

Spatially resolved polarization data are broadly consistent with the predicted evolution in a hotspot model. This first effort comparing such models directly to GRAVITY data shows the promise of using the observations to study magnetic field structure and strength on event horizon scales around black holes.

Acknowledgements

JD is pleased to thank D.P. Marrone, J. Moran, M.D. Johnson, G.C. Bower, and A.E. Broderick for helpful discussions related to signatures of orbital motion around black holes from polarized synchrotron radiation. We thank the anonymous referee for their constructive comments. This work was supported by a CONACyT/DAAD grant (57265507) and by a Sofja Kovalevskaja award from the Alexander von Humboldt foundation. A.A. and P.G. were supported by Fundação para a Ciência e a Tecnologia, with grants reference UIDB/00099/2020 and SFRH/BSAB/142940/2018.

Appendix A: Vertical plus radial field in Boyer-Lindquist coordinates

In Boyer-Lindquist coordinate frame, a magnetic field with a vertical plus radial components can be written as:

$$\begin{aligned} \underline{B} &= (B^t,\ B^r,\ B^\theta,\ B^\phi) \\ &= (B^t,\ \delta_c B^\theta,\ B^\theta,\ 0) \end{aligned} \tag{5.9}$$

where B^μ are the contravariant components of $\underline{B}$ and $\delta_c \equiv B^r/B^\theta$. The magnetic field must satisfy the following conditions:

$$\begin{aligned} B_\mu u^\mu &= g_{\mu\nu} B^\nu u^\mu = 0 \\ B_\mu B^\mu &= g_{\mu\nu} B^\nu B^\mu = B^2 \end{aligned} \tag{5.10}$$

where u^μ are the contravariant components of the four-velocity, B is the magnitude of $\underline{B}$ and $g_{\mu\nu}$ are the covariant components of the Kerr metric. In Boyer-Lindquist coordinates with $G = c = M = 1$, the non-zero components of the metric are:

$$\begin{aligned} g_{tt} &= -\left(1 - \frac{2r}{\Sigma}\right) \\ g_{rr} &= \frac{\Sigma}{\Delta} \\ g_{\theta\theta} &= \Sigma \\ g_{t\phi} &= g_{\phi t} = -\frac{2r}{\Sigma} a \sin^2\theta \\ g_{\phi\phi} &= \left[r^2 + a^2 + \frac{2ra^2}{\Sigma}\sin^2\theta\right]\sin^2\theta \end{aligned} \tag{5.11}$$

where

$$\begin{aligned} \Delta &\equiv r^2 - 2r + a^2 \\ \Sigma &\equiv r^2 + a^2\cos^2\theta \end{aligned}$$

with a the dimensionless angular momentum of the black hole.

Using Eq. (5.9), (5.10) and (5.11), it follows that the Boyer-Lindquist coordinate frame contravariant components of the magnetic field are

$$\begin{aligned} &B^t = -CB^\theta; \\ &B^r = \delta_c B_\theta = B_\theta\ \delta_{LNRF}/r; \\ &B^\theta = B\ (g_{tt}C^2 + g_{rr}\delta_c^2 + g_{\theta\theta})^{-1/2}; \\ &B^\phi = 0; \\ &\text{with} \\ &\quad C \equiv \frac{\delta_c g_{rr} u^r + g_{\theta\theta}u^\theta}{g_{tt}u^t + g_{t\phi}u^\phi}() \\ &\text{and} \\ &\quad \delta_c = \delta_{LNRF}/r \quad ; \quad \delta_{LNRF} = \frac{B^{(r)}}{B^{(\theta)}} \end{aligned} \tag{5.12}$$

where δ^{LNRF} is the ratio of the radial and poloidal magnetic field components in the locally-non rotating frame (LNRF, Bardeen, Carter, & Hawking, 1973) and $B^{(\mu)}$ are the contravariant components of $\underline{B}$ in the LNRF:

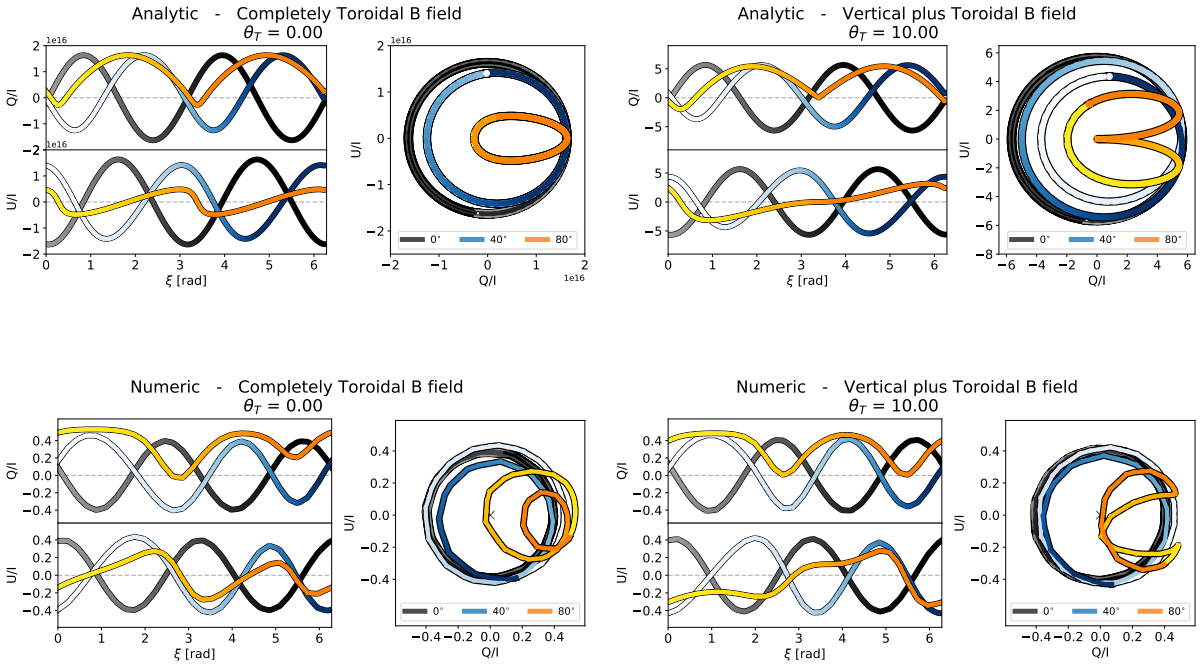

Figure 5.9: Analytic and ray tracing calculations of Q and U curves in the case of a toroidal magnetic field. Two loops are always observed. In the case of the analytic case (top), both are superimposed. This is broken by the accounting for light bending in the ray tracing calculations (bottom). It can also be seen that toroidal and completely radial configurations produce the same curves, save for a a scaling factor and a phase offset.

$$
\begin{aligned}
B^{(t)} &= (\Sigma\Delta/A)^{1/2} B^t \sim B^t; \\
B^{(r)} &= (\Sigma/\Delta)^{1/2} B^r \sim B^r; \\
B^{(\theta)} &= \Sigma^{1/2} B^\theta \sim r B^\theta; \\
B^{(\phi)} &= -\frac{2ra\sin\theta}{(\Sigma A)^{1/2}} B^t + (A/\Sigma)^{1/2} \sin\theta B^\phi \sim r\sin\theta B^\phi;
\end{aligned}
\tag{5.13}
$$

with

$$A \equiv (r^2 + a^2)^2 - a^2\Delta\sin^2\theta.$$

where the expression to the far right is obtained by assuming $r \gg a$ (as it is in the hotspot case). The variable δ used in the main text (Eq. (5.5)) corresponds to $\delta_{\rm LNRF}$ defined here, as calculated using the $r \gg a$ approximation.

Appendix B: Analytic approximation with a vertical plus toroidal magnetic field

In the case of a vertical plus toroidal magnetic field, the magnetic field can be written as $\bar{B} \propto \hat{z} + \lambda\hat{\phi}$, where $\lambda \propto \tan\theta_T$ is the strength of the toroidal component, θ_T is the angle measured from the toroidal component to the vertical component ($\theta_T = 0$ denotes a completely toroidal field), and

$$\hat{\phi} = -\sin\xi\ \hat{\alpha} + \cos i\cos\xi\ \hat{\beta} - \sin i\cos\xi\ \hat{k} \tag{5.14}$$

is the canonical vector in the azimuthal direction (Figure 5.3). Note that $\hat{r}\cdot\hat{\phi} = 0$.

The polarization vector in a flat space given by $\hat{k}\times\bar{B}$ is then

$$\bar{P} \propto -(\sin i + \lambda\cos i\cos\xi)\ \hat{\alpha} - \lambda\sin\xi\ \hat{\beta} \tag{5.15}$$

and the polarization angle is given by

$$\psi = \tan^{-1}\left(\frac{\lambda\sin\xi}{\sin i + \lambda\cos i\cos\xi}\right). \tag{5.16}$$

It can be seen from expression (5.15) that at low inclinations or when $\lambda >> 1$ (complete toroidal magnetic field), the polarization has a radial configuration ($\bar{P} \propto \hat{r}$, Eq. 5.4). This is geometrically equivalent to the polarization having a toroidal configuration (like the one generated by a completely radial magnetic field, see Section 5.3) with a phase offset of $\pi/2$ in Q and U. In this case, we would expect to have two superimposed QU loops in one revolution of the hotspot.

Figure 5.9 shows a comparison between the analytic (top) and numeric (bottom) calculations for a vertical plus toroidal magnetic field (Appendix 5.5). As expected, in the analytic case there are always two superimposed loops in QU space in the case of a completely toroidal field. In the numeric calculations this is also the case given that light bending favours the presence of loops. As a vertical component in the field is introduced, the loops no longer overlay on each other. This effect increases with viewer inclination. It can also be seen that the toroidal and completely radial case produce the same Q and U curves at low inclinations, save for a phase offset and scaling factor.

Appendix C: Vertical plus toroidal field in Boyer-Lindquist coordinates

In Boyer-Lindquist coordinate frame, a magnetic field with a vertical plus toroidal components can be written as:

$$\begin{aligned}\underline{B} &= (B^t,\ B^r,\ B^\theta,\ B^\phi)\\ &= (B^t, 0,\ \eta_c B^\theta, B^\phi)\end{aligned} \tag{5.17}$$

where B^μ are the contravariant components of $\underline{B}$ and $\eta_c \equiv B^\theta/B^\phi$. Just like in the vertical plus radial case, the magnetic field must satisfy Eqs. (5.10).

Using Eqs. (5.17), (5.10) and (5.11), it follows that the Boyer-Lindquist coordinate frame contravariant components of the magnetic field are

$$\begin{aligned} B^t &= B^\theta/C; \\ B^r &= 0; \\ B^\theta &= \frac{\sqrt{A}}{\rho}\eta_{LNRF}\sin\theta(C-\omega)B^t; \\ B^\phi &= \frac{C\ B}{\sqrt{g_{tt}+2g_{t\phi}C+g_{\theta\theta}\frac{B^\theta}{B^t}+g_{\phi\phi}C^2}}; \end{aligned} \tag{5.18}$$

with

$$C \equiv -\frac{g_{tt}u^t+g_{t\phi}u^\phi}{g_{t\phi}u^t+g_{\phi\phi}u^\phi} \quad ; \quad \omega = \frac{2ra}{A}; \tag{5.19}$$

$B^{(\mu)}$ are the contravariant components of $\underline{B}$ in the LNRF (Eq. (5.12)), $\eta_{LNRF} = B^{(\theta)}/B^{(\phi)} = \tan\theta_T$ the ratio of the poloidal and toroidal magnetic field components in the LNRF and θ_T is the angle measured from the toroidal component to the vertical ($\theta_T = 0$ implies a completely toroidal field, Appendix 5.5).

We have fit the July 28$^{\text{th}}$ data considering this magnetic geometry. Just like in the vertical plus radial case, we compute a grid of models with i, θ, s and nT as parameters: $i \in [0-180]$ in increments of $\Delta i = 4°$; $\theta_T \in [0-90]$, $\Delta\theta_T = 5°$; $s \in [0.4-0.8]$, $\Delta s = 0.05$ and nT such that the allowed range of radii for the fit is $R = 8-11\ R_g$ with $\Delta R = 0.2$. The best fit is shown in Figure 5.10. Though a better reduced χ^2 is found at a somewhat higher inclination than the best fit with a vertical plus radial magnetic field (Fig. 5.7), the presence of a poloidal component in the magnetic field is still needed. Considering $\theta_T \in [0°-90°]$, clockwise motion is preferred ($i > 90°$). Identical curves can be obtained when the direction of motion is counter clockwise ($i < 90°$) and the magnetic field angle is $\theta'_T = 180° - \theta_T$.

Figure 5.11 presents a model of a vertical plus toroidal magnetic field with similar parameters to those of the vertical plus radial field best fit.

Appendix D: Spin effects

We present the effects of spin in our calculations. Figure 5.12 shows three models with the best fit parameters found for the July 28$^{\text{th}}$ flare, at three different dimensionless spin values a=$0.0, 0.9, -0.9$. The corresponding reduced χ^2 values are reported in Table 5.1. It can be seen that changes in spin do not alter the curves significantly and can therefore be ignored.

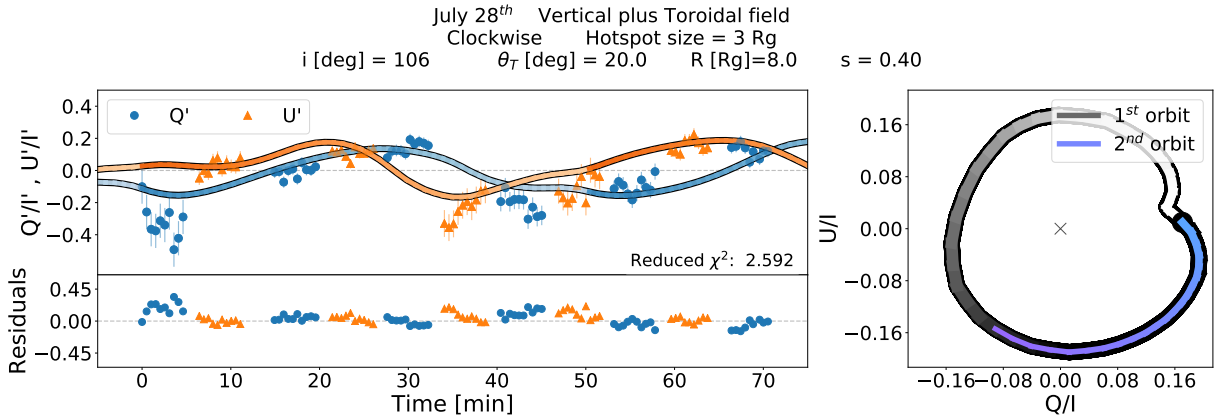

Figure 5.10: Best fit to the July 28$^{\text{th}}$ flare with a vertical plus toroidal magnetic field. The color gradient denotes the periodic evolution of the hotspot along its orbit, moving from darker shades to lighter as the hotpot completes a revolution. Considering $\theta_T \in [0° - 90°]$, clockwise motion is preferred. The fit has a smaller reduced χ^2 at slightly higher inclination than the best fit with a vertical plus radial field. The presence of a vertical component in the magnetic field is still required to fit the data better.

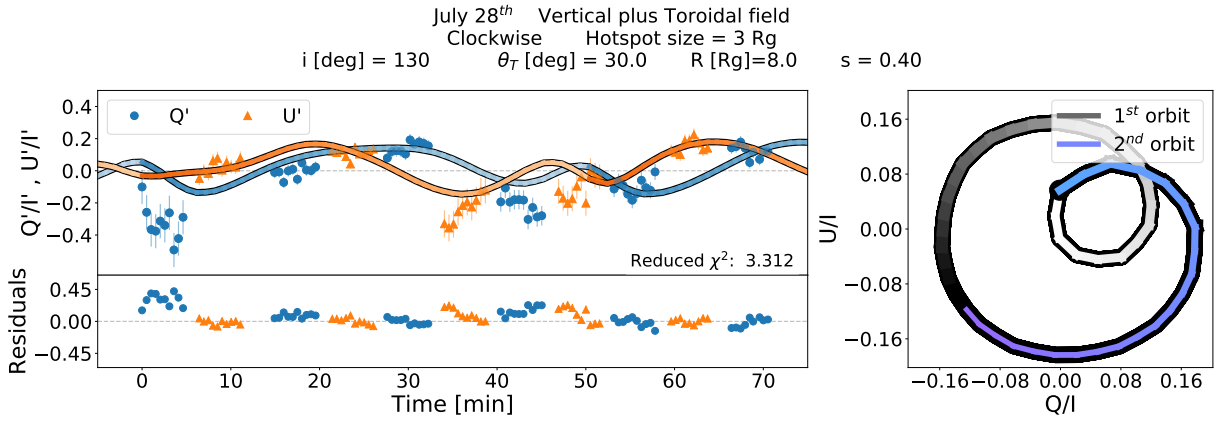

Figure 5.11: Vertical plus toroidal model fit with similar parameters to those of the best fit with a vertical plus radial field.

Table 5.1: Reduced χ^2 of best fit of the July 28$^{\text{th}}$ flare data with three dimensionless spins: $0.0, 0.9, -0.9$.

R [R_g]	a	χ^2
8.0	0.0	3.104
8.0	0.9	3.194
8.0	−0.9	3.080

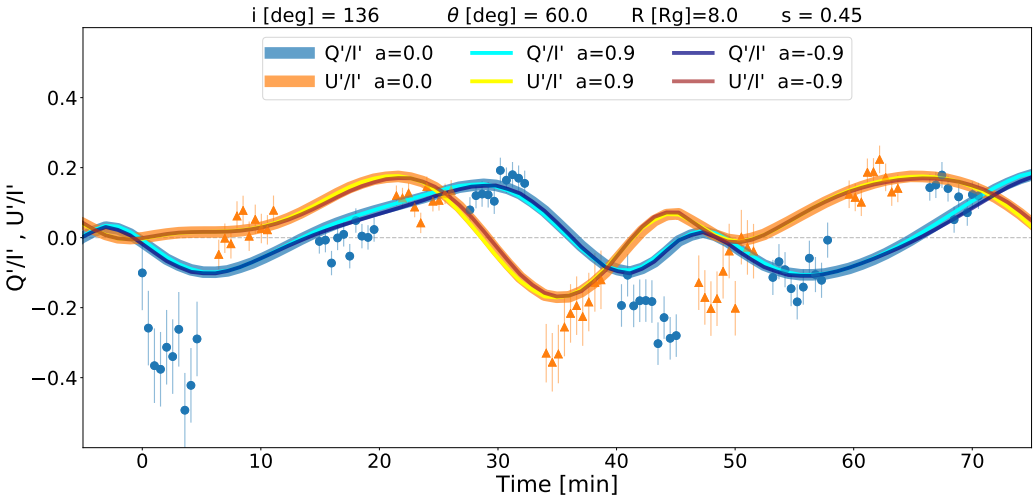

Figure 5.12: Best fit model of the July 28$^{\text{th}}$ flare calculated with three different values of dimensionless spin (a$= 0.0, 0.9, -0.9$). The reduced χ^2 are reported in Table 5.1. Changes in spin do not affect the curves significantly.

Appendix E: Qualitative beam depolarization

In the absence of other mechanisms, such as self absorption or Faraday rotation and conversion, infrared emission from an orbiting hotspot will be depolarized by beam depolarization.

Beam depolarization works by capturing different contributions from polarization (or magnetic field) structure and averaging them out.

More beam depolarization will occur the larger the emitting region that samples the underlying magnetic field is, or the more disordered the field itself is. Given the simple magnetic field geometries considered in this work, disorder at small scales is non existent. We discuss qualitatively the impact of emission size in the following.

As the hotspot goes around the black hole, it samples a wedge of angles in the azimuthal direction with arc length of R_{spot}/R_0. Larger beam depolarization will occur with the increase of this factor. Figure 5.13 shows example curves of numerical calculations at moderate inclination and magnetic field tilt, where only the hotspot size has been changed. As expected, with increasing R_{spot} at fixed orbital radius, not only the amplitude of the polarized curves and QU loops diminishes (and with it the linear polarization fraction), but the features in them are smoothed out as well.

Within the hotspot model, beam depolarization can therefore be used to constrain the size of the emitting region as a function of the observed linear polarization fraction.

Appendix F: Scaling period effects

We explore the effects of scaling the period of model curves. Figure 5.14 shows the best fit model found for the July 28$^{\text{th}}$ flare and one calculated at $R = 11\ R_g$ scaled down to

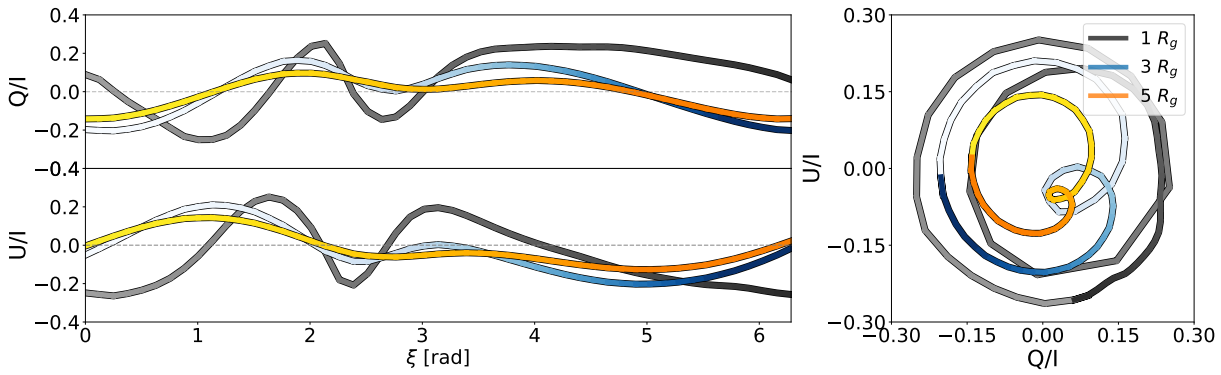

Figure 5.13: Comparison of three numerical calculations with all parameters the same but $R_{\rm spot}$: 1, 3 and 5 $R_{\rm g}$. As the hotspot size increases, the curve features are smoothed from beam depolarization by sampling larger magnetic field regions and averaging out the different polarization directions in time.

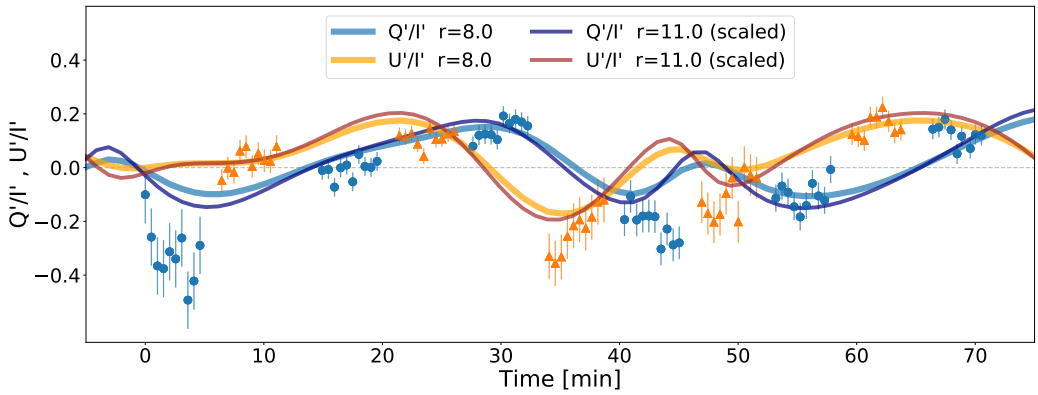

Figure 5.14: Models calculated at $R = 8\ R_g$ and at $R = 11\ R_g$, the latter scaled down to match the orbital period at 8 R_g. The rest of the parameters are those found for the best fit for the July 28$^{\rm th}$ flare. The reduced χ^2 are reported in Table 5.2. For better clarity, the $R = 11\ R_g$ not-scaled model fit is not shown, but the χ^2 is reported.

Table 5.2: Reduced χ^2 of models calculated at $R = 8\ R_g$ and at $R = 11\ R_g$, the latter scaled down to match the orbital period at 8 R_g.

R [$R_{\rm g}$]	a	χ^2
8.0	0.0	3.104
11.0 (scaled)	0.0	3.256
11.0 (not scaled)	0.0	6.424

match the period at 8 R_g, with the rest of the parameters fixed to those of the best fit. The corresponding reduced χ^2 values are reported in Table 5.2. It can be seen that the curves show similar behaviours. Scaled models might have a better reduced χ^2 than their not-scaled versions, but they are still not better than the best fit.

Chapter 6

Conclusions and Outlook

The aim of this thesis is to study and develop tools in which polarization information from polarized GRMHD simulations can be used to study the properties of the surrounding medium around accreting black holes. At the time when this thesis is written, technological and scientific advancements are at their peak, with great new spatially resolved polarized data of the SMBHs Sgr A* and M87* at submillimetre and near infrared frequencies from large VLBI experiments like the EHT (e.g., Event Horizon Telescope Collaboration et al., 2019a,b,c,d,e,f) and the GRAVITY interferometer on the VLT (e.g., Gravity Collaboration et al., 2017, 2018a,b, 2019, 2020c,d,a), as well as state of the art GRMHD simulations that self-consistently evolve electron densities simultaneously with the MHD fluid.

Historically, polarization has proven to be a very useful tool in restricting model parameters. Image integrated quantities, including linear polarization fractions, have been used to restrict accretion model quantities including accretion rates and electron temperatures in the plasma. Faraday effects, sensitive tracers of plasma parameters, have been estimated with rotation measure measurements (frequency-dependent, external rotation of the polarization vector). Now, the new upcoming spatially resolved polarization measurements will open the door for the study of polarization configuration in the innermost regions of the accretion flow, all the way down to the event horizon of the putative black hole, and with it, allow for estimates of Faraday effects within the emission region and study magnetic field structure at event horizon scales for the first time.

The supermassive black hole candidates Sgr A* and M87*'s spatially resolved polarization measurements from the EHT Collaboration will allow for the reconstruction of polarization maps at event horizon scales. The comparison of these and state of the art GRMHD studies, will make it potentially possible to learn about the environmental conditions around these sources, including whether the inner accreting region is weakly magnetised or dominated by strong, dynamically important, magnetic fields.

Polarization patterns from two dimensional GRMHD calculations reveal substantial information on the models, information that, based on total intensity information alone, would be otherwise unattainable. The spatial correlation scale in them is a quantity that depends strongly on plasma parameters and has been shown to serve as a restriction on the strength of Faraday effects in axisymmetric simulations. For the models studied in

Chapter 2, where the electron temperature of the system was assigned in post-process, this quantity not only appears to be model independent but can be linked to observables.

Particularly for Sgr A*, an extension to three-dimensional time-dependent calculations (Chapter 3) has shown that the broad submillimetre spectral shape of Sgr A* can be reproduced by both weakly magnetised systems with turbulent electron heating ("SANE/turbulence") and strongly magnetised systems where electrons heat from magnetic reconnection events ("MAD/reconnection"). While the former do not match at all the observed linear polarization fraction due to heavy depolarization from Faraday rotation internal to the emission region, some MAD/reconnection models satisfy all observational constraints and remain viable (Dexter et al., 2020a).

In addition, the polarization patterns associated to these simulations display different morphologies. Low magnetic field strengths produce more scrambled polarization maps causing very low linear polarization fractions, regardless of the electron heating mechanism and inclination. Strong magnetic fields combined with magnetic reconnection evolve into magnetically arrested disc models with very ordered polarization patterns, showing an azimuthal configurations that resembles that of vertical magnetic fields at low inclinations (Dexter et al., 2020a). This is of particular interest, since this type of magnetic field is used to explain the general polarized properties of the recent GRAVITY near-infrared (NIR) flare results (Gravity Collaboration et al., 2018a).

The EHT has now made it possible to conduct direct studies with shadows of supermassive black hole candidates using electromagnetic waves. In 2021, two new stations will be added to the original array, Kitt Peak and NOEMA, increasing the number of baselines at small and intermediate scales that will increase the coverage of the visibility plane, improving the detail on the reconstructed images.

Upcoming observing campaigns and follow-ups of Sgr A* and M87* will not only increase the number of reconstructed images, but allow for the study of real-time evolution of black holes as well. Features like shape, size and variability of the compact objects' image at horizon scales will be able to be studied for the first time. In addition, time evolution of polarization, which has been essentially unexplored to this day, could be used to measure the properties of MRI turbulence in the upcoming EHT data. With it, more could be learnt on how accretion onto black holes is initiated.

Particularly for M87*, this also includes the study of the stability of the accretion flow direction with time and a more accurate measurement of its shadow which allow for a more precise mass estimate together. Since the mass of this object is not expected to change measurably on human timescales, short-timescale changes in the total intensity and polarized images would challenge our current understanding of the accretion flow properties and spacetime theories.

To this day, general relativity is the preferred theory used to describe the spacetime around these massive objects. The EHT Collaboration's published images of M87*, show a bright ring of emission surrounding a dark interior (Event Horizon Telescope Collaboration et al., 2019d) within which, according to the theory, there should be a photon ring surrounding the black hole shadow (Falcke & Markoff, 2000a) and whose properties depend exclusively on the mass and the spin of the black hole. As shown in Chapter 4, indirect

photon ring features in images of GRMHD simulations show polarization properties that are constant in time and are different to the rest of the image. This has motivated the development a technique that enhances the photon ring in an image and that takes advantage of source variability. Studies of these polarized photon ring properties have shown that the feature is typically about a factor of two less polarized and that the principal reasons behind this are neither related greatly to self absorption nor Faraday effects in the source, but rather to a combination of magnetic field turbulence and parallel transport. Though measuring the photon ring properties with the current state of the EHT array is still an unrealisable task, larger baselines that include even an extension to space could make this challenging task achievable (Johnson et al., 2020). While this is left for future developments, complementary multi wavelength studies of these sources, another exciting advantage of the present times, will certainly improve our understanding of them. VLBI measurements at 345GHz will probe the surroundings of the black hole in regions where optical and Faraday effects are not so present.

High-resolution observations in the NIR of the Galactic Centre done with GRAVITY at the VLT have the power to probe the physics of Sgr A* and the environment around it. Tests of general relativity have already been conducted with such measurements, including the detection of the relativistic effects of gravitational redshift and Schwarzschild precession in the orbit of the star S2, as well as the validity of the weak equivalence principle.

Sgr A* is known for its flaring activity. In 2018, continuous clockwise motion associated with three bright NIR flares from Sgr A* was reported by the GRAVITY Collaboration. The data seemed to be compatible with a model of a compact emission region, a "hotspot", orbiting the massive black hole in a vertical magnetic field. Further detailed study of this polarization information (Chapter 5) has shown that the data are broadly consistent with the predicted evolution in a hotspot model in a static magnetic field with a significant poloidal component, which in relation to GRMHD results, implies that there might be dynamically important magnetic fields in the vicinity of Sgr A*. The work has been conducted without considering shearing of the hotspot in the vicinity of the black hole, which would be help for lower the high linear polarization fractions in the model. A next natural step would be to not only include this or to consider more general morphologies of the magnetic field, but to also jointly fit the astrometry and the polarization data.

This first attempt to use time-dependent spatially resolved polarization information from these simple models promises a new way of studying magnetic field structure and strength on event horizon scales around black holes, turning it into an observable for the first time. More measurements with GRAVITY of these important NIR flaring events will not only improve our information on the magnetic filed structure, but will shine a light on the mechanisms that power these bright emissions and, with it, provide an insight of the properties of the orbiting plasma and the spacetime around the compact object.

Polarization will continue to be a very powerful tool in the upcoming years. Whether it is time-dependent behaviour or spatial structure, polarization information adds another dimension to the analysis of data that enables the extraction of new information from these and other mysterious sources, opening a door to the understanding of the intricacies of accretion physics, spacetime and nature.

Bibliography

B. P. Abbott et al., *Observation of Gravitational Waves from a Binary Black Hole Merger*, Physical Review Letters, 116(6), 061102 (2016).

A. A. Abdo et al., *Fermi Large Area Telescope Gamma-Ray Detection of the Radio Galaxy M87*, Astrophysical Journal, 707(1), 55–60 (2009).

M. A. Abramowicz & P. C. Fragile, *Foundations of Black Hole Accretion Disk Theory*, Living Reviews in Relativity, 16(1), 1 (2013).

A. Abramowski et al., *The 2010 Very High Energy γ-Ray Flare and 10 Years of Multi-wavelength Observations of M 87*, Astrophysical Journal, 746(2), 151 (2012).

E. Agol, *Sagittarius A* Polarization: No Advection-dominated Accretion Flow, Low Accretion Rate, and Nonthermal Synchrotron Emission*, Astrophysical Journal, 538, L121–L124 (2000).

D. K. Aitken et al., *Detection of Polarized Millimeter and Submillimeter Emission from Sagittarius A**, Astrophysical Journal, Letters, 534(2), L173–L176 (2000).

J. Albert et al., *Very High Energy Gamma-Ray Observations of Strong Flaring Activity in M87 in 2008 February*, Astrophysical Journal, Letters, 685(1), L23 (2008).

J. C. Algaba, K. Asada, & M. Nakamura, *Helical magnetic fields in the M87 jet at arc-second scales*, arXiv e-prints, arXiv:1308.5429 (2013).

R. Anantua, S. Ressler, & E. Quataert, *On the Comparison of AGN with GRMHD Simulations: I. Sgr A**, MNRAS(2020).

K. Asada & M. Nakamura, *The Structure of the M87 Jet: A Transition from Parabolic to Conical Streamlines*, Astrophysical Journal, Letters, 745(2), L28 (2012).

W. Baade & R. Minkowski, *On the Identification of Radio Sources.*, Astrophysical Journal, 119, 215 (1954).

D. C. Backer, *Scattering of radio emission from the compact object in Sagittarius A.*, Astrophysical Journal, Letters, 222, L9–L12 (1978).

F. K. Baganoff et al., *Rapid X-ray flaring from the direction of the supermassive black hole at the Galactic Centre*, Nature, 413, 45–48 (2001).

F. K. Baganoff et al., *Chandra X-Ray Spectroscopic Imaging of Sagittarius A* and the Central Parsec of the Galaxy*, Astrophysical Journal, 591, 891–915 (2003).

S. A. Balbus & J. F. Hawley, *A powerful local shear instability in weakly magnetized disks. I - Linear analysis. II - Nonlinear evolution*, Astrophysical Journal, 376, 214–233 (1991).

S. A. Balbus & J. F. Hawley, *Instability, turbulence, and enhanced transport in accretion disks*, Reviews of Modern Physics, 70(1), 1–53 (1998).

S. A. Balbus, J. F. Hawley, & J. M. Stone, *Nonlinear Stability, Hydrodynamical Turbulence, and Transport in Disks*, Astrophysical Journal, 467, 76 (1996).

B. Balick & R. L. Brown, *Intense sub-arcsecond structure in the galactic center.*, Astrophysical Journal, 194, 265–270 (1974).

D. Ball et al., *Particle Acceleration and the Origin of X-Ray Flares in GRMHD Simulations of SGR A*, Astrophysical Journal, 826(1), 77 (2016).

D. Ball et al., *A Plasmoid Model for the Sgr A* Flares Observed with GRAVITY and Chandra*, arXiv e-prints, arXiv:2005.14251 (2020).

A. Ballone et al., *Hydrodynamical Simulations of a Compact Source Scenario for the Galactic Center Cloud G2*, Astrophysical Journal, 776(1), 13 (2013).

C. Bambi, *Astrophysical Black Holes: A Review*, arXiv e-prints, arXiv:1906.03871 (2019).

C. Bambi & S. Nampalliwar, *Fundamental Concepts*, arXiv e-prints, arXiv:1810.07032 (2018).

J. M. Bardeen, B. Carter, & S. W. Hawking, *The four laws of black hole mechanics*, Communications in Mathematical Physics, 31(2), 161–170 (1973).

J. M. Bardeen, W. H. Press, & S. A. Teukolsky, *Rotating Black Holes: Locally Nonrotating Frames, Energy Extraction, and Scalar Synchrotron Radiation*, Astrophysical Journal, 178, 347–370 (1972).

N. M. Barrière et al., *NuSTAR Detection of High-energy X-Ray Emission and Rapid Variability from Sagittarius A^{sstarf} Flares*, Astrophysical Journal, 786(1), 46 (2014).

H. Bartko et al., *Evidence for Warped Disks of Young Stars in the Galactic Center*, Astrophysical Journal, 697(2), 1741–1763 (2009).

K. Beckwith & C. Done, *Extreme gravitational lensing near rotating black holes*, Monthly Notices of the Royal Astronomical Society, 359(4), 1217–1228 (2005).

G. S. Bisnovatyi-Kogan & A. A. Ruzmaikin, *The Accretion of Matter by a Collapsing Star in the Presence of a Magnetic Field*, Astrophysics and Space Science, 28(1), 45–59 (1974).

C. I. Bjornsson, *Polarization properties of a source in relativistic motion.*, Astrophysical Journal, 260, 855–867 (1982).

O. Blaes, *General Overview of Black Hole Accretion Theory*, Space Science Reviews, 183(1-4), 21–41 (2014).

R. D. Blandford & M. C. Begelman, *On the fate of gas accreting at a low rate on to a black hole*, MNRAS, 303(1), L1–L5 (1999).

R. D. Blandford & A. Königl, *Relativistic jets as compact radio sources.*, Astrophysical Journal, 232, 34–48 (1979).

R. D. Blandford & D. G. Payne, *Hydromagnetic flows from accretion disks and the production of radio jets.*, MNRAS, 199, 883–903 (1982).

R. D. Blandford & R. L. Znajek, *Electromagnetic extraction of energy from Kerr black holes.*, MNRAS, 179, 433–456 (1977).

A. Boehle et al., *An Improved Distance and Mass Estimate for Sgr A* from a Multistar Orbit Analysis*, Astrophysical Journal, 830(1), 17 (2016).

H. Bondi, *On Spherically Symmetrical Accretion*, Monthly Notices of the Royal Astronomical Society, 112(2), 195–204 (1952).

H. Bondi & F. Hoyle, *On the mechanism of accretion by stars*, MNRAS, 104, 273 (1944).

K. Bouman, *Extreme imaging via physical model inversion : seeing around corners and imaging black holes* (2017).

K. L. Bouman et al., *Reconstructing Video from Interferometric Measurements of Time-Varying Sources*, arXiv e-prints, arXiv:1711.01357 (2017).

G. C. Bower, H. Falcke, & D. C. Backer, *Detection of Circular Polarization in the Galactic Center Black Hole Candidate Sagittarius A**, Astrophysical Journal, Letters, 523(1), L29–L32 (1999).

G. C. Bower et al., *The Linear Polarization of Sagittarius A*. II. VLA and BIMA Polarimetry at 22, 43, and 86 GHz*, Astrophysical Journal, 527(2), 851–855 (1999).

G. C. Bower et al., *Interferometric Detection of Linear Polarization from Sagittarius A* at 230 GHz*, Astrophysical Journal, 588, 331–337 (2003).

G. C. Bower et al., *Detection of the Intrinsic Size of Sagittarius A* Through Closure Amplitude Imaging*, Science, 304(5671), 704–708 (2004).

G. C. Bower et al., *The Intrinsic Size of Sagittarius A* from 0.35 to 6 cm*, Astrophysical Journal, 648, L127–L130 (2006).

G. C. Bower et al., *Radio and Millimeter Monitoring of Sgr A*: Spectrum, Variability, and Constraints on the G2 Encounter*, Astrophysical Journal, 802, 69 (2015).

G. C. Bower et al., *What Is the Hidden Depolarization Mechanism in Low-luminosity AGNs?*, Astrophysical Journal, Letters, 843(2), L31 (2017).

G. C. Bower et al., *ALMA Polarimetry of Sgr A*: Probing the Accretion Flow from the Event Horizon to the Bondi Radius*, Astrophysical Journal, 868(2), 101 (2018).

G. C. Bower et al., *ALMA Observations of the Terahertz Spectrum of Sagittarius A**, Astrophysical Journal, Letters, 881(1), L2 (2019).

R. H. Boyer & R. W. Lindquist, *Maximal Analytic Extension of the Kerr Metric*, Journal of Mathematical Physics, 8(2), 265–281 (1967).

A. E. Broderick & A. Loeb, *Imaging bright-spots in the accretion flow near the black hole horizon of Sgr A**, MNRAS, 363(2), 353–362 (2005).

A. E. Broderick & A. Loeb, *Frequency-dependent Shift in the Image Centroid of the Black Hole at the Galactic Center as a Test of General Relativity*, Astrophysical Journal, 636, L109–L112 (2006a).

A. E. Broderick & A. Loeb, *Imaging optically-thin hotspots near the black hole horizon of Sgr A* at radio and near-infrared wavelengths*, MNRAS, 367, 905–916 (2006b).

A. E. Broderick & A. Loeb, *Imaging the Black Hole Silhouette of M87: Implications for Jet Formation and Black Hole Spin*, Astrophysical Journal, 697, 1164–1179 (2009).

A. E. Broderick et al., *Evidence for Low Black Hole Spin and Physically Motivated Accretion Models from Millimeter-VLBI Observations of Sagittarius A**, Astrophysical Journal, 735, 110 (2011).

A. E. Broderick et al., *The Event Horizon of M87*, Astrophysical Journal, 805(2), 179 (2015).

B. C. Bromley, F. Melia, & S. Liu, *Polarimetric Imaging of the Massive Black Hole at the Galactic Center*, Astrophysical Journal, 555(2), L83–L86 (2001).

A. Burkert et al., *Physics of the Galactic Center Cloud G2, on Its Way toward the Supermassive Black Hole*, Astrophysical Journal, 750(1), 58 (2012).

A. Chael, *Simulating and Imaging Supermassive Black Hole Accretion Flows* (2019).

A. Chael, R. Narayan, & M. D. Johnson, *Two-temperature, Magnetically Arrested Disc simulations of the jet from the supermassive black hole in M87*, MNRAS, submitted (2019).

A. Chael et al., *The role of electron heating physics in images and variability of the Galactic Center black hole Sagittarius A**, ArXiv e-prints (2018).

A. A. Chael, R. Narayan, & A. Sadowski, *Evolving non-thermal electrons in simulations of black hole accretion*, MNRAS, 470(2), 2367–2386 (2017).

C.-k. Chan et al., *Fast Variability and Millimeter/IR Flares in GRMHD Models of Sgr A* from Strong-field Gravitational Lensing*, Astrophysical Journal, 812, 103 (2015a).

C.-K. Chan et al., *The Power of Imaging: Constraining the Plasma Properties of GRMHD Simulations using EHT Observations of Sgr A**, Astrophysical Journal, 799, 1 (2015b).

M. Chandra, F. Foucart, & C. F. Gammie, *grim: A Flexible, Conservative Scheme for Relativistic Fluid Theories*, Astrophysical Journal, 837(1), 92 (2017).

S. Chandrasekhar, *The Stability of Non-Dissipative Couette Flow in Hydromagnetics*, Proceedings of the National Academy of Science, 46(2), 253–257 (1960).

S. Chandrasekhar, *The mathematical theory of black holes* (1983).

K. Chatterjee et al., *Observational signatures of disk and jet misalignment in images of accreting black holes*, arXiv e-prints, arXiv:2002.08386 (2020).

X. Chen et al., *Unified Description of Accretion Flows around Black Holes*, Astrophysical Journal, Letters, 443, L61 (1995).

P. A. Connors & R. F. Stark, *Observable gravitational effects on polarised radiation coming from near a black hole*, Nature, 269(5624), 128–129 (1977).

A. Cotera et al., *Mid-Infrared Imaging of the Central Parsec with Keck*, in: H. Falcke et al., eds., *The Central Parsecs of the Galaxy*, vol. 186 of *Astronomical Society of the Pacific Conference Series*, page 240 (1999).

J. Cuadra et al., *Galactic Centre stellar winds and Sgr A* accretion*, MNRAS, 366(2), 358–372 (2006).

C. T. Cunningham & J. M. Bardeen, *The Optical Appearance of a Star Orbiting an Extreme Kerr Black Hole*, Astrophysical Journal, 183, 237–264 (1973).

H. D. Curtis, *Descriptions of 762 Nebulae and Clusters Photographed with the Crossley Reflector*, Publications of Lick Observatory, 13, 9–42 (1918).

J. Davelaar et al., *General relativistic magnetohydrodynamical κ-jet models for Sagittarius A**, Astronomy and Astrophysics, 612, A34 (2018).

J. Davelaar et al., *Modeling non-thermal emission from the jet-launching region of M 87 with adaptive mesh refinement*, Astronomy and Astrophysics, 632, A2 (2019).

F. De Colle et al., *A Stellar Wind Origin for the G2 Cloud: Three-dimensional Numerical Simulations*, Astrophysical Journal, Letters, 789(2), L33 (2014).

F. de Gasperin et al., *M 87 at metre wavelengths: the LOFAR picture*, Astronomy and Astrophysics, 547, A56 (2012).

J.-P. De Villiers, J. F. Hawley, & J. H. Krolik, *Magnetically Driven Accretion Flows in the Kerr Metric. I. Models and Overall Structure*, Astrophysical Journal, 599(2), 1238–1253 (2003).

J.-P. De Villiers et al., *Magnetically Driven Accretion in the Kerr Metric. III. Unbound Outflows*, Astrophysical Journal, 620(2), 878–888 (2005).

J. Dexter, *A public code for general relativistic, polarised radiative transfer around spinning black holes*, MNRAS, 462, 115–136 (2016).

J. Dexter & E. Agol, *A Fast New Public Code for Computing Photon Orbits in a Kerr Spacetime*, Astrophysical Journal, 696, 1616–1629 (2009).

J. Dexter, E. Agol, & P. C. Fragile, *Millimeter Flares and VLBI Visibilities from Relativistic Simulations of Magnetized Accretion Onto the Galactic Center Black Hole*, Astrophysical Journal, Letters, 703(2), L142–L146 (2009).

J. Dexter & P. C. Fragile, *Tilted black hole accretion disc models of Sagittarius A*: time-variable millimetre to near-infrared emission*, MNRAS, 432, 2252–2272 (2013).

J. Dexter et al., *The Submillimeter Bump in Sgr A* from Relativistic MHD Simulations*, Astrophysical Journal, 717, 1092–1104 (2010).

J. Dexter et al., *An 8 h characteristic time-scale in submillimetre light curves of Sagittarius A**, MNRAS, 442, 2797–2808 (2014).

J. Dexter et al., *A parameter survey of Sgr A* radiative models from GRMHD simulations with self-consistent electron heating*, MNRAS, 494(3), 4168–4186 (2020a).

J. Dexter et al., *Sgr A* near-infrared flares from reconnection events in a magnetically arrested disc*, arXiv e-prints, arXiv:2006.03657 (2020b).

P. Dhang & P. Sharma, *3D global simulations of RIAFs: convergence, effects of azimuthal extent, and dynamo*, MNRAS, 482(1), 848–869 (2019).

T. Di Matteo et al., *Accretion onto the Supermassive Black Hole in M87*, Astrophysical Journal, 582, 133–140 (2003).

S. Dibi et al., *General relativistic magnetohydrodynamic simulations of accretion on to Sgr A*: how important are radiative losses?*, MNRAS, 426(3), 1928–1939 (2012).

T. Do et al., *A Near-Infrared Variability Study of the Galactic Black Hole: A Red Noise Source with NO Detected Periodicity*, Astrophysical Journal, 691(2), 1021–1034 (2009).

T. Do et al., *Relativistic redshift of the star S0-2 orbiting the Galactic Center supermassive black hole*, Science, 365(6454), 664–668 (2019a).

T. Do et al., *Unprecedented Near-infrared Brightness and Variability of Sgr A**, Astrophysical Journal, Letters, 882(2), L27 (2019b).

K. Dodds-Eden et al., *Evidence for X-Ray Synchrotron Emission from Simultaneous Mid-Infrared to X-Ray Observations of a Strong Sgr A* Flare*, Astrophysical Journal, 698, 676–692 (2009).

K. Dodds-Eden et al., *The Two States of Sgr A* in the Near-infrared: Bright Episodic Flares on Top of Low-level Continuous Variability*, Astrophysical Journal, 728, 37 (2011).

S. S. Doeleman et al., *Event-horizon-scale structure in the supermassive black hole candidate at the Galactic Centre*, Nature, 455, 78–80 (2008).

S. S. Doeleman et al., *Jet-Launching Structure Resolved Near the Supermassive Black Hole in M87*, Science, 338, 355– (2012).

J. C. Dolence et al., *grmonty: A Monte Carlo Code for Relativistic Radiative Transport*, Astrophysical Journal, Supplement, 184, 387–397 (2009).

S. Drappeau et al., *Self-consistent spectra from radiative GRMHD simulations of accretion on to Sgr A**, MNRAS, 431(3), 2872–2884 (2013).

A. Eckart et al., *First simultaneous NIR/X-ray detection of a flare from Sgr A**, Astronomy and Astrophysics, 427, 1–11 (2004).

A. Eckart et al., *Polarimetry of near-infrared flares from Sagittarius A**, Astronomy and Astrophysics, 455(1), 1–10 (2006).

A. Eckart et al., *Polarized NIR and X-ray flares from Sagittarius A**, Astronomy and Astrophysics, 479, 625–639 (2008a).

A. Eckart et al., *Simultaneous NIR/sub-mm observation of flare emission from Sagittarius A**, Astronomy and Astrophysics, 492, 337–344 (2008b).

A. Eckart et al., *Simultaneous NIR/sub-mm observation of flare emission from Sagittarius A**, Astronomy and Astrophysics, 492, 337–344 (2008c).

A. Eckart et al., *Luminous Accretion onto the Dark Mass at the Center of the Milky way*, in: H. V. Klapdor-Kleingrothaus & I. V. Krivosheina, eds., *Dark Matter in Astrophysics and Particle Physics, Dark 2009*, pages 303–319 (2010).

A. Einstein, *Die Grundlage der allgemeinen Relativitätstheorie*, Annalen der Physik, 354(7), 769–822 (1915).

A. Einstein, *Kosmologische Betrachtungen zur allgemeinen Relativitätstheorie*, Sitzungsberichte der Königlich Preußischen Akademie der Wissenschaften (Berlin, pages 142–152 (1917).

F. Eisenhauer et al., *SINFONI in the Galactic Center: Young Stars and Infrared Flares in the Central Light-Month*, Astrophysical Journal, 628(1), 246–259 (2005).

F. Eisenhauer et al., *GRAVITY: getting to the event horizon of Sgr A**, vol. 7013 of *Society of Photo-Optical Instrumentation Engineers (SPIE) Conference Series*, page 70132A (2008).

Event Horizon Telescope Collaboration et al., *First M87 Event Horizon Telescope Results. I. The Shadow of the Supermassive Black Hole*, Astrophysical Journal, 875(1), L1 (2019a).

Event Horizon Telescope Collaboration et al., *First M87 Event Horizon Telescope Results. II. Array and Instrumentation*, Astrophysical Journal, 875(1), L2 (2019b).

Event Horizon Telescope Collaboration et al., *First M87 Event Horizon Telescope Results. III. Data Processing and Calibration*, Astrophysical Journal, 875(1), L3 (2019c).

Event Horizon Telescope Collaboration et al., *First M87 Event Horizon Telescope Results. IV. Imaging the Central Supermassive Black Hole*, Astrophysical Journal, 875(1), L4 (2019d).

Event Horizon Telescope Collaboration et al., *First M87 Event Horizon Telescope Results. V. Physical Origin of the Asymmetric Ring*, Astrophysical Journal, 875(1), L5 (2019e).

Event Horizon Telescope Collaboration et al., *First M87 Event Horizon Telescope Results. VI. The Shadow and Mass of the Central Black Hole*, Astrophysical Journal, 875(1), L6 (2019f).

H. Falcke & S. Markoff, *The jet model for Sgr A*: Radio and X-ray spectrum*, Astronomy and Astrophysics, 362, 113–118 (2000a).

H. Falcke & S. Markoff, *The jet model for Sgr A*: Radio and X-ray spectrum*, Astronomy and Astrophysics, 362, 113–118 (2000b).

H. Falcke & S. B. Markoff, *Toward the event horizon — the supermassive black hole in the Galactic Center*, Classical and Quantum Gravity, 30(24), 244003 (2013).

H. Falcke, F. Melia, & E. Agol, *Viewing the Shadow of the Black Hole at the Galactic Center*, Astrophysical Journal, 528, L13–L16 (2000).

H. Falcke et al., *The Simultaneous Spectrum of Sagittarius A* from 20 Centimeters to 1 Millimeter and the Nature of the Millimeter Excess*, Astrophysical Journal, 499(2), 731–734 (1998).

V. L. Fish et al., *1.3 mm Wavelength VLBI of Sagittarius A*: Detection of Time-variable Emission on Event Horizon Scales*, Astrophysical Journal, 727(2), L36 (2011).

L. G. Fishbone & V. Moncrief, *Relativistic fluid disks in orbit around Kerr black holes*, Astrophysical Journal, 207, 962–976 (1976).

J. Font, *Numerical Hydrodynamics in General Relativity*, Living Rev. Relativ., 3, 2 (2000).

P. C. Fragile & O. M. Blaes, *Epicyclic Motions and Standing Shocks in Numerically Simulated Tilted Black Hole Accretion Disks*, Astrophysical Journal, 687(2), 757–766 (2008).

C. F. Gammie & P. K. Leung, *A Formalism for Covariant Polarized Radiative Transport by Ray Tracing*, Astrophysical Journal, 752(2), 123 (2012).

C. F. Gammie, J. C. McKinney, & G. Tóth, *HARM: A Numerical Scheme for General Relativistic Magnetohydrodynamics*, Astrophysical Journal, 589, 444–457 (2003).

K. Gebhardt & J. Thomas, *The Black Hole Mass, Stellar Mass-to-Light Ratio, and Dark Halo in M87*, Astrophysical Journal, 700(2), 1690–1701 (2009).

K. Gebhardt et al., *The Black Hole Mass in M87 from Gemini/NIFS Adaptive Optics Observations*, Astrophysical Journal, 729(2), 119 (2011).

R. Genzel, F. Eisenhauer, & S. Gillessen, *The Galactic Center massive black hole and nuclear star cluster*, Reviews of Modern Physics, 82(4), 3121–3195 (2010).

R. Genzel et al., *The Dark Mass Concentration in the Central Parsec of the Milky Way*, Astrophysical Journal, 472, 153 (1996).

R. Genzel et al., *Near-infrared flares from accreting gas around the supermassive black hole at the Galactic Centre*, Nature, 425(6961), 934–937 (2003).

A. M. Ghez et al., *Variable Infrared Emission from the Supermassive Black Hole at the Center of the Milky Way*, Astrophysical Journal, Letters, 601(2), L159–L162 (2004).

A. M. Ghez et al., *Measuring Distance and Properties of the Milky Way's Central Supermassive Black Hole with Stellar Orbits*, Astrophysical Journal, 689(2), 1044–1062 (2008).

S. Gillessen et al., *Variations in the Spectral Slope of Sagittarius A* during a Near-Infrared Flare*, Astrophysical Journal, Letters, 640(2), L163–L166 (2006).

S. Gillessen et al., *Monitoring Stellar Orbits Around the Massive Black Hole in the Galactic Center*, Astrophysical Journal, 692(2), 1075–1109 (2009).

S. Gillessen et al., *A gas cloud on its way towards the supermassive black hole at the Galactic Centre*, Nature, 481(7379), 51–54 (2012).

S. Gillessen et al., *An Update on Monitoring Stellar Orbits in the Galactic Center*, Astrophysical Journal, 837(1), 30 (2017).

S. Gillessen et al., *Detection of a Drag Force in G2's Orbit: Measuring the Density of the Accretion Flow onto Sgr A* at 1000 Schwarzschild Radii*, Astrophysical Journal, 871(1), 126 (2019).

R. Gold et al., *Probing the Magnetic Field Structure in Sgr A* on Black Hole Horizon Scales with Polarized Radiative Transfer Simulations*, Astrophysical Journal, 837(2), 180 (2017).

J. E. Goldston, E. Quataert, & I. V. Igumenshchev, *Synchrotron Radiation from Radiatively Inefficient Accretion Flow Simulations: Applications to Sagittarius A**, Astrophysical Journal, 621(2), 785–792 (2005).

Gravity Collaboration et al., *First light for GRAVITY: Phase referencing optical interferometry for the Very Large Telescope Interferometer*, Astronomy and Astrophysics, 602, A94 (2017).

Gravity Collaboration et al., *Detection of orbital motions near the last stable circular orbit of the massive black hole SgrA**, Astronomy and Astrophysics, 618, L10 (2018a).

Gravity Collaboration et al., *Detection of the gravitational redshift in the orbit of the star S2 near the Galactic centre massive black hole*, Astronomy and Astrophysics, 615, L15 (2018b).

Gravity Collaboration et al., *Spatially resolved rotation of the broad-line region of a quasar at sub-parsec scale*, Nature, 563(7733), 657–660 (2018c).

Gravity Collaboration et al., *A geometric distance measurement to the Galactic center black hole with 0.3% uncertainty*, Astronomy and Astrophysics, 625, L10 (2019).

GRAVITY Collaboration et al., *Hunting Exoplanets with Single-Mode Optical Interferometry*, The Messenger, 178, 47–49 (2019).

Gravity Collaboration et al., *Detection of the Schwarzschild precession in the orbit of the star S2 near the Galactic centre massive black hole*, Astronomy and Astrophysics, 636, L5 (2020a).

Gravity Collaboration et al., *Detection of the Schwarzschild precession in the orbit of the star S2 near the Galactic centre massive black hole*, arXiv e-prints, arXiv:2004.07187 (2020b).

Gravity Collaboration et al., *Modeling the orbital motion of Sgr A*'s near-infrared flares*, Astronomy and Astrophysics, 635, A143 (2020c).

Gravity Collaboration et al., *The flux distribution of Sgr A**, Astronomy and Astrophysics, 638, A2 (2020d).

Gravity Collaboration et al., *The resolved size and structure of hot dust in the immediate vicinity of AGN*, Astronomy and Astrophysics, 635, A92 (2020e).

J. Guillochon et al., *Possible Origin of the G2 Cloud from the Tidal Disruption of a Known Giant Star by Sgr A**, Astrophysical Journal, Letters, 786(2), L12 (2014).

C. R. Gwinn et al., *Discovery of Substructure in the Scatter-broadened Image of Sgr A**, Astrophysical Journal, Letters, 794, L14 (2014).

K. Hada et al., *An origin of the radio jet in M87 at the location of the central black hole*, Nature, 477(7363), 185–187 (2011).

K. Hada et al., *High-sensitivity 86 GHz (3.5 mm) VLBI Observations of M87: Deep Imaging of the Jet Base at a Resolution of 10 Schwarzschild Radii*, Astrophysical Journal, 817(2), 131 (2016).

D. Haggard et al., *Chandra Spectral and Timing Analysis of Sgr A*'s Brightest X-Ray Flares*, Astrophysical Journal, 886(2), 96 (2019).

J. W. Haller, *The Galactic Center Stellar Population in the Near Infrared.*, Ph.D. thesis, Arizona Univ., Tucson. (1992).

N. Hamaus et al., *Prospects for Testing the Nature of Sgr A*'s Near-Infrared Flares on the Basis of Current Very Large Telescope—and Future Very Large Telescope Interferometer—Observations*, Astrophysical Journal, 692(1), 902–916 (2009).

D. E. Harris et al., *Variability Timescales in the M87 Jet: Signatures of E^2 Losses, Discovery of a Quasi Period in HST-1, and the Site of TeV Flaring*, Astrophysical Journal, 699(1), 305–314 (2009).

S. W. Hawking, *Black hole explosions?*, Nature, 248(5443), 30–31 (1974).

J. F. Hawley, X. Guan, & J. H. Krolik, *Assessing Quantitative Results in Accretion Simulations: From Local to Global*, Astrophysical Journal, 738, 84 (2011).

J. F. Hawley et al., *Testing Convergence for Global Accretion Disks*, Astrophysical Journal, 772(2), 102 (2013).

E. Himwich et al., *Universal Polarimetric Signatures of the Black Hole Photon Ring*, arXiv e-prints, arXiv:2001.08750 (2020).

G. G. Howes, *A prescription for the turbulent heating of astrophysical plasmas*, MNRAS, 409, L104–L108 (2010).

F. Hoyle & G. R. Burbidge, *On the Nature of the Quasi-Stellar Objects*, Astrophysical Journal, 144, 534 (1966).

S. Ichimaru, *Theory of strongly correlated charged-particle systems: Plasma turbulence and high-density electron liquids*, Physical Review A, 15(2), 744–754 (1977).

I. V. Igumenshchev, *Magnetically Arrested Disks and the Origin of Poynting Jets: A Numerical Study*, Astrophysical Journal, 677(1), 317–326 (2008).

I. V. Igumenshchev, R. Narayan, & M. A. Abramowicz, *Three-dimensional Magnetohydrodynamic Simulations of Radiatively Inefficient Accretion Flows*, Astrophysical Journal, 592(2), 1042–1059 (2003).

S. Issaoun et al., *The Size, Shape, and Scattering of Sagittarius A* at 86 GHz: First VLBI with ALMA*, Astrophysical Journal, 871(1), 30 (2019).

A. Jiménez-Rosales & J. Dexter, *The impact of Faraday effects on polarized black hole images of Sagittarius A**, MNRAS, 478, 1875–1883 (2018).

T. Johannsen & D. Psaltis, *Testing the No-hair Theorem with Observations in the Electromagnetic Spectrum. II. Black Hole Images*, Astrophysical Journal, 718, 446–454 (2010).

M. D. Johnson et al., *Resolved magnetic-field structure and variability near the event horizon of Sagittarius A**, Science, 350, 1242–1245 (2015).

M. D. Johnson et al., *The Scattering and Intrinsic Structure of Sagittarius A* at Radio Wavelengths*, Astrophysical Journal, 865, 104 (2018).

M. D. Johnson et al., *Universal interferometric signatures of a black hole's photon ring*, Science Advances, 6(12), eaaz1310 (2020).

T. W. Jones & P. E. Hardee, *Maxwellian synchrotron sources*, Astrophysical Journal, 228, 268–278 (1979).

B. Junor & J. Biretta, *CMVA and VLBA 3mm Observations of Vir A.*, in: *American Astronomical Society Meeting Abstracts*, vol. 199 of *American Astronomical Society Meeting Abstracts*, page 98.01 (2001).

W. Junor, J. A. Biretta, & M. Livio, *Formation of the radio jet in M87 at 100 Schwarzschild radii from the central black hole*, Nature, 401(6756), 891–892 (1999).

A. B. Kamruddin & J. Dexter, *A geometric crescent model for black hole images*, MNRAS, 434(1), 765–771 (2013).

Y. Kawazura, M. Barnes, & A. A. Schekochihin, *Thermal disequilibration of ions and electrons by collisionless plasma turbulence*, Proceedings of the National Academy of Science, 116(3), 771–776 (2019).

R. P. Kerr, *Gravitational Field of a Spinning Mass as an Example of Algebraically Special Metrics*, Physical Review Letters, 11(5), 237–238 (1963).

J. Y. Kim et al., *The limb-brightened jet of M87 down to the 7 Schwarzschild radii scale*, Astronomy and Astrophysics, 616, A188 (2018).

A. King, *Black Holes, Galaxy Formation, and the M_{BH}-σ Relation*, Astrophysical Journal, Letters, 596(1), L27–L29 (2003).

S. Koide, K. Shibata, & T. Kudoh, *General Relativistic Jet Formation from Black-Hole Magnetized Accretion Disks*, vol. 240 of *Astrophysics and Space Science Library*, page 215 (1999).

S. S. Komissarov, *Direct numerical simulations of the Blandford-Znajek effect*, MNRAS, 326(3), L41–L44 (2001).

A. Koratkar & O. Blaes, *The Ultraviolet and Optical Continuum Emission in Active Galactic Nuclei: The Status of Accretion Disks*, Publications of the ASP, 111(755), 1–30 (1999).

J. Kormendy & L. C. Ho, *Coevolution (Or Not) of Supermassive Black Holes and Host Galaxies*, Annual Review of Astron and Astrophys, 51(1), 511–653 (2013).

J. Kormendy & D. Richstone, *Inward Bound—The Search For Supermassive Black Holes In Galactic Nuclei*, Annual Review of Astron and Astrophys, 33, 581 (1995).

Y. Y. Kovalev et al., *The Inner Jet of the Radio Galaxy M87*, Astrophysical Journal, Letters, 668(1), L27–L30 (2007).

T. P. Krichbaum et al., *VLBI observations of the galactic center source SGR A* at 86 GHz and 215 GHz*, Astronomy and Astrophysics, 335, L106–L110 (1998).

T. P. Krichbaum et al., *Sub-Milliarcsecond Imaging of Sgr A* and M 87*, in: *Journal of Physics Conference Series*, vol. 54 of *Journal of Physics Conference Series*, pages 328–334 (2006).

C. Y. Kuo et al., *Measuring Mass Accretion Rate onto the Supermassive Black Hole in M87 Using Faraday Rotation Measure with the Submillimeter Array*, Astrophysical Journal, 783(2), L33 (2014).

J. H. Lacy, C. H. Townes, & D. J. Hollenbach, *The nature of the central parsec of the Galaxy*, Astrophysical Journal, 262, 120–134 (1982).

J. H. Lacy et al., *Observations of the motion and distribution of the ionized gas in the central parsec of the Galaxy. II.*, Astrophysical Journal, 241, 132–146 (1980).

P. S. Laplace (1976).

Y.-P. Li et al., *Statistics of X-Ray Flares of Sagittarius A*: Evidence for Solar-like Self-organized Criticality Phenomena*, Astrophysical Journal, 810(1), 19 (2015).

H. B. Liu et al., *Linearly polarized millimeter and submillimeter continuum emission of Sgr A* constrained by ALMA*, Astronomy and Astrophysics, 593, A107 (2016).

K. Y. Lo & M. J. Claussen, *High-resolution observations of ionized gas in central 3 parsecs of the Galaxy: possible evidence for infall*, Nature, 306(5944), 647–651 (1983).

K. Y. Lo et al., *VLBI observations of the compact radio source in the center of the Galaxy.*, Astrophysical Journal, Letters, 202, L63–L65 (1975).

M. S. Longair, *High Energy Astrophysics* (2011).

R.-S. Lu et al., *Detection of Intrinsic Source Structure at?3 Schwarzschild Radii with Millimeter-VLBI Observations of SAGITTARIUS A**, Astrophysical Journal, 859(1), 60 (2018).

J.-P. Luminet, *Image of a spherical black hole with thin accretion disk*, Astronomy and Astrophysics, 75, 228–235 (1979).

J.-P. Luminet, *Black Holes* (1992).

C. Ly, R. C. Walker, & W. Junor, *High-Frequency VLBI Imaging of the Jet Base of M87*, Astrophysical Journal, 660(1), 200–205 (2007).

D. Lynden-Bell, *Galactic Nuclei as Collapsed Old Quasars*, Nature, 223(5207), 690–694 (1969).

D. Lynden-Bell & J. E. Pringle, *The evolution of viscous discs and the origin of the nebular variables.*, MNRAS, 168, 603–637 (1974).

J.-P. Macquart et al., *The Rotation Measure and 3.5 Millimeter Polarization of Sagittarius A**, Astrophysical Journal, Letters, 646(2), L111–L114 (2006).

R. Mahadevan & E. Quataert, *Are Particles in Advection-dominated Accretion Flows Thermal?*, Astrophysical Journal, 490(2), 605–618 (1997).

T. Manmoto, S. Mineshige, & M. Kusunose, *Spectrum of Optically Thin Advection-dominated Accretion Flow around a Black Hole: Application to Sagittarius A**, Astrophysical Journal, 489(2), 791–803 (1997).

S. A. Mao, J. Dexter, & E. Quataert, *The impact of non-thermal electrons on event horizon scale images and spectra of Sgr A**, MNRAS, 466(4), 4307–4319 (2017).

S. Markoff, G. C. Bower, & H. Falcke, *How to hide large-scale outflows: size constraints on the jets of Sgr A**, MNRAS, 379(4), 1519–1532 (2007).

S. Markoff et al., *The Nature of the 10 kilosecond X-ray flare in Sgr A**, Astronomy and Astrophysics, 379, L13–L16 (2001).

D. P. Marrone, *Submillimeter properties of Sagittarius A*: The polarization and spectrum from 230 to 690 GHz and the submillimeter array polarimeter*, Ph.D. thesis, Harvard University (2006).

D. P. Marrone et al., *Interferometric Measurements of Variable 340 GHz Linear Polarization in Sagittarius A**, Astrophysical Journal, 640(1), 308–318 (2006).

D. P. Marrone et al., *An Unambiguous Detection of Faraday Rotation in Sagittarius A**, Astrophysical Journal, Letters, 654(1), L57–L60 (2007).

D. P. Marrone et al., *An X-Ray, Infrared, and Submillimeter Flare of Sagittarius A**, Astrophysical Journal, 682, 373–383 (2008).

J. M. Martí & E. Müller, *Numerical Hydrodynamics in Special Relativity*, Living Reviews in Relativity, 6(1), 7 (2003).

J. McClintock, *Black Hole Spin Via Continuum Fitting and the Role of Spin in Powering Transient Jets*, in: *From the Dolomites to the Event Horizon: Sledging Down the Black Hole Potential Well*, page 1 (2013).

J. C. McKinney, *General relativistic magnetohydrodynamic simulations of the jet formation and large-scale propagation from black hole accretion systems*, MNRAS, 368, 1561–1582 (2006).

J. C. McKinney, A. Tchekhovskoy, & R. D. Blandford, *General relativistic magnetohydrodynamic simulations of magnetically choked accretion flows around black holes*, MNRAS, 423, 3083–3117 (2012).

J. C. McKinney et al., *Three-dimensional general relativistic radiation magnetohydrodynamical simulation of super-Eddington accretion, using a new code HARMRAD with M1 closure*, MNRAS, 441(4), 3177–3208 (2014).

S. Mei et al., *The ACS Virgo Cluster Survey. XIII. SBF Distance Catalog and the Three-dimensional Structure of the Virgo Cluster*, Astrophysical Journal, 655(1), 144–162 (2007).

F. Mertens et al., *Kinematics of the jet in M 87 on scales of 100-1000 Schwarzschild radii*, Astronomy and Astrophysics, 595, A54 (2016).

L. Meyer et al., *The Shortest-Known-Period Star Orbiting Our Galaxy's Supermassive Black Hole*, Science, 338(6103), 84 (2012).

J. Michell, *On the Means of Discovering the Distance, Magnitude, &c. of the Fixed Stars, in Consequence of the Diminution of the Velocity of Their Light, in Case Such a Diminution Should be Found to Take Place in any of Them, and Such Other Data Should be Procured from Observations, as Would be Farther Necessary for That Purpose. By the Rev. John Michell, B. D. F. R. S. In a Letter to Henry Cavendish, Esq. F. R. S. and A. S.*, Philosophical Transactions of the Royal Society of London Series I, 74, 35–57 (1784).

C. W. Misner, K. S. Thorne, & J. A. Wheeler, *Gravitation* (1973).

M. Miyoshi et al., *Evidence for a black hole from high rotation velocities in a sub-parsec region of NGC4258*, Nature, 373(6510), 127–129 (1995).

M. Mościbrodzka & H. Falcke, *Coupled jet-disk model for Sagittarius A*: explaining the flat-spectrum radio core with GRMHD simulations of jets*, Astronomy and Astrophysics, 559, L3 (2013).

M. Mościbrodzka, H. Falcke, & H. Shiokawa, *General relativistic magnetohydrodynamical simulations of the jet in M 87*, Astronomy and Astrophysics, 586, A38 (2016).

M. Mościbrodzka & C. F. Gammie, *IPOLE - semi-analytic scheme for relativistic polarized radiative transport*, MNRAS, 475(1), 43–54 (2018).

M. Mościbrodzka et al., *Radiative Models of SGR A* from GRMHD Simulations*, Astrophysical Journal, 706, 497–507 (2009).

M. Mościbrodzka et al., *Pair Production in Low-luminosity Galactic Nuclei*, Astrophysical Journal, 735(1), 9 (2011).

M. Mościbrodzka et al., *Observational appearance of inefficient accretion flows and jets in 3D GRMHD simulations: Application to Sagittarius A**, Astronomy and Astrophysics, 570, A7 (2014).

M. Mościbrodzka et al., *Faraday rotation in GRMHD simulations of the jet launching zone of M87*, MNRAS, 468, 2214–2221 (2017).

D. J. Muñoz et al., *The Circular Polarization of Sagittarius A* at Submillimeter Wavelengths*, Astrophysical Journal, 745(2), 115 (2012).

N. M. Nagar, A. S. Wilson, & H. Falcke, *Evidence for Jet Domination of the Nuclear Radio Emission in Low-Luminosity Active Galactic Nuclei*, Astrophysical Journal, Letters, 559(2), L87–L90 (2001).

R. Narayan, I. V. Igumenshchev, & M. A. Abramowicz, *Magnetically Arrested Disk: an Energetically Efficient Accretion Flow*, Publications of the Astronomical Society of Japan, 55, L69–L72 (2003).

R. Narayan & I. Yi, *Advection-dominated Accretion: A Self-similar Solution*, Astrophysical Journal, Letters, 428, L13 (1994).

R. Narayan & I. Yi, *Advection-dominated Accretion: Underfed Black Holes and Neutron Stars*, Astrophysical Journal, 452, 710 (1995).

R. Narayan, I. Yi, & R. Mahadevan, *Explaining the spectrum of Sagittarius A* with a model of an accreting black hole*, Nature, 374, 623–625 (1995a).

R. Narayan, I. Yi, & R. Mahadevan, *Explaining the spectrum of Sagittarius A* with a model of an accreting black hole*, Nature, 374, 623–625 (1995b).

R. Narayan et al., *Advection-dominated accretion model of Sagittarius A*: evidence for a black hole at the Galactic center.*, Astrophysical Journal, 492(2), 554–568 (1998).

R. Narayan et al., *GRMHD simulations of magnetized advection-dominated accretion on a non-spinning black hole: role of outflows*, MNRAS, 426, 3241–3259 (2012).

E. T. Newman et al., *Metric of a Rotating, Charged Mass*, Journal of Mathematical Physics, 6(6), 918–919 (1965).

S. C. Noble et al., *Primitive Variable Solvers for Conservative General Relativistic Magnetohydrodynamics*, Astrophysical Journal, 641, 626–637 (2006).

S. C. Noble et al., *Simulating the emission and outflows from accretion discs*, Classical and Quantum Gravity, 24, S259–S274 (2007).

G. Nordström, *On the Energy of the Gravitation field in Einstein's Theory*, Koninklijke Nederlandse Akademie van Wetenschappen Proceedings Series B Physical Sciences, 20, 1238–1245 (1918).

I. D. Novikov & Y. B. Zel'dovich, *Physical Processes Near Cosmological Singularities*, Annual Review of Astron and Astrophys, 11, 387 (1973).

S. P. O'Sullivan et al., *Faraday rotation at low frequencies: magnetoionic material of the large FRII radio galaxy PKS J0636-2036*, MNRAS, 475, 4263–4277 (2018).

F. N. Owen, J. A. Eilek, & N. E. Kassim, *M87 at 90 Centimeters: A Different Picture*, Astrophysical Journal, 543(2), 611–619 (2000).

F. N. Owen, J. A. Eilek, & W. C. Keel, *Detection of Large Faraday Rotation in the Inner 2 Kiloparsecs of M87*, Astrophysical Journal, 362, 449 (1990).

F. Özel, D. Psaltis, & R. Narayan, *Hybrid Thermal-Nonthermal Synchrotron Emission from Hot Accretion Flows*, Astrophysical Journal, 541, 234–249 (2000).

H. P. Palmer et al., *Radio Diameter Measurements with Interferometer Baselines of One Million and Two Million Wavelengths*, Nature, 213(5078), 789–790 (1967).

T. Paumard et al., *Scientific Prospects for VLTI in the Galactic Centre: Getting to the Schwarzschild Radius*, in: A. Richichi et al., eds., *The Power of Optical/IR Interferometry: Recent Scientific Results and 2nd Generation*, page 313 (2008).

R. Penrose & R. M. Floyd, *Extraction of Rotational Energy from a Black Hole*, Nature Physical Science, 229(6), 177–179 (1971).

E. S. Perlman et al., *Deep 10 Micron Imaging of M87*, Astrophysical Journal, Letters, 561(1), L51–L54 (2001).

E. S. Perlman et al., *The Mid-Infrared Emission of M87*, Astrophysical Journal, 663(2), 808–815 (2007).

E. S. Perlman et al., *Optical Polarization and Spectral Variability in the M87 Jet*, Astrophysical Journal, 743(2), 119 (2011).

O. Pfuhl et al., *The Galactic Center Cloud G2 and its Gas Streamer*, Astrophysical Journal, 798(2), 111 (2015).

P. Plewa, *The galactic center in motion* (2018).

P. M. Plewa et al., *The Post-pericenter Evolution of the Galactic Center Source G2*, Astrophysical Journal, 840(1), 50 (2017).

G. Ponti et al., *A powerful flare from Sgr A* confirms the synchrotron nature of the X-ray emission*, MNRAS, 468(2), 2447–2468 (2017).

D. Porquet et al., *XMM-Newton observation of the brightest X-ray flare detected so far from Sgr A**, Astronomy and Astrophysics, 407, L17–L20 (2003).

O. Porth et al., *The black hole accretion code*, Computational Astrophysics and Cosmology, 4(1), 1 (2017).

O. Porth et al., *The Event Horizon General Relativistic Magnetohydrodynamic Code Comparison Project*, Astrophysical Journal, Supplement, 243(2), 26 (2019).

M. A. Prieto et al., *The central parsecs of M87: jet emission and an elusive accretion disc*, MNRAS, 457, 3801–3816 (2016).

J. E. Pringle, *Model for Cygnus X-3*, Nature, 247(5435), 21–22 (1974).

D. Psaltis, N. Wex, & M. Kramer, *A Quantitative Test of the No-hair Theorem with Sgr A* Using Stars, Pulsars, and the Event Horizon Telescope*, Astrophysical Journal, 818(2), 121 (2016).

D. Psaltis et al., *A General Relativistic Null Hypothesis Test with Event Horizon Telescope Observations of the Black Hole Shadow in Sgr A**, Astrophysical Journal, 814, 115 (2015).

E. Quataert, *Radiatively Inefficient Accretion Flow Models of Sgr A**, Astronomische Nachrichten, 324(S1), 435–443 (2003).

E. Quataert, *A Dynamical Model for Hot Gas in the Galactic Center*, Astrophysical Journal, 613(1), 322–325 (2004).

E. Quataert & A. Gruzinov, *Constraining the Accretion Rate onto Sagittarius A* Using Linear Polarization*, Astrophysical Journal, 545(2), 842–846 (2000).

E. Quataert & R. Narayan, *Spectral Models of Advection-dominated Accretion Flows with Winds*, Astrophysical Journal, 520, 298–315 (1999).

M. J. Rees et al., *Ion-supported tori and the origin of radio jets*, Nature, 295, 17–21 (1982).

M. J. Reid et al., *VLBI observations of the nucleus and jet of M 87.*, Astrophysical Journal, 263, 615–623 (1982).

M. J. Reid et al., *Limits on the Position Wander of Sgr A**, Astrophysical Journal, 682(2), 1041–1046 (2008).

H. Reissner, *Über die Eigengravitation des elektrischen Feldes nach der Einsteinschen Theorie*, Annalen der Physik, 355(9), 106–120 (1916).

R. A. Remillard & J. E. McClintock, *X-Ray Properties of Black-Hole Binaries*, Annual Review of Astron and Astrophys, 44(1), 49–92 (2006).

S. M. Ressler, *Towards More Predictive Models of Galactic Center Accretion*, Ph.D. thesis, University of California, Berkeley (2019).

S. M. Ressler, E. Quataert, & J. M. Stone, *Hydrodynamic simulations of the inner accretion flow of Sagittarius A* fuelled by stellar winds*, MNRAS, 478, 3544–3563 (2018).

S. M. Ressler, E. Quataert, & J. M. Stone, *The surprisingly small impact of magnetic fields on the inner accretion flow of Sagittarius A* fueled by stellar winds*, MNRAS, 492(3), 3272–3293 (2020).

S. M. Ressler et al., *Electron thermodynamics in GRMHD simulations of low-luminosity black hole accretion*, MNRAS, 454, 1848–1870 (2015).

S. M. Ressler et al., *The disc-jet symbiosis emerges: modelling the emission of Sagittarius A* with electron thermodynamics*, MNRAS, 467(3), 3604–3619 (2017).

S. M. Ressler et al., *Ab Initio Horizon-Scale Simulations of Magnetically Arrested Accretion in Sagittarius A* Fed by Stellar Winds*, arXiv e-prints, arXiv:2006.00005 (2020).

C. S. Reynolds et al., *The matter content of the jet in M87: evidence for an electron-positron jet*, MNRAS, 283(3), 873–880 (1996).

A. Ricarte & J. Dexter, *The Event Horizon Telescope: exploring strong gravity and accretion physics*, MNRAS, 446, 1973–1987 (2015).

M. E. Rowan, L. Sironi, & R. Narayan, *Electron and Proton Heating in Transrelativistic Magnetic Reconnection*, Astrophysical Journal, 850, 29 (2017).

B. R. Ryan, J. C. Dolence, & C. F. Gammie, *bhlight: General Relativistic Radiation Magnetohydrodynamics with Monte Carlo Transport*, Astrophysical Journal, 807(1), 31 (2015).

B. R. Ryan et al., *Two-temperature GRRMHD Simulations of M87*, Astrophysical Journal, 864, 126 (2018).

G. B. Rybicki & A. P. Lightman, *Radiative processes in astrophysics* (1979).

A. Sadowski et al., *Energy, momentum and mass outflows and feedback from thick accretion discs around rotating black holes*, MNRAS, 436(4), 3856–3874 (2013).

A. Sadowski et al., *Radiative, two-temperature simulations of low-luminosity black hole accretion flows in general relativity*, MNRAS, 466(1), 705–725 (2017).

E. E. Salpeter, *Accretion of Interstellar Matter by Massive Objects.*, Astrophysical Journal, 140, 796–800 (1964).

R. J. Sault & J. P. Macquart, *Confirmation and Analysis of Circular Polarization from Sagittarius A**, Astrophysical Journal, Letters, 526(2), L85–L88 (1999).

R. Schödel et al., *A star in a 15.2-year orbit around the supermassive black hole at the centre of the Milky Way*, Nature, 419(6908), 694–696 (2002).

R. Schödel et al., *The mean infrared emission of Sagittarius A**, Astronomy and Astrophysics, 532, A83 (2011).

R. Schoedel et al., *Coordinated multi-wavelength observations of Sgr A**, ATNF Proposal (2007).

K. Schwarzschild, *Über das Gravitationsfeld eines Massenpunktes nach der Einsteinschen Theorie*, Sitzungsberichte der Königlich Preußischen Akademie der Wissenschaften (Berlin, pages 189–196 (1916).

E. Serabyn et al., *High-Frequency Measurements of the Spectrum of Sagittarius A**, Astrophysical Journal, Letters, 490(1), L77–L81 (1997).

B. Shahzamanian et al., *Polarized light from Sagittarius A* in the near-infrared K_s-band*, Astronomy and Astrophysics, 576, A20 (2015).

N. I. Shakura & R. A. Sunyaev, *Reprint of 1973A&A....24..337S. Black holes in binary systems. Observational appearance.*, Astronomy and Astrophysics, 500, 33–51 (1973).

S. L. Shapiro, *Accretion onto Black Holes: the Emergent Radiation Spectrum. III. Rotating (kerr) Black Holes*, Astrophysical Journal, 189, 343–352 (1974).

P. Sharma et al., *Electron Heating in Hot Accretion Flows*, Astrophysical Journal, 667, 714–723 (2007).

R. V. Shcherbakov, *Propagation Effects in Magnetized Transrelativistic Plasmas*, Astrophysical Journal, 688, 695–700 (2008).

R. V. Shcherbakov & L. Huang, *General relativistic polarized radiative transfer: building a dynamics-observations interface*, MNRAS, 410, 1052–1063 (2011).

R. V. Shcherbakov & J. C. McKinney, *Submillimeter Quasi-periodic Oscillations in Magnetically Choked Accretion Flow Models of SgrA**, Astrophysical Journal, Letters, 774(2), L22 (2013).

R. V. Shcherbakov, R. F. Penna, & J. C. McKinney, *Sagittarius A* Accretion Flow and Black Hole Parameters from General Relativistic Dynamical and Polarized Radiative Modeling*, Astrophysical Journal, 755, 133 (2012).

Z. Q. Shen et al., *VLBA Imaging of Sgr A* at 86 GHz*, in: J. Romney & M. Reid, eds., *Future Directions in High Resolution Astronomy*, vol. 340 of *Astronomical Society of the Pacific Conference Series*, page 263 (2005).

H. Shiokawa, *General-relativistic magnetohydrodynamics simulations of black hole accretion disks: Dynamics and radiative properties*, Ph.D. thesis, University of Illinois at Urbana-Champaign (2013).

H. Shiokawa et al., *Global General Relativistic Magnetohydrodynamic Simulations of Black Hole Accretion Flows: A Convergence Study*, Astrophysical Journal, 744(2), 187 (2012).

A. Soltan, *Masses of quasars.*, MNRAS, 200, 115–122 (1982).

Ł. Stawarz et al., *Dynamics and high-energy emission of the flaring HST-1 knot in the M 87 jet*, MNRAS, 370(2), 981–992 (2006).

J. M. Stone et al., *A Test Suite for Magnetohydrodynamical Simulations*, Astrophysical Journal, 388, 415 (1992).

J. M. Stone et al., *Far Infrared Variability of Sagittarius A*: 25.5 hr of Monitoring with Herschel*, Astrophysical Journal, 825(1), 32 (2016).

R. Takahashi, *Radiation hydrodynamics in Kerr space-time: equations without coordinate singularity at the event horizon*, MNRAS, 383(3), 1155–1165 (2008).

A. Tchekhovskoy, *HARMPI: 3D massively parallel general relativictic MHD code* (2019).

A. Tchekhovskoy, R. Narayan, & J. C. McKinney, *Black Hole Spin and The Radio Loud/Quiet Dichotomy of Active Galactic Nuclei*, Astrophysical Journal, 711(1), 50–63 (2010).

A. Tchekhovskoy, R. Narayan, & J. C. McKinney, *Efficient generation of jets from magnetically arrested accretion on a rapidly spinning black hole*, MNRAS, 418, L79–L83 (2011).

P. Tiede et al., *Spacetime Tomography Using The Event Horizon Telescope*, arXiv e-prints, arXiv:2002.05735 (2020).

G. Trap et al., *Concurrent X-ray, near-infrared, sub-millimeter, and GeV gamma-ray observations of Sagittarius A**, Astronomy and Astrophysics, 528, A140 (2011).

S. Trippe et al., *A polarized infrared flare from Sagittarius A* and the signatures of orbiting plasma hotspots*, MNRAS, 375(3), 764–772 (2007).

B. D. Turland, *Observations of M87 at 5 GHz with the 5-km telescope.*, MNRAS, 170, 281–294 (1975).

S. E. Vázquez & E. P. Esteban, *Strong-field gravitational lensing by a Kerr black hole*, Nuovo Cimento B Serie, 119(5), 489 (2004).

E. Velikhov, *Stability of an Ideally Conducting Liquid Flowing between Cylinders Rotating in a Magnetic Field*, Sov. Phys. Journal of Experimental and Theoretical Physics, 9(5), 995–998 (1959).

S. U. Viergutz, *Image generation in Kerr geometry. I. Analytical investigations on the stationary emitter-observer problem*, Astronomy and Astrophysics, 272, 355 (1993).

S. D. von Fellenberg et al., *A Detection of Sgr A* in the Far Infrared*, Astrophysical Journal, 862(2), 129 (2018).

I. Waisberg et al., *What stellar orbit is needed to measure the spin of the Galactic centre black hole from astrometric data?*, MNRAS, 476(3), 3600–3610 (2018).

I. R. Waisberg, *Optical interferometry of compact objects* (2019).

R. C. Walker et al., *The Structure and Dynamics of the Subparsec Jet in M87 Based on 50 VLBA Observations over 17 Years at 43 GHz*, Astrophysical Journal, 855(2), 128 (2018).

J. L. Walsh et al., *The M87 Black Hole Mass from Gas-dynamical Models of Space Telescope Imaging Spectrograph Observations*, Astrophysical Journal, 770(2), 86 (2013).

B. L. Webster & P. Murdin, *Cygnus X-1-a Spectroscopic Binary with a Heavy Companion ?*, Nature, 235(5332), 37–38 (1972).

G. R. Werner et al., *Non-thermal particle acceleration in collisionless relativistic electron-proton reconnection*, MNRAS, 473(4), 4840–4861 (2018).

C. J. White, E. Quataert, & O. Blaes, *Tilted Disks around Black Holes: A Numerical Parameter Survey for Spin and Inclination Angle*, Astrophysical Journal, 878(1), 51 (2019).

C. J. White, E. Quataert, & C. F. Gammie, *The Structure of Radiatively Inefficient Black Hole Accretion Flows*, Astrophysical Journal, 891(1), 63 (2020).

C. J. White, J. M. Stone, & C. F. Gammie, *An Extension of the Athena++ Code Framework for GRMHD Based on Advanced Riemann Solvers and Staggered-mesh Constrained Transport*, Astrophysical Journal, Supplement, 225(2), 22 (2016).

C. J. White, J. M. Stone, & E. Quataert, *A Resolution Study of Magnetically Arrested Disks*, Astrophysical Journal, 874(2), 168 (2019).

C. J. White et al., *The Effects of Tilt on the Images of Black Hole Accretion Flows*, arXiv e-prints, arXiv:2001.02361 (2020).

A. S. Wilson & Y. Yang, *Chandra X-ray Imaging and Spectroscopy of the M87 Jet and Nucleus*, in: *American Astronomical Society Meeting Abstracts*, vol. 199 of *American Astronomical Society Meeting Abstracts*, page 150.05 (2001).

G. Witzel et al., *Variability Timescale and Spectral Index of Sgr A* in the Near Infrared: Approximate Bayesian Computation Analysis of the Variability of the Closest Supermassive Black Hole*, Astrophysical Journal, 863, 15 (2018).

E. R. Wollman et al., *Ne II 12.8 micron emission from the galactic center. II.*, Astrophysical Journal, Letters, 218, L103–L107 (1977).

F. Yuan, S. Markoff, & H. Falcke, *A Jet-ADAF model for Sgr A**, Astronomy and Astrophysics, 383, 854–863 (2002).

F. Yuan & R. Narayan, *Hot Accretion Flows Around Black Holes*, Annual Review of Astron and Astrophys, 52, 529–588 (2014).

F. Yuan, E. Quataert, & R. Narayan, *Nonthermal Electrons in Radiatively Inefficient Accretion Flow Models of Sagittarius A**, Astrophysical Journal, 598, 301–312 (2003).

F. Yuan, E. Quataert, & R. Narayan, *On the Nature of the Variable Infrared Emission from Sagittarius A**, Astrophysical Journal, 606(2), 894–899 (2004).

F. Yusef-Zadeh et al., *A Multiwavelength Study of Sgr A*: The Role of Near-IR Flares in Production of X-Ray, Soft γ-Ray, and Submillimeter Emission*, Astrophysical Journal, 644, 198–213 (2006).

F. Yusef-Zadeh et al., *An Inverse Compton Scattering Origin of X-Ray Flares from Sgr A**, Astronomical Journal, 144(1), 1 (2012).

M. Zamaninasab et al., *Near infrared flares of Sagittarius A*. Importance of near infrared polarimetry*, Astronomy and Astrophysics, 510, A3 (2010).

R. T. Zavala & G. B. Taylor, *Faraday Rotation Measures in the Parsec-Scale Jets of the Radio Galaxies M87, 3C 111, and 3C 120*, Astrophysical Journal, Letters, 566(1), L9–L12 (2002).

R. T. Zavala & G. B. Taylor, *A View through Faraday's Fog: Parsec-Scale Rotation Measures in Active Galactic Nuclei*, Astrophysical Journal, 589, 126–146 (2003).

Y. B. Zel'dovich, *The Fate of a Star and the Evolution of Gravitational Energy Upon Accretion*, Soviet Physics Doklady, 9, 195 (1964).

J.-H. Zhao, G. C. Bower, & W. M. Goss, *Radio Variability of Sagittarius A*-a 106 Day Cycle*, Astrophysical Journal, Letters, 547(1), L29–L32 (2001).

V. Zhdankin et al., *Electron and Ion Energization in Relativistic Plasma Turbulence*, Physical Review Letters, 122(5), 055101 (2019).

R. Zylka et al., *Anatomy of the Sagittarius A complex. IV. SGR A* and the Central Cavity revisited.*, Astronomy and Astrophysics, 297, 83–97 (1995).

Acknowledgements

This work was supervised by Prof. Dr. Reinhard Genzel. Thank you for your support, your scientific insight and your sincere advice.

To my advisor Jason Dexter, thank you for your patience, for the positive and encouraging words and for always making the time to listen to my questions and interests. Thank you for your valuable mentorship and for caring.

I would like to thank the Consejo Nacional de Ciencia y Tecnología (CONACYT) and the Deutscher Akademischer Austauschdienst (DAAD) for their financial support during my PhD.

Many thanks to the Infrared group, particularly the GCs, for the motivating work atmosphere, collaborations and stimulating scientific discussions. Linda Tacconi, thank you for your good advice on how to go about in the academic life. Many thanks to Tim de Zeeuw, Frank Eisenhauer and Stefan Gillessen for being supportive and always offering useful feedback. Thank you so much to Susanne Dengler and Adriane Richter for all your valuable help with getting around in the office and getting things done.

To the past and present members of the "Coffee after lunch gang", thanks for the weird discussions that we were definitely not qualified enough to hold, but still enjoyed having.

Michi, thank you for listening and for your tremendous help with all kinds of problems. Thank you for going through calculations with me, for the useful feedback and above all, thank you for teaching me how to ski and then leaving me stranded on a mountain.

Hannah, thank you for being supportive, for listening and celebrating our accomplishments. We'll always have our birthday beers.

Many thanks go to my other pals from Munich Miriam, Chiarita (tigli!), Lili, Linda, Vlas, Thales and Ema. To the Gsus4 members (...terrible name guys), Tony, John and Robin. You rock! Thanks for the memorable pizza afternoon jams. To my fellow Scuba Drivers, specially Peter, Sarah, Barbara, Blair and Alex. Thank you for the after jam evenings at Café Mozart, for all the laughs and for being such a great company with whom to be creative and push the limits of our, often crazy, imaginations. A la bandita latina de Munich, Mariano, Ismael y Conrado; y a mis grandes amigos de México Fecha, Cuadernito, Santiago y Srita. Torres. Luego nos vemos para echar el chisme.

Agradezco especialmente a mis papás Angélica y José y a mis hermanos Angélica y Juan Ray. Muchísimas gracias por siempre apoyarme incondicionalmente, por impulsarme para salir adelante y superarme, por su confianza y por su cariño. Me enorgullece ser parte de esta familia. Esta tesis se las dedico a ustedes.

Vielen Dank Gudrun, Rolf und Malte für das Lächeln und weil ich mich bei euch immer willkommen fühle.

Annie, ich bin so froh dass du in mein Leben bist. Du bist die beste Überraschung, die ich je hatte. Von ganzem Herzen danke ich dir für die Unterstützung, deine schöne Gesellschaft und deine Liebe.